Dissertation

submitted to the

Combined Faculties of the Natural Sciences and Mathematics

of the Ruperto-Carola-University of Heidelberg, Germany

for the degree of

Doctor of Natural Sciences

Put forward by

Dipl.-Phys. Max Neuner

born in: Heidelberg, Germany

Oral examination: 21.06.2017

Determination of the b-hadron production cross-section and measurement of CP violation in $B_s^0 \to \phi\phi$ decays at the LHCb experiment

Referees: Prof. Dr. Ulrich Uwer

Prof. Dr. Klaus Reygers

Abstract: The production cross-sections of beauty hadrons in proton-proton collisions at centre-of-mass energies of $\sqrt{s} = 7\,\text{TeV}$ and $\sqrt{s} = 13\,\text{TeV}$ are determined with semileptonic b-hadron decays in the first part of this thesis. Using the collected data samples that correspond to integrated luminosities of $\mathcal{L} = 284\,\text{pb}^{-1}$ and $\mathcal{L} = 4.60\,\text{pb}^{-1}$, the cross-sections in the LHCb acceptance, the range in pseudorapidity η from 2 to 5, are determined to be $69.0 \pm 0.3(\text{stat}) \pm 6.1(\text{syst})\,\mu\text{b}$ and $137.5 \pm 1.1(\text{stat}) \pm 12.8(\text{syst})\,\mu\text{b}$ at $\sqrt{s} = 7\,\text{TeV}$ and $\sqrt{s} = 13\,\text{TeV}$, respectively. A good agreement of the η-dependent cross-sections and their ratios is found between the data and theoretical fixed-order next-to-leading log (FONLL) calculations. The production rate of b hadrons allows for precision measurements of physics parameters in rare b-hadron decays that offer a great sensitivity to test the quantum corrections predicted by the Standard Model and to probe possible contributions from physics beyond the Standard Model. Time-dependent CP violation in $B_s^0 \to \phi\phi$ decays is a sensitive observable which could be influenced by new heavy degrees of freedom contributing to the loop-induced B_s^0 mixing and decay processes. The measurement of CP violation in this decay mode is performed in the second part of this thesis with the LHC Run I dataset corresponding to an integrated luminosity of $3\,\text{fb}^{-1}$. The CP-violating phase is determined to be $\phi_s(B_s^0 \to \phi\phi) = -0.17 \pm 0.15\,(\text{stat}) \pm 0.03\,(\text{syst})\,\text{rad}$ which is compatible with Standard-Model predictions of zero. No evidence for physics beyond the Standard Model is found. Most of LHCb's current measurements are limited by statistical uncertainties. To overcome this shortcoming, LHCb plans to upgrade the detector after 2018. Starting in 2021, the detector can be operated at a higher instantaneous luminosity with a triggerless 40 MHz readout system. Amongst others, the current main tracking detector will be replaced by a scintillating fibre detector. The third part of this thesis presents the measurement of the performance of prototype modules of this tracking detector. The spatial resolution is determined to be $77.2 \pm 1.3\,\mu\text{m}$ and the single-hit detection efficiency is measured as $98.8 \pm 0.1\%$, which meets the requirements of the new tracking detector.

Kurzfassung: Im ersten Teil der vorliegenden Arbeit wird der Produktionswirkungsquerschnitt von b Hadronen in Proton-Proton Kollisionen bei Schwerpunktsenergien von $\sqrt{s} = 7\,\text{TeV}$ und $\sqrt{s} = 13\,\text{TeV}$ mit Hilfe semileptonischer b Hadronzerfällen gemessen. Mit Datensätzen, die integrierten Luminositäten von $\mathcal{L} = 284\,\text{pb}^{-1}$ bzw. $\mathcal{L} = 4.60\,\text{pb}^{-1}$ entsprechen, werden die Wirkungsquerschnitte für einen Pseudorapiditätsbereich η von 2 bis 5, zu 69.0 ± 0.3 (stat) ± 6.1 (syst) μb bzw. 137.5 ± 1.1 (stat) ± 12.8 (syst) μb für $\sqrt{s} = 7\,\text{TeV}$ bzw. $\sqrt{s} = 13\,\text{TeV}$ bestimmt. Die η-Abhängigkeit der beiden Wirkungsquerschnitte und deren Verhältnis stimmen mit theoretischen fixed-order next-to-leading log (FONLL) Berechnungen überein. Diese hohe Produktionsrate von b Hadronen ermöglicht Präzisionsmessungen von physikalischen Parametern in sehr seltenen Zerfällen von b Hadronen. Viele dieser Zerfälle sind im Standardmodell nur aufgrund von Quantenkorrekturen möglich. Mögliche Beiträge neuer Physik jenseits des Standardmodells modifizieren die Quantenkorrekturen und führen zu messbaren Abweichungen in den Observablen. Die zeitabhängige CP Verletzung in $B_s^0 \to \phi\phi$ Zerfällen ist eine Observable, die eine hohe Sensitivität für Beiträge neuer Physik aufweist. Die Messung der zeitabhängigen CP Verletzung für diesen Zerfall wird im zweiten Teil dieser Arbeit anhand des Datensatzes des LHC Run I mit einer integrierten Luminosität von $3\,\text{fb}^{-1}$ vorgestellt. Die CP-verletzende Phase wird zu $\phi_s(B_s^0 \to \phi\phi) = -0.17 \pm 0.15$ (stat) ± 0.03 (syst) rad bestimmt, was im Einklang mit der Standardmodellvorhersage von Null steht. Es werden somit keine Hinweise auf Beiträge neuer Physik gefunden. Die meisten derzeitigen LHCb Messungen sind durch statistische Unsicherheiten limitiert. Um dieses Defizit zu überwinden, wird der LHCb Detektor bis Anfang 2021 umgebaut, damit er bei einer höheren Luminosität und einer Datenausleserate von 40 MHz betrieben werden kann. Unter anderem wird der Hauptspurrekonstruktionsdetektor durch einen Detektor mit szintillierenden Fasern ersetzt. Der dritte Teil dieser Arbeit präsentiert die Messung der Eigenschaften von Prototypen eines solchen Detektors. Die Ortsauflösung wird zu $77.2 \pm 1.3\,\mu\text{m}$ und die Detektionseffizienz eines einzelnen Teilchens zu $98.8 \pm 0.1\%$ bestimmt. Damit erfüllt er die Anforderungen, die an den neuen Detektor gestellt werden.

Contents

Preface

This thesis has been prepared using data of the LHCb experiment, a collaboration of about 800 scientists and engineers. It would have been impossible to perform the analyses without the implicit help of many.

The determination of the b-hadron production cross-section presented in Part I has been performed within the corresponding working group. The major analysis work was performed by three students including the author. The author has contributed to all analysis steps documented in this thesis. The measurements were published in Phys. Rev. Lett. 118, 052002 [1] and documented in detail in the internal note [2] with the author as one of the main contributors.

The measurement of CP violation in $B_s^0 \to \phi\phi$ decays presented in Part II is the work of four main proponents including the author. The main contributions of the author were the determination of the decay-time resolution, the implementation of the fit procedure to extract the results and some particular evaluations of the systematic uncertainties. The fit procedure was implemented separately by two students including the author. The fit procedure used by the author had been developed for the measurement of CP violation in $B_s^0 \to J/\psi\,\phi$, documented in Refs. [3] and [4]. It was modified by the author to be applied to $B_s^0 \to \phi\phi$ decays. The selection of the $B_s^0 \to \phi\phi$ signal candidates and the determination of the decay-time acceptance is the joint work, amongst others, of a master student and the author. It is documented in Ref. [5]. The measurement of CP violation in $B_s^0 \to \phi\phi$ decays was published in Phys. Rev. D 90, 052011 [6] and documented in detail in the internal note [7] with the author as one of the main contributors.

The measurement of the Scintillating Fibre Tracker performance described in Part III is based on work of the LHCb Scintillating Fibre Tracker Collaboration. The data has been collected by a large group of people taking shifts during the test-beam campaign including the author. The author is one of the main contributors to the software that processed and analysed the test-beam data. The analysis presented in this thesis was solely performed by the author. The results of the test-beam campaign were documented in the public note [8] with the author as one of the main contributors.

1 Introduction

For the last decades, the Standard Model of particle physics has been very successful in explaining the fundamental physics at the quantum scale and predicting the observations of particle-physics experiments. However, it is not a complete theory that explains all observed phenomena in nature and is insufficient to describe, amongst others, the existence of dark matter and dark energy, the masses of neutrinos and the magnitude of the asymmetry of matter over anti-matter in the universe. Mathematically, it exhibits inconsistencies such as the hierarchy problem and the fine-tuning of parameters.

The Large Hadron Collider (LHC) in Geneva, the world's largest proton accelerator, is designed to reach energy scales that might reveal the limits of the Standard Model. New theories can be tested that may answer open questions of particle physics and cosmology. During the LHC Run I in the years 2011 and 2012, the exploration of the regimes at centre-of-mass energies of 7 TeV and 8 TeV provided numerous exciting results, including the confirmation of the existence of a Higgs-like particle [9, 10]. In 2015, the LHC began to collide protons at the energy of 13 TeV which opens a new era of physics to explore.

The LHCb experiment, one of the four major experiments at the LHC, is designed to study the decays of charm and beauty hadrons that are produced at a high rate of about 10^{11} $b\bar{b}$ pairs per fb^{-1} of integrated luminosity. The cross-section for the production of heavy-flavour hadrons, the process that the LHCb detector has been built for, is not only useful to estimate the expected amount of decays of interest and ascertain future sensitivities to SM parameters. It is also of great interest to the theory community as the production through gluon-fusion processes provides a test of the knowledge of Quantum Chromodynamics (QCD) [11]. The LHCb detector, with its unique forward design, probes gluons that have highly asymmetric momentum fractions. In part I of this thesis, the b-hadron production cross-section is measured with semileptonic b-hadron decays at centre-of-mass energies of 7 TeV and 13 TeV. In the ratio of cross-sections, the large theoretical uncertainties partially cancel which allows for a precise comparison of the data with theory predictions using fixed-order plus next-to-leading log (FONLL) calculations [12].

The large number of produced b hadrons allows for the study of decay modes that happen rarely, up to branching fractions of $\sim 10^{-9}$, but offer sensitivity to physics phenomena beyond the description of the Standard Model. One of these interesting decays is the channel $B_s^0 \to \phi\phi$ in which time-dependent CP violation can arise from the interference between the direct decay and the decay after mixing of the b meson. In the Standard Model, CP violation is expected to be small as the contributions to the loop-induced B_s^0 mixing and *penguin decay* diagrams almost exactly cancel. However, since only virtual particles are exchanged in the loops, they are very sensitive to new heavy degrees of freedom whose mass scale can be much higher than the actual accessible energy scale. Due to the different loop structure, these unknown contributions can be different in the mixing and the decay amplitude. Any non-trivial CP violation would be a hint for New Physics. The measurement of CP violation in $B_s^0 \to \phi\phi$ decays is presented in part II of this thesis.

Among the many interesting results of the LHC Run I, none of them showed clear evidence for a breakdown of the Standard-Model description in the observed energy range within the current uncertainty. It is the goal of the coming years to further improve the statistical sensitivity of the key results and put more stringent limits on possible new effects. The heavy-flavour production rate at 13 TeV is about twice as high, but the readout rate of the LHCb front-end electronics is limited to 1 MHz and the proton-proton interaction rate is kept low because the detector cannot cope with higher particle occupancies. Therefore, the LHCb detector will undergo a major upgrade after Run II during the Long Shutdown 2, from the end of 2018 until the end of 2020. This will allow for an operation at a five times higher instantaneous luminosity of $\mathcal{L} = 2 \cdot 10^{33}\,\mathrm{cm}^{-2}\mathrm{s}^{-1}$. Additionally, the data will be recorded without a hardware trigger system at the full collision rate of 40 MHz. Especially the trigger system to select hadrons suffers from large inefficiencies such that the triggerless readout will largely improve the reconstruction and selection efficiency of the four-hadronic final state of the $B_s^0 \to \phi\phi(\to K^+K^-K^+K^-)$ decay mode. The upgrade will significantly extend the statistical precision of the experiment. The current main tracking detector consists of a silicon-based Inner Tracker and an Outer Tracker built with 5 mm straw tubes. It will be replaced by a single technology using low-mass scintillating fibres with high granularity. Part III of this thesis presents performance results, namely light yield, spatial resolution and single-hit efficiency measurements, of prototypes of this Scintillating Fibre (SciFi) Tracker, obtained during a test-beam campaign at the SPS accelerator at CERN in May 2015.

This thesis is organised as follows: Chapter 2 describes the Standard Model, the theoretical framework of particle physics. The LHCb experiment and its detector components are presented in Chap. 3, followed by a review of commonly used methods to extract physics parameters in Chap. 4. The actual measurements are covered in Parts I to III. Part I presents the determination of the b-hadron production cross-section at centre-of-mass energies of 13 TeV and 7 TeV and their ratio. The measurement of CP violation in the b-hadron decay $B_s^0 \to \phi\phi$ is performed in Part II. The last Part III shows the results of performance test of the upgrade Scifi tracking detector, followed by some concluding remarks.

2 Description of the theoretical framework

This chapter presents a short overview of the Standard Model, the theory framework for particle physics, which was developed in Refs. [13–15]. As the research at the LHCb experiment is focused on the decays of heavy-flavour hadrons, this introduction will be restricted to the CKM mechanism which is responsible for transitions between quarks. Further specific details needed for the analyses will be presented in the individual Parts I and II.

2.1 The Standard Model of Particle Physics

The Standard Model is a relativistic renormalisable quantum field theory that forms the basis of particle physics. It comprises all elementary particles, the building blocks of nature, and three of the four fundamental interactions between them: the strong interaction which is described by the theory of quantum chromodynamic (QCD) [11] and the weak and the electromagnetic interactions that are combined to the Glashow-Salam-Weinberg electroweak theory [13–15]. The following brief overview is based on review articles taken from Refs. [16–18].

2.1.1 Elementary Particles

The elementary particles of the Standard Model can be divided into two groups, the fermions with spin 1/2 that make up matter and the integer-spin bosons of which the gauge bosons mediate the fundamental forces between them. Each fermion has an antiparticle with the same physical properties except for the opposite charge. Depending on how they interact, the fermions are classified as quarks and leptons and further grouped into three generations as shown in Table 2.1. Whereas leptons only interact via the electromagnetic and the weak interaction, quarks also carry colour charge and interact via the strong interaction. Each generation contains two fermions, an up-type and a down-type quark with electric charges of $+2/3e$ and $-1/3e$, respectively, and a charged and a neutral lepton. The charged leptons are the electrons, muons and taus and the neutral leptons are the corresponding neutrinos. The properties stated are taken from the PDG [19] and the quark masses refer to the current masses of the quarks themselves in contrast to the constituent masses when they are in bound states. The masses of the fermions increase with the generation, thus the fermions of the first generation do not decay and form atoms.

The gauge bosons of the Standard model are the photon γ, the gluon, the W^+/W^- bosons and the Z boson which have spin 1. The massless photon couples to the electric charge but has no charge itself. The weak interaction is mediated by massive bosons, the charged W^+/W^- and the neutral Z, that couple to the weak charge, the flavour. The massless gluons mediate the strong interaction and couple to the colour charge of the quarks, red, green and blue. Having a colour charge themselves, gluons couple to other

Table 2.1: The fermions of the Standard Model with properties taken from [19].

		Quarks			Leptons	
generation	**type**	**charge**[e]	**mass**	**type**	**charge**[e]	**mass**
I	u	$+2/3$	1.8 - 2.8 MeV/c^2	e	-1	511 keV/c^2
	d	$-1/3$	4.3 - 5.2 MeV/c^2	ν_e	0	< 2 eV/c^2
II	c	$+2/3$	1.27 ± 0.03 GeV/c^2	μ	-1	105.7 MeV/c^2
	s	$-1/3$	96^{+8}_{-4} MeV/c^2	ν_μ	0	< 2 eV/c^2
III	t	$+2/3$	173.21 ± 0.87 GeV/c^2	τ	-1	1777 MeV/c^2
	b	$-1/3$	4.15 - 4.70 GeV/c^2	ν_τ	0	< 2 eV/c^2

gluons. Since free particles are found in a colour-neutral state, gluons carry a combination of colour and anti-colour charges in a colour-octet state. Table 2.2 lists the bosons of the Standard Model. The recently discovered Higgs boson, H^0 [9, 10], is a scalar boson and generates the particle masses through its couplings.

Table 2.2: Bosons of the Standard Model with properties taken from [19]. The gauge bosons, the photon γ, the gluon, the W^+/W^- bosons and the Z boson mediate the fundamental forces and the scalar Higgs boson generates the masses of the leptons and quarks.

type	**mass**	**interaction**
γ(photon)	0	electomagnetic
gluon	0	strong
$W^\pm$	80.39 GeV/c^2	weak
Z	91.19 GeV/c^2	
H^0	125.09 ± 0.24 GeV/c^2	–

The gauge symmetry group of the Standard Model is $\mathrm{SU(3)_C} \otimes \mathrm{SU(2)_L} \otimes U(1)_\mathrm{Y}$. Each symmetry is related to a quantum number that is conserved in the corresponding interaction. The strong force describes interactions between particles with the color quantum number C, the quarks and gluons, and the theory is therefore called quantum chromodynamics (QCD). It is defined by the local symmetry group $\mathrm{SU(3)_C}$. As a result of the structure of the gauge group, quarks do not appear as free particles, but only in bound states of so-called hadrons. The energy needed to pull quarks apart is so large that a pair of new quarks is created before quarks become free. This property is referred to as *confinement*. Bound states of a quark and an anti-quark are called mesons and baryons are composites of three quarks.

The electromagnetic and the weak interactions are unified to the electroweak interaction under an $\mathrm{SU(2)_L} \otimes U(1)_\mathrm{Y}$ gauge group. The $\mathrm{SU(2)_L}$ symmetry is called the weak isospin group with the weak isospin, I, and its third component I_3. Left-handed (L) fermions have

$I = 1/2$ whereas right-handed fermions have $I = 0$. The $U(1)_{\mathrm{Y}}$ group is related to the weak hypercharge Y. The symmetries introduce three W bosons, W_1, W_2 and W_3, associated to $\mathrm{SU}(2)_{\mathrm{L}}$ and the B boson from $U(1)_{\mathrm{Y}}$. Due to the Higgs mechanism, the gauge symmetry is spontaneously broken down into $U(1)_{\mathrm{em}}$ with the electromagnetic charge $Q = Y/2 + I_3$. Linear combinations of the massless W_1 and W_2 bosons form the massive W^+/W^- bosons which are responsible for charged-current weak interactions of left-handed fermions. The uncharged photon and the Z bosons are formed by linear combinations of the W_3 and B bosons, of which the Z boson mediates neutral-current weak interactions of left-handed and right-handed fermions. The photon is the massless gauge boson of the unbroken electromagnetic symmetry group. The Higgs boson is the quantum excitation of the Higgs field.

2.1.2 Introduction to flavour physics

Similar to the gauge bosons, the quarks acquire mass through the interaction with the Higgs field. After electroweak symmetry breaking, so-called Yukawa terms in the Lagrangian give rise to quark masses [18]:

$$\mathcal{L}_{\mathrm{Y}} = -\frac{v}{\sqrt{2}}\left(\bar{d}'_{\mathrm{L}} Y_{\mathrm{d}} d'_{\mathrm{R}} + \bar{u}'_{\mathrm{L}} Y_{\mathrm{u}} u'_{\mathrm{R}}\right) + h.c., \tag{2.1}$$

where the quark fields, $u'_{\mathrm{L/R}}$ and $d'_{\mathrm{L/R}}$, refer to the electroweak eigenstates of the left-handed and right-handed up-type and down-type quarks, respectively, and $\bar{q}'_{\mathrm{L/R}}$ denotes the corresponding anti-quark field. The Yukawa matrices, Y_{d} and Y_{u}, are three-by-three complex matrices. Since their off-diagonal elements are non-zero, the mass eigenstates, $q_{\mathrm{L/R}}$, of the quarks are not equal to the electroweak eigenstates, $q'_{\mathrm{L/R}}$, and they are obtained from unitary transformations, $u_{\mathrm{L/R}} = V_{\mathrm{L/R,u}} u'_{\mathrm{L/R}}$ and $d_{\mathrm{L/R}} = V_{\mathrm{L/R,d}} d'_{\mathrm{L/R}}$, with unitary matrices $V_{\mathrm{L/R,u}}$ and $V_{\mathrm{L/R,d}}$. The unitary matrices also appear in transitions between up-type and down-type quarks via charged-current interactions. Defining the Cabbibo-Kobayashi-Maskawa [20] matrix as $V_{\mathrm{CKM}} = V_{\mathrm{L,u}} V^{\dagger}_{\mathrm{L,d}}$, the Lagrangian of the charged current is written as

$$\mathcal{L}_{\mathrm{cc}} = -\frac{g_2}{\sqrt{2}}\left(\bar{u}_{\mathrm{L}} \gamma^{\mu} W^{+}_{\mu} V_{\mathrm{CKM}} d_{\mathrm{L}} + \bar{d}_{\mathrm{L}} \gamma^{\mu} W^{-}_{\mu} V^{\dagger}_{\mathrm{CKM}} u_{\mathrm{L}}\right). \tag{2.2}$$

The non-trivial off-diagonal elements of the CKM matrix allow for transitions between quarks of different generations and the notation is

$$V_{\mathrm{CKM}} = \begin{pmatrix} V_{ud} & V_{us} & V_{ub} \\ V_{cd} & V_{cs} & V_{cb} \\ V_{td} & V_{ts} & V_{tb} \end{pmatrix}. \tag{2.3}$$

The diagonal elements are close to 1 and the off-diagonals are small so that transitions within the same generation are strongly preferred. As a product of unitary matrices, the CKM matrix is unitary itself, $V_{\mathrm{CKM}} V^{\dagger}_{\mathrm{CKM}} = 1$, and the number of parameters is nine: three angles and six complex phases of which five can be absorbed as unobservable relative quark phases. This results in 4 parameters, the three mixing angles, θ_{12}, θ_{13} and θ_{23}, and the phase δ. A parameterisation of the CKM matrix that reflects the hierarchy of the matrix elements was proposed by Lincoln Wolfenstein in Ref. [21] that expresses the parameters

according to their absolute values in expansions of a small parameter λ:

$$\begin{aligned} \sin\theta_{12} &= \lambda \\ \sin\theta_{23} &= A\lambda^2 \\ \sin\theta_{13}e^{-i\delta} &= A\lambda^3\ (\rho - i\eta), \end{aligned}$$

where λ, A, ρ and η are the four Wolfenstein parameters. The CKM matrix takes the form

$$V_{\mathrm{CKM}} = \begin{pmatrix} 1-\frac{\lambda^2}{2}-\frac{\lambda^4}{8} & \lambda & A\lambda^3(\rho - i\eta) \\ -\lambda & 1-\frac{\lambda^2}{2}-\frac{\lambda^4}{8}(1\ +\ 4A^2) & A\lambda^2 \\ A\lambda^3(1-\rho-i\eta) & -A\lambda^2+\frac{1}{2}A\lambda^4\ (1-2\ (\rho+i\eta)) & 1-\frac{1}{2}A^4\ \lambda^4 \end{pmatrix}.$$

With the measured values of λ and A of approximately 0.23 and 0.82 [19], the diagonal elements are close to 1 and the small off-diagonal elements are on the order of λ^2 and λ^3, respectively.

Unitarity of the CKM matrix results in six equations for the off-diagonal elements that represent so-called unitarity triangles in the complex plane, for example

$$V_{ud}V_{ub}^* + V_{cd}V_{cb}^* + V_{td}V_{tb}^* = 0, \tag{2.4}$$

which is referred to as the "B_d^0" triangle because its elements can be obtained from measurements of B_d^0 decays. It is drawn in Fig. 2.1 where the sides are normalised to $V_{cd}V_{cb}^*$. The generalised parameters, $\bar{\rho}$ and $\bar{\eta}$, are defined by the location of the apex of the triangle and can be approximated by $\rho(1-1/2\lambda^2)$ and $\eta(1-1/2\lambda^2)$, respectively.

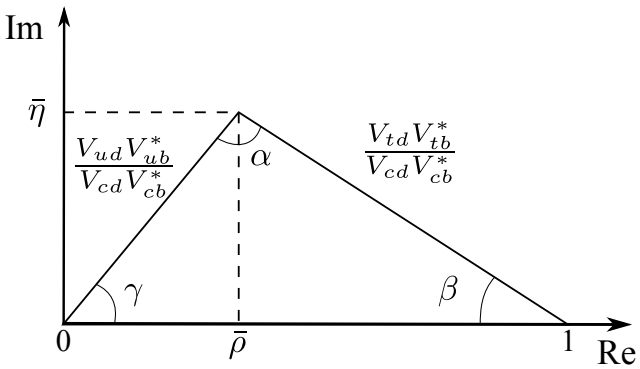

Figure 2.1: "B_d^0" unitarity triangle, defined by Eq. 2.4 with normalising the side length to $V_{cd}V_{cb}^*$.

The three angles of the triangle are defined as

$$\alpha \equiv arg\left(-\frac{V_{td}V_{tb}^*}{V_{ud}V_{ub}^*}\right), \qquad \beta \equiv arg\left(-\frac{V_{cd}V_{cb}^*}{V_{td}V_{tb}^*}\right), \qquad \gamma \equiv arg\left(-\frac{V_{ud}V_{ub}^*}{V_{cd}V_{cb}^*}\right). \tag{2.5}$$

The corresponding angle β_s in the "B_s^0" triangle is given by

$$\beta_s \equiv arg\left(-\frac{V_{ts}V_{tb}^*}{V_{cs}V_{cb}^*}\right). \tag{2.6}$$

Using these angles and the flavour representation, the CKM matrix can be approximated by

$$V_{\mathrm{CKM}} = \begin{pmatrix} |V_{ud}| & |V_{us}| & |V_{ub}|\, e^{-i\gamma} \\ -|V_{cd}| & |V_{cs}| & |V_{cb}| \\ |V_{td}|\, e^{-i\beta} & -|V_{ts}|\, e^{i\beta_s} & |V_{tb}| \end{pmatrix} + \mathcal{O}(\lambda^5), \tag{2.7}$$

where in this order only, the elements V_{ub}, V_{td} and V_{ts} have non-trivial imaginary parts.

The CP transformation is defined as the consecutively application of the charge (C) transformation, which converts particles into anti-particles, and the parity (P) transformation, that inverts the spatial coordinates. When the Lagrangian of the charged current interaction in Equation 2.2 is CP-transformed,

$$\mathcal{L}_{\mathrm{cc}}^{\mathrm{CP}} = -\frac{g_2}{\sqrt{2}}\left(\bar{d}_{\mathrm{L}}\gamma^{\mu}W_{\mu}^{-}V_{\mathrm{CKM}}^{\mathrm{T}}\tilde{u}_{\mathrm{L}} + \bar{u}_{\mathrm{L}}\gamma^{\mu}W_{\mu}^{+}V_{\mathrm{CKM}}^{*}d_{\mathrm{L}}\right), \tag{2.8}$$

one can see that CP symmetry is violated if $V_{\mathrm{CKM}} \neq V_{\mathrm{CKM}}^*$, i.e. the phase is not zero. Hence, CP violation is introduced by a non-trivial complex phase of the CKM matrix.

2.1.3 Experimental status of the unitarity triangles

A large variety of flavour-physics measurements have been performed to determine the CKM-matrix elements and over-constrain the unitarity triangles. Figure 2.2 shows the experimental status of the "B_d^0" and the "B_s^0" triangles, presented at ICHEP 2016. The length of the left side depends on the CKM-matrix elements $|V_{ub}|^2$ and $|V_{cb}|^2$ that are obtained from branching fraction measurements of semileptonic b-hadron decays, $B \to l\nu h$, where h refers to a hadron with a u or a c quark. The length of the right side of the triangles is determined with measurements of the mixing frequencies, Δm_s and Δm_d, of b-hadron mixing. The angles are obtained from CP-violation measurements in b-meson decays. Neutral kaon-physics experiments are used to constrain the apex of the triangles. All measurements are compatible with the Standard Model.

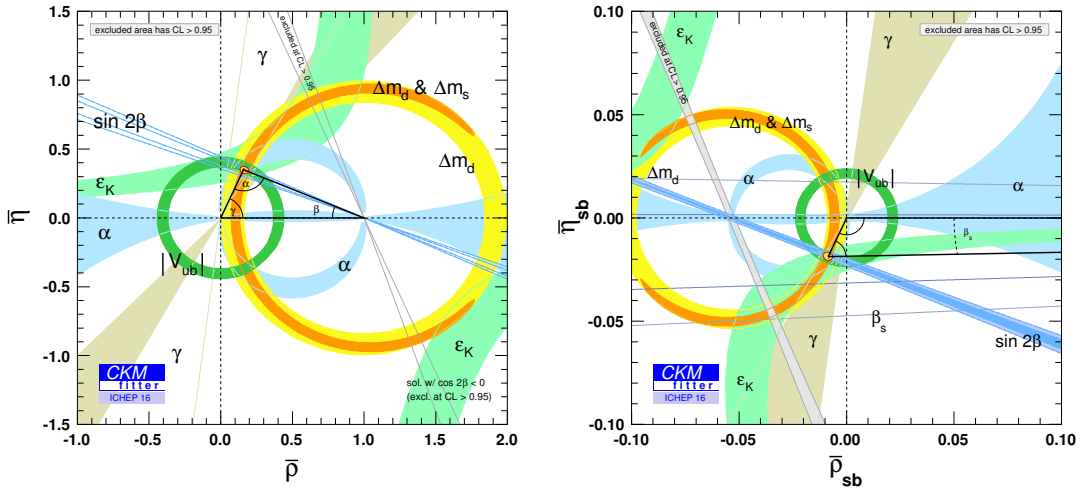

(a) (b)

Figure 2.2: Current experimental status of the unitarity triangles, (a) the "B_d^0" triangle and (b) the "B_s^0" triangle. The red hashed region of the global combination corresponds to 68% CL. Both figures are taken from Ref. [22]

3 The LHCb experiment

Although it is known that the Standard Model is not a complete theory that describes all phenomena in nature, its predictions have not been directly disproved in particle-physics experiments. The Large Hadron Collider (LHC) is built to explore the never-reached energy region where new phenomena may become relevant. The Large Hadron Collider beauty (LHCb) experiment, one of the four major experiments at the LHC, is designed to perform precision measurements of Standard-Model parameters in hadronic decays. This chapter presents the LHCb detector with its subcomponents and describes how relevant decays are reconstructed.

3.1 The Large Hadron Collider

The Large Hadron Collider (LHC) is the world's largest particle accelerator that collides protons at a maximum centre-of-mass energy of $\sqrt{s} = 14\,\text{TeV}$[1] at an instantaneous luminosity of $\mathcal{L} = 2 \cdot 10^{34}\,\text{cm}^{-2}\text{s}^{-1}$ [23]. Instead of protons, it can also collide heavy lead ions. The LHC ring has a circumference of approximately 27 km which is built underground below the Swiss-French border near the town of Geneva. The proton beams are bundled in 2808 bunches, each with approximately 10^{11} protons, with a bunch spacing of 25 ns. This results in a bunch-crossing rate of 40 MHz. Collisions take place at four interaction points where the experiments, ATLAS, CMS, ALICE and LHCb, are located. ATLAS and CMS are multi-purpose experiments and ALICE is designed to study heavy-ion collisions.

The LHCb experiment studies the decays of charm and beauty hadrons that are copiously produced in proton-proton collisions. The production cross-section of b-hadrons was measured to be $284 \pm 20 \pm 49$ μb [24] at a centre-of-mass energy of 7 TeV. Heavy-flavour hadrons are predominantly produced in gluon-fusion processes which are described in detail in Part I. Due to the high centre-of-mass energy of the protons, the related gluons have highly asymmetric momentum fractions such that the hadrons are boosted along the beam direction, forward and backward, as it is shown for the simulated production of $b\bar{b}$ quark pairs at a centre-of-mass energy of 14 TeV in Fig. 3.1. This is the reason why the LHCb detector is built as a single-arm forward spectrometer with an angular coverage of 10-300 mrad in the horizontal bending plane and 10-250 mrad in the vertical non-bending plane [25]. This corresponds to a pseudorapidity, η[2], of approximately $1.6 < \eta < 4.9$.

[1] not yet reached

[2] The pseudorapidity is defined as $\eta = -\log(\tan\frac{\theta}{2})$, where θ denotes the angle of the flight direction of the particles relative to the beam axis.

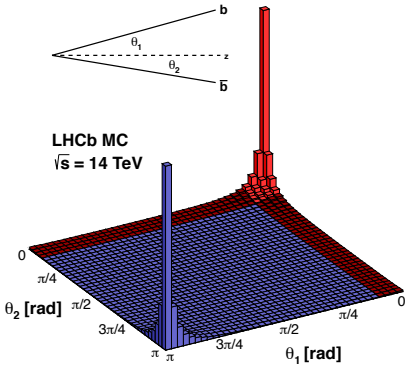

Figure 3.1: Simulated two-dimensional polar angle distribution of produced $b\bar{b}$ quark pairs at a centre-of-mass energy of 14 TeV. The red bars refers to the LHCb acceptance. The figure is taken from Ref. [26]

3.2 The LHCb detector

Due to the longitudinal boost and the relatively long lifetime of charm and b hadrons of about 1 ps, their flight distances from the proton-proton vertex to the decay vertices are of the order of 1 cm. In order to resolve the displaced decay vertex, the LHCb detector has a very good vertex resolution which is provided by the Vertex Locator (VELO), a silicon strip detector that is mounted around the interaction region. Signal decays are identified via the invariant mass of the final-state particles, thus the momenta are measured to high precision using a dipole magnet and a tracking system. Furthermore, the LHCb detector profits from a hadronic particle identification system, consisting of two Ring-Imaging Cherenkov detectors, to separate kaons from pions and protons in order to properly identify the signal decays.

In contrast to the larger experiments, ATLAS and CMS, LHCb is operated at a lower instantaneous luminosity of $\mathcal{L} = 2 \cdot 10^{32}\,\mathrm{cm}^{-2}\mathrm{s}^{-1}$ by slightly separating the colliding beams and focusing them less strongly compared to the other experiments[3]. The average number of proton-proton interactions per bunch crossing is about 1.4 which simplifies the association of the primary and decay vertices. Additionally, the occupancy of the detector is lower which reduces combinatorial background and allows for a more efficient isolation of the decay of interest. Nevertheless, approximately $3 \cdot 10^{11}$ $b\bar{b}$ pairs are produced per year of data-taking, of which about 24% within the LHCb acceptance. A schematic illustration of the LHCb detector with all components is shown in Fig. 3.2 which is taken from Ref. [25]. Using a right-handed coordinate system, the z-axis is equal to the beam axis and the y-axis is along the vertical of the cavern.

The main components of the detector are listed here briefly and are described in detail in the following:

- The proton-proton collision takes place on the left within the Vertex Locator (VELO), a silicon strip detector with excellent vertex resolution to resolve the proton-proton

[3] At LHCb, $\beta^* = 3$ compared to a β^* value less than 1 at the collision points of ATLAS and CMS.

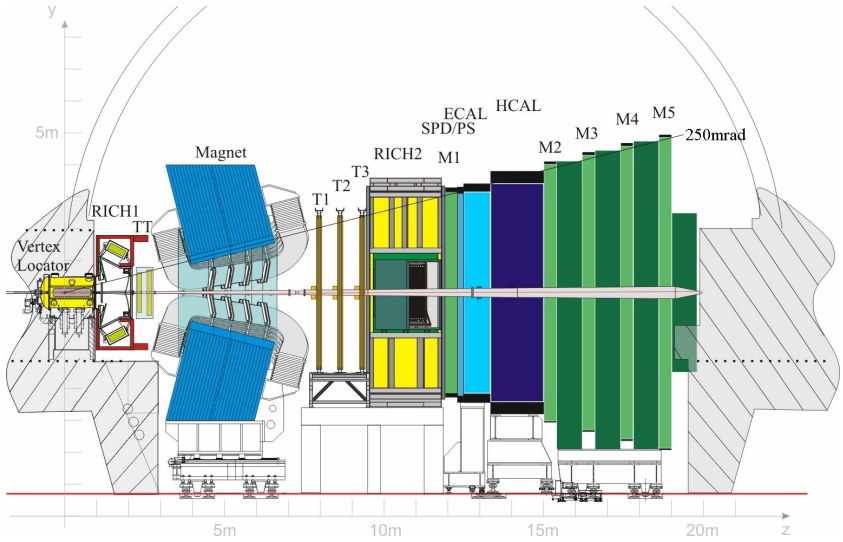

Figure 3.2: Schematic illustration of the side view of the LHCb detector: The proton-proton collision takes place on the left in the Vertex Locator (VELO); RICH1 and RICH2 are Cherenkov detectors; TT is the Tracker Turicensis, T1 - T3 the main tracking system, SPD is the Scintillating Pad Detector and PS the Preshower detector; ECAL is the electromagnetic calorimeter, HCAL the hadronic calorimeter and M1 - M5 the muon chambers

interaction point and the displaced decay vertices of charm and b hadrons.

- The Ring Imaging Cherenkov counters (RICH1 and RICH2) are used to identify hadron species via the emittance of Cherenkov radiation.
- The dipole magnet provides an integrated field of 4 Tm which bends charged particles in order to determine their momenta. The space within the magnet is almost completely empty to reduce material interactions that dilute the momentum resolution.
- The rest of the tracking system is essential to match the VELO tracks, measure momenta and determine the decay time of a particle. It consists of the Tracker Turicensis (TT), a silicon microstrip detector, in front of the magnet and three main tracking stations behind (T1 - T3). Their inner parts, where the particle multiplicities are higher, are formed by the Inner Tracker (IT), made of silicon microstrips, and the outer parts consist of straw-tube gas detectors, the Outer Tracker (OT).
- The calorimeter system is used to measure the energy deposited by electromagnetic and hadronic showers, but more important it also delivers trigger signals. It consists of a Scintillator Pad (SPD) and a Preshower (PS) detector and an electromagnetic calorimeter (ECAL) followed by a hadronic calorimeter (HCAL).
- The muon detection system (M1 - M5) is composed of multi-wire proportional chambers (MWPC) and triple-gas electron multipliers (GEM) in the region with the highest detection rate.

3.2.1 Track reconstruction detectors

The track reconstruction system of the LHCb detector is essential to reconstruct particle trajectories, measure momenta and determine the decay time of a particle.

Vertex Locator

The Vertex Locator is a silicon strip detector consisting of 25 disk-shaped silicon modules that immediately surround the proton-proton interaction point. Each module measures the radial and azimuthal coordinates, R and ϕ, of the particle with a minimal pitch of 38 µm [27]. They are arranged along the beam pipe because the heavy-flavour hadrons are produced, on average, with high longitudinal momenta. A sketch of one VELO disk is given on the left-hand side of Fig. 3.3 and the arrangement of the disks along the beam pipe is shown on the right.

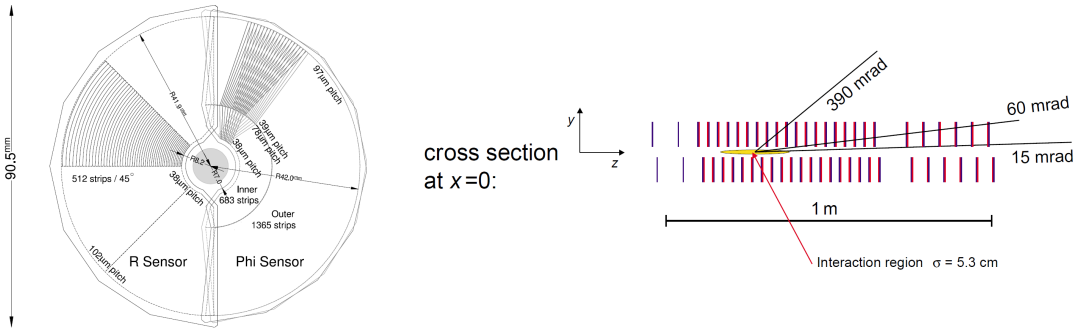

Figure 3.3: Sketch of one (left) Vertex Locator (VELO) disk with R- and ϕ-measuring sensors and the (right) arrangement of the disks along the beam pipe, taken from [27]. On the right, the blue disks refer to sensors measuring in R-direction and the red disks refer to sensors that are sensitive in the ϕ-direction.

During the injection of the proton bunches into the LHC or in phases of machine development, the halves of one VELO module are separated from each other by 6 cm to protect them from the beam. During the nominal run, the halves are moved together and approach the nominal beam axis up to a distance of 5 mm [25] with the sensitive area starting at a radius of 8 mm.

Tracker Turicensis and main tracking stations

The Tracker Turicensis in front of the magnet and the Inner Tracker, the inner part of the main tracking system behind the magnet, both consist of silicon microstrip sensors as they have to cope with high particle multiplicities. To allow for a two-dimensional spatial resolution, the four layers are arranged in a so-called x-u-v-x geometry, where two layers are rotated by ±5° with respect to the vertical axis. With pitches of 183 µm and 198 µm, respectively, the spatial resolution along the x-direction of both trackers is approximately 50 µm [25].

The Outer Tracker forms the outer part of the main tracking station behind the magnet and covers the large area of 6 m × 5 m. It is built from straw-tube drift chamber modules

with a mixture of Argon and CO_2 that are as well arranged in a x-u-v-x geometry. The lower particle occupancy allows for the operation of the coarsely granular straw tubes that are 5 mm wide. The tubes exhibit a maximum drift time of approximately 45 ns which enables to distinguish consecutive proton bunch collisions. A spatial resolution of 200 µm [25] along the x-axis can be achieved for single cells.

Track reconstruction

After the pattern recognition that assigns hits to tracks, the tracks are fit using Kalman-filter algorithms [28] which account for multiple scattering of the particle. The quality of the track reconstruction is estimated from the track fit χ^2 value divided by the number of degrees of freedom, n_{dof}. At LHCb, so-called *long tracks* are defined as tracks that are reconstructed by the VELO and the main tracking stations. Their momenta are measured to high precision thanks to the long lever arm with a momentum resolution of $\delta p/p = 0.35\%$ for low-momentum tracks ($p < 20\,\text{GeV}/c$) and $\delta p/p = 0.55\%$ [25] for high-momentum tracks ($p > 120\,\text{GeV}/c$). It can also occur that tracks are partially reconstructed by single detector components which is the case for particles with very low momenta that are bent out of the magnet and do not reach the main tracking stations or for decay products of long-lived particles that may remain undetected in the VELO. *Upstream tracks* refer to tracks that are only built from hits in the VELO and the TT whereas *downstream tracks* are only reconstructed in the TT and the tracking stations. The number of tracks refers to the number of all types of tracks. In the momentum region between 5 GeV/c and 200 GeV/c, the track reconstruction efficiency is of the order of 95% [29].

3.2.2 Calorimeter System

The calorimeters are built from thick metallic absorber materials in which all particles except for neutrinos and muons produce a cascade of secondary particles, a so-called shower. As these particles are mostly stopped in the calorimeters, their energy can be obtained from the deposited energy. At LHCb, the main purpose of the calorimeter system is to deliver trigger signals from photons, electrons and hadrons with large transverse momenta. In the electromagnetic calorimeter (ECAL), charged particles and photons produce electromagnetic showers via bremsstrahlung and e^+e^--pair production. Electrons and photons are absorbed whereas hadrons also cause a hadronic shower in the subsequent hadronic calorimeter (HCAL). The response to different particle species is used to distinguish hadrons from electrons and photons. The plates of the absorber are interleaved with plates of plastic scintillator and the emitted photons are read out by photomultipliers. The absorber materials are lead and iron for the electromagnetic and hadronic calorimeters, respectively. To allow for a two-dimensional spatial resolution, the calorimeters are segmented into cells whose granularities are higher in the inner sections of the calorimeters where occupancies are higher. The energy resolutions are $\sigma_E/E = 10\%/\sqrt{E} \oplus 1.5\%$ (E in GeV) for the electromagnetic calorimeter and $\sigma_E/E = (69 \pm 5)\%/\sqrt{E} \oplus (9 \pm 2)\%$ (E in GeV) [25] for the hadronic calorimeter.

The scintillating pad detector (SPD) and the preshower detector (PS) are located directly in front of the electromagnetic calorimeter and consist of scintillating pads that detect charged particles. A 12 mm thick lead absorber is placed between them that causes photons

and electrons to shower. Since photons are not detected in the SPD, the system allows to distinguish electrons from photons.

3.2.3 Muon chambers

The muon detector system is constructed to identify muons. It consists of five chambers, of which M2-M5 are located behind the calorimeter system. Muons are the only particles, except for neutrinos, that can traverse the thick absorber material and reach the muon chambers. In order to stop the small fraction of other particles that may have traversed the calorimeter system, the muon stations M2 to M5 are interleaved with additional 80 cm thick iron absorbers. Due to the fast and distinct response, the signal of the muon chambers can be used as a trigger signal for muons and the hits allow for a measurement of the muon momentum. The first muon chamber, M1, is placed in front of the calorimeters to improve the momentum resolution that suffers from multiple scattering in the absorber material. The muon chambers are built from multi-wire proportional chambers, except for the inner part of M1 where triple-GEM detectors are used due to the larger particle multiplicity. The time to collect the signal is less than 20 ns with an efficiency larger than 95 % [25]. Despite the forward design of the detector, about 20% of all muons produced in the entire solid angle in semileptonic b-hadron decays are detected in the muon chambers.

3.2.4 Particle Identification

Particle identification of the final-state particles is essential to isolate the signal decays from background decays and compute the correct invariant mass of the heavy-flavour hadrons. As described before, muons are identified in the muon chambers. According to the number of traversed muon chambers and matching hits within a field of interest around the track extrapolation, the muon candidates are assigned a loose binary classification, denoted as *isMuon* [30]. A more stringent variable based on a smaller defined field of interest is given by the variable *isMuonTight*. Photons are distinguished from electrons with the SPD and PS system and the calorimeters allow for a separation of hadrons and electrons, but the hadron species leave very similar traces in the whole detector. Therefore, an additional hadronic particle identification detector is needed.

Cherenkov radiation is emitted when charged particles traverse a dense medium with the refractive index n. This happens when the velocity, $v = \beta c$, is larger than the light velocity in the medium, $c' = c/n$. The Cherenkov radiation is emitted on a cone of an angle, θ, around the flight direction of the particle,

$$\cos\theta = \frac{c'}{v} = \frac{1}{n\beta},$$

At LHCb, two Ring-Imaging Cherenkov counters are mounted in front of and behind the magnet, RICH1 and RICH2. RICH1 uses C_4F_{10} as radiator that covers the low-momentum range from $\sim 1\,\mathrm{GeV}/c$ – $60\,\mathrm{GeV}/c$ and the upstream RICH2 covers the momentum range from $\sim 15\,\mathrm{GeV}/c$ – $100\,\mathrm{GeV}/c$ with CF_4 as radiator [25]. Figure 3.4 shows the measured Cherenkov angle at RICH1 as a function of the track momentum for different hadron species which are well separated in the given momentum range. At a pion-as-kaon misidentification rate of 5%, the average efficiency of the kaon identification is 95% [31].

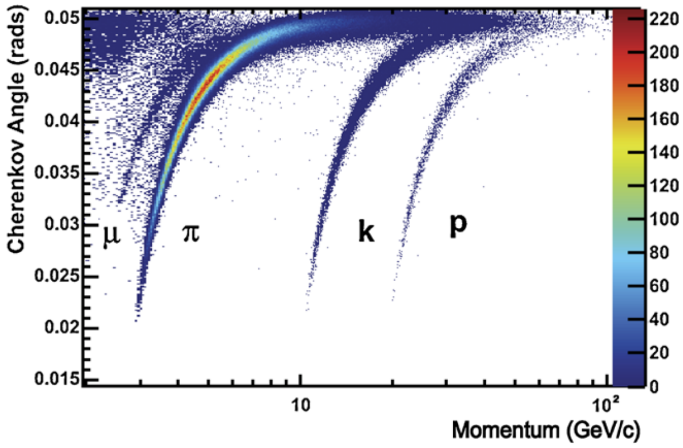

Figure 3.4: Cherenkov angle as a function of the momentum of different hadron species, taken from Ref. [31].

The information provided by the two RICH detectors, the calorimeter system and the muon chambers is combined to a particle hypothesis in the form of a so-called likelihood $\mathcal{L}(\pi,\ \mu\ or\ K)$. It should be noted that, although the name suggests a form of probability, it is not a probability in the mathematical sense. Since pions are produced most frequently in proton-proton collisions, the difference of the logarithmic likelihoods for a particle of type X and a pion are computed as the relative particle hypothesis

$$\Delta\log\mathcal{L}_{X-\pi} = \log\mathcal{L}(X) - \log\mathcal{L}(\pi). \tag{3.1}$$

This variable is used to separate particle species X from pions. Additionally, neural networks are used to evaluate the available particle identification information to provide the so-called ProbNN_X variable. The dimensionless output takes values between 0 and 1 which is correlated but not identical to the probability of a particle being of type X. The ProbNN variable is constructed such that the sum over the ProbNN values of all particle hypotheses gives unity.

3.2.5 Trigger system

At the LHC, protons collide at a bunch-crossing rate of 40 MHz. Due to the resulting huge amount of data, not every event is recorded and saved on disk, but the trigger system is constructed to filter out events with interesting decays and reject others. The trigger system consists of a hardware trigger and a software trigger. The hardware trigger, also referred to as the level-0 (L0) trigger, uses characteristic signatures in the muon chambers and the calorimeters that can be provided in real time during data-taking. Events that satisfy the hardware trigger requirements are accepted and the data rate is reduced to 1 MHz. In the software trigger, also called the high-level trigger (Hlt), the recorded events are processed with computer farms that have access to the full detector information and the rate is further reduced to $\sim$4 kHz[4] that is saved on disk.

[4]The rate of 4 kHz refers to the value during LHC Run I. It is larger than 5 kHz for Run II.

Hardware trigger

The hardware trigger system searches for signals of particles with large transverse momenta, p_{T}, that are characteristic for light secondary particles from heavy-hadron decays, whereas particles that are produced in QCD processes in the proton interaction, tend to have a softer p_{T} spectrum. The calorimeter signals are used to form clusters of calorimeter cells and measure the transverse energy, E_{T}, for electrons, photons and hadrons. The muon trigger system reconstructs tracks in the muon chambers and the slope provides a quick measurement of the transverse momentum by using an average proton-proton collision point [32]. The combination of all information to a level-0 decision takes only 2 µs.

Software trigger

The software trigger consists of two stages, Hlt1 and Hlt2, in which the larger computing time allows for a more precise measurement of the momenta and the reconstruction of vertices. In the first level, the events are partially reconstructed to confirm the level-0 tracks. This reduces the event rate to about 30 kHz. In the second level, the event is fully reconstructed and the information from the RICH detectors allows for a separation of hadron species. Specific decay modes are reconstructed and selected with loose selection criteria of so-called trigger lines.

Instead of reconstructing complete decay modes, there are also trigger lines that reconstruct general types of decays such as decays with a J/ψ meson in the final state. Others, so-called topological triggers partially reconstruct b-hadron decays by exploiting the characteristic topology: A small number of tracks in the event, that exhibit large impact parameters and transverse momenta, are combined at a common vertex. As the tracks mostly compose a subset of the final-state particles, the reconstructed invariant mass is smaller than the b-hadron mass. However, the missing momentum transverse to the flight direction of the b-hadron candidate, $p_{\mathrm{T}\,\mathrm{miss}}$, can be used to recover the missing mass to the so-called corrected mass defined by

$$m_{\mathrm{corr}} = \sqrt{m_{\mathrm{rec}}^2 + p_{\mathrm{T}\,\mathrm{miss}}^2} + p_{\mathrm{T}\,\mathrm{miss}}, \tag{3.2}$$

where m_{rec} is the invariant mass of the subset of particles. For real b hadrons, the corrected mass is typically within 2 GeV/c^2 of the known mass and the accuracy increases with the number of reconstructed final-state particles.

3.3 Topology of b-hadron decays

Figure 3.5 shows an illustration of the production and decay topologies of a b meson. It is produced at the proton-proton interaction point, the primary vertex PV, and typically decays at a displaced decay vertex, DV. As an example, the $B_s^0 \to \phi\phi$ decay is drawn where both ϕ mesons decay into a pair of charged kaons. Particles that are produced directly in the proton-proton interaction at the primary vertex are mostly pions and kaons, but also charm and beauty hadrons. In average, they are boosted along the longitudinal direction due to the kinematics of the colliding partons. In this thesis, these particles are further referred to as *prompt* particles. The ϕ mesons decay immediately via the strong interaction

such that their flight distance cannot be resolved. The tracking detectors only reconstruct the meta-stable light hadrons and their combined vertex defines the B_s^0 decay vertex. The quality of the vertex reconstruction fit is described by the vertex fit χ^2 value divided by the number of degrees of freedom, n_{dof}. As the kaons originate from the decay of a heavier meson, they tend to have larger transverse momenta than prompt particles as indicated in the sketch.

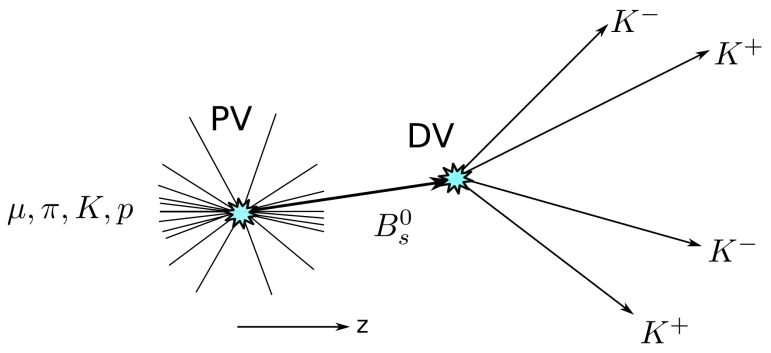

Figure 3.5: Illustration of topologies of the b-hadron production at the primary vertex (PV) and the decay at the decay vertex (DV), here exemplary $B_s^0 \to \phi\phi(\to K^+K^-K^+K^-)$.

The impact parameter, IP, of a track is defined as the distance of closest approach of the prolongation of a track to the primary vertex. The left-hand side of Fig. 3.6 shows the impact parameter of one of the K^+ mesons. Secondary particles that do not originate from the primary vertex have, on average, larger impact parameters. However, when prompt particles have small transverse momenta, the probability to scatter in the detector material is higher which also leads to large impact parameters. For this reason, selection criteria on both, large impact parameters and transverse momenta, are applied to select secondary particles from b-hadron decays. Another measure of the compatibility of a track with the primary vertex is the so-called χ^2_{IP} value. It is defined as the difference of the two fit χ^2/n_{dof} values of the primary vertex fit, with and without including the track. The χ^2_{IP} value is directly related to the significance of the impact parameter of the given track, the ratio between the impact parameter and its measured uncertainty.

The pointing angle of the B_s^0 candidate is sketched on the right-hand side of Fig. 3.6. It is defined as the angle between the flight distance vector, $\vec{d}$, that connects the primary vertex with the decay vertex, and the momentum vector, $\vec{p}_{B_s^0}$, of the b-hadron candidate that is determined by the reconstructed sum of the four kaon momenta. Since the B_s^0 meson moves along the flight distance, the angle is small for a correctly reconstructed B_s^0 and deviates from zero for falsely combined kaons.

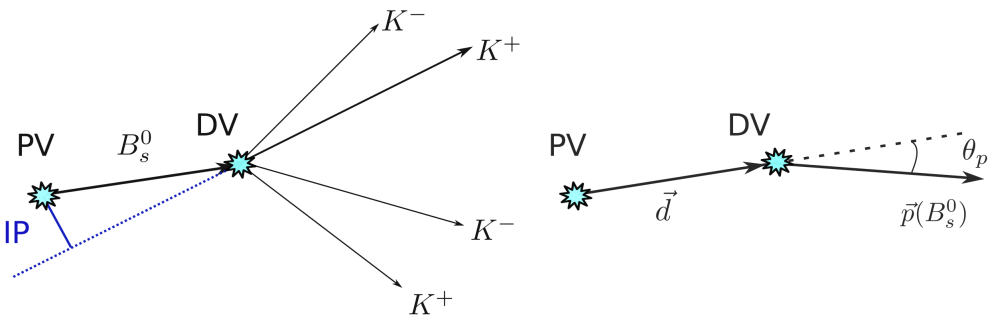

Figure 3.6: Illustration of the (left) impact parameter (IP) and (right) the pointing angle θ_p.

3.3.1 Observables in b-hadron decays

The kinematics of b-hadron decays are determined by several observables of which the most important ones are defined in the following.

Pseudorapidity

The pseudorapidity, η, of a track is a spatial coordinate that is related to the angle, θ, of the flight direction relative to the beam axis. It is defined as

$$\eta = -\log(\tan\frac{\theta}{2}). \tag{3.3}$$

The pseudorapidity of the b-hadron can be obtained from the reconstructed momentum direction or from the flight distance vector from the primary vertex to the decay vertex[5].

Invariant mass

The masses of the final-state particles are not directly measured, but their known values, m_{PDG}, given by the PDG [19] are assigned as particle masses according to the particle hypothesis. The invariant mass of the b-hadron candidate is obtained from the four-momentum, P_B, of the b meson calculated as the summed momenta of the N final-state particles

$$P_B = \sum_{i=1}^{N} \begin{pmatrix} \sqrt{m^2_{\mathrm{PDG},i} + \vec{p}_i^{\,2}} \\ \vec{p}_i \end{pmatrix}, \tag{3.4}$$

where $\vec{p}_i$ is the measured three-momentum of the i^{th} reconstructed track.

[5] For massless particles, the pseudorapidity is equal to the rapidity $y = \frac{1}{2}\log\left(\frac{E+p_{\mathrm{L}}}{E-p_{\mathrm{L}}}\right)$, where p_{L} refers to the longitudinal momentum.

Decay time

The decay time of the b hadron is obtained from the reconstructed flight distance and the velocity. Using the flight distance vector, $\vec{d}$, as before, and denoting the invariant mass as m and the measured momentum vector as $\vec{p}$, the reconstructed decay time t_{rec} of the b-hadron is computed via[6]

$$t_{\text{rec}} = \frac{m\ \vec{d} \cdot \vec{p}}{|\vec{p}|^2}. \tag{3.5}$$

As the track momenta are determined very precisely, the uncertainty on the decay time is dominated by the reconstruction of the decay vertex.

3.4 Determination of the luminosity

With a known proton current, the luminosity of the beam can be obtained by measuring the Gaussian-shaped beam profiles. At LHCb, the beam profiles are determined in two independent ways, using the *van-der-Meer scan* and the *beam-gas imaging* luminosity calibration methods [33]. In the van-der-Meer method, the proton beams are displaced by a distance perpendicular to their direction while measuring the average number of interactions per bunch-crossing to scan the overlap region. This is done at different relative beam positions and the relative rates allow for an extraction of the beam profiles. In the beam-gas imaging method, neon gas is injected into the vertex region inside the VELO vacuum tank that serve as a target for the protons while the beams are not displaced. By reconstructing the interaction vertices between the beam particles and the gas nuclei, the angles, positions and shapes of the individual beams are measured.

3.5 Generation of fully simulated events

Simulations are imitations of real-world processes that are generated by a computer according to a theoretical model. In particle physics, simulated events are very important to perform physics analyses with detector data and test analysis procedures. The detector is not a passive uniform object but it is built from sub-components that cover certain areas and interact with the particles. Additionally, it has finite particle detection efficiencies and resolutions and suffers from noise such that distributions of reconstructed observables deviate from the original ones. These dilutions are used as input for the simulation which allows for the study of the resulting impact on the observable quantities and physics analyses. Moreover, simulated kinematic distributions are needed to choose selection criteria that efficiently isolate signal decays and reject background contributions. The arising reconstruction and selection efficiencies are then determined with simulated events. Physics parameters are extracted from complex, often multi-dimensional, fits to the collected datasets while correcting for detector artefacts. These fit procedures are also tested with simulated events. Furthermore, the impact of new theory models on the measured observables has to be simulated properly in order to draw meaningful conclusions.

[6] in natural units c =1

At LHCb, the proton-proton interaction is simulated using the general-purpose Monte Carlo event generator Pythia [34]. It uses measured parton distribution functions and describes the hard and soft parton interactions with QCD models, including initial- and final-state radiation. It also contains multi-parton interactions and the fragmentation process into hadrons. The corresponding b-hadron and subsequent decays are modelled with the EvtGen library [35] that describes the decays using decay amplitudes. This allows for the simulation of the entire decay chain, including all angular correlations and decay-time distributions that are important in CP-violating processes. The related branching fractions are continuously updated to the current measured values. The simulation of the detector response is provided by the Geant4 package [36, 37] that simulates interactions with matter and the resulting hits. The track and decay reconstructions are performed with the same tools that are used for real data.

4 Description of fit techniques

Physics parameters that are used as model parameters for theoretical models are usually extracted by fitting these models to measured distributions of observables of collected particle candidates. This chapter reviews the concept of maximum likelihood estimations in multiple dimensions and describes a procedure to subtract background contributions on a statistical basis. It is based on Ref. [38].

4.1 Maximum likelihood fit

The maximum likelihood fit is a fit method that obtains a best estimate for a set of parameters, $\vec{a}$, that are used as model parameters for a theoretical model. The model is fitted to a data sample with N_{ev} number of events, where for each event e, a set of observables $\vec{x}_e$, is measured. The model uses a theoretical function $\mathcal{P}(\vec{x}|\vec{a})$ that depends on $\vec{a}$ to describe the data. Requiring the function to be positive with the normalisation condition

$$\int \mathcal{P}(\vec{x}|\vec{a})\mathrm{d}\vec{x} = 1, \tag{4.1}$$

$\mathcal{P}(\vec{x}|\vec{a})$ becomes a probability density function (PDF) that gives for each set of parameters the probability to measure the observables within the range $[\vec{x}, \vec{x} + \mathrm{d}\vec{x}]$.

Parameters parameterise a theoretical model which is based on a probability density function (PDF) $\mathcal{P}(\vec{x}|\vec{a})$

The maximum likelihood fit is a fit method that obtains a best estimate for a set of parameters, $\vec{a}$, from a data sample with N_{ev} number of events, where for each event e, a set of observables $\vec{x}_e$, is measured. A probability density function (PDF) $\mathcal{P}(\vec{x}|\vec{a})$ describes the probability to measure the observables within the range $[\vec{x}, \vec{x} + \mathrm{d}\vec{x}]$, under the assumption of the given set of parameters $\vec{a}$. Therefore, $\mathcal{P}(\vec{x}|\vec{a})$ is a function of $\vec{x}$ that is defined to be positive and to obey the normalisation condition

$$\int \mathcal{P}(\vec{x}|\vec{a})\mathrm{d}\vec{x} = 1. \tag{4.2}$$

The likelihood function, $\mathcal{L}$, is defined by the product of the single-event probability densities of all events,

$$\mathcal{L}(\vec{a}) = \prod_{e=1}^{N_{\text{ev}}} \mathcal{P}(\vec{x}_e|\vec{a}). \tag{4.3}$$

Although $\mathcal{L}$ is a function of $\vec{a}$, it still refers to the probability to measure the data sample $\vec{x}_1, ...\vec{x}_{N_{\text{ev}}}$ under the assumption of the parameter set $\vec{a}$. The best estimate of the parameter set $\vec{a}$ is obtained by maximizing the likelihood to observe the given data sample. Taking the logarithm of the likelihood function simplifies the procedure because terms are added instead of being multiplied with each other. Applying negative sign turns it into a minimization

problem

$$-\log\mathcal{L} = -\sum_{e=1}^{N_{\text{ev}}} \log\mathcal{P}(\vec{x}_e|\vec{a}), \tag{4.4}$$

that can be solved by determining the root of the first derivative

$$-\frac{\partial}{\partial a_j}\log\mathcal{L} = -\frac{\partial}{\partial a_j}\sum_{e}^{N_{\text{ev}}} \log\mathcal{P}(\vec{x_e}|\vec{a}) = 0, \tag{4.5}$$

where a_j refers to the j^{th} parameter of the set $\vec{a}$. This procedure is performed by minimization algorithms like Minuit [39]. In the limit of a large number of events, $N \to \infty$, the best estimate of the maximum likelihood fit converges to the true value as it is shown in Ref. [38].

4.1.1 Determination of uncertainties on the fit result

The log-likelihood function of one single parameter, a, can be approximated, in the limit of large number of events, by a Taylor expansion around the best estimate, a_0, within a small interval $|a - a_0|$ [38]:

$$\begin{aligned} -\log\mathcal{L}(a) = \; & -\log\mathcal{L}(a_0) - (a-a_0)\frac{\partial}{\partial a_0}\log\mathcal{L}(a)\Big|_{a=a_0} \\ & - \frac{(a-a_0)^2}{2}\frac{\partial^2}{\partial a_0^2}\log\mathcal{L}(a)\Big|_{a=a_0} + \mathcal{O}((a-a_0)^3), \end{aligned} \tag{4.6}$$

where the derivatives are taken at the best estimate. Since the first derivative is zero by construction, the second term drops and exponentiating Eq. 4.6 results in

$$\mathcal{L}(a) = -\mathcal{L}(a_0)\cdot\exp\left(-\frac{(a-a_0)^2}{2\sigma^2}\right), \tag{4.7}$$

where higher-order terms are omitted. The parameter σ is given by

$$\sigma^2 = -\left(\frac{\partial^2}{\partial a_0^2}\log\mathcal{L}(a)\Big|_{a=a_0}\right)^{-1}. \tag{4.8}$$

Hence, the likelihood function can be approximated by a Gaussian function and the standard deviation σ is the uncertainty on the fitted parameter. In case of a set of parameters $\vec{a}$, the likelihood function turns into a multi-dimensional Gaussian function and the correlations between the fitted parameters are given by the covariance matrix

$$\text{cov}(a_i, a_j) = -\left(\frac{\partial^2}{\partial a_i \partial a_j}\log\mathcal{L}(a)\Big|_{\vec{a}=\vec{a}_0}\right)^{-1}. \tag{4.9}$$

4.2 Description of the sFit technique

A typical problem in particle physics is the pollution of signal candidates from background contributions. This section presents a method, called the sFit technique [40], of subtracting background contributions on a statistical basis.

4.2.1 Description of the ${}_s\mathcal{P}lot$ technique

Signal candidates among the selected data samples are, in general, isolated from background contributions with kinematic selection criteria and particle identification information. However, there are also background contributions that mimic the signal decay and can only be identified on a statistical basis by comparing the distributions of observables for a sufficient number of events. Besides random combinations of final-state particles, these can also originate from other hadron decays that have the same final-state particles, are partially reconstructed or have one of the particles falsely identified. In the following, the case is considered where the individual contributions can be identified in fits to observables, $\vec{y}$, that have discriminative power, for example the invariant mass of the hadron signal candidate. The mass of the combinatorial background is usually linearly distributed, whereas the signal component has a clear peak structure. The ${}_s\mathcal{P}lot$ technique [41, 42] is a procedure that uses the fit results to reconstruct the distributions of other, so-called control variables, $\vec{x}$, without background contributions. Describing the signal and the background distributions with PDFs, $\mathcal{P}_s(\vec{x},\vec{y})$ and $\mathcal{P}_b(\vec{x},\vec{y})$, the total distribution $f(\vec{x},\vec{y})$ is written as

$$f(\vec{x},\vec{y}) = N_s\mathcal{P}_s(\vec{x},\vec{y}) + N_b\mathcal{P}_b(\vec{x},\vec{y}), \tag{4.10}$$

where N_s and N_b are the number of signal and background events, respectively. According to the fit result, every event is assigned a weight, a so-called sWeight, which can be positive or negative. Events for which the measured discriminating observables are within the signal region have a positive weight than can be larger than unity, whereas the weights are negative when the discriminating observables are distinctly separated from the signal region. The sWeights, $W_s(\vec{y})$, are constructed such that they project out the signal

$$N_s\mathcal{P}_s(\vec{x}) = \int W_s(\vec{y}) f(\vec{x},\vec{y})\mathrm{d}\vec{y}. \tag{4.11}$$

When the distributions $\mathcal{P}(\vec{x})$ and $\mathcal{P}(\vec{y})$ are independent from each other, for signal and background, the PDFs factorise into $\mathcal{P}(\vec{x},\vec{y}) = \mathcal{P}(\vec{x})\mathcal{P}(\vec{y})$ and the weights are independent of $\vec{x}$ such that this equation is given by

$$N_s\mathcal{P}_s(\vec{x}) = \int W_s(\vec{y})\Big[N_s\mathcal{P}_s(\vec{x})\mathcal{P}_s(\vec{y}) + N_b\mathcal{P}_b(\vec{x})\mathcal{P}_b(\vec{y})\Big]\mathrm{d}\vec{y}, \tag{4.12}$$

which implies $\int W_s(\vec{y})\mathcal{P}_s(\vec{y})\mathrm{d}\vec{y} = 1$ and $\int W_s(\vec{y})\mathcal{P}_b(\vec{y})\mathrm{d}\vec{y} = 0$. This is solved in Ref. [41] by

$$W_s(\vec{y}) = \frac{\langle V_{ss}\rangle\mathcal{P}_s(\vec{y}) + \langle V_{sb}\rangle\mathcal{P}_b(\vec{y})}{N_s\mathcal{P}_s(\vec{y}) + N_b\mathcal{P}_b(\vec{y})}, \tag{4.13}$$

where V_{nj} is obtained by inverting the matrix

$$\langle V_{nj}^{-1} \rangle = \int \frac{\mathcal{P}_n(\vec{y})\mathcal{P}_j(\vec{y})}{(N_s\mathcal{P}_s(\vec{y}) + N_b\mathcal{P}_b(\vec{y}))^2}. \tag{4.14}$$

When the sWeights are used to weight the events, the distributions of the measured control variables have the background contributions subtracted on a statistical basis and correspond therefore to the signal distribution only. However, this is only possible for control variables that are uncorrelated to the discriminating variables due to the requirement that the distribution of $\vec{y}$ is independent of $\vec{x}$.

4.2.2 Application of sWeights in a maximum likelihood fit

In the sFit technique [40], the weighted datasets are used to perform maximum likelihood fits to the control variables. Since the weighted dataset corresponds to the pure signal sample, there is no need to model the background contributions in the control variables which simplifies the fit procedure. Technically, the sWeights, W_s, are used to weight the likelihood function via

$$\mathcal{L}_W(\vec{a}) = \prod_{e=1}^{N_{\text{ev}}} \left[\mathcal{P}(\vec{x}_e, \vec{a})\right]^{\alpha W_s(y_e)}, \tag{4.15}$$

which corresponds to

$$-\log \mathcal{L}_W(\vec{a}) = -\alpha \sum_{e=1}^{N_{\text{ev}}} W_s(y_e) \log \mathcal{P}(\vec{x}_e|\vec{a}). \tag{4.16}$$

Due to the re-weighting procedure, the statistics of the sample size is reduced and the computed uncertainty is changed. This is taken into account with the factor

$$\alpha = \frac{\sum_{e=1}^{N_{\text{ev}}} W_s(y_e)}{\sum_{e=1}^{N_{\text{ev}}} W_s^2(y_e)}. \tag{4.17}$$

Part I:
Measurement of the *b*-hadron production cross-section

5 Introduction

Most of the measurements of the properties of heavy-flavour hadrons require a large number of produced particles. Therefore, there is great interest in their production cross-section in proton-proton collisions. The number of expected hadrons can be used to ascertain the future sensitivity of LHCb analyses and quantify SM backgrounds in searches for New-Physics phenomena. Since heavy quarks are predominantly produced in gluon-fusion processes at the LHC, their production also provides important tests of perturbative Quantum Chromodynamics (QCD) predictions. The unique forward range of the LHCb detector allows to probe production processes where the related gluons have highly asymmetric momenta and the momentum fraction of the initial-state partons, x, reaches down to 5×10^{-5} [43, 44]. In order to assess the various kinematic regions, measurements are compared to QCD predictions as a function of the pseudorapidity of the heavy hadron. Furthermore, it is also important to note that the LHCb simulation framework has to be tuned to properly reflect the measured b-hadron production, especially in terms of kinematic dependencies.

The determination of the b-hadron production cross-section in proton-proton collisions, one of the first analyses at LHCb [24], was performed at the centre-of-mass energy of 7 TeV using semileptonic decays of $\overline{B}^0$ and B^- mesons with a muon and a D^0 meson reconstructed in the final state. Thanks to the large branching fraction of approximately 10% and an efficient muon identification, these decays provide large amount of signal candidates. In 2015, the unprecedented centre-of-mass energy of 13 TeV at the LHC opened a new era in searches for new particles and precision tests of the Standard Model and the first measurements are again cross-section determinations of the known physics processes as they can be performed with small data samples. Due to the restriction to only $\overline{B}^0$ and B^- mesons, the previous 7 TeV analysis relied on the b-quark hadronisation fractions, measured at the e^+e^--machine LEP [45], to extrapolate to the total b-hadron cross-section. However, this assumes that the same fractions are valid for the relevant higher-energy hadronic proton-proton collisions. Therefore, a new approach has been developed that also includes D^+ from $B^{0/+}$, D_s from B_s^0 and Λ_c from Λ_b decays, such that the most abundant b hadrons are considered which reduces the sensitivity to the hadronisation fractions. Using the very first proton-proton collision data at the centre-of-mass energy of 13 TeV as well as previously collected data at 7 TeV, the first part of this thesis presents the measurement of the production cross-section of b hadrons within the acceptance of the LHCb detector as a function of the pseudorapidity. The data is compared to theoretical predictions using the fixed-order plus next-to-leading log (FONLL) formalism [12]. Performing the new analysis approach again with the 7 TeV data allows to form the ratio of cross-sections between 13 TeV and 7 TeV in which theoretical uncertainties partially cancel, allowing for a more precise comparison to data. The analysis has been published in Phys. Rev. Lett. 118, 052002 [1] and the author was one of the main contributors.

This first part of this thesis is organised as follows: Chapter 6 presents the theoretical

assumptions and experimental inputs that are needed to extract the production cross-section from semileptonic b-hadron decays, including the description of the theoretical predictions made with the FONLL formalism. Chapter 7 sketches the analysis approach. Chapter 8 describes the reconstruction and selection of the signal decays, followed by the extraction of the signal yields in Chap. 9. In Chap. 10, possible background contributions are investigated and Chap. 11 summarises the reconstruction and selection efficiencies. After analysing the systematic uncertainties in Chap. 12, the final results are presented in Chap. 13, followed by a discussion in Chap. 14.

6 Description of the theoretical framework for b-hadron production measurements

The following chapter summarises the theoretical assumptions and measured parameters that are needed to extract the b-hadron production cross-section from semileptonic b-hadron decays. Moreover, a theory framework, the fixed-order plus next-to-leading log (FONLL) formalism, is presented which is used to predict the b-hadron production cross-section.

6.1 Extraction of the b-hadron production cross-section

This analysis aims to measure the cross-section of producing a b hadron, H_b, in proton-proton collisions, $\sigma(pp \to H_b X)$. The production cross-section is determined by summing over the contributions from all possible b-hadron species and can be written as

$$\begin{aligned}\sigma(pp \to H_b X) = \quad & \frac{1}{2}\left[\sigma(B^0) + \sigma(\overline{B}^0)\right] + \frac{1}{2}\left[\sigma(B^+) + \sigma(B^-)\right] \\ & + \frac{1}{2}\left[\sigma(B_s^0) + \sigma(\overline{B}_s^0)\right] + \frac{1+\delta}{2}\left[\sigma(\Lambda_b^0) + \sigma(\overline{\Lambda}_b^0)\right],\end{aligned} \tag{6.1}$$

where $\sigma(B_i)$ is a short notation of $\sigma(pp \to B_i X)$ and the factor 2 is due to the definition that the b hadron contains a specific quark, either a b or a $\overline{b}$ quark. δ is a correction factor that accounts for Ξ_b and Ω_b baryons that are also produced in significant numbers, but are not reconstructed here. The contributions from B_c^+ mesons are neglected because their production is very rare, determined to be only 0.8% percent of B_s^0, using $B_c^+ \to B_s^0 \pi^+$ decays [46].

This analysis uses semileptonic decays of the b hadrons, $H_b \to H_c \mu \nu X$, into charm hadrons, H_c, muons, neutrinos and other additional particles X, which are mainly pions and kaons. The overall semileptonic branching fractions, $\mathcal{B}_{\mathrm{SL}}$, are large and the muon can be reconstructed efficiently, but the drawback is that the neutrino remains undetected and the b-hadron mass cannot be fully reconstructed. As the number of X particles varies, only the muon and the charm hadron are reconstructed. In the following, the combined system of the charm hadron and the muon is referred to as the *charm-plus-muon* system. Figure 6.1 shows the Feynman diagram of the most basic semileptonic $\overline{B}^0$ decay to a D^+ meson, a muon and a neutrino. Additional final-state hadrons can be formed from quark anti-quark pairs. The $b \to c$ transition proceeds via the emission of a W boson that decays leptonically. Figure 6.2 shows a list of all reconstructed decay modes where D^0 and D^+ mesons originate from the decays of both $\overline{B}^0$ and B^- mesons, whereas the D_s^+ indicates a $\overline{B}_s^0$ decay and the Λ_c^+ hadron a Λ_b^0 decay. The charm hadrons are reconstructed using their most abundant decay modes $D^0 \to K^-\pi^+$, $D^+ \to K^-\pi^+\pi^+$, $D_s^+ \to K^-K^+\pi^+$ and $\Lambda_c^+ \to pK^-\pi^+$. It should be noted that due to the specific quark charges, the only allowed charge compositions for the signal decays are $H_c\mu^-$ and $\overline{H}_c\mu^+$. Experimentally, the

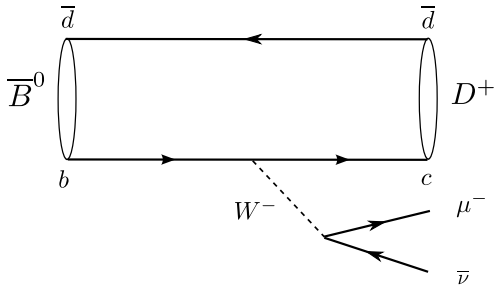

Figure 6.1: Feynman diagram of the semileptonic decay $\overline{B}^0 \to D^+\mu^-\bar{\nu}_\mu$.

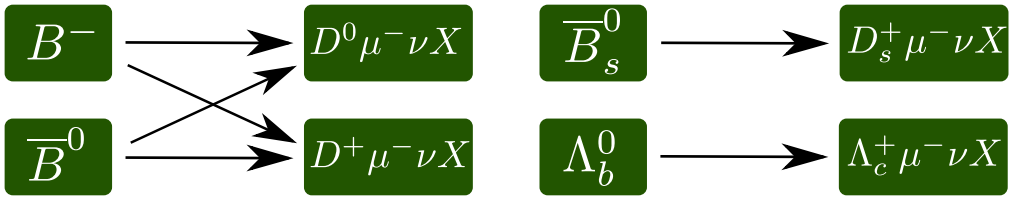

Figure 6.2: Considered semileptonic decay modes of b hadrons into charm hadrons, muons, neutrinos and additional particles, X, which are mainly pions and kaons. The charge-conjugated modes are not listed here but are also taken into account.

production cross-section, here exemplary for the B_s^0 mode, is computed via

$$\sigma(B_s^0) \propto \left[\frac{n(D_s^+\mu)}{2\mathcal{L} \times \varepsilon_{D_s^+\mu} \times \mathcal{B}_{D_s^+}}\right] \frac{1}{\mathcal{B}_{\mathrm{SL}}(B_s^0)},$$

where $n(D_s^+\mu)$ is the number of reconstructed signal decays, $\mathcal{L}$ is the integrated luminosity corresponding to the collected dataset, $\varepsilon_{D_s^+\mu}$ refers to the related reconstruction and selection efficiencies of the charm-plus-muon candidate and $\mathcal{B}_{D_s^+}$ is the branching fraction of the decay $D_s^+ \to K^-K^+\pi^+$. For simplicity, this notation implies that the charge-conjugated mode is included.

Summing all b-hadron modes, the total b-hadron cross-section is written as

$$\begin{aligned}\sigma(pp \to H_b X) = &\left[\frac{n(D^0\mu)}{2\mathcal{L} \times \varepsilon_{D^0\mu} \times \mathcal{B}_{D^0}} + \frac{n(D^+\mu)}{2\mathcal{L} \times \varepsilon_{D^+\mu} \times \mathcal{B}_{D^+}}\right] \frac{1}{\mathcal{B}_{\mathrm{SL}}(B^{0/+})} \\ &+ \left[\frac{n(D_s^+\mu)}{2\mathcal{L} \times \varepsilon_{D_s^+\mu} \times \mathcal{B}_{D_s^+}}\right] \frac{1}{\mathcal{B}_{\mathrm{SL}}(B_s^0)} \\ &+ \left[\frac{n(\Lambda_c^+\mu)}{2\mathcal{L} \times \varepsilon_{\Lambda_c^+\mu} \times \mathcal{B}_{\Lambda_c^+}}\right] \frac{1+\delta}{\mathcal{B}_{\mathrm{SL}}(\Lambda_b^0)},\end{aligned} \tag{6.2}$$

where $\mathcal{B}_{\mathrm{SL}}(B^{0/+})$ denotes the average inclusive semileptonic branching fraction from B^+ and B^0 decays. Since this approach only includes $b \to c\mu\nu$ modes, the result has to be corrected for the small and known $b \to u\ell\nu$ component, estimated to be $(2.0 \pm 0.3)\%$ of all

decay modes [19].

The production cross-section is evaluated in intervals of the pseudorapidity, η, of the b hadron as the theory prediction is provided as a function of η. The reconstruction and selection efficiencies are, in general, obtained from fully simulated events. In order to properly reflect them, a correct modelling of the simulated decay kinematics is essential. A deviation of the transverse momentum modelling of the charm-plus-muon system is observed in simulated events in Sec. 8.4. For this reason, the signal yields and efficiencies of all charm-hadron decay modes are determined not only in bins of the b-hadron pseudorapidity, but also in bins of the transverse momentum of the charm-plus-muon system, p_{T}, such that the signal yields are corrected for their p_{T}-specific efficiencies. The production cross-section of one type of b hadron, again exemplary the B_s^0, per bin in η, is computed with the integrated cross-section over the full p_{T} range

$$\sigma(B_s^0)(\eta) \;\propto\; \sum_{i=1}^{N_{\mathrm{bins}}} \left[\frac{n(D_s^+\mu)(\eta, p_{\mathrm{T}i})}{2\mathcal{L} \times \varepsilon_{D_s^+\mu}(\eta, p_{\mathrm{T}i}) \times \mathcal{B}_{D_s^+}} \right] \frac{1}{\mathcal{B}_{\mathrm{SL}}(B_s^0)}, \tag{6.3}$$

where N_{bins} is the number of bins in p_{T}.

6.2 Usage of externally provided parameters

The value of δ, the correction factor for other baryons than Λ_b^0, is partly obtained from Tevatron data and the assumption of SU(3) symmetry. In Ref. [47], the ratio of production cross-sections and decay widths are estimated as

$$\begin{aligned} \sigma(\Xi_b^-)/\sigma(\Lambda_b^0) &= 0.11 \pm 0.03 \pm 0.03, \\ \Gamma(\Xi_b^- \to \Xi_c^- X \mu^- \overline{\nu}) &= \Gamma(\Lambda_b^0 \to \Lambda_c^+ X \mu^- \overline{\nu}), \end{aligned} \tag{6.4}$$

To compute δ, this contribution must be doubled, using isospin invariance, to account for Ξ_b^0 decays. Additionally, there is a contribution from Ω_b, which is not measured but assumed to be much smaller and on the order of 15% of Ξ_b. This is expressed by a very large relative uncertainty of 40%, thus arriving at an estimate of δ of 0.25 ± 0.10.

The measured semileptonic b-hadron branching fractions are given in Table 6.1. To obtain them, a general principle is, liberally applied here, that the semileptonic decay widths, Γ_{SL}, are equal for all b-hadron species used in this analysis except for a small correction for Λ_b^0 decays [48–50]. Using the relation, $\mathcal{B}_{\mathrm{SL}} = \Gamma_{\mathrm{SL}}/\Gamma = \Gamma_{\mathrm{SL}} \times \tau$, the semileptonic branching fraction can be obtained from the measured lifetime. The B^0 and B^+ semileptonic branching fractions are obtained from three measurements by CLEO [51], BaBar [52] and Belle [53] that are averaged. Details of this averaging can be found in Ref. [7]. The B_s^0 lifetime was measured in the flavour-specific decay $\overline{B}_s^0 \to D_s^+\pi^-$ at CDF [54] and LHCb [55]. Finally, the Λ_b^0 lifetime is taken from the HFAG average [45].

The measured charm branching fractions, along with their sources, are tabulated in Table 6.2. The PDG average is used for the D^0 and D_s^+ modes. The D^+ mode is obtained from a CLEO III measurement [56] and the Λ_c^+ average was measured at BES III [57] and Belle [58].

Table 6.1: Measured semileptonic branching fractions for B^0 and B^+ mesons and derived branching fractions for B_s^0 and Λ_b^0, based on the equality of semileptonic decay widths.

Particle	τ (ps) measured	$\mathcal{B}_{\mathrm{SL}}$ (%) measured	Γ_{SL} (ps^{-1}) measured	$\mathcal{B}_{\mathrm{SL}}$ (%) to be used
B^0	1.519 ± 0.005	10.30 ± 0.19	0.0678 ± 0.0013	
B^+	1.638 ± 0.004	11.09 ± 0.20	0.0680 ± 0.0013	
$\langle B^0 + B^+ \rangle$		10.70 ± 0.19		10.70 ± 0.19
B_s^0	1.533 ± 0.018			10.40 ± 0.30
Λ_b^0	1.467 ± 0.010			10.35 ± 0.28

Table 6.2: Charm-hadron branching fractions of the decay modes used in this analysis.

Particle and decay	$\mathcal{B}_{H_c}$ (%)	Source
$D^0 \to K^-\pi^+$	3.91 ± 0.05	PDG average [19]
$D^+ \to K^-\pi^+\pi^+$	9.22 ± 0.17	CLEO III [56]
$D_s^+ \to K^-K^+\pi^+$	5.44 ± 0.18	PDG average [19]
$\Lambda_c^+ \to pK^-\pi^+$	$5.84 \pm 0.27 \pm 0.23$	BES III [57]
	$6.84 \pm 0.24^{+0.21}_{-0.27}$	Belle [58]
	6.36 ± 0.35	Average

6.3 Cross-feeds

The list of the semileptonic signal decays, sketched in Fig. 6.2, only includes the most abundant decay modes and neglects others that are suppressed by two orders of magnitude but exhibit different final-state charm hadrons. These lead to additional cross-feeds between the b-hadron modes. Denoting a proton or a neutron as N, these are $B^+ \to D_s K X \mu\nu$, $\Lambda_b^0 \to D N X \mu\nu$, and $B_s^0 \to D K X \mu\nu$ decays for which the charm hadrons do not originate from the expected b hadron. The measured branching fractions of the cross-feeds are given in Table 6.3, where the values for the b-meson modes are taken from the PDG [19] and the Λ_b^0 mode has been measured in the context of a master thesis [59]. It should be noted that, although the B_s^0 decay has a relatively large branching fraction of 0.71%, it is suppressed by an additional factor of 6 due to the smaller hadronisation fraction of a b quark forming a B_s^0 meson compared to B^0 and B^+ mesons. The impact on the b-quark production cross-section is small because all the individual charm contributions are added to the total b-hadron cross-section. When decays are falsely assigned to a b hadron, it is only the small difference in the branching fractions and the efficiencies that differ. Their contributions to the overall semileptonic branching fraction are small and the change in cross-section negligible compared to the overall accuracy. Therefore, they are only considered as a source

Table 6.3: Branching fractions of additional cross-feed decays taken from the PDG [19] and a master thesis [59].

cross-feed mode	branching fraction
$B^+ \to D_s^{(*)} K^+ X \mu^+ \nu_\mu$	0.12 ± 0.03% [19]
$B_s^0 \to DKX\mu^+\nu_\mu$	0.71 ± 0.16% [19]
$\Lambda_b^0 \to D^0 p \mu^- \bar{\nu}_\mu X$	0.19 ± 0.05% [59]

of systematic uncertainty.

6.4 Simulated event samples

For each decay mode and centre-of-mass energy, a sample of 1.1 to 1.5 million simulated semileptonic b-hadron decays is generated. As described in Sec.3.5, the proton-proton interaction is simulated with the event generator Pythia 8 [34] and the EvtGen library [35] describes the b-hadron decays. The samples are produced such that each event contains at least one b-hadron decay into a muon and a charm hadron where the relative occurrence of the excited $H_c^{**}\mu^-\nu$, $H_c^*\mu^-\nu$ and $H_c\mu^-\nu$ states and the additionally produced particles X are taken from the PDG [19]. The decays are reconstructed the same way as the data, taking into account reconstruction and selection artefacts of the detector and the track reconstruction algorithms.

6.5 Theoretical models of heavy-quark production

The production of heavy-flavour hadrons in proton-proton collisions is theoretically described by the convolution of the parton distribution function of the incoming protons, the partonic hard scattering rate, and the fragmentation function of the heavy quark into the respective hadron. While the parton distribution functions and the non-perturbative fragmentation function have to be obtained from data, the hard scattering process can be computed perturbatively using a power expansion in the strong coupling constant α_s. However, emerging singularities in the series are treated differently in theoretical models that are valid either in the regime of small transverse momenta of the produced quarks or in the limit where the transverse momentum is much larger than the quark mass. The fixed-order-plus-next-to-leading log (FONLL) framework [60] merges the two models in order to provide predictions for the whole p_T range.

6.5.1 Next-to-leading order QCD calculations of heavy-quark production

The leading-order diagrams responsible for heavy-quark production in proton-proton collisions are gluon-fusion and quark anti-quark annihilation processes shown in Fig. 6.3 (a) and (b), respectively. For centre-of-mass energies in the TeV range and for proton-proton collisions in general, gluon fusion dominates over quark annihilation. At lowest order, the total production cross-section is finite without diverging poles in the intermediate propagators and the minimum transverse momentum, transferred by the propagators, sets the scale of the strong coupling constant α_s. Since this scale is on the order of the

heavy-quark mass, the strong coupling constant α_s is small and the production cross-section can be calculated perturbatively [60–62].

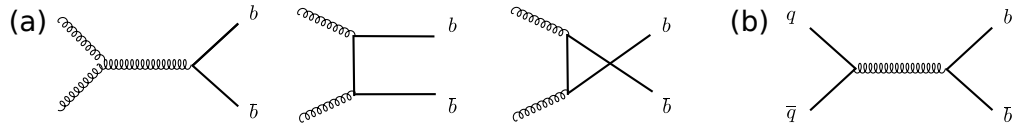

Figure 6.3: Lowest-order Feynman diagrams for $b\bar{b}$ production via (a) gluon fusion and (b) quark anti-quark annihilation.

Next-to-leading order (NLO) corrections are sketched in Fig. 6.4. They include real-gluon emission processes in (a), interferences of the tree-level diagrams with virtual-gluon-exchange processes in (b), flavour-excitation processes in (c) and gluon-splitting processes in (d).

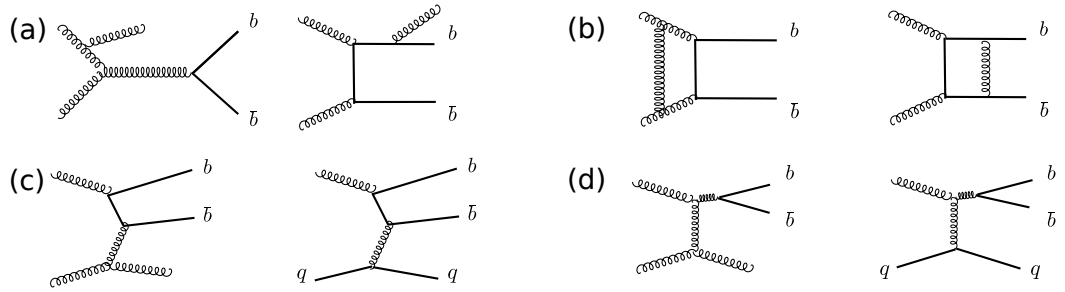

Figure 6.4: Next-to-leading (NLO) order Feynman diagrams for $b\bar{b}$ production via gluon fusion with additional (a) real-gluon and (b) virtual-gluon emission, (c) flavour-excitation processes and (d) gluon-splitting processes. At NLO, the virtual-gluon emission appears only in the interference with tree-level diagrams.

In these processes, several divergences appear. Ultraviolet divergences from high-energy gluons in the virtual diagrams are removed by the renormalisation process. Infrared divergences from low-energy gluons emerge both in the virtual and real-gluon emission diagrams where contributions partly cancel each other. Collinear divergences appear when the gluon is emitted with very small transverse momentum relative to the parton. In case of heavy quarks, these are suppressed because the collinearly emitted gluons do not alter the transverse momentum of heavy quarks. It is important to note that this is exclusively valid for heavy quarks and does not hold for the light up- and down-quarks. The production cross-section for the inclusive production of a heavy-quark pair is a function of the square of the partonic centre-of-mass energy s, the heavy quark mass m and transverse momentum p_{T}, the renormalisation scale μ_R and the factorisation scale μ_F[1]. With the choice of scales, $\mu_R = \mu_F = \mu$, the cross-section can be written as [60]

$$\frac{\mathrm{d}\sigma}{\mathrm{d}{p_{\mathrm{T}}}^2}(s, m, p_{\mathrm{T}}, \mu) = a_0\ \alpha_s^2 + \Big(a_1\ \log(\mu/m) + b_0\Big)\alpha_s^3 + \mathcal{O}(\alpha_s^4), \tag{6.5}$$

[1]The renormalisation scale μ_R is the energy scale used in the evaluation of α_s . The factorisation scale μ_F is the scale used in the evolution of the parton densities [61].

where the coefficients a_i and b_i depend upon s, p_{T} and μ and $\alpha_s = \alpha_s(\mu_R)$. The logarithmic terms are remnants of the collinear singularity screened by the finite quark mass. However, this model is only applicable when the mass is the only relevant energy scale. This does not hold in case of the transverse momentum being larger than the mass because all momenta in the range of the mass and the momentum are equally involved. When choosing μ of order p_{T}, large logarithms of the ratio p_{T}/m arise to all orders in the perturbative expansion and spoil the convergence.

6.5.2 Resummation approach for heavy-quark production

The afore-described NLO calculations are only valid in the regime of small transverse momenta. When considering the opposite situation with a very high quark p_{T}, its mass does not play a role in the scattering process and the quark can be considered as produced as a massless parton at the high-energy scale $\mu_F \sim p_{\mathrm{T}}$. This is done in the fragmentation-function formalism [63] in which the massless parton b only successively fragments into a massive heavy quark Q_b, modelled by a perturbative fragmentation function (PFF), $\mathrm{f}(b \to Q_b)$. The key difference to the non-perturbative hadronic fragmentation function, $\mathrm{f}(Q_b \to H_b)$, is that these PFFs are calculable from first principles in QCD. The initial-state conditions of the fragmentation function at an energy scale μ_0 can be obtained in the chosen normalisation scheme. Any desired higher factorisation scale μ_F is then accessible via the Altarelli-Parisi evolution equation at NLO accuracy. As a result, the diverging logarithmic term is split into three terms, $\log(p_{\mathrm{T}}/\mathrm{m}) = \log(p_{\mathrm{T}}/\mu_F) + \log(\mu_F/\mu_0) + \log(\mu_0/\mathrm{m})$. The finite $\log(p_{\mathrm{T}}/\mu_F)$ term is incorporated in the short-distance cross-section of the massless quark, whereas the remaining large $\log(\mu_F/\mu_0)$ terms are resummed by the evolution of the perturbative fragmentation function and only the small $\log(\mu_0/\mathrm{m})$ of the initial-state condition is treated at fixed order in perturbation theory. With the choice of scales, $\mu_R = \mu_F = \mu$, the resummed calculation (RS) is given by [60]

$$\begin{aligned}\frac{\mathrm{d}\sigma}{\mathrm{d}{p_{\mathrm{T}}}^2}(s, m, p_{\mathrm{T}}, \mu) = \alpha_s^2 \sum_{i=0}^{\infty} a_i (\alpha_s \ \log(\mu/m))^i + \alpha_s^3 \sum_{i=0}^{\infty} b_i (\alpha_s \ \log(\mu/m))^i \\ + \mathcal{O}(\alpha_s^4 (\alpha_s \ \log(\mu/m))^i) + \mathcal{O}(\alpha_s^2 \times \mathrm{PST}),\end{aligned} \tag{6.6}$$

where the coefficients a_i and b_i again depend upon s, p_{T} and μ and $\alpha_s = \alpha_s(\mu)$. PST stands for suppressed terms, in the large-p_{T} limit, by powers of $\mathrm{m}/p_{\mathrm{T}}$, irrespectively of further powers of logarithms and of α_s. The logarithmic terms are classified in terms of the leading-logarithmic (LL) form $\alpha_s^2 \ (\alpha_s \ \log(\mu/m))^k$ and terms of next-to-leading-log (NLL) form $\alpha_s^3 \ (\alpha_s \ \log(\mu/m))^k$. Due to the massless nature in the hard scattering process, this model cannot be valid when p_{T} approaches the heavy quark mass.

6.5.3 Fixed-order-plus-next-to-leading log (FONLL) framework

The fixed-order-plus-next-to-leading log (FONLL) framework [60] merges the low-p_{T} formalism up to fixed order (FO) and the fragmentation-function approach such that all terms of order α_s^2 and α_s^3 and all terms of order $\alpha_s^2 \ (\alpha_s \ \log(p_{\mathrm{T}}/m))^k$ and $\alpha_s^3 \ (\alpha_s \ \log(p_{\mathrm{T}}/m))^k$ are included in the perturbation series. The heavy-quark production cross-section is then

given by

$$\frac{\mathrm{d}\sigma}{\mathrm{d}{p_\mathrm{T}}^2}(s,m,p_\mathrm{T},\mu) = a_0\ \alpha_s^2 + \Big(a_1\ \log(\mu/m) + b_0\Big)\alpha_s^3 + \left(\alpha_s^2 \sum_{i=2}^{\infty} a_i(\alpha_s\ \log(\mu/m))^i + \alpha_s^3 \sum_{i=1}^{\infty} b_i(\alpha_s\ \log(\mu/m))^i\right) \times G(m,p_\mathrm{T}) + \mathcal{O}(\alpha_s^4(\alpha_s\ \log(\mu/m))^i) + \mathcal{O}(\alpha_s^4 \times PST), \tag{6.7}$$

where the function G(m,p_T) can be chosen relatively freely, but must approach 1 in the limit $m/p_\mathrm{T} \to 0$. It should be noted that the sums start from i=2 and i=1 to avoid double counting. Technically, the previously-developed fixed-order computation [62] of the $\mathcal{O}(\alpha_s^3)$ and the resummed (RS) [63] approach in the massless limit are combined. Terms of the RS formalism that are already present in the fixed-order one have to be subtracted. These terms are called the massless limit, FOM0, of the fixed order. Equation 6.7 can be illustrated as

$$\mathrm{FONLL} = \mathrm{FO} + (\mathrm{RS} - \mathrm{FOM0}) \times G(m,p_\mathrm{T}).$$

Problems occur because the normalisation schemes of the two approaches are not compatible with each other. This was solved in Ref. [60] by formulating the FO formalism in the same scheme as the RS framework with minor modifications to the partonic cross-sections. Finally, the resummation procedure and the fixed-order formalism are combined by matching the massless fixed-order approach FOM0 with the resummation up to the order α_s^3.

In order to predict the resulting kinematics of the produced b hadrons, the FONLL prediction of heavy-quark production is convolved with the non-perturbative hadronic fragmentation function, f($Q_b \to H_b$), whose parameters are extracted from e^+e^- collisions data. The FONLL formalism has been successful in describing bottom and charm hadron production at the Tevatron and RHIC [12]. For the present analysis, the predictions of the 7 TeV and 13 TeV b-hadron production cross-sections have been provided directly by M. Cacciari and M. L. Mangano.

6.5.4 Uncertainties of the FONLL prediction

To compute the central FONLL prediction, the renormalisation and factorisation scales are taken to be equal to the transverse mass, $\mu_{R,F} = \mu_0 \equiv \sqrt{{p_\mathrm{T}}^2 + m^2}$, of the heavy quark. The uncertainties are estimated [12] by varying the scales and the heavy quark mass and from uncertainties of the parton distribution functions. The scales are varied independently from each other with factors of 0.5, 1 and 2[2]. The beauty-quark mass is varied within 0.25 GeV/c^2 of the nominal mass of 4.75 GeV/c^2. The three components, where the uncertainties due to the chosen scale are largely dominant, are added in quadrature to a relatively large uncertainty of about 40-50%. The previous measurement of the b-hadron production cross-section at LHCb [24] showed good agreement in the distribution of pseudorapidity and integrated cross-section within the experimental and theoretical uncertainties. Forming the ratio of cross-sections at different centre-of-mass energies, in which the theoretical uncertainties cancel, especially in terms of the scales, allows for a much more precise comparison of the FONLL framework with experimental data.

[2]The scales (μ_R, μ_F) are sequentially varied with factors (1,1), (0.5,0.5), (2,2), (0.5,1), (1,0.5), (2,1), (1,2).

7 Analysis strategy

This analysis aims to measure the b-hadron production cross-section at 7 TeV and 13 TeV proton-proton centre-of-mass energies as a function of the pseudorapidity, η, of the b hadron. This is done using semileptonic decays into charm hadrons, muons and possible additional particles. As the neutrino remains undetected, only the muon and the charm hadron are reconstructed. Experimentally, the production cross-section is proportional to the number of reconstructed signal events, $n(H_c\mu)$, divided by the integrated luminosity, $\mathcal{L}$, the related efficiencies, $\varepsilon_{H_c\mu}$, and the branching fractions, $\mathcal{B}$, of the corresponding decays:

$$\sigma(pp \to H_b^0 X) \propto \left[\frac{n(H_c\mu)}{2\mathcal{L} \times \varepsilon_{H_c\mu} \times \mathcal{B}_{H_c}}\right] \frac{1}{\mathcal{B}_{\mathrm{SL}}(H_b)}.$$

Restricting to the b hadrons B^0, B^+, B_s^0 and Λ_b^0 as a simplification, the b-hadron production cross-section per bin in η is the sum of the individual b-hadron components. The measurement is performed in the following steps:

- The signal decays are recorded by the LHCb experiment when the muon satisfies the trigger requirements, which combine information from the muon chambers and the tracking detectors, as described in Chap. 8. The charm hadrons are reconstructed in their most abundant decay modes $D^0 \to K^-\pi^+$, $D^+ \to K^-\pi^+\pi^+$, $D_s^+ \to K^-K^+\pi^+$ and $\Lambda_c^+ \to pK^-\pi^+$. Due to the relatively long lifetime of b hadrons, the muon and the charm hadron are produced significantly away from the proton-proton interaction point. This characteristic decay topology is exploited to select the signal candidates.

- A certain fraction of the selected charm-hadron candidates do not originate from a b hadron, but are produced directly in the proton-proton interaction. As they exhibit a smaller impact parameter, the number of signal decays is extracted, per bin in η of the b hadron and p_{T} of the charm-plus-muon candidate, with a simultaneous fit to the invariant mass and the logarithmic impact parameter distribution of the charm-hadron candidate. The mass fit is needed to identify non-charm combinatorial background.

- Contributions from random combinations of charm hadrons and muons are modelled by events with the wrong charge combination which is not allowed in the signal decay. Remaining real signal-like background decays are determined with fully simulated samples of these types.

- The reconstruction and selection efficiencies of the signal events are obtained from fully simulated samples. In order to provide a more accurate result, data-driven methods using calibration samples are applied to determine the particle identification, trigger and track reconstruction efficiencies and the efficiency due to selection criteria on the occupancy of the detector.

- The results are compared with fixed-order next-to-leading logarithmic (FONLL) theoretical predictions that are provided as a function of the pseudorapidity. In the ratio of production cross-sections at 7 TeV and 13 TeV centre-of-mass energies, the theoretical uncertainties cancel partially which allows for a more precise test of the theory model.

8 Reconstruction and selection of the signal candidates

The data samples used in this analysis correspond to integrated luminosities of $284.10 \pm 4.86\,\mathrm{pb}^{-1}$ at the centre-of-mass energy of 7 TeV and $4.60 \pm 0.18\,\mathrm{pb}^{-1}$ at 13 TeV. They were collected in 2011 and 2015, respectively. From now on, the two datasets are referred to as the 7 TeV and the 13 TeV datasets for simplicity. This chapter describes and motivates the selection criteria to reconstruct and select the semileptonic signal decays. The b-hadron decays are partially reconstructed by combining a charm hadron with a muon to form a common vertex as it is illustrated for the $B^- \to D^0\mu^-\bar{\nu}_\mu$ decay mode shown in Fig. 8.1. Prompt background particles that are produced directly in the proton-proton interaction have to be rejected. This can be achieved by exploiting the relatively long lifetime of b hadrons and their characteristic decay vertices that are significantly away from the primary vertex.

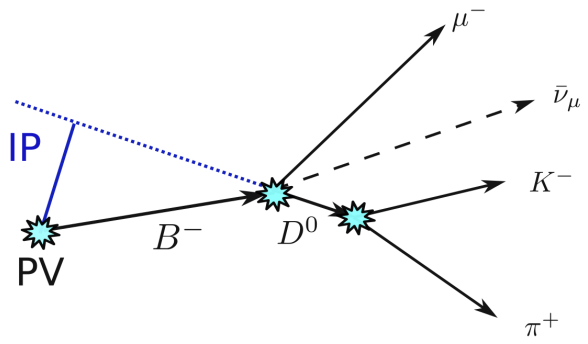

Figure 8.1: Topology of the decay $B^- \to D^0\mu^-\bar{\nu}_\mu$, where the D^0 meson decays into a kaon and a pion.

8.1 Trigger strategy and reconstruction of the muon

Muons are the only particles that can traverse the whole detector and leave a signal in the muon chambers. Therefore, their signal can be easily used as a hardware *level-0* (L0) trigger for the semileptonic b decay. A muon track is defined as a track that is reconstructed in all five muon chambers and the hits provide a quick measurement of the transverse momentum, p_T, by using an average proton-proton collision point [32]. Due to the heavy b-hadron mass, the light final-state particles tend to have larger transverse momenta compared to prompt particles that are, on average, boosted along the longitudinal direction, residually from the

kinematics of the colliding partons. The event is accepted if the transverse momentum is above 1480 MeV/c for the 7 TeV dataset and 900 MeV/c for the 13 TeV dataset as tabulated in Table 8.1. Since the software trigger system cannot cope with large track multiplicities due to the computation time of the track reconstruction algorithms, the occupancy of the detector is reduced by demanding that the total number of hits in the Scintillating Pad Detector, n_{SPD}, is less than 600 for the 7 TeV data. In case of the 13 TeV data-taking, more computation time is granted for the trigger because the run period is dedicated to cross-section measurements, and no selection criterion is enforced.

The software *high-level(Hlt)* trigger is split into two stages for which the larger computation time allows for a full track reconstruction. In the first stage, *Hlt1*, the track that satisfies the hardware trigger requirements, is confirmed by associating track segments in the VELO or tracking stations to the track in the muon chambers [64]. In the second stage, *Hlt2*, the full detector information is available such that momenta are measured with higher precision and secondary vertices are obtained. The requirements on the transverse momentum, the impact parameter, IP, and the χ^2_{IP} value discriminate against prompt particles. For the 7 TeV dataset, the impact parameter is required to be larger than 0.5 mm whereas there is no selection criterion on the absolute impact parameter for the 13 TeV dataset. Additionally, the selection criteria on the χ^2_{IP} value of 200 and 16 for the 7 TeV and 13 TeV datasets, respectively, are very different. Besides the larger bandwidth available during the 13 TeV data-taking, it is also the experience with the detector after two years of data-taking that motivates the modifications of the selections. It is important to note that the significantly different trigger requirements have a large impact on the whole analysis in terms of selection efficiencies and background contributions. The binary muon selections, *isMuon* and *isMuonTight*, that are also enforced at this stage are also more stringent for the 7 TeV data than for the 13 TeV data. Due to the large amount of events with final-state muons and the limited computational capacities, the trigger rate is downscaled to 50% for both datasets by accepting only every second event.

Apart from the trigger requirements, additional selection criteria are applied to the recorded muons, which are denoted as *offline* criteria: the momentum, p, has to be larger than 6 GeV/c and the hits in the detectors that are assigned to the muon are not supposed to be shared with other muon tracks. This impedes misidentification of particles and improves the momentum resolution. The occupancy of the detector is further reduced by limiting the number of long tracks to 250. In order to reduce misidentification of hadron tracks, the particle identification (PID) criterion, the difference of logarithmic likelihoods to separate muons from pions of $\Delta\log\mathcal{L}_{\mu-\pi} > 0$, is used.

8.2 Reconstruction of the charm hadron

Using the recorded data that satisfies all muon trigger requirements, the charm hadrons are now reconstructed and isolated from background contributions. The four charm hadrons are reconstructed in their most abundant decays $D^0 \to K^-\pi^+$, $D^+ \to K^-\pi^+\pi^+$, $D_s^+ \to K^-K^+\pi^+$ and $\Lambda_c^+ \to pK^-\pi^+$. As well as for the muons, the χ^2_{IP} value of the final-state hadrons is supposed to be larger than 9 to suppress prompt background. The criteria on the transverse momenta are less stringent because the charm hadron is not as massive. The average transverse momentum per charm daughter must be larger than

Table 8.1: Trigger and additional offline muon selection requirements for the 7 TeV and 13 TeV datasets.

	parameter	7 TeV	13 TeV
L0	n_{SPD}	< 600	-
	p_{T} [MeV/c]	> 1480	> 900
Hlt1	p [MeV/c]	> 8000	> 3000
	p_{T} [MeV/c]	> 1000	> 800
	IP [mm]	> 0.1	–
	χ^2_{IP}	> 16	> 4
	PID	isMuonTight	isMuon
Hlt2	accept fraction	0.5	
	p_{T} [GeV/c]	> 1.3	
	IP[mm]	> 0.5	–
	χ^2_{IP}	> 200	> 16
Offline	p [GeV/c]	> 6	
	detector hits	no shared hits with other muon tracks	
	# of long tracks	< 250	
	PID	$\Delta\log\mathcal{L}_{\mu-\pi} > 0$	

700 MeV/c for the two-body decay of the D^0 mode and 600 MeV/c for the three-body decay modes as listed in the summary Table 8.2. Again, it is the experience with the detector that drives the differing selection requirements for the 13 TeV dataset.

To identify the decays, particle identification requirements for the individual particle species are demanded: for protons, the differences of logarithmic likelihoods to separate them from kaons and pions, are $\Delta\log\mathcal{L}_{p-K}(p) > 0$ and $\Delta\log\mathcal{L}_{p-\pi}(p) > 10$; to separate kaons from pions $\Delta\log\mathcal{L}_{K-\pi}(K) > 4$; and the pion requirements are $\Delta\log\mathcal{L}_{K-\pi}(\pi) < 4$ for the 7 TeV and $\Delta\log\mathcal{L}_{K-\pi}(\pi) < 10$ for the 13 TeV dataset.

The light-particle tracks are combined to form the charm hadrons at a common vertex whose reconstruction fit must fulfil a χ^2 value divided by the number of degrees of freedom, n_{dof}, of less than 6. In order to further constrain the number of prompt charm hadrons, the significance of the distance from the charm-hadron decay vertex to the primary vertex must be larger than 100 for the 7 TeV and 25 for the 13 TeV dataset. Since the b hadron typically carries high longitudinal momentum from the beam energy, its decay products are emitted in a relatively narrow cone around the flight direction. Therefore, the cosine of the pointing angle between the distance from the charm-hadron decay vertex to the primary vertex and the measured charm-hadron momentum vector must be greater than 0.99[1]. The logarithm of the charm-hadron impact parameter is loosely restricted to the range from -7 to 2.

[1]The pointing angle has been defined in Sec. 3.3 for the b hadron. It should be noted that the pointing angle for the charm hadron is not defined with respect to the b-hadron decay vertex.

Table 8.2: Selection criteria for the charm hadrons and their decay particles for the 7 TeV and 13 TeV datasets. The value on the average p_{T} per charm daughter in parentheses is for the three-body decays of $(D^+|D_s^+|\Lambda_c^+)$.

parameter	7 TeV	13 TeV
Charm hadron daughters		
χ^2_{IP}	> 9	
p [GeV/c]	> 2	
proton p [GeV/c]	-	> 8
kaon p [GeV/c]	-	> 5
p_{T} [GeV/c]	> 0.3	> 0.25
PID for pions	$\Delta\log\mathcal{L}_{K-\pi}(\pi) < 4$	$\Delta\log\mathcal{L}_{K-\pi}(\pi) < 10$
PID for kaons	$\Delta\log\mathcal{L}_{K-\pi}(K) > 4$	
PID for protons	$\Delta\log\mathcal{L}_{p-\pi}(p) > 10$	
	$\Delta\log\mathcal{L}_{p-K}(p) > 0$	
Charm hadron		
average p_{T} per daughter[MeV/c]	$> 700(600)$	
vertex χ^2/n_{dof}	< 6	
χ^2 of distance to PV	> 100	> 25
cos of the angle between distance and $\vec{p}$	> 0.99	
log(IP/mm)	$\in [-7, 2]$	

8.3 Reconstruction of the b-hadron decay vertex

Due to the missing neutrino, the b hadron is only partially reconstructed and it is only the kinematics of the combined charm-plus-muon system that is accessible. The b-hadron decay vertex is defined by the combined vertex of the determined charm-hadron trajectory and the muon track. The χ^2/n_{dof} value of the vertex reconstruction fit is required to be less than 6 for the 7 TeV and 9 for the 13 TeV dataset as given in Table 8.3. Furthermore, the cosine of the pointing angle between the b-hadron flight distance to the decay vertex and the measured momentum vector, is demanded to be greater than 0.999. Due to the missing neutrino, the pseudorapidity $\eta = -\log\tan(\theta/2)$ of the b hadron is not defined by the related track momenta but exclusively by the angle, θ, between the beam axis and the flight direction of the b hadron. The accepted pseudorapidity range spans from 2 to 5.

Having a finite lifetime, the charm hadrons are required to decay at a larger z-position along the beam direction than the b hadron. The invariant mass distribution of the charm-plus-muon system is demanded to be in the range of approximately 3 GeV/c^2 to 5 GeV/c^2, depending on the decay mode. The maximum allowed distance between the primary vertex and the b-hadron decay vertex, denoted as the *flight radius*, is 4.8 mm because of material interactions with the insensitive inner part of the VELO disks at a radius of 5 mm.

Table 8.3: Selection requirements to reconstruct the b-hadron decay vertex using the charm-plus-muon system for the 7 TeV and 13 TeV datasets.

parameter	7 TeV	13 TeV
charm-plus-muon system		
vertex χ^2/n_{dof}	< 6	< 9
cos of the angle between distance and $\vec{p}$	> 0.999	
z(charm)-z(b)[mm]	> 0	
η	$\in [2, 5]$	
invariant mass [GeV/c^2]	$3 < m(D^0(D^+) + \mu) < 5$	
invariant mass [GeV/c^2]	$3.1 < m(D_s^+ + \mu) < 5.1$	
invariant mass [GeV/c^2]	$3.3 < m(\Lambda_c + \mu) < 5.3$	
flight radius [mm]	< 4.8	

8.4 Comparison of kinematic distributions from data and fully simulated events

Separately for the 7 TeV and 13 TeV datasets, Figs. 8.2 and 8.3 show the normalised distributions of the transverse momentum of the charm-plus-muon system, the logarithmic charm-hadron impact parameter, the muon transverse momentum and the logarithmic muon χ^2_{IP} distributions of the selected $B \to D^0 \mu \nu X$ candidates from data and simulation. Combinatorial and prompt background contributions have been subtracted using the ${}_s\mathcal{P}lot$ technique[2] with sWeights obtained from the fit results to the invariant mass and the logarithmic impact parameter of the charm-hadron candidate, described in the following chapter. However, the technique is only valid for variables that are not correlated to the discriminating variables. Therefore, the sWeights are not applied to the log(IP) distributions of the charm hadrons. They still contain the prompt background component as it can be seen for the 13 TeV data where the lower tail in data clearly overshoots the simulated distribution. The reason why the prompt contribution in the 7 TeV data is smaller is due to the different trigger requirements which is also reflected in the unequal logarithmic muon impact parameter distributions. The agreement between the data and the simulation is satisfactory except for a small deviation of the transverse momentum distribution of the charm-plus-muon candidate and of the tails of the logarithmic muon χ^2_{IP} distributions. The distributions of other kinematic variables that are also part of the selection, are given in Appendix A.

[2]The ${}_s\mathcal{P}lot$ technique has been described in Sec. 4.2

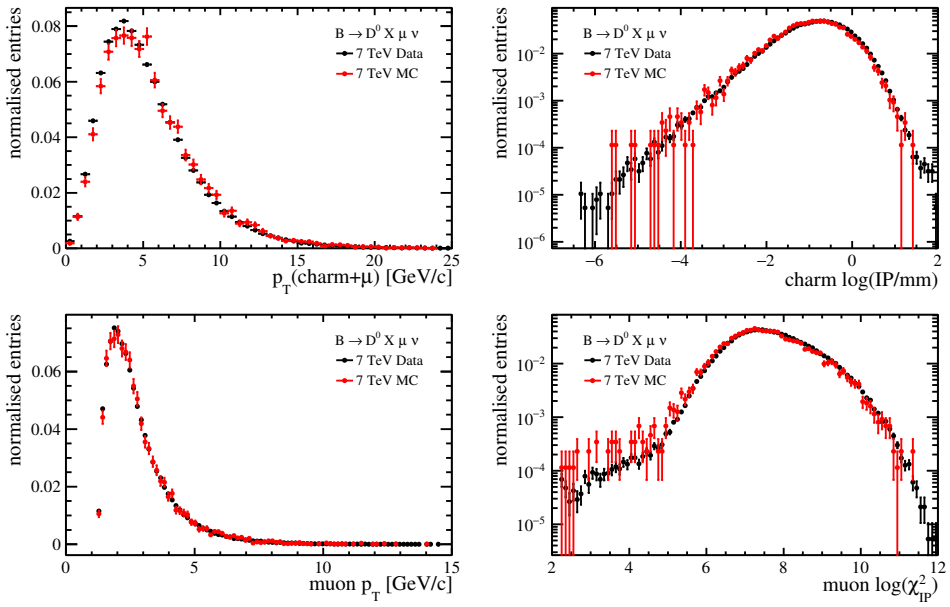

Figure 8.2: Distributions of (top left) transverse momentum of the combined D^0-plus-muon system, (top right) logarithmic D^0 impact parameter distribution, (bottom left) muon transverse momentum and (bottom right) logarithmic muon χ^2_{IP} from $B \to D^0 X \mu\nu$ decays in 7 TeV (black) data and (red) simulation.

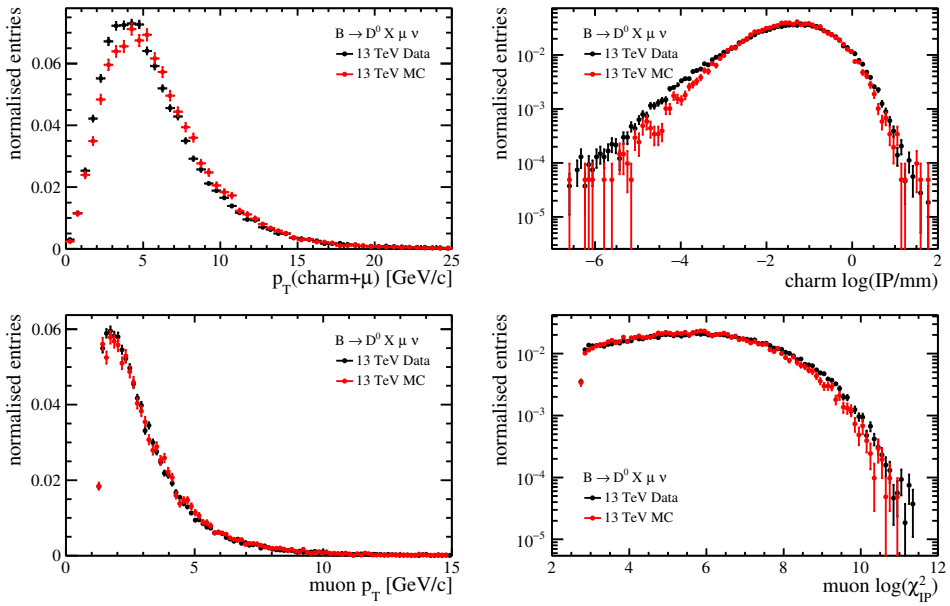

Figure 8.3: Distributions of (top left) transverse momentum of the combined D^0-plus-muon system, (top right) logarithmic D^0 impact parameter distribution, (bottom left) muon transverse momentum and (bottom right) logarithmic muon χ^2_{IP} from $B \to D^0 X \mu\nu$ decays in 13 TeV (black) data and (red) simulation.

For all b-meson decays, the description is as good as for $B \to D^0 \mu\nu X$, but in the baryon mode $\Lambda_b^0 \to \Lambda_c^+ \mu\nu X$, the transverse momentum spectrum of the charm-plus-muon system is shifted significantly in the simulation. The corresponding distributions are shown in Figs. 8.4 and 8.5 for the 7 TeV and 13 TeV data, respectively. The simulated transverse momentum of the muon also deviates from the data. The reason for this is that the transverse momentum distribution of the produced b hadrons is not known to this precision. The generated momentum spectra even vary slightly for different Pythia versions and tunes of the simulation. As it was described in Chap. 6, it is for this reason that the efficiencies of all charm modes are determined not only in bins of the b-hadron pseudorapidity, but also in bins of the charm-plus-muon transverse momentum. The efficiencies on the trigger and muon requirements are evaluated with data-driven methods as a function of the transverse momentum, the impact parameter and the pseudorapidity of the muon. In this way, observed differences in the modelling of the muon transverse momentum and logarithmic χ^2_{IP} value do not affect the efficiencies which reduces the systematic uncertainties and leads to a more precise result.

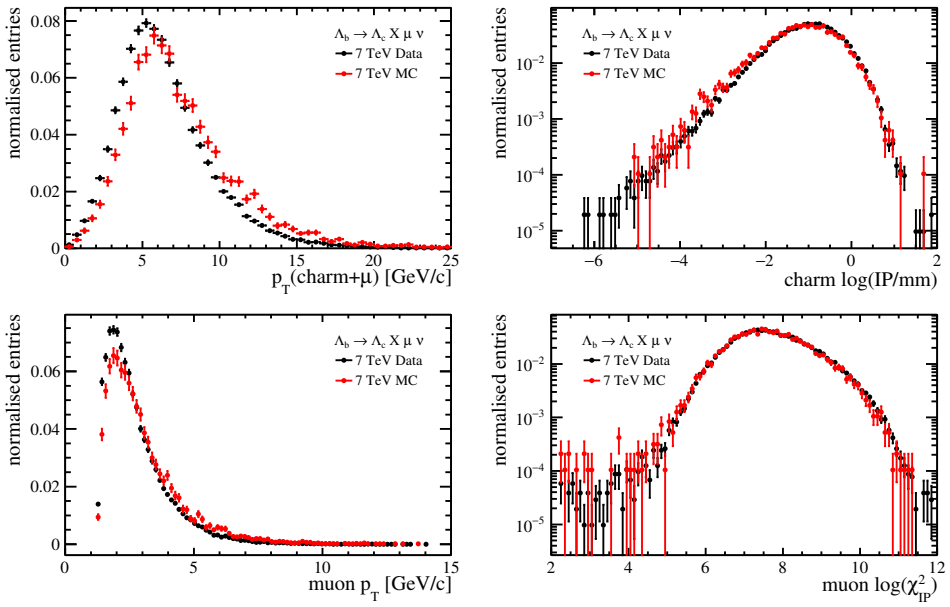

Figure 8.4: Distributions of (top left) transverse momentum of the combined Λ_c-plus-muon system, (top right) logarithmic Λ_c impact parameter distribution, (bottom left) muon transverse momentum and (bottom right) logarithmic muon χ^2_{IP} from $\Lambda_b \to \Lambda_c X \mu\nu$ decays in 7 TeV (black) data and (red) simulation.

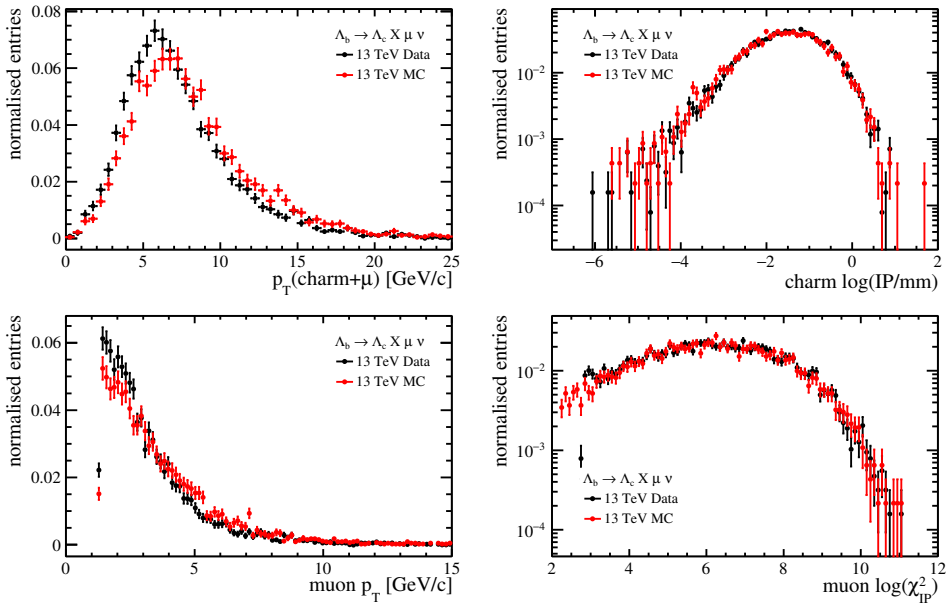

Figure 8.5: Distributions of (top left) transverse momentum of the combined Λ_c-plus-muon system, (top right) logarithmic Λ_c impact parameter distribution, (bottom left) muon transverse momentum and (bottom right) logarithmic muon χ^2_{IP} from $\Lambda_b \to \Lambda_c X \mu\nu$ decays in 13 TeV (black) data and (red) simulation.

9 Extraction of the number of signal events

The signal yields are obtained from simultaneous fits to the invariant mass and the logarithmic impact parameter distributions of the charm-hadron signal candidates using an unbinned maximum likelihood fit. The mass fit determines the contributions from real charm hadrons and combinatorial background and the log(IP) fit is used to identify prompt charm hadrons that originate from the primary vertex and not from a b hadron. The fit is performed in 6 bins of the b-hadron pseudorapidity from 2 to 5 and 13 bins of the transverse momentum of the charm-plus-muon system from 0 to 25 GeV/c.

9.1 Description of the mass model

The charm-hadron mass distribution is modelled by the sum of two Gaussian functions

$$\begin{aligned}\mathcal{P}_m(m; m_{H_c}, f_{1,m}, \sigma_{m,1}, \sigma_{m,2}) \;=\; & \left\{ \frac{f_{1,m}}{\sqrt{2\pi\sigma^2_{m,1}}} \; exp\left(-\frac{(m-m_{H_c})^2}{2\;\sigma^2_{m,1}}\right) \right. \\ & \left. + \frac{1-f_{1,m}}{\sqrt{2\pi\sigma^2_{m,2}}} \; exp\left(-\frac{(m-m_{H_c})^2}{2\;\sigma^2_{m,2}}\right) \right\}\end{aligned}$$

with shared means, the charm-hadron mass m_{H_c}. $f_{1,m}$ is the fraction of the first Gaussian and the two widths $\sigma_{m,i}$ model the mass resolution of the detector. The combinatorial background model is given by a linear function. The mass fit does not have any discriminative power to distinguish the signal from the prompt component, thus the latter is described by the same Gaussian functions with shared means and widths but different yields. The left-hand side of Fig. 9.1 shows the fit to the invariant mass of fully simulated 13 TeV signal decays. The fit quality in each bin can be assessed by defining the pull as the difference between the number of events observed in data and the number of events according to the fit, divided by the statistical uncertainty. For a valid fit model, the pull should be centred around zero within statistical fluctuations of one. The pull distribution that is shown below the nominal distribution has no significant deviations from zero.

9.2 Description of the logarithmic impact parameter model

The shapes that are used to model the logarithmic impact parameter distribution are chosen empirically such that they describe simulated decays. Due to the asymmetric shape, a function is needed that exhibits different widths on the left and the right side of the peak

position. A so-called bifurcated Gaussian is a modified Gaussian function

$$\mathcal{P}_{\text{bif}}(x; x_{\text{peak}}, \sigma_l, \sigma_r) = N \cdot \begin{cases} \exp\left(-\frac{(x-x_{\text{peak}})^2}{2\,\sigma_l^2}\right) & \text{for } x < x_{\text{peak}} \\ \exp\left(-\frac{(x-x_{\text{peak}})^2}{2\,\sigma_r^2}\right) & \text{for } x > x_{\text{peak}} \end{cases}, \tag{9.1}$$

that is defined section-wise below and above the maximum value, x_{peak}, with two different widths, σ_l and σ_r. On the right-hand side of Fig. 9.1, the fit to the D^0 logarithmic impact parameter distribution of fully simulated 13 TeV signal decays is shown where only single events overshoot the fit at the edge of the lower tail.

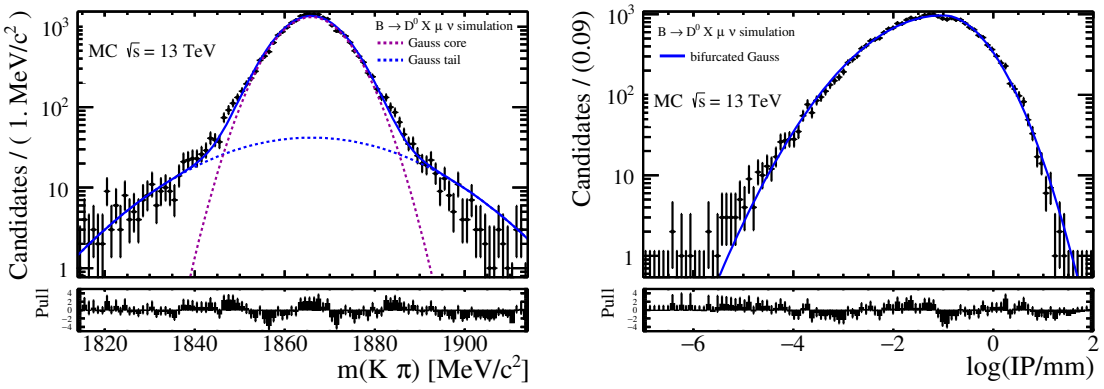

Figure 9.1: Fits to the (left) invariant mass and (right) log(IP/mm) distributions of the D^0 candidate of simulated $B \to D^0 \mu\nu X$ decays at a centre-of-mass energy of 13 TeV, given by black points, in the pseudorapidity range from 2 to 5. In the mass fit, the blue curve shows the total fit, the dashed purple line the Gaussian core and the dashed blue line the Gaussian tail. The D^0 log(IP/mm) distribution is described by a bifurcated Gaussian in blue.

The prompt charm-hadron and the combinatorial background components are modelled by the sum of a bifurcated Gaussian and a single Gaussian function with separate means in order to include the tails of the distributions. The shape of the prompt component is obtained from simulated events with prompt charm hadrons that are combined with a random track of the event which mimics a charm-plus-muon candidate. Whereas the charm hadron is subject to the signal selection, only the kinematic muon criteria are required for the additional track, but not the muon identification criteria as there are not sufficiently many real muons. However, this is not important as the topological characteristics of the charm-hadron decay after combining it with a random track at a common vertex, are not affected by the muon identification. On the left-hand side of Fig. 9.2, the fit to the logarithmic impact parameter distribution of this sample is shown. The description is good with only small deviations in the tails where only few events are left. The combinatorial background shape is obtained from a fit to the selected charm-hadron candidates from data whose invariant masses are distinctly separated from the signal peak in the sidebands of the mass distribution. The right-hand side of Fig. 9.2 shows the fit to these combinatorial background events which are well modelled. In the fit of the signal yields, the background

shapes are fixed to their pre-determined values and only the yields are extracted.

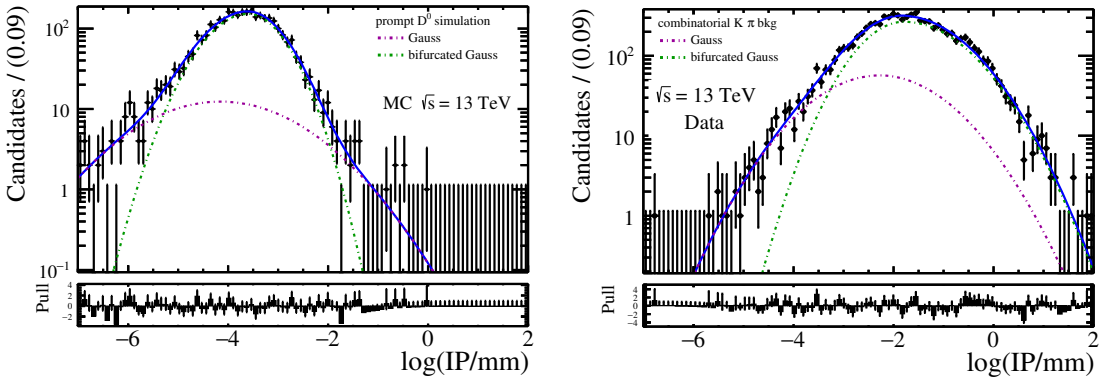

Figure 9.2: Fits of the sum of a bifurcated Gaussian and a Gaussian function to the log(IP/mm) background distributions of the (left) simulated prompt D^0 decays and the (right) combinatorial background sample obtained from the sidebands of the invariant kaon-pion mass distribution at a centre-of-mass energy of 13 TeV. The black points show the simulation and the data, respectively, the blue curves the total fit, the dashed purple lines the Gaussian functions and the dashed green lines the bifurcated Gaussians.

9.3 Fit results

Although the fit is performed in bins of the pseudorapidity of the b hadron and the transverse momentum of the charm-plus-muon system, the results are only given here for the fits to all candidates in the full η and p_{T} range. The fitted signal yields for all bins separately can be found in Appendix A. In case of the D_s^+ decay mode, the D_s^+ candidates contain contributions from real D^* decays into a D^0 meson and a pion with the D^0 decaying into two kaons. Having a higher mass of about 2010 MeV/c^2, this component is easily identified and fitted with a different sum of two Gaussian functions whose widths are computed in the fit to events in the full η and p_{T} range. The log(IP) component of the D^* mode shares the same parameters as the signal. Table 9.1 gives the fitted parameters of the fit to the charm-hadron candidates in the full η and p_{T} range of the 7 TeV data. The corresponding distributions of the invariant mass and log(IP) overlaid with the fitted functions are shown in Fig. 9.3, exemplary for the D^0 mode, plotted with logarithmic scale in the top and with linear scale in the bottom. The distributions of the other modes are attached in Appendix A. The prompt component is below the percent level of the summed signal yield of about 440'000 semileptonic signal b-hadron decays. The fit parameters to the 13 TeV data are listed in Table 9.2 and the distributions are shown in Fig. 9.4. Due to the different trigger requirements, the relative prompt charm-hadron yield is higher, up to 7% of the summed signal yield of 90'000 semileptonic b-hadron decays. The signal peak of the mass distribution of the 7 TeV dataset is slightly asymmetric which leads to some structures in the pull distribution of the Gaussian tails. This is not observed in the 13 TeV

dataset so it becomes only apparent for a large number of events. As the signal yields in the intervals of η and p_{T} are smaller, this does not significantly affect the measurement of the signal yields. The pull distribution of the logarithmic impact parameter also exhibits a structure in the upper tail. Since the fit to the log(IP) distribution is done to identify the prompt component in the lower tail, the upper tail is not of great concern. The choice of the fit models for the mass and the logarithmic impact parameter is taken into account as a systematic uncertainty in Sec. 12.3.7, but it is very small compared to the overall precision.

Table 9.1: Parameters of the fit to b-hadron candidates in the full η and p_{T} range of the 7 TeV dataset.

Parameter	D^0	D^+	D_s^+	Λ_c^+
μ_{H_c} [MeV/c^2]	1866.49 ± 0.02	1870.90 ± 0.02	1969.79 ± 0.05	2288.04 ± 0.03
$\sigma_{m,1}$[MeV/c^2]	12.47 ± 0.22	6.08 ± 0.11	10.92 ± 0.35	4.76 ± 0.09
$\sigma_{m,2}$ [MeV/c^2]	6.72 ± 0.06	10.41 ± 0.26	5.26 ± 0.06	10.09 ± 0.56
$f_{1,m}$	0.28 ± 0.01	0.59 ± 0.03	0.36 ± 0.02	0.74 ± 0.03
$\mu_{log(IP)}$	-0.61 ± 0.004	-0.648 ± 0.005	-0.68 ± 0.01	-0.79 ± 0.01
$\sigma_{l,log(IP)}$	0.92 ± 0.003	0.916 ± 0.004	0.919 ± 0.009	0.893 ± 0.006
$\sigma_{r,log(IP)}$	0.58 ± 0.002	0.574 ± 0.003	0.563 ± 0.007	0.557 ± 0.005
Signal Yield	205'311 ± 486	142'283 ± 436	40'049 ± 299	53'459 ± 300
Prompt Yield	1227 ± 51	1199 ± 51	262 ± 26	270 ± 23
Comb. Bkg Yield	22270 ± 229	54891 ± 320	79108 ± 535	42495 ± 281
D^* Yield	–	–	3597 ± 340	–

Table 9.2: Parameters of the fit to b-hadron candidates in the full η and p_{T} range of the 13 TeV dataset.

Parameter	D^0	D^+	D_s^+	Λ_c^+
μ_{H_c} [MeV/c^2]	1865.53 ± 0.04	1870.03 ± 0.06	1969.09 ± 0.13	2287.45 ± 0.08
$\sigma_{m,1}$ [MeV/c^2]	6.40 ± 0.14	6.21 ± 0.35	5.32 ± 0.21	4.60 ± 0.27
$\sigma_{m,2}$ [MeV/c^2]	10.99 ± 0.76	10.53 ± 1.05	11.05 ± 2.15	8.76 ± 0.94
$f_{1,m}$	0.63 ± 0.04	0.64 ± 0.12	0.67 ± 0.05	0.65 ± 0.10
$\mu_{log(IP)}$	-1.171 ± 0.013	-1.151 ± 0.021	-1.226 ± 0.046	-1.282 ± 0.032
$\sigma_{l,log(IP)}$	1.107 ± 0.014	1.110 ± 0.023	1.014 ± 0.043	0.978 ± 0.026
$\sigma_{r,log(IP)}$	0.736 ± 0.007	0.719 ± 0.012	0.730 ± 0.026	0.690 ± 0.019
Signal Yield	55'714 ± 288	21'706 ± 200	4917 ± 105	6430 ± 93
Prompt Yield	2410 ± 135	1481 ± 88	215 ± 29	84 ± 17
Comb. Bkg Yield	11936 ± 153	13419 ± 163	9570 ± 140	3038 ± 71
D^* Yield	–	–	281 ± 78	–

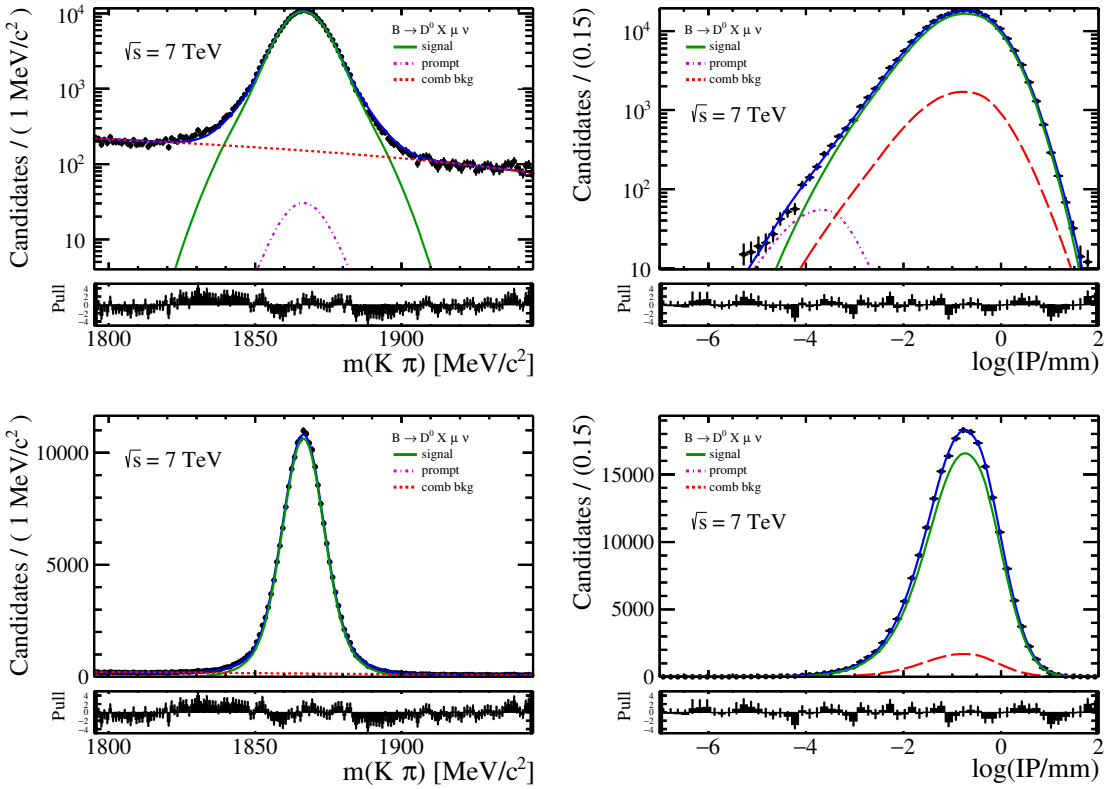

Figure 9.3: Simultaneous fit to the D^0 candidate (left) invariant mass and (right) log(IP/mm) distributions in the pseudorapidity range from 2 to 5 taken at a center-of-mass energy of 7 TeV, plotted with (top) logarithmic scale and (bottom) with linear scale. The black points show the data, the blue curves the total fit, the green curves the signal, the purple curves the prompt charm-hadron component from the primary vertex and the red curves the combinatorial background.

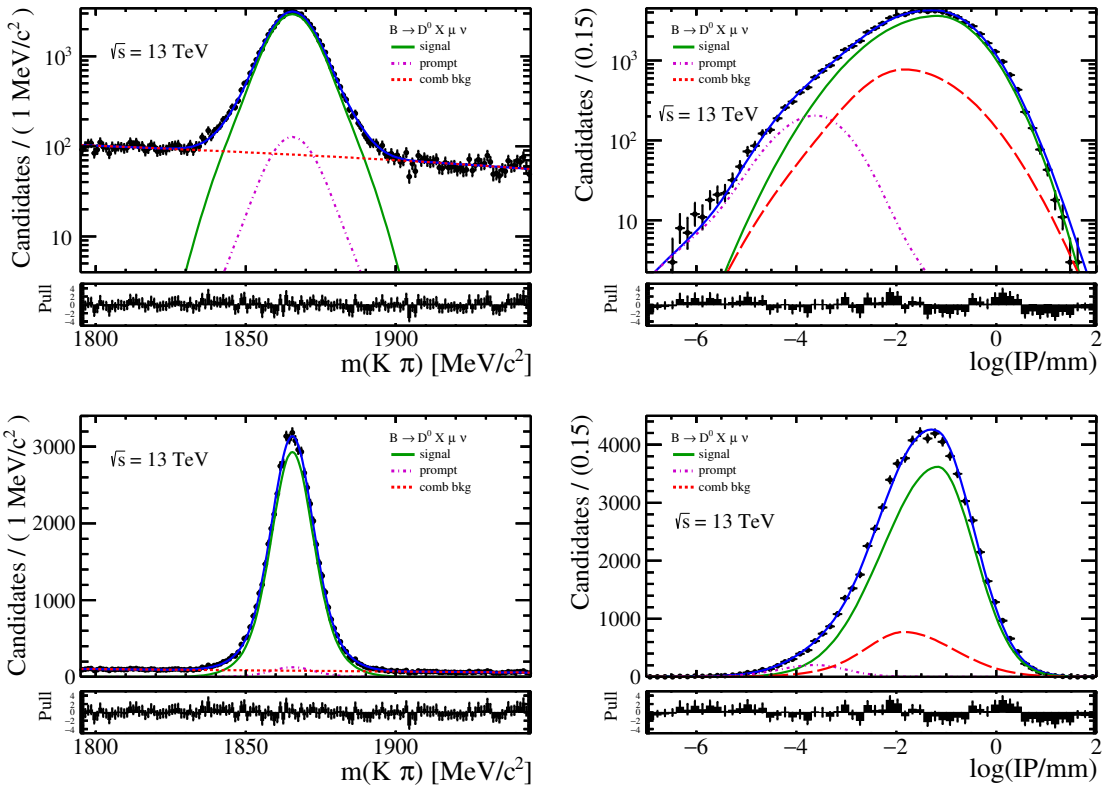

Figure 9.4: Simultaneous fit to the D^0 candidate (left) invariant mass and (right) log(IP/mm) distributions in the pseudorapidity range 2 from to 5 taken at a center-of-mass energy of 13 TeV, plotted with (top) logarithmic scale and (bottom) with linear scale. The black points show the data, the blue curves the total fit, the green curves the signal, the purple curves the prompt charm-hadron component from the primary vertex and the red curves the combinatorial background.

10 Backgrounds

Apart from the prompt charm-hadron component that is identified in the fit of the signal yield, there are additional sources of backgrounds that are not completely discriminated against by the selection and are indistinguishable from the signal decays. The first contribution is due to pions and kaons that are misidentified as muons and combined with a charm hadron. The pollution from these so-called *fake muons* is estimated by using a sample that is selected with inverted particle identification requirements on the muon. Random combinations of real muons and charm hadrons that originate from different b decays are modelled by events where the final-state particles have the wrong charge combination compared to the signal. Real b decays into two charm hadrons are misidentified as semileptonic decays when one of the charm hadrons undergoes a semileptonic decay. Their rate relative to the signal decays is investigated using simulated samples.

10.1 Backgrounds from fake muons

A hadron h is misidentified as a muon when it satisfies the muon trigger requirements and the particle identification selection criterion, $\mathcal{L}_{\mu-\pi}(h) > 0$. The crucial discriminating power to distinguish between hadrons and muons is provided by the muon chambers. Therefore, the muon PID criterion does not only separate muons from pions but also from kaons. Given a known misidentification efficiency for a hadron to pass the muon trigger and particle identification selection requirements, the number of hadrons that are falsely identified as muons and combined with a charm hadron is obtained from a sample with inverted requirements on the muon particle identification.

10.1.1 Determination of the hadron-as-muon misidentification efficiency

The efficiency for a hadron to pass the muon trigger requirements and the particle identification selection criterion is determined by selecting a pure calibration sample of $D^{*+} \to D^0\pi^+$ decays, where the D^0 decays into a $K^-\pi^+$ pair. In order to apply no selection criteria on the final-state hadrons, they are not required to satisfy any trigger requirements. Instead, the data sample is recorded and saved on disk when any other track of the rest of the event satisfies the muon trigger requirements[1]. The D^{*+} mesons are found among these events only coincidentally as they are produced copiously in proton-proton collisions. Only the kinematic requirements that are applied to the muon in the signal selection are applied to the probe hadron h, either the kaon or the pion. To distinguish between kaons and pions, the difference of the logarithmic likelihood for the hadronic particle identification is chosen in favour of a kaon or a pion, $\Delta\log\mathcal{L}_{K-\pi}(h) > 0$ and $\Delta\log\mathcal{L}_{K-\pi}(h) < 0$, respectively.

[1] In principle, a different set of trigger requirements can be chosen for this other track, but the muon trigger is a well-known system that applies selection criteria to only one track.

Hence, the hadron-as-muon misidentification probability, $\varepsilon_{h\to\mu}$, is given by the ratio of the number of D^0 mesons for which the hadron track satisfies the muon trigger and particle identification requirements, denoted as $N_{D^0}(h\text{-trigg} \;\&\; \Delta\log\mathcal{L}_{\mu-\pi}(h) > 0)$, to the total number of D^0 mesons, N_{D^0}, used as probes:

$$\varepsilon_{h\to\mu} = \frac{N_{D^0}(h\text{-trigg} \;\&\; \Delta\log\mathcal{L}_{\mu-\pi}(h) > 0)}{N_{D^0}}. \tag{10.1}$$

The misidentification efficiencies obtained with this method are

$$\begin{aligned} \varepsilon_{\pi\to\mu,\ 7\,\text{TeV}} &= (0.019 \pm 0.004)\% & \varepsilon_{\pi\to\mu,\ 13\,\text{TeV}} &= (0.32 \pm 0.08)\% \\ \varepsilon_{K\to\mu,\ 7\,\text{TeV}} &= (0.026 \pm 0.003)\% & \varepsilon_{K\to\mu,\ 13\,\text{TeV}} &= (0.96 \pm 0.11)\%. \end{aligned}$$

The misidentification efficiency for the 7 TeV data, as defined here, is more than an order of magnitude smaller than for the 13 TeV data due to the tighter trigger requirements applied for the 7 TeV data-taking.

10.1.2 Combinations of fake muons with charm hadrons

The sample of fake muons combined with charm hadrons is selected using the same selection criteria as for the signal decays but the hadron h faking a muon is not required to satisfy the muon trigger requirements and the particle identification criterion is inverted, $\Delta\log\mathcal{L}_{\mu-\pi}(h) < 0$. The requirements for the charm-hadron and b-hadron candidates remain unchanged. As it was done for the hadronic calibration sample in the previous subsection, the data sample is recorded and saved on disk when any other track of the rest of the event satisfies the muon trigger requirements. This is done such that no trigger requirements are applied to the tracks. The sample is further divided into a kaon and a pion sub-sample by choosing the kaon PID criterion of the fake muon in favour of a kaon and a pion, respectively. The charm-hadron yields combined with a fake muon, $N_{H_c,h}(\Delta\log\mathcal{L}_{\mu-\pi}(h) < 0)$, are fitted the same way as the signal yields in the previous chapter, in bins of the pseudorapidity of the b-hadron candidate, η, in order to remove combinatorial and prompt charm-hadron background. Among these fake muons, the pollution from real muons is tiny because the criterion, $\Delta\log\mathcal{L}_{\mu-\pi} > 0$, is almost perfectly efficient for them [30]. Hence, the number of charm hadrons combined with fake muons that satisfy the muon trigger and PID requirements can be approximated by

$$N_{H_c,h}(h\text{-trigg} \;\&\; \Delta\log\mathcal{L}_{\mu-\pi}(h) > 0) = \frac{N_{H_c,h}(\Delta\log\mathcal{L}_{\mu-\pi}(h) < 0)}{1 - \varepsilon_{h\to\mu}} \cdot \varepsilon_{h\to\mu}, \tag{10.2}$$

where it has to be divided by $(1 - \varepsilon_{h\to\mu})$ to compensate for the hadrons in the positive $\Delta\log\mathcal{L}_{\mu-\pi}$-range[2]. The fake-muon rates relative to the signal yields are all determined to be below 0.1% and thus negligible, considering the precision of the production cross section. The exact values are listed in Appendix A.1 in Tables A.9 - A.16.

[2] Equation 10.2 is an approximation because it assumes that pions are not misidentified as kaons and vice versa which is true to the percent level [31]. Since the two hadron-as-muon efficiencies are in the same order of magnitude, the error due to this simplification is small.

10.2 Random combinations of muons and charm hadrons

Another possible source of background originates from random combinations of charm hadrons from another b-hadron decay with real muons. It is modelled by events in which the charm-hadron candidates are combined with muons with a charge that is not compatible with a b-hadron decay (wrong charge). As discussed in Chap. 6, the only allowed charge compositions for the signal decays are $H_c\mu^-$ and $\bar{H}_c\mu^+$ whereas the inverted, so-called *wrong-sign*, charge composite can only stem from random combinations.

When requiring the signal criteria to these wrong-sign events, they also contain contributions from prompt charm hadrons. Therefore, the background yields are determined using the same fit procedure as for the signal events in bins of the pseudorapidity of the b hadron and the transverse momentum of the charm-plus-muon system. The fitted yields in the full η and p_{T} range, relative to the signal yields, are given in Table 10.1 for the 7 TeV and 13 TeV datasets. They are below 1% in the 7 TeV data and slighlty higher in the 13 TeV data, with about 1% to 3%, because of the looser trigger requirements during the 13 TeV data-taking. The uncertainties are obtained from the fit. For the production cross-section, the wrong-sign yields are subtracted from the signal yields bin-by-bin and the uncertainties are taken into account as a systematic uncertainty.

Table 10.1: Rate of random combinations of charm hadrons with muons for events in the full η and p_{T} range of the 7 TeV and 13 TeV datasets, relative to the signal. The numbers are obtained from combinations of charm hadrons with wrong-sign muons.

dataset	D^0 [%]	D^+ [%]	D_s^+ [%]	Λ_c^+ [%]
7 TeV	0.76 ± 0.04	0.51 ± 0.05	0.70 ± 0.18	0.18 ± 0.12
13 TeV	2.04 ± 0.13	1.75 ± 0.22	3.34 ± 0.76	0.81 ± 0.3

10.3 Backgrounds from doubly-charmed events

Besides the aforementioned random combinations of muons and charm hadrons, there are also real b decays that mimic the signal decays. These are b-hadron decays into two charm hadrons (*e.g.* $B^0 \to D^*(2010)D_s^{*+}$) where one of the charm hadrons undergoes a semileptonic decay into a muon and the other one decays hadronically as in the signal mode. Due to the finite lifetime of the charm hadron and the possible additional number of non-reconstructed final-state particles, a large fraction of these events does not satisfy the selection criteria on the vertex quality and the transverse momentum. However, simulated samples are needed to quantify the reconstruction and selection efficiencies and estimate the yields for these decays.

There is a large variety of doubly-charmed decays from b hadrons and Table 10.2 lists the most significant B^0, B^+, B_s^0 and Λ_b^0 decays with their branching fractions. They include decays into D mesons and the D^* and $D^*_{0/1/2}$ states, where $D^*_{0/1/2}$ refers to higher-excited charm states that decay into a charm hadron and pions. These can be accompanied by kaons and pions. A list of all known contributing decays is given in Appendix A.1 in Tables A.17 - A.20.

Table 10.2: Branching fractions from b decays to two charm hadrons with branching fractions taken from the PDG [19] and a recent LHCb measurement [65]. Modes without entries indicate channels that are assumed to contribute in a similar order of magnitude, but have not been measured.

doubly-charmed decay mode	branching fraction	
$B^0 \to D^*(2010)^- D_s^{*+}$	(1.77 ± 0.14) %	
$B^0 \to (\overline{D} + \overline{D}^*)(D + D^*)$ K	(3.68 ± 0.26) %	
$B^0 \to D_{s,0/1}^{(*)+}\ \overline{D}^{(*)-}$	(1.8 ± 0.3) %	
$B^+ \to \overline{D}^*(2007)^0 D_s^{*+}$	(1.71 ± 0.24) %	
$B^+ \to D_s^{(*)+}\ \overline{D}^{**0}$	(2.7 ± 1.2) %	
$B^+ \to (\overline{D} + \overline{D}^*)\ (D + D^*)$ K	(4.05 ± 0.30) %	
$B^+ \to D_{s,0/J}^{(*)+}\ \overline{D}^{(*)0}$	(2.4 ± 0.4) %	
$B_s^0 \to D_s^{(*)+}\ D_s^{(*)-}$	(3.05 ± 0.41) %	[65]
$B_s^0 \to (D_s^{(*)-} + D_{(s)}^{(*)+})\ (D^{(*)0} + D^{(*)\pm})$ K	–	
$\Lambda_b^0 \to \Lambda_c^+\ D_s^-$	(1.1 ± 0.1) %	
$\Lambda_b^0 \to \Lambda_c^{*+} D_s^{(*)-}$	–	
$\Lambda_b^0 \to (\Lambda_c^+ + \Lambda_c^{(*)+})(D^{(*)0} + D^{(*)-})$ K	–	

For B^0 and B^+ mesons, most of the branching fractions have been measured and documented in the PDG [19], but for the B_s^0 and the Λ_b^0 hadrons, only few modes have been determined quantitatively. In these cases, one can only estimate the branching fractions from the measured values in the B^0 and B^+ modes as their Feynman diagrams differ only by exchanging the s and d quarks in the initial and final state. The B_s^0 decay modes into two charm hadrons and a kaon are expected to have significant branching fractions thanks to the various possible ways of arranging the quarks in the Feynman diagrams. Nonetheless, contributions without measured branching fractions are only taken into account as a systematic uncertainty. Due to the lower b-hadronisation fractions to B_s^0 and Λ_b^0, their contributions to the overall background only play a minor role. Therefore, even when conservatively assigning a large 20% branching fraction to doubly-charmed B_s^0 and Λ_b^0 decays as a systematic uncertainty, the number of background decays remains small compared to the contributions from B^0 and B^+ decays.

10.3.1 Strategy to measure the relative background yield

Simulated events of all doubly-charmed decays that are given in Appendix A.1, have been generated where one of the charm hadrons is forced to decay semileptonically whereas the other one has the same hadronic final state as the signal charm particle. They are reconstructed and selected the same way as the signal decays. Hence, the contamination of backgrounds among the selected events is obtained by comparing the related simulated reconstruction and selection efficiencies with the ones of the signal decays. In order to compute the occurring rates in real data, the doubly-charmed yields have to be corrected for the possible difference in the b-quark hadronisation fractions, $f(b \to B_{u,d,s}/\Lambda_b)$, the branching fraction of the b-hadron decay, $\mathcal{B}(H_b \to X)$, and the semileptonic decay of one of the charm hadrons, $\mathcal{B}(H_c \to \mu X)$. The resulting rate of selected decays of one

doubly-charmed decay mode (DD) relative to the signal decay (sig) is given by

$$r_{\mathrm{DD,sig}} = \frac{N_{\mathrm{DD,sel}}}{N_{\mathrm{DD,gen}}} \left(\frac{N_{\mathrm{sig,sel}}}{N_{\mathrm{sig,gen}}}\right)^{-1} \frac{f(b \to H_{b,\mathrm{DD}})}{f(b \to H_{b,\mathrm{sig}})} \frac{\mathcal{B}(H_b \to DDX)}{\mathcal{B}_{\mathrm{sig}}} \mathcal{B}(H_{c,\mathrm{DD}} \to \mu X),$$

where $N_{\mathrm{DD,sel}}$ and $N_{\mathrm{sig,sel}}$ refer to the numbers of reconstructed and selected decays and $N_{\mathrm{DD,gen}}$ and $N_{\mathrm{sig,gen}}$ are the corresponding numbers of generated decays. The contributions from all known doubly-charmed decay modes are summed to the total relative background.

The inclusive semileptonic charm branching fractions, $\mathcal{B}(D \to \mu X)$, are only given by the PDG [19] for the D^0 and D^+ mesons as stated in Table 10.3. Assuming equality of the semileptonic decay widths, Γ_{SL}, for the charm species as it was done in Chap. 6 for the b-decay modes, the value of the D_s^+ mode can be computed as the ratio $\mathcal{B}_{\mathrm{SL}} = \Gamma_{\mathrm{SL}}/\Gamma = (8.17 \pm 0.73)\%$ when inserting Γ_{SL}, measured in the D^0 mode. Since the charged D_s^+ meson can also decay purely leptonically with a branching fraction of $\mathcal{B}(D_s^+ \to \mu^+\nu) = (0.556 \pm 0.025)\%$, the total branching fraction of the D_s^+ to decay into a muon is the sum of the rates, $(8.73 \pm 0.73)\%$.

Table 10.3: Inclusive semileptonic charm branching fractions taken from the PDG [19] for the D^0 and D^+ and computed for the D_s^+, assuming equality of Γ_{SL} for all semileptonic charm-hadron decay modes and $\mathcal{B}_{\mathrm{SL}} = \Gamma_{\mathrm{SL}}/\Gamma$.

decay mode	branching fraction	
$D^+ \to \mu^+ X$	$17.6 \pm 3.2\%$	[19]
$D^0 \to \mu^+ X$	$6.7 \pm 0.6\%$	[19]
$D_s^+ \to \mu^+ X$	$8.73 \pm 0.73\%$	[estimation]

The relative hadronisation fractions, $f_s/(f_u + f_d)$ and $f_{\Lambda_b^0}/(f_u + f_d)$[3] have been measured by LHCb at a centre-of-mass energy of 7 TeV in Ref. [66]. The absolute b fractions of Table 10.4 are computed by correcting for the contribution δ of other baryons, introduced in Chap. 6, and assuming that the fractions f_u, f_d, f_s and $f_{\Lambda_b^0} \cdot (1 + \delta)$ sum to unity. Hereby, f_u and f_d are considered to be identical. The corresponding fractions at 13 TeV are assumed to be the same as they are not expected to change by more than the uncertainties stated. The uncertainties of the branching fractions and the hadronisation fractions are taken into account as a systematic uncertainty on the background contribution.

Table 10.4: Absolute b-hadron production fractions computed from relative fractions measured in [66]. Note that numbers do not sum up to unity because of the possible production of other baryons, denoted by the correction factor δ in the text.

	hadron production fraction
$f(b \to B_u)$	$30.5 \pm 9.1\%$
$f(b \to B_d)$	$30.5 \pm 9.1\%$
$f(b \to B_s)$	$8.2 \pm 2.5\%$
$f(b \to \Lambda_b^0)$	$24.6 \pm 8.1\%$

[3] f_u is a short notation for $f(b \to B_u)$

10.3.2 Determination of the doubly-charmed background contribution

The contributions of doubly-charmed decays relative to the four charm-hadron signal yields are given as a function of the pseudorapidity of the b-hadron, η, in Tables 10.5 and 10.6 for the simulated 7 TeV and 13 TeV selections, respectively. The related uncertainties include the statistical uncertainties due to the finite statistics of the simulated samples and the systematic uncertainties which will be presented in Chap. 12. The uncertainties for the D_s^+ and Λ_c^+ modes are larger and asymmetric because the unknown B_s^0 and Λ_b^0 branching fractions are set to 20% as a systematic check, which mainly affects the D_s^+ and Λ_c^+ final states. The largest background contribution by far is present in the D_s^+ mode with fractions up to 15% relative to the signal yield. In the D^0 and D^+ modes, the relative background rates vary between 1% and 4% and the Λ_c^+ background contribution is almost negligible. To estimate the overall background contribution to the b-hadron production cross-section, these numbers are averaged in the column "$b\bar{b}$" according to the measured contributions of the individual charm decay modes to the total b-hadron production cross-section that will be presented in Sec. 13.2. These fractional contributions are, in average, 51% for D^0, 19% for D^+, 9% for D_s^+ and 21% for Λ_c^+. This gives a total background fraction of about 2% which is subtracted from the signal yield, individually for each bin in η.

Table 10.5: Contribution of doubly-charmed background decays relative to the signal decays as a function of η for the four charm-hadron decay modes determined with simulated samples at a centre-of-mass energy of 7 TeV.

mode	$2.0 < \eta < 2.5$	$2.5 < \eta < 3.0$	$3.0 < \eta < 3.5$	$3.5 < \eta < 4.0$	$4.0 < \eta < 4.5$	$4.5 < \eta < 5.0$
D^0 [%]	1.5 ± 0.4	1.3 ± 0.2	1.4 ± 0.2	1.7 ± 0.3	1.3 ± 0.2	1.5 ± 0.3
D^+ [%]	4.2 ± 1.0	3.3 ± 0.5	3.6 ± 0.5	2.8 ± 0.4	3.1 ± 0.5	3.1 ± 0.8
D_s^+ [%]	15.4 ± 6.2	13.5 ± 5.1	14.4 ± 5.4	13.4 ± 5.2	10.9 ± 4.4	5.9 ± 2.7
Λ_c^+ [%]	$0.1\ ^{+1.7}_{-0.04}$	$0.1\ ^{+1.2}_{-0.02}$	$0.1\ ^{+1.4}_{-0.02}$	$0.1\ ^{+1.3}_{-0.02}$	$0.1\ ^{+1.2}_{-0.02}$	$0.1\ ^{+1.3}_{-0.05}$
$b\bar{b}$ [%]	$2.6\ ^{+1.1}_{-0.8}$	$2.3\ ^{+0.8}_{-0.6}$	$2.5\ ^{+0.9}_{-0.6}$	$2.4\ ^{+0.8}_{-0.6}$	$2.2\ ^{+0.7}_{-0.5}$	$1.9\ ^{+0.8}_{-0.6}$

Table 10.6: Contribution of doubly-charmed background decays relative to the signal decays as a function of η for the four charm-hadron decay modes determined with simulated samples at a centre-of-mass energy of 13 TeV.

mode	$2.0 < \eta < 2.5$	$2.5 < \eta < 3.0$	$3.0 < \eta < 3.5$	$3.5 < \eta < 4.0$	$4.0 < \eta < 4.5$	$4.5 < \eta < 5.0$
D^0 [%]	1.7 ± 0.3	1.9 ± 0.2	1.8 ± 0.2	1.8 ± 0.2	1.8 ± 0.2	1.8 ± 0.3
D^+ [%]	3.2 ± 0.5	3.3 ± 0.4	3.5 ± 0.4	3.4 ± 0.4	3.9 ± 0.5	3.1 ± 0.6
D_s^+ [%]	12.2 ± 4.6	13.3 ± 4.8	13.1 ± 4.7	12.9 ± 4.6	10.5 ± 3.9	8.6 ± 3.6
Λ_c^+ [%]	$0.1\ ^{+2.1}_{-0.04}$	$0.1\ ^{+1.8}_{-0.02}$	$0.1\ ^{+1.6}_{-0.02}$	$0.1\ ^{+1.4}_{-0.02}$	$0.1\ ^{+1.1}_{-0.02}$	$0.05\ ^{+0.8}_{-0.02}$
$b\bar{b}$ [%]	$2.6\ ^{+1.0}_{-0.6}$	$2.6\ ^{+0.9}_{-0.5}$	$2.5\ ^{+0.8}_{-0.5}$	$2.7\ ^{+0.8}_{-0.5}$	$2.7\ ^{+0.7}_{-0.5}$	$2.4\ ^{+0.7}_{-0.6}$

11 Determination of reconstruction and selection efficiencies

The reconstruction and selection efficiencies of the signal decays are, in general, obtained from fully simulated samples. In order to reduce the systematic uncertainties related to the simulation, calibration samples from data are used to determine the efficiencies of the track reconstruction, the muon trigger and hadronic particle identification requirements and the selection criteria on the occupancy of the detector.

11.1 Strategy to combine efficiencies

The overall reconstruction and selection efficiency of the selection requirements, presented in Chap. 8, is assumed to factorise into the following components:

- $\varepsilon_{\text{trigger}}$: efficiency of the muon trigger and particle identification (PID) requirements
- ε_{occ}: efficiency of the selection criteria on the occupancy of the detector
- $\varepsilon_{\text{track}}$: efficiency of the track reconstruction
- $\varepsilon_{\text{hadPID}}$: efficiency of the hadronic particle identification requirements
- ε_{off}: efficiency of the remaining selection criteria on the kinematics of the final-state hadrons and the charm-plus-muon vertex, shown in Tables 8.2 and 8.3 without particle identification criteria. This efficiency is further referred to as the *offline* selection efficiency.

With these components, the overall efficiency is written as

$$\varepsilon = \varepsilon_{\text{trigger}} \cdot \varepsilon_{\text{occ}} \cdot \varepsilon_{\text{track}} \cdot \varepsilon_{\text{hadPID}} \cdot \varepsilon_{\text{off}}. \tag{11.1}$$

The factors of the efficiency are partly obtained from fully simulated decays and partly from data-driven methods with well-known calibration channels that provide large number of decays and can be separated efficiently from background contributions. However, the final-state particles of the calibration modes have different kinematic distributions, so the efficiency is determined as a function of relevant kinematic observables. This kinematic-dependent efficiency is then folded into the kinematics of the simulated signal decay as it is described in the following.

The fully simulated decays have been tuned to properly reflect the track reconstruction efficiency. It is also known that the simulation accordingly models the decay topology. Therefore, the combined offline and track reconstruction efficiency is obtained from fully simulated decays as a function of the pseudorapidity of the b hadron, η, and the transverse

momentum of the charm-plus-muon candidate, p_{T}. It is computed as the ratio of the number of reconstructed and selected events, n_{off}, after the offline selection, to the total number of generated simulated events, N_{gen}:

$$(\varepsilon_{\mathrm{track}} \cdot \varepsilon_{\mathrm{off}})\ (\eta, p_{\mathrm{T}}) = \frac{n_{\mathrm{off}}}{N_{\mathrm{gen}}}(\eta, p_{\mathrm{T}}). \tag{11.2}$$

Remaining differences between the track reconstruction efficiencies in simulation and data are corrected for with factors, r_{track}, that depend on a set of kinematics of all related tracks, $\vec{x}_{\mathrm{tracks}}$, and are usually compatible with unity. For each simulated event i, the factor is evaluated for the corresponding kinematics of the related tracks. This per-event correction is used to re-weight the simulated events via

$$(\varepsilon_{\mathrm{track}} \cdot \varepsilon_{\mathrm{off}})\ (\eta, p_{\mathrm{T}}) = \frac{\sum_{i}^{n_{\mathrm{off}}(\eta, p_{\mathrm{T}})} r_{\mathrm{track}}(\vec{x}_{\mathrm{tracks},i})}{N_{\mathrm{gen}}(\eta, p_{\mathrm{T}})}. \tag{11.3}$$

The muon trigger and hadron PID efficiencies, $\varepsilon_{\mathrm{trigger}}(\vec{y}_{\mu})$ and $\varepsilon_{\mathrm{hadPID}}(\vec{z}_{\mathrm{had}})$, are determined with data-driven methods as a function of the kinematics of the final-state muons and hadrons, denoted by the set of observables $\vec{y}_{\mu}$ and $\vec{z}_{\mathrm{had}}$. As it is done with the correction factors, the efficiencies are evaluated for each simulated semileptonic decay according to the related kinematics. The resulting per-event efficiency is used to weight each simulated event. The efficiency due to requirements on the occupancy of the detector can depend on η and is obtained from a data sample that is subject to looser requirements. The overall efficiency as a function of η and p_{T} is given by

$$\varepsilon(\eta, p_{\mathrm{T}}) = \frac{\sum_{i}^{n_{\mathrm{off}}(\eta, p_{\mathrm{T}})} r_{\mathrm{track}}(\vec{x}_{\mathrm{tracks},i}) \cdot \varepsilon_{\mathrm{trigger}}(\vec{y}_{\mu,i}) \cdot \varepsilon_{\mathrm{hadPID}}(\vec{z}_{\mathrm{had},i})}{N_{\mathrm{gen}}(\eta, p_{\mathrm{T}})} \cdot \varepsilon_{\mathrm{occ}}(\eta). \tag{11.4}$$

11.2 Hadronic particle identification efficiency

The hadronic particle identification efficiencies are determined with calibration samples of hadronic decays on which the PID criteria are probed. The overall hadronic particle identification efficiencies of the signal decay modes are given by the product of the individual efficiencies of the related hadrons.

11.2.1 Description of the fit procedure

As it was done for the hadron-to-muon misidentification efficiencies in Sec. 10.1, calibration samples of hadronic decays are selected without particle identification requirements and the final-state hadrons are used to probe the PID selection criteria. $D^{*+} \to D^0\pi^+$ decays, where the D^0 decays into a $K^-\pi^+$ pair, are chosen to probe kaons and pions whereas the protons are obtained from $\Lambda^0 \to p\pi^-$ decays. The hadron pairs are classified into pass- and fail categories according to the PID response. For each category, the invariant $K\pi$ or $p\pi$ mass distribution is described by a Gaussian function for signal and a linear function for background in a simultaneous fit to both categories. The number of signal

events and the widths of the Gaussian functions are shared between the two fits and the efficiency is determined by the fraction of signal events that have passed the PID criterion. Due to the dependence on the event kinematics, these efficiencies are obtained on a three-dimensional grid of the momentum and pseudorapidity of the hadron, and the number of reconstructed tracks in the event.

11.2.2 Particle identification efficiencies for the charm modes

As described in Sec. 11.1, the hadronic PID efficiency grid is folded into the kinematics of the simulated semileptonic signal decays via Eq. 11.4. This is done for each of the N_{hadrons} number of hadrons. For each simulated event i, the combined hadronic particle identification efficiency is the product of the efficiencies for all final-state hadrons

$$\varepsilon_{\text{hadPID},i} = \prod_{h}^{N_{\text{hadrons}}} \varepsilon_{\text{hadPID}}\big(p(h_i), \eta(h_i), N_{\text{tracks},i}\big), \tag{11.5}$$

where $p(h_i)$ and $\eta(h_i)$ refer to the momentum and the pseudorapidity of the simulated final-state hadron h and $N_{\text{tracks},i}$ corresponds to the total number of tracks in the event.

In this section, the pure hadronic particle identification efficiencies for the charm modes of the semileptonic b-decays are presented as a function of the b-hadron pseudorapidity, $\eta(H_b)$. Therefore, only the hadronic PID efficiency is folded into the kinematics of the simulated semileptonic decay samples via

$$\varepsilon_{\text{hadPID}}(\eta(H_b)) = \frac{\sum_{i}^{n_{\text{off}}(\eta(H_b))} \varepsilon_{\text{hadPID},i}}{n_{\text{off}}(\eta(H_b))}, \tag{11.6}$$

where the denominator is formed by n_{off} because this definition does not include the track reconstruction and offline selection efficiency. Tables 11.1 and 11.2 list the $\eta(H_b)$-dependent efficiencies, averaged over the full transverse momentum range of the charm-plus-muon candidate, for the charm modes of the 7 TeV and 13 TeV datasets, respectively. Figure 11.1 visualises the efficiencies in a diagram. The highest PID efficiency is the one for the D^0 mode as it has only two hadrons in the final state that are subject to PID requirements. Among the other three-hadronic final states, the D^+ mode is identified most efficiently and the Λ_c^+ mode is identified with the lowest overall efficiency because the proton exhibits the lowest PID efficiency. The average hadronic particle identification efficiencies for all considered decays are estimated in the row "$b\bar{b}$" according to the contributions of the individual charm modes to the total b-hadron production cross-section that will be presented in Sec. 13.2. The uncertainties stated include both statistical uncertainties due to the finite statistics of the calibration samples and systematic uncertainties that will be presented in Chap. 12.

Table 11.1: Hadronic particle identification efficiencies for the four charm modes for the 7 TeV dataset, with combined statistical and systematic uncertainties, as a function of the b-hadron pseudorapidity η. The efficiencies for the single final-state hadrons are obtained from hadronic calibration samples.

mode	$2.0 < \eta < 2.5$	$2.5 < \eta < 3.0$	$3.0 < \eta < 3.5$	$3.5 < \eta < 4.0$	$4.0 < \eta < 4.5$	$4.5 < \eta < 5.0$
D^0 [%]	88.18 ± 1.41	88.07 ± 1.33	88.40 ± 1.24	84.69 ± 1.16	79.52 ± 1.20	79.68 ± 1.30
D^+ [%]	78.82 ± 1.34	79.47 ± 1.23	81.01 ± 1.12	78.72 ± 1.07	74.41 ± 1.11	73.80 ± 1.20
D_s^+ [%]	85.92 ± 1.89	85.36± 1.74	85.90 ± 1.48	80.92 ± 1.29	72.50 ± 1.30	71.50 ± 1.54
Λ_c^+ [%]	66.03 ± 1.42	69.17 ± 1.42	72.73 ± 1.38	70.07 ± 1.22	63.01 ± 1.13	57.18 ± 1.11
$b\bar{b}$ [%]	81.89 ± 1.43	82.94 ± 1.36	83.74 ± 1.26	80.57 ± 1.16	75.20 ± 1.18	74.31 ± 1.27

Table 11.2: Hadronic particle identification efficiencies for the four charm modes for the 13 TeV dataset, with combined statistical and systematic uncertainties, as a function of the b-hadron pseudorapidity η. The efficiencies for the single final-state hadrons are obtained from hadronic calibration samples.

mode	$2.0 < \eta < 2.5$	$2.5 < \eta < 3.0$	$3.0 < \eta < 3.5$	$3.5 < \eta < 4.0$	$4.0 < \eta < 4.5$	$4.5 < \eta < 5.0$
D^0 [%]	91.63 ± 1.46	91.38 ± 1.38	90.89 ± 1.28	85.83 ± 1.20	77.33 ± 1.23	77.04 ± 1.33
D^+ [%]	87.00 ± 1.37	88.26 ± 1.26	90.23 ± 1.14	87.01 ± 1.09	80.59 ± 1.13	79.20 ± 1.22
D_s^+ [%]	89.57 ± 1.98	88.80 ± 1.81	89.11 ± 1.54	81.79 ± 1.33	70.57 ± 1.34	67.70 ± 1.60
Λ_c^+ [%]	77.79 ± 1.47	78.36 ± 1.47	80.58 ± 1.42	74.46 ± 1.25	60.82 ± 1.15	55.66 ± 1.13
$b\bar{b}$ [%]	87.77 ± 1.48	88.10 ± 1.40	88.79 ± 1.29	83.96 ± 1.20	74.96 ± 1.21	74.21 ± 1.30

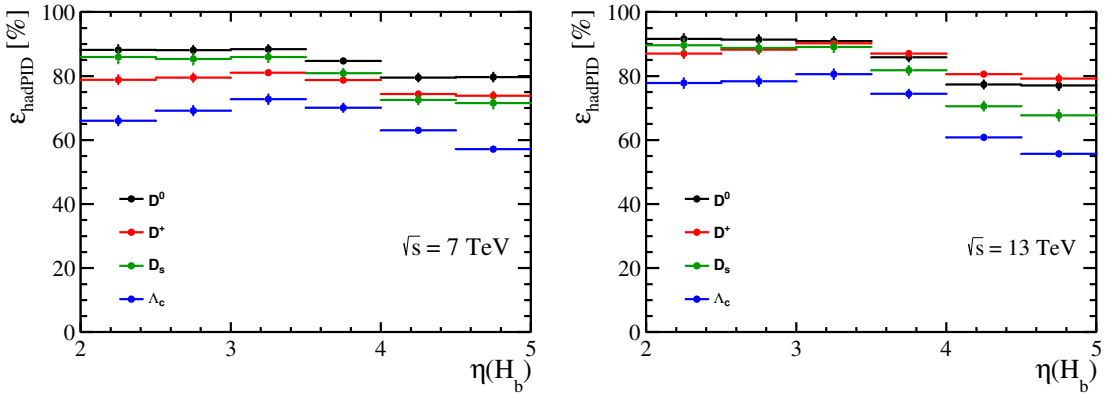

Figure 11.1: Hadronic particle identification efficiencies for the four charm hadrons as a function of $\eta(H_b)$ for (left) 7 TeV and (right) 13 TeV data, with combined statistical and systematic uncertainties. The efficiencies for the single final-state hadrons are obtained from the calibration samples $D^{*+} \to D^0\pi^+$ and $\Lambda^0 \to p\pi^-$ and are folded into the kinematics of the simulated semileptonic signal decays via Eq. 11.6.

11.3 Trigger and muon identification efficiencies

The combined efficiency of the muon trigger and particle identification requirements is obtained from a calibration sample of J/ψ mesons decaying into two muons. To enlarge the purity of the sample, the J/ψ mesons are required to originate from b-hadron decays whose decay vertices are significantly away from the primary vertex. Since the efficiency

depends on the kinematics of the muon, it is determined in a three-dimensional grid of the muon transverse momentum, pseudorapidity and impact parameter. In the following, the short term trigger efficiency refers to the combined efficiency of the muon trigger and particle identification requirements.

11.3.1 Measurement strategy

To select a sample of J/ψ mesons from b-hadron decays, at least one of the muons is required to fulfil tight selection criteria in order to serve as the so-called *tag* muon whereas the trigger efficiency is tested on the other muon, the *probe*. This method is called the *tag-and-probe* method. The trigger efficiency is defined such that it probes the efficiency of the selection criteria listed in Table 8.1, except for the maximum number of SPD hits and long tracks.

The relevant data is collected by requiring the tag muon to satisfy the L0 and Hlt1 signal trigger criteria. However, it has been observed in simulation that applying the tight Hlt2 selection requirements on the tag muon affects the trigger efficiency of the probe muon, thus it does not serve as a model for a general isolated single muon. Therefore, a looser Hlt2 approach is followed, namely that a track of the rest of the event satisfies the requirements of the topological two-body trigger. As described in Sec. 3.2.5, a topological trigger combines few tracks at a displaced decay vertex which might originate from b-hadron decays. In this case, two tracks are reconstructed that may be produced together with the J/ψ meson or just happen to be coincidentally in the same event as the muons. For the purpose of the trigger efficiency, it is only important that the recorded probe muon is subject to loose selection criteria such that it serves as a general isolated muon.

As it was done for the hadronic PID efficiency in the previous section, the muon pair is classified into two categories according to the trigger and PID response of the probe muon and the trigger efficiency is obtained from a simultaneous fit to both categories. For each category, the signal component of the invariant dimuon mass distribution is described by a Gaussian function and the combinatorial background model is an exponential function. The number of signal events and the widths of the Gaussian functions are again shared between the two fits and the efficiency is determined by the fraction of signal events that have passed the trigger and PID criteria. This simultaneous fit is performed on a three-dimensional grid of the probe muon transverse momentum p_{T}, pseudorapidity η and impact parameter IP and the binning scheme is chosen such that there are more bins where the efficiency changes steeply.

11.3.2 Determination of the muon trigger efficiencies

The one-dimensional projections of the three-dimensional trigger efficiency grids are shown in Figs. 11.2 and 11.3 for the 7 TeV and 13 TeV data, respectively. The error bars only include the statistical uncertainties due to the statistics of the calibration samples.

The efficiencies for the 13 TeV data are larger, because the trigger at 7 TeV includes criteria on the impact parameter >0.5 and $\chi^2_{\mathrm{IP}} > 200$ whereas for 13 TeV, there is no IP criterion and $\chi^2_{\mathrm{IP}} > 16$ only. Additionally, the momentum criteria are tighter for 7 TeV. Due to these harder requirements, the efficiencies for the 7 TeV data drop more steeply towards low η and p_{T}. It is important to note that the down-scaling of 50%, applied at

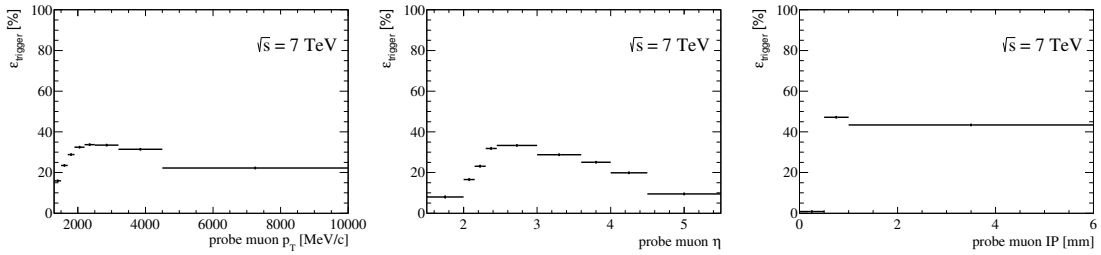

Figure 11.2: Efficiencies of the overall muon trigger and PID requirements in bins of the probe muon (left) p_{T}, (centre) η and (right) impact parameter determined with J/ψ mesons from b-hadron decays in 7 TeV data.

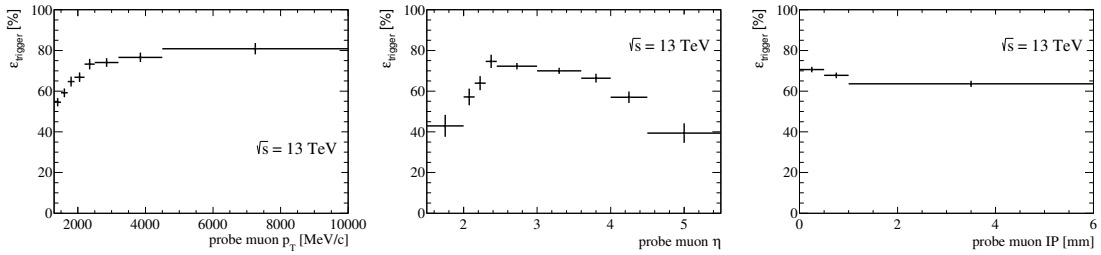

Figure 11.3: Efficiencies of the overall muon trigger and PID requirements in bins of the probe muon (left) p_{T}, (centre) η and (right) impact parameter determined with J/ψ mesons from b-hadron decays in 13 TeV data.

the Hlt2 stage, is not included in the efficiency determined with the tag-and-probe method because the down-scaling equally affects the tag muon.

In order to compute the overall efficiencies, the trigger efficiency is evaluated according to the muon kinematics of the simulated signal decays in Eq. 11.4. In the following, the pure muon trigger and PID efficiencies for the charm-hadron modes of the semileptonic b-decays are presented as a function of the b-hadron pseudorapidity. Therefore, only $\varepsilon_{\text{trigger}}$ is folded into the kinematics of the simulated semileptonic decays analogous to the hadronic PID efficiency:

$$\varepsilon_{\text{trigger}}(\eta(H_b)) = \frac{\sum_{i}^{n_{\text{off}}(\eta(H_b))} \varepsilon_{\text{trigger}}(p_{\mathrm{T}}(\mu_i), \eta(\mu_i), \mathrm{IP}(\mu_i))}{n_{\text{off}}(\eta(H_b))}, \tag{11.7}$$

where μ_i refers to the muon of the simulated event i.

11.3.3 Validation of the tag-and-probe method

The tag-and-probe method is only applicable when the trigger efficiency is the same for a single isolated muon and a probe muon, originating from a J/ψ decay, after the selection of a tag muon. This is investigated with simulated events. The trigger response of the semileptonic signal sample itself is used to extract the simulated three-dimensional trigger efficiency grid of an isolated muon, further denoted as the binned *true* efficiency. Figure 11.4

shows the trigger efficiencies for the charm-hadron decay modes of the semileptonic b-decays as a function of the b-hadron pseudorapidity after applying the efficiency grids from the tag-and-probe method and the binned true efficiency. It can be seen that there are relative deviations between 1% and 3% for the 7 TeV and below 3% for the 13 TeV simulation, where the efficiencies are overestimated by the tag-and-probe method. To adjust for this remaining discrepancy, the relative differences in the two simulated three-dimensional efficiency grids are used to correct the efficiency grid in data. The uncertainties on this correction and the effect of applying a finite three-dimensional binning scheme are investigated in Chap. 12.

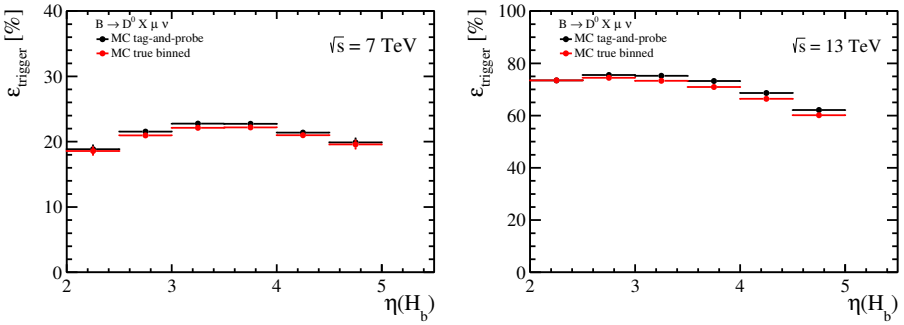

Figure 11.4: Simulated trigger efficiencies as a function of the b-hadron pseudorapidity in the D^0 mode. The trigger efficiencies of the muon are obtained from the tag-and-probe method (black) and the semileptonic signal sample (red), denoted as *true*, in a three-dimensional grid of the muon kinematics. The 3D grid is used to assign weights to the semileptonic signal sample according to Eq. 11.7. Remaining differences between the two methods are corrected for in data.

11.3.4 Trigger efficiencies for the b-hadron decay modes

Tables 11.3 and 11.4 tabulate the muon trigger and PID efficiencies for the semileptonic b-hadron decays in the four charm modes for the two centre-of-mass energies. They are also drawn into diagrams in Fig. 11.5. The uncertainties refer to the combined statistical and systematic uncertainties which will be presented in Chap. 12. For the 7 TeV data, the efficiencies drop towards low η as expected from the one-dimensional projections of the 3D efficiency grid and less steeply towards high η, whereas they only gradually decrease towards high η at 13 TeV. The 7 TeV trigger requirements lead to different efficiencies for the four charm modes which is due to different responses to the tight IP and momentum requirements. With the looser 13 TeV trigger requirements, the differences of the efficiencies between the charm modes are hardly visible. The average trigger efficiencies for all considered decays are estimated in the row "$b\bar{b}$" according to the contributions of the individual charm modes to the total b-hadron production cross-section that will be presented in Sec. 13.2.

Table 11.3: Trigger efficiencies for the various charm modes of the semileptonic b-hadron decays for 7 TeV centre-of-mass energies, with combined statistical and systematic uncertainties. The muon trigger efficiencies are obtained from J/ψ-meson decays using the tag-and-probe method, and applied to the simulated semileptonic signal decays. Remaining relative deviations of the simulated efficiencies between the tag-and-probe method and the true efficiencies have been corrected for.

mode	$2.0 < \eta < 2.5$	$2.5 < \eta < 3.0$	$3.0 < \eta < 3.5$	$3.5 < \eta < 4.0$	$4.0 < \eta < 4.5$	$4.5 < \eta < 5.0$
D^0 [%]	15.3 ± 0.7	18.3 ± 0.7	19.8 ± 0.7	20.2 ± 0.6	19.2 ± 0.6	17.7 ± 0.6
D^+ [%]	14.7 ± 0.7	18.7 ± 0.8	20.1 ± 0.5	19.8 ± 0.6	17.4 ± 0.5	16.2 ± 1.4
D_s^+ [%]	16.2 ± 0.9	20.3 ± 0.9	21.7 ± 0.7	21.5 ± 0.7	20.9 ± 0.7	19.2 ± 1.4
Λ_c^+ [%]	16.3 ± 1.3	20.4 ± 0.7	22.9 ± 0.8	23.9 ± 0.8	23.3 ± 0.9	21.2 ± 1.7
$b\bar{b}$ [%]	15.5 ± 0.8	18.9 ± 0.7	20.6 ± 0.7	20.9 ± 0.7	19.6 ± 0.6	18.0 ± 1.0

Table 11.4: Trigger efficiencies for the various charm modes of the semileptonic b-hadron decays for 13 TeV centre-of-mass energies, with combined statistical and systematic uncertainties. The muon trigger efficiencies are obtained from J/ψ-meson decays using the tag-and-probe method, and applied to the simulated semileptonic signal decays. Remaining relative deviations of the simulated efficiencies between the tag-and-probe method and the true efficiencies have been corrected for.

mode	$2.0 < \eta < 2.5$	$2.5 < \eta < 3.0$	$3.0 < \eta < 3.5$	$3.5 < \eta < 4.0$	$4.0 < \eta < 4.5$	$4.5 < \eta < 5.0$
D^0 [%]	73.2 ± 1.8	73.9 ± 1.3	71.9 ± 2.0	67.9 ± 2.2	63.1 ± 2.3	57.2 ± 2.5
D^+ [%]	74.0 ± 2.3	73.7 ± 1.2	71.8 ± 2.0	67.8 ± 2.1	61.9 ± 2.2	55.7 ± 2.2
D_s^+ [%]	72.6 ± 0.9	74.2 ± 1.2	71.8 ± 1.8	67.9 ± 2.0	62.0 ± 2.3	54.5 ± 2.0
Λ_c^+ [%]	74.8 ± 1.7	75.5 ± 1.1	73.1 ± 1.7	68.9 ± 2.0	63.1 ± 1.9	56.7 ± 1.7
$b\bar{b}$ [%]	73.6 ± 1.8	74.2 ± 1.2	72.1 ± 1.9	68.1 ± 2.1	62.8 ± 2.2	56.6 ± 2.3

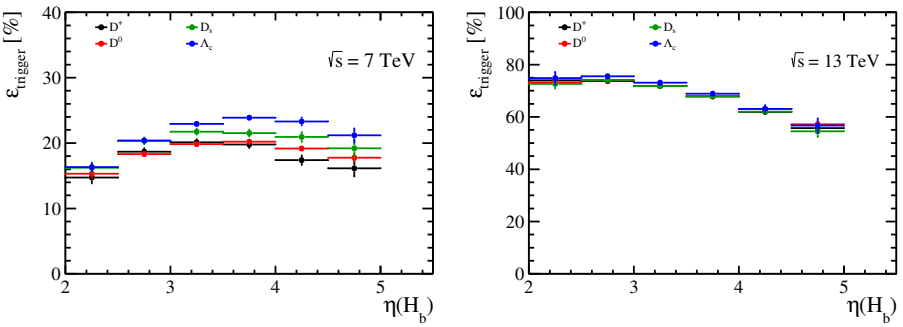

Figure 11.5: Trigger efficiencies for the various charm modes of the semileptonic b-hadron decays with combined statistical and systematic uncertainties as a function of the b-hadron pseudorapidity for 7 TeV (left) and 13 TeV (right) centre-of-mass energies. The muon trigger efficiencies are obtained from J/ψ-meson decays using the tag-and-probe method, and applied to the simulated semileptonic signal decays. Remaining relative deviations of the simulated efficiencies between the tag-and-probe method and the true efficiencies have been corrected for.

11.4 Efficiencies due to requirements on the occupancy of the detector

The trigger requirements at a centre-of-mass energy of 7 TeV limit the number of SPD hits to 600 which is not the case for 13 TeV[1]. Furthermore, the number of long tracks is demanded not to exceed 250 in the offline selection, which is 100% efficient for 7 TeV, but affects the 13 TeV dataset.

The efficiencies of these criteria are obtained from a sample of J/ψ mesons from b-hadron decays, further denoted as $B \to J/\psi X$. The relevant data is recorded and saved on disk when the event satisfies the dimuon trigger requirements which contain a looser criterion on the number of SPD hits of 900. The number of long tracks is not restricted at all. However, the distributions of the number of SPD hits and the number of long tracks do not agree for the selected J/ψ sample and the semileptonic events. As the total number of reconstructed tracks is not restricted for both of the samples, weights are applied to the events such that the distribution of number of tracks of the $B \to J/\psi X$ sample agrees with the one of the semileptonic b-hadron samples, which also aligns the distributions of interest.

11.4.1 Efficiencies due to requirements on the number of SPD hits

After re-weighting the $B \to J/\psi X$ sample for the total number of tracks in the event, the left-hand side of Fig. 11.6 shows the normalised distributions of number of SPD hits of the $B \to D^0 \mu\nu X$ and $B \to J/\psi X$ samples over the full $\eta(H_b)$ range of the 7 TeV data. They agree below the cut value of 600. On the right, the right side of a Gaussian distribution is fitted to the tail of the distribution of number of SPD hits of the re-weighted $B \to J/\psi X$ sample and the fitted number of events above the value of 600 determines the inefficiency of the selection criterion.

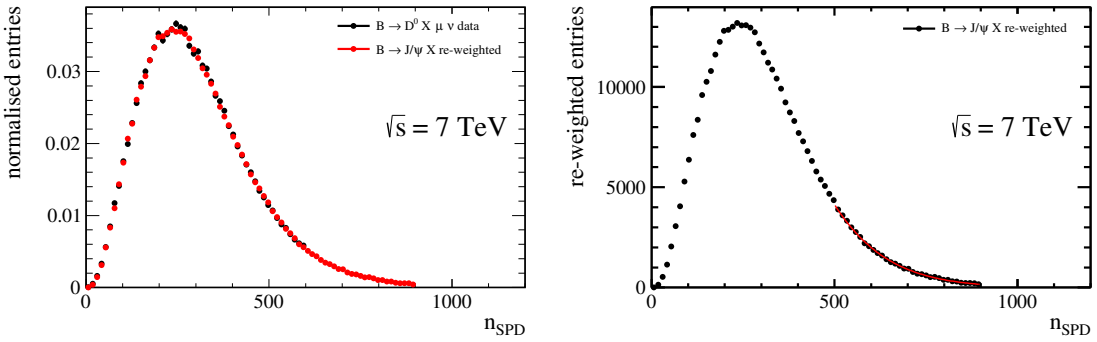

Figure 11.6: Left: Distributions of number of SPD hits of $B \to D^0 \mu\nu X$ (black) and $B \to J/\psi X$ (red) decays from 7 TeV data, after re-weighting the $B \to J/\psi X$ events to align the total number of tracks in the event. Right: Distribution of number of SPD hits of $B \to J/\psi X$ from 7 TeV data after re-weighting, overlaid with the fitted pdf, the right tail of a Gaussian. The fitted number of events above the value of 600 determines the inefficiency.

[1] As described in Sec. 11.3, the definition of the trigger efficiency does not include the efficiency on the criterion on the maximum number of SPD hits and long tracks.

The resulting efficiencies are given in Table 11.5, for each bin of $\eta(B)$, for $B \to D^0\mu\nu X$ decays of the 7 TeV data. The efficiencies are computed for each charm mode individually and are about 95%. The uncertainties on the efficiencies are obtained from the fit.

Table 11.5: Efficiencies of the selection criterion on the number of SPD hits, n_{SPD}, of 600 for the $B \to D^0\mu\nu X$ mode of the 7 TeV data for all bins of $\eta(B^{0/+})$.

$\eta(B^{0/+})$	efficiency of ($n_{\mathrm{SPD}} < 600$)
2.0 - 2.5	(95.17 ± 0.13) %
2.5 - 3.0	(94.98 ± 0.07) %
3.0 - 3.5	(94.77 ± 0.07) %
3.5 - 4.0	(94.58 ± 0.08) %
4.0 - 4.5	(94.89 ± 0.10) %
4.5 - 5.0	(95.60 ± 0.17) %

11.4.2 Efficiencies due to requirements on the number of long tracks

Following the same approach, the distributions of number of long tracks from $B \to D^0\mu\nu X$ and $B \to J/\psi X$ events of the full $\eta(H_b)$ range agree below the value of 250 after re-weighting $B \to J/\psi X$ to align the distributions of the total number of tracks in the event. The two normalised distributions are shown on the left of Fig. 11.7. The fit of a Gaussian function to the re-weighted $B \to J/\psi X$ data is shown on the right from which the efficiencies of almost 100% are extracted and tabulated in Table 11.6. Again, these efficiencies are computed for each charm mode individually with the uncertainties taken from the fit.

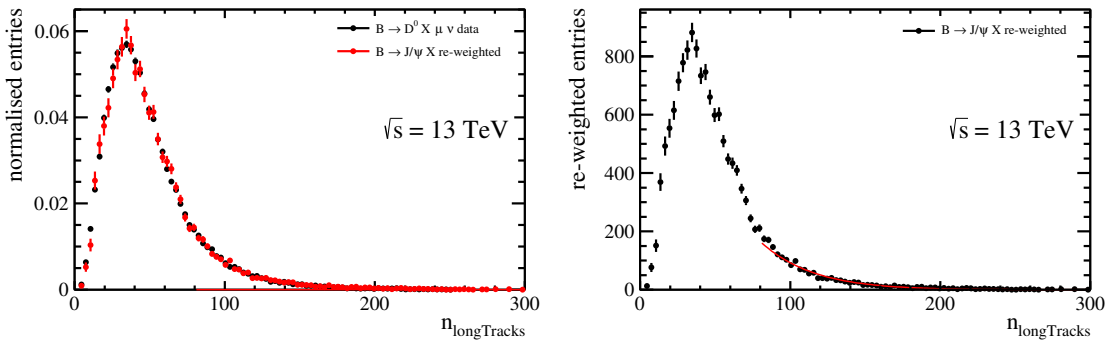

Figure 11.7: Left: Distributions of number of long tracks of $B \to D^0\mu\nu X$ (black) and $B \to J/\psi X$ (red) decays from 13 TeV data, after re-weighting $B \to J/\psi X$ to align the distributions of the total number of tracks in the event. Right: Distributions of number of long tracks of $B \to J/\psi X$ from 13 TeV data after re-weighting, overlaid with the fitted pdf, the tail of a Gaussian. The fitted number of events above the value of 250 determines the inefficiency.

Table 11.6: Efficiencies of the selection criteria on the number of long tracks, $n_{\text{longTracks}}$, at 250 for the $B \to D^0 \mu\nu X$ mode of the 13 TeV data for all bins of $\eta(B^{0/+})$.

$\eta(B^{0/+})$	efficiency of ($n_{\text{longTracks}} < 250$)
2.0 - 2.5	(99.88 ± 0.08) %
2.5 - 3.0	(99.91 ± 0.05) %
3.0 - 3.5	(99.91 ± 0.05) %
3.5 - 4.0	(99.95 ± 0.04) %
4.0 - 4.5	(99.95 ± 0.05) %
4.5 - 5.0	(99.99 ± 0.01) %

11.5 Track reconstruction efficiency corrections

Due to the coverage and inefficient response of the detector and high particle occupancies in the region near the beam pipe, it can happen that the track reconstruction algorithms do not find the track of the relevant particles. Additionally, there are no sensitive detector layers within the 4 m of dipole magnet over which the track has to be extrapolated and matched to. The track reconstruction efficiencies are continuously studied by the tracking group at LHCb with calibration samples of $J/\psi \to \mu\mu$ decays. Details can be found in Ref. [29]. The measured efficiencies have been used to tune the simulated event samples such that the track reconstruction efficiency is properly modelled. In order to correct for differences between the efficiencies in simulation and data of specific data-taking periods, correction factors are computed in intervals of the track momentum and pseudorapidity. For each event simulated i, the correction factor is the product of the individual factors of all N_{tracks} number of related tracks

$$r_{\text{track},i} = \prod_{t}^{N_{\text{tracks}}} r_{\text{track}}(p(t_i), \eta(t_i)), \tag{11.8}$$

where $p(t_i)$ and $\eta(t_i)$ refer to the momentum and the pseudorapidity of the track t. The average correction factors as a function of the b-hadron pseudorapidity for the charm modes of the 7 TeV and 13 TeV data are given in Tables 11.7 and 11.8, respectively. They are almost unity for the 7 TeV simulation and slightly smaller but compatible with one for the 13 TeV simulation. The uncertainties refer to the combined statistical and systematic uncertainties which will be presented in Chap. 12. Due to the smaller number of events in the calibration samples of the 13 TeV data, the uncertainties are larger. The average correction factors for all considered decays is estimated in the row "$b\bar{b}$" according to the contributions of the individual charm modes to the total b-hadron production cross-section that will be presented in Sec. 13.2.

11.6 Summary of the overall efficiencies

Figure 11.8 illustrates the overall reconstruction and selection efficiencies of the signal decay modes for the 7 TeV selection as a function of the transverse momentum of the combined charm-plus-muon system with separate graphs for the regions of the b-hadron

Table 11.7: Average correction factors of the simulated 7 TeV track reconstruction efficiencies for the charm modes as a function of the b-hadron pseudorapidity with combined statistical and systematic uncertainties. The track reconstruction efficiencies are obtained from $J/\psi \to \mu\mu$ from data.

mode	$2.0 < \eta < 2.5$	$2.5 < \eta < 3.0$	$3.0 < \eta < 3.5$	$3.5 < \eta < 4.0$	$4.0 < \eta < 4.5$	$4.5 < \eta < 5.0$
D^0	1.01 ± 0.03	1.01 ± 0.03	1.00 ± 0.03	0.99 ± 0.03	0.99 ± 0.03	0.99 ± 0.03
D^+	1.01 ± 0.04	1.01 ± 0.04	1.00 ± 0.04	0.99 ± 0.04	0.99 ± 0.04	0.99 ± 0.04
D_s^+	1.01 ± 0.04	1.01 ± 0.04	1.00 ± 0.04	0.99 ± 0.04	0.99 ± 0.04	0.99 ± 0.04
Λ_c^+	1.01 ± 0.04	1.01 ± 0.04	1.00 ± 0.04	0.99 ± 0.04	0.99 ± 0.04	0.99 ± 0.04
$b\bar{b}$	1.01 ± 0.03	1.01 ± 0.03	1.00 ± 0.03	0.99 ± 0.03	0.99 ± 0.03	0.99 ± 0.03

Table 11.8: Average correction factors of the simulated 13 TeV track reconstruction efficiencies for the charm modes as a function of the b-hadron pseudorapidity with combined statistical and systematic uncertainties. The track reconstruction efficiencies are obtained from $J/\psi \to \mu\mu$ from data.

mode	$2.0 < \eta < 2.5$	$2.5 < \eta < 3.0$	$3.0 < \eta < 3.5$	$3.5 < \eta < 4.0$	$4.0 < \eta < 4.5$	$4.5 < \eta < 5.0$
D^0	0.98 ± 0.04	0.98 ± 0.04	0.97 ± 0.03	0.97 ± 0.03	0.96 ± 0.03	0.96 ± 0.03
D^+	0.98 ± 0.07	0.97 ± 0.06	0.97 ± 0.05	0.96 ± 0.05	0.95 ± 0.05	0.95 ± 0.05
D_s^+	0.97 ± 0.07	0.97 ± 0.06	0.96 ± 0.05	0.95 ± 0.04	0.95 ± 0.04	0.95 ± 0.04
Λ_c^+	0.97 ± 0.06	0.97 ± 0.06	0.96 ± 0.05	0.95 ± 0.04	0.95 ± 0.04	0.95 ± 0.04
$b\bar{b}$	0.98 ± 0.05	0.98 ± 0.05	0.97 ± 0.04	0.96 ± 0.04	0.96 ± 0.04	0.96 ± 0.04

pseudorapidity. The uncertainties only refer to the limited statistics of the fully simulated events. The corresponding efficiencies for the 13 TeV selection are shown in Fig. 11.9 and the exact numbers are tabulated in Appendix A.2. The efficiencies vary between 0%-5% for 7 TeV and 0%-20% for 13 TeV where the difference mainly originates from the deviating trigger requirements. It can be seen that there are regions where the efficiency vanishes, especially at low transverse momenta for all bins of η. This reflects the kinematic acceptance of the detector because particles with small momenta are bent out of the detector acceptance. In regions with high η, there are only few b-hadrons with high p_{T} because this requires the momentum to be even larger. As the b-hadron production cross-section is evaluated by dividing by the efficiency, it cannot be computed for a vanishing efficiency. The treatment of this p_{T} acceptance is discussed in the following section.

11.7 Determination the transverse momentum acceptance

Due to the kinematic acceptance of the detector, regions with low and high transverse momenta of the charm-plus-muon system exhibit a vanishing overall efficiency. As this causes a singularity in the evaluation of the b-hadron production cross-section, these bins cannot be included in the measurement. Therefore, events with low and high transverse momenta are rejected and only the p_{T} region with finite efficiencies is accepted. The arising additional efficiency of this selection criterion is determined with simulated decays. The p_{T} acceptance, $\varepsilon p_{\mathrm{T}}(\eta(H_b))$, is defined as the $\eta(H_b)$-dependent ratio between the number of simulated signal decays within the defined accepted p_{T} region, and the total number of

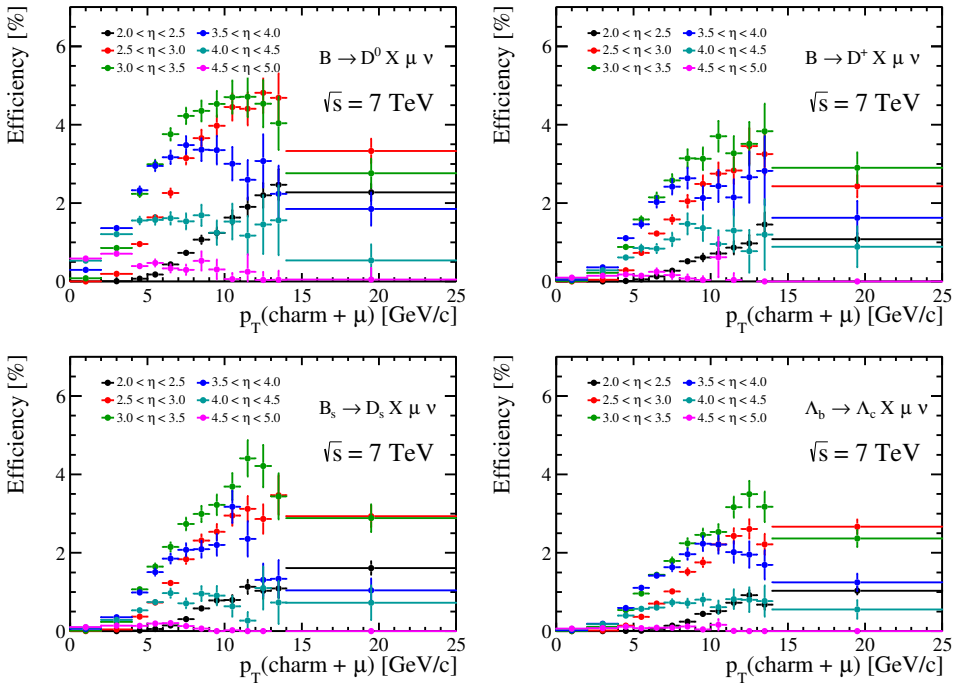

Figure 11.8: Overall reconstruction and selection efficiencies as a function of p_{T} (charm+μ) and $\eta(H_b)$ for the four charm modes determined with 7 TeV simulated decays weighted with efficiencies obtained from data-driven methods.

generated signal decays, N_{tot},

$$\varepsilon p_{\mathrm{T}}(\eta(H_b)) = \frac{N_{acc}(\eta(H_b))}{N_{tot}(\eta(H_b))}. \tag{11.9}$$

The b-hadron production cross-section within the accepted p_{T} region is computed according to Eq. 6.3 as the summed cross-section over all bins of p_{T}. In order to extrapolate the cross-section to the full p_{T} range, it is corrected for by the p_{T} acceptance that is purely determined from simulated events. The drawback of this method is that mismodelling of the simulated p_{T} distribution of the charm-plus-muon system affects the determination of the acceptance. Since the transverse momentum in data before reconstruction and selection is not known, differences observed in the measured p_{T} distributions from simulation and data, after reconstruction, are only taken into account as a systematic uncertainty which will be described in detail in Chap. 12.

Tables 11.9 and 11.10 list the p_{T} acceptance for the four charm-hadron decay modes for each bin of $\eta(H_b)$, separately for the simulated 7 TeV and 13 TeV signal decays. Uncertainties refer to the combined statistical and systematic uncertainties. The last row, "$b\bar{b}$", gives the average p_{T} acceptance for all considered decays according to the individual charm-hadron contributions to the b-hadron production cross-section.

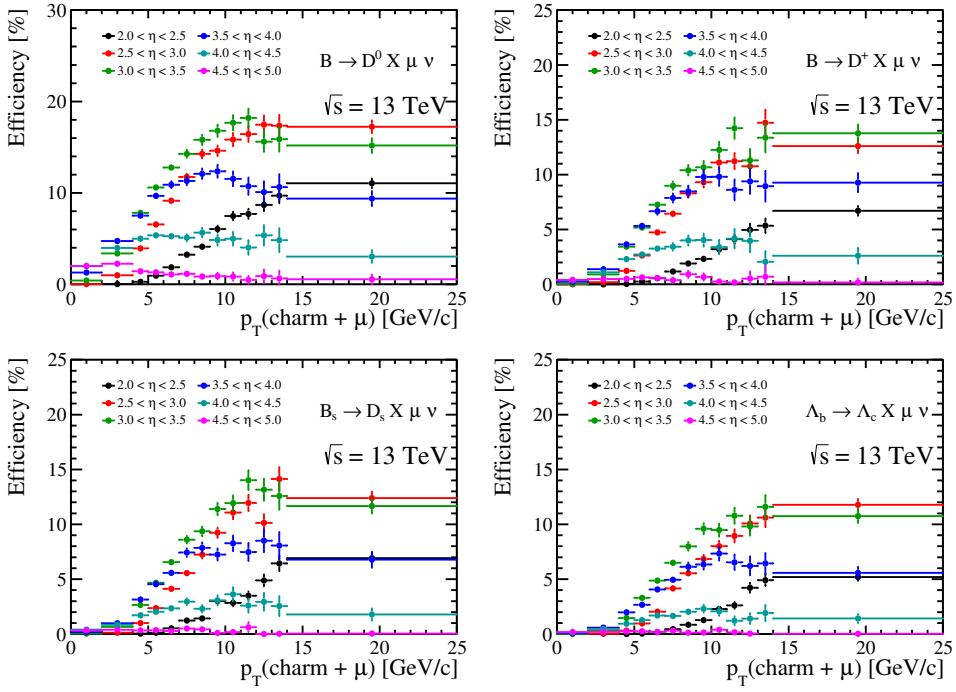

Figure 11.9: Overall reconstruction and selection efficiencies as a function of p_{T} (charm+μ) and $\eta(H_b)$ for the four charm modes determined with 13 TeV simulated decays weighted with efficiencies obtained from data-driven methods.

Table 11.9: Transverse momentum acceptance of the charm-plus-muon system, as defined in Eq. 11.9, determined with simulated 7 TeV signal decays.

mode	$2.0 < \eta < 2.5$	$2.5 < \eta < 3$	$3.0 < \eta < 3.5$	$3.5 < \eta < 4$	$4.0 < \eta < 5.5$	$4.5 < \eta < 5$
D^0 [%]	27.2 ± 0.3	35.8 ± 0.1	100.0 ± 0.0	100.0 ± 0.0	100.0 ± 0.0	100.0 ± 0.0
D^+ [%]	26.0 ± 3.0	34.7 ± 1.5	67.8 ± 0.9	64.0 ± 0.2	59.0 ± 0.7	52.4 ± 0.4
D_s^+ [%]	29.1 ± 1.5	38.2 ± 0.5	71.1 ± 0.7	67.3 ± 1.5	62.6 ± 2.8	54.3 ± 1.9
Λ_c^+ [%]	34.8 ± 4.8	44.6 ± 6.3	77.6 ± 5.6	74.5 ± 6.5	70.4 ± 11.2	64.0 ± 5.6
$b\bar{b}$[%]	28.7 ± 1.7	37.3 ± 1.5	87.5 ± 1.3	86.0 ± 1.3	83.1 ± 2.2	80.5 ± 1.1

Table 11.10: Transverse momentum acceptance of the charm-plus-muon system, as defined in Eq. 11.9, determined with simulated 13 TeV signal decays.

mode	$2.0 < \eta < 2.5$	$2.5 < \eta < 3$	$3.0 < \eta < 3.5$	$3.5 < \eta < 4$	$4.0 < \eta < 5.5$	$4.5 < \eta < 5$
D^0 [%]	30.8 ± 1.0	40.1 ± 1.1	100.0 ± 0.0	100.0 ± 0.0	100.0 ± 0.0	99.3 ± 0.02
D^+ [%]	29.5 ± 1.8	38.9 ± 0.9	71.3 ± 0.3	68.5 ± 3.1	65.2 ± 4.6	59.6 ± 2.0
D_s^+ [%]	33.1 ± 0.1	42.6 ± 1.9	74.4 ± 1.8	71.4 ± 4.5	68.2 ± 4.2	53.2 ± 1.2
Λ_c^+ [%]	26.9 ± 4.5	46.6 ± 7.4	77.2 ± 5.1	74.6 ± 6.7	71.8 ± 9.4	64.2 ± 8.7
$b\bar{b}$ [%]	29.9 ± 1.8	41.3 ± 2.3	88.6 ± 1.1	87.7 ± 2.0	86.2 ± 2.7	82.5 ± 1.6

12 Estimation of systematic uncertainties

The determination of the b-hadron production cross-section is subject to various sources of systematic uncertainties that dominate the total uncertainty of the measurement. Due to correlations between the measurements at the two centre-of-mass energies, some of the uncertainties cancel fully or partly in the ratio of cross-sections.

The systematic uncertainties are determined separately for the specific charm-hadron decay modes. To compute the uncertainties for the production cross-section measurement, the fractional charm-hadron contributions to the total cross-section are used to weight the related uncertainties. In the following, the systematic uncertainties are grouped into uncertainties that depend on $\eta(H_b)$ and those that do not.

12.1 Treatment of correlated uncertainties

Correlations between different sources of uncertainty, A and B, are taken into account with the correlation coefficient ρ_{AB}. Uncertainties of A and B, δ_A and δ_B, are added via

$$\delta = \sqrt{\delta_A^2 + \delta_B^2 + 2\ \rho_{AB}\delta_A\delta_B}. \tag{12.1}$$

In case A and B are uncorrelated, $\rho_{AB} = 0$, this simplifies to the quadratic sum. In case they are fully correlated, $\rho_{AB} = 1$, they are added linearly. In the ratio of cross-sections $r = \sigma_{13}/\sigma_7$, the uncertainties of each source i for the 7 TeV and 13 TeV data, $\delta_{i,7}$ and $\delta_{i,13}$, are added via

$$\delta_{i,r} = r\ \sqrt{\left(\frac{\delta_{i,13}}{\sigma_{i,13}}\right)^2 + \left(\frac{\delta_{i,7}}{\sigma_{i,7}}\right)^2 - 2\ \frac{\rho_{i,7,13}\delta_{i,13}\delta_{i,7}}{\sigma_{A,13}\sigma_{A,7}}}, \tag{12.2}$$

where $\rho_{i,7,13}$ is the correlation coefficient of the uncertainties of source i for the 7 TeV and 13 TeV data. In case of full positive correlation between the two centre-of-mass energies, $\rho_{i,7,13} = 1$, the uncertainties in the ratio cancel when the uncertainties are equal.

12.2 Results of the η-independent uncertainties

Among the η-independent systematic uncertainties, the leading uncertainties are due to the luminosity and the branching fraction measurements. The η-independent uncertainties are tabulated in Table 12.1 for the 7 TeV and 13 TeV measurements and the ratio of 13/7, respectively and are composed of the following sources:

- The luminosity calibration methods, the *van-der-Meer scan* and the *beam-gas imaging* methods have been described in Sec. 3.4. Due to the smaller calibration sample and the fact that for the run period at 13 TeV, only the beam-gas imaging method was used, the relative uncertainties of 1.7% and 3.9% are different for the 7 TeV and

13 TeV data, respectively. The individual uncertainties are determined to be 50% correlated [67] yielding an uncertainty in the ratio of 3.4%.

- The uncertainties of the semileptonic and charm branching fractions, shown in Tables 6.1 and 6.2, are weighted with the related charm-hadron contributions to the cross-section. In the ratio, the uncertainties fully cancel.

- This analysis includes semileptonic decays of b hadrons into various excited charm-hadron states and possible additional particles such as pions and kaons. In the samples of fully simulated events, presented in Sec. 6.4, the composition of these decays is modelled according to the measured relative occurrence. The uncertainty on the composition of this so-called *B cocktail* contributes to an uncertainty on the overall efficiency which is estimated by the difference between the efficiencies of the excited $D^{*(*)}\mu^-\nu$ states and the $D\mu^-\nu$ states and taking into account the uncertainties on the measured branching fractions. These are then added in quadrature to 1.0% which fully cancels in the ratio.

- The correction for higher-mass b-baryon states with respect to the Λ_b^0 is given by $(1+\delta) = 1.25 \pm 0.10$ in Chap. 6. This correction only affects the Λ_b^0 component and the resulting uncertainty on the b-hadron production cross-section is 2.0%. In the ratio, it contributes only if the number of heavy b baryons changes with the centre-of-mass energy. Assigning a conservative uncertainty of 10% on the shift of the fraction of heavy b baryons leads to an uncertainty of 0.4% in the ratio.

- The systematic uncertainty due to ignoring the additional cross-feeds between the b-hadron decays, discussed in Sec. 6.3, is given by the difference in efficiencies for the cross-feeds compared to the signal modes. Using simulated events, the efficiencies are determined to differ, on average, by about 0.6% per mode which sums up to 1.8% when conservatively assuming that the differences in efficiencies are fully correlated for the three modes. Although the branching fraction of cross-feeding decays is small, this number is conservatively taken as the systematic uncertainty on the total cross-section.

- As described in Chap. 6, the reconstruction of semileptonic decays is restricted to $b \to c$ quark transitions and a 2% correction for $b \to u$ decays with an uncertainty of 0.3% is applied [19].

- The efficiencies of the selection criteria on the occupancy of the detector have been determined in Sec. 11.4 where the small uncertainties are taken from the fit of the Gaussian function to the related distributions. Since the methods to determine the efficiencies are identical for the two datasets, they are assumed to be fully correlated.

12.3 Results of the η-dependent uncertainties

The η-dependent systematic uncertainties are summarised in Table 12.2. They are dominated by the finite statistics of the simulated decay sample, the uncertainties on the muon

Table 12.1: Relative systematic uncertainties independent of $\eta(H_b)$ on the $pp \to H_b X$ production cross-sections at 7 TeV and 13 TeV centre-of-mass energies and their ratio. Rows in bold refer to the leading systematics.

Source	7 TeV	13 TeV	Ratio 13/7
Luminosity	1.7%	3.9%	3.4%
***b* semileptonic BR**	2.1%	2.1%	0
Charm hadron BR	2.6%	2.6%	0
B decay cocktail	1.0%	1.0%	0
δ	2.0%	2.0%	0.4%
Ignoring b cross-feeds	1.8%	1.8%	0
$b \to u$ decays	0.3%	0.3%	0
selection criteria on the occupancy	0.1%	0.05%	0.05%
Total	4.7%	5.9%	3.4%

trigger and particle identification efficiencies, the correction of the track reconstruction efficiencies and the transverse momentum acceptance. The determination of the η-dependent systematic uncertainties are presented in detail in the following.

12.3.1 Systematic uncertainties due to the finite statistic of the simulated events

The finite statistics of the simulated semileptonic signal events represents a source of uncertainty in the lower and upper bins in η where kinematic acceptance effects emerge. The calculation of the uncertainties is based on the assumption that the application of selection criteria is a binomial process with the probability given by the true efficiency ε. Considering a sample size with N events, the expected number of events passing the selection criterion is theoretically given by $\langle k \rangle = \varepsilon N$, with the variance of the binomial distribution, $\mathrm{Var}(k) = N\varepsilon(1-\varepsilon)$. Taking $\varepsilon' = k/N$ as the estimated efficiency results in the uncertainty

$$\delta_{\varepsilon'} = \sqrt{1/N\ \varepsilon'(1-\varepsilon')}. \tag{12.3}$$

For each bin of the transverse momentum of the charm-plus-muon system within the accepted p_{T} region, the uncertainty is given by the binomial uncertainty. The uncertainties of all bins are added in quadrature to calculate the uncertainty per interval in η. In the ratio, the uncertainties are fully uncorrelated and therefore constitute the major uncertainty.

12.3.2 Systematic uncertainties on the track reconstruction efficiencies

The uncertainties on the track reconstruction efficiency correction originate from the finite statistics of the calibration samples and the uncertainties on the interactions of the different particle species with the material. The systematic uncertainty due to the finite statistics is obtained from 200 variations of the two-dimensional grid of correction factors, where each bin is varied by a random number that is Gaussian-distributed around zero with the

statistical uncertainty in that bin. The varied grids of correction factors are sequentially applied to the simulated decays. For each variation, an overall average correction factor per η bin is computed. The root mean square of the resulting distribution of the 200 average correction factors is taken as the statistical uncertainty. Systematic uncertainties arise due to the fact that the track reconstruction efficiency is obtained in one specific decay, $J/\psi \to \mu^+\mu^-$, and not from an arbitrary track. It is measured to be 0.4% and 0.8% per muon track for the 7 TeV and the 13 TeV data, respectively [29]. Since hadrons interact differently with matter, there is an uncertainty on the simulated hadronic interaction of 1.1% per kaon or proton track [29] and 1.4% per pion track. The hadronic uncertainties are dominated by the uncertainty on the material budget and hence full correlation between them is assumed. After adding the hadronic uncertainties linearly, they are added in quadrature with the muon contribution and the statistical uncertainty. For 7 TeV, the systematic uncertainties are dominated by the hadronic interactions. For 13 TeV, the uncertainties due to the limited statistics are comparable to the uncertainties of the material interactions. The uncertainties are weighted by the fraction of two-track and three-track final states according to the contributions of the individual charm-hadron decay modes to the overall cross-section. In the ratio, the uncertainties due to the material budget are fully correlated and only the statistical uncertainties of the calibration samples and the difference in the muon contributions are added in quadrature.

12.3.3 Systematic uncertainties on the muon trigger and particle identification efficiencies

The systematic uncertainties on the trigger efficiencies include the uncertainties on the validity of the tag-and-probe method, the effect of using a finite three-dimensional binning scheme and the statistical uncertainty due to the finite statistics of the calibration samples. Although the remaining relative differences of the simulated trigger efficiencies between the tag-and-probe method and the binned true efficiency, shown in Fig. 11.4, have been corrected for, it is not obvious that the same differences as in simulation are observed in data. Therefore, the relative deviations of the simulated efficiencies are taken into account as a systematic uncertainty, separately for each charm-hadron decay mode.

The uncertainties due to the finite statistics of the calibration sample leads to statistical uncertainties of the efficiencies for each bin of the three-dimensional grid. As it was done for the tracking corrections, the resulting changes on the trigger efficiencies per b-hadron pseudorapidity are investigated with 1000 variations of the efficiency grid in which each bin is randomly varied within its uncertainty.

The impact of using a finite binning scheme of the trigger efficiency is analysed in two ways. In Sec. 11.3, the trigger response of the semileptonic signal sample itself was used to extract the three-dimensional true trigger efficiency grid which was compared to the tag-and-probe method by applying them to the simulated events according to the muon kinematics. The trigger response can, however, also been extracted directly in an unbinned way. Figure 12.1 shows, separately for the two centre-of-mass energies, the trigger efficiencies for simulated $B \to D^0\mu\nu X$ decays as a function of the b-hadron pseudorapidity, with and without applying the three-dimensional binning scheme. Differences between the two originate from the binning procedure.

However, few bins exhibit no deviation because the variations vanish in average. Al-

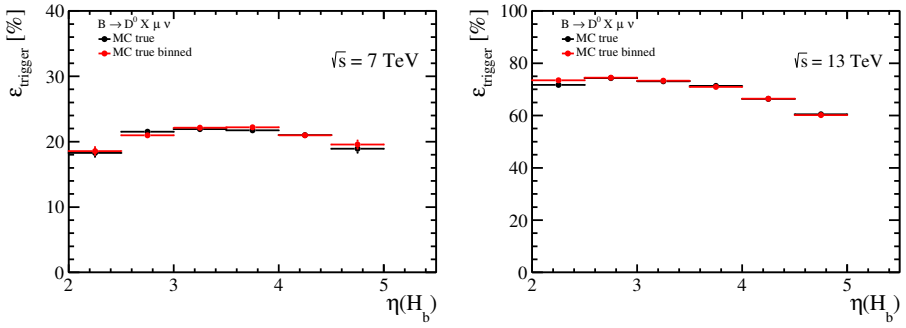

Figure 12.1: Simulated trigger efficiencies as a function of the b-hadron pseudorapidity in the D^0 mode, obtained from simulated (left) 7 TeV and (right) 13 TeV events, by computing the trigger efficiencies in an unbinned way (black) and extracting it from a three-dimensional binned grid (red).

ternatively, the impact of the choice of the binning scheme is investigated by applying in total 18 different schemes in data where the maximum deviation of the efficiencies from the nominally binned efficiency is taken as the systematic uncertainty. Since the two methods determine the same source of uncertainty, they are not added but the maximum deviation observed in the two is taken as the systematic uncertainty due to the finite binning. For the 7 TeV data, the uncertainties due to the binning scheme are larger because the efficiencies increase more steeply towards low transverse momenta and pseudorapidities of the muon which is due to the tighter trigger requirements. The total systematic uncertainty is given by the quadrature of these uncertainties. In the ratio, the uncertainties of the two datasets are highly correlated but due to the large differences in the trigger selection, they are conservatively assumed to be only 50% correlated.

12.3.4 Systematic uncertainties on the hadronic particle identification efficiencies

As it is done for the trigger efficiencies, the uncertainties due to the finite size of the calibration samples are investigated by varying each bin of the three-dimensional efficiency grid 1000 times by a random number that is Gaussian distributed around zero with the statistical uncertainty in this bin. Each time, the simulated events are weighted with the varied grid to compute the impact on the overall efficiencies.

The uncertainty due to the choice of the binning scheme is evaluated by determining the one-dimensional efficiencies with a very fine-graded binning. For each nominal coarse bin, the observed deviation of the efficiencies is weighted with the number of events in that bin and used as the systematic uncertainty. The two sources of uncertainties are added in quadrature to the overall systematic uncertainties. In the ratio, they are assumed to be fully correlated.

12.3.5 Systematic uncertainties on the transverse momentum acceptance

Since the transverse momentum of the charm-plus-muon system after reconstruction is not perfectly modelled in simulated decays, especially for the Λ_b^0 mode, the observed difference

is taken into account as a systematic uncertainty on the transverse momentum acceptance. For each charm-hadron decay mode and bin of $\eta(H_b)$, the relative difference of the means of the p_{T} distributions of data and simulation, given in Sec. 8.4, is used to shift the transverse momentum of the generated charm-plus-muon system. The applied shift is smeared by the statistical uncertainty of the relative difference by varying it with a random number that is Gaussian distributed around zero with the statistical uncertainty.

The deviation of the recomputed efficiency from the nominal value is taken as the systematic uncertainty on the p_{T} acceptance. In the ratio, the uncertainties are assumed to be fully correlated as the simulated events at 7 TeV and 13 TeV have been generated with the same event generator that is responsible for the shifted transverse momentum spectra.

12.3.6 Systematic uncertainties on the background contributions

The systematic uncertainties on the random combinations of charm hadrons and real muons from different b-hadron decays are extracted from the fit of the yields with the wrong charge combination. Compared to the uncertainties on the background contribution from doubly-charmed b-hadron decays, they are small. For those, the uncertainties due to the finite statistics of the simulated samples are computed using binomial uncertainties. The uncertainties on the branching fractions and hadronisation fractions are taken from Tables 10.2-10.4 in Sec. 10.3, where the uncertainties on the b-quark hadronisation fractions are dominant. The uncertainties due to the unknown doubly-charmed B_s^0 and Λ_b^0 branching fractions are investigated by increasing them to 20% which leads to large uncertainties for the D_s^+ and Λ_c^+ background yields. 20% is a conservative value as the modes would have been observed with significant numbers in other experiments. Since the corrections due to background contributions are only in the percent level, the relatively large uncertainties of the corrections have a small impact on the measurement. The systematic uncertainties are of the one-percent level and are fully correlated for the two centre-of-mass energies such that they cancel in the ratio.

12.3.7 Systematic uncertainties on the signal yield

The fit functions to describe the components of the signal candidates, in terms of mass and logarithmic impact parameter, have been chosen empirically to model the distributions of simulated decays. Therefore, the choice of the fit models is a source of systematic uncertainty which is investigated by performing the fits with alternative functions.

A different parameterisation of asymmetric distributions is given by the so-called Crystal Ball function P_{CB} that was used in the Crystal Ball(CB) experiment [68]. This function consists of a Gaussian core at the peak position, x_{peak}, with the width, σ, and one long tail that flattens out towards one direction. It is section-wise defined by

$$\mathcal{P}_{\mathrm{CB}}(x;\alpha,n,x_{\mathrm{peak}},\sigma) = N \cdot \begin{cases} \exp\left(-\frac{(x-x_{\mathrm{peak}})^2}{2\,\sigma^2}\right) & \text{for } \frac{x-x_{\mathrm{peak}}}{\sigma} > -\alpha \\ A \cdot (B - \frac{x-x_{\mathrm{peak}}}{\sigma})^{-n} & \text{for } \frac{x-x_{\mathrm{peak}}}{\sigma} \leq -\alpha \end{cases}, \tag{12.4}$$

where n is the exponent of the power-law tail below a threshold $(-\alpha\sigma + x_{\mathrm{peak}})$, N is the

normalisation and A and B are defined as

$$\begin{aligned} A &= \left(\frac{n}{|n|}\right)^n \cdot \exp\left(-\frac{|\alpha|^2}{2}\right), \\ B &= \frac{n}{|\alpha|} - |\alpha|. \end{aligned}$$

All binned fits are repeated with replacing only one function at a time. The signal component of the charm-hadron mass distribution is described by a Crystal Ball function instead of the sum of two Gaussian functions and the combinatorial background by an exponential function instead of a linear function. For the logarithmic impact parameter distribution of the signal, an additional single Gaussian function is added to the nominal bifurcated Gaussian. The model for the background components of the logarithmic impact parameter distribution, prompt or combinatorial, is substituted by a bifurcated Gaussian only or a Crystal Ball function. The root mean square of the distribution of fitted yields, using the various fit models, is taken as the systematic uncertainty. In the ratio of cross-sections, the uncertainties cancel because they are fully correlated.

12.3.8 Summary of the η-dependent uncertainties

Table 12.2 summarises the η-dependent systematic uncertainties for the 7 TeV and 13 TeV measurements and the ratio of 13/7, respectively. All components, including the η-independent ones, are added in quadrature for the total systematic uncertainties listed in the last row.

Table 12.2: Relative systematic uncertainties (%) as a function of $\eta(H_b)$ on the $pp \to H_b X$ production cross-sections at 7 TeV and 13 TeV centre-of-mass energies and their ratio. The trigger efficiency includes the muon detection efficiency. Rows in bold refer to the leading systematics. The bottom lines in each section give the total systematic uncertainty in each η bin.

			7 TeV			
Source	$2.0< \eta <2.5$	$2.5< \eta <3.0$	$3.0< \eta <3.5$	$3.5< \eta <4.0$	$4.0< \eta <4.5$	$4.5< \eta <5.0$
MC statistics	7.6	2.5	3.4	2.6	2.9	5.1
Tracking efficiency	3.1	3.1	3.2	3.1	3.1	3.1
Trigger	5.4	3.8	3.2	3.1	3.3	5.7
Hadron PID	1.7	1.6	1.5	1.4	1.6	1.7
p_T acceptance	6.1	3.9	1.5	1.6	2.6	1.4
Backgrounds	1.2	0.8	0.9	0.8	0.8	0.8
Fit model	0.4	0.3	0.3	0.3	0.4	0.5
Sum η-dependent	11.8	7.0	6.1	5.6	6.2	8.6
Total	12.7	8.4	7.7	7.3	7.8	9.8
			13 TeV			
Source	$2.0< \eta <2.5$	$2.5< \eta <3.0$	$3.0< \eta <3.5$	$3.5< \eta <4.0$	$4.0< \eta <4.5$	$4.5< \eta <5.0$
MC statistics	3.5	1.8	2.1	1.7	2.1	3.9
Tracking efficiency	5.4	4.9	4.1	3.7	3.8	3.8
Trigger	2.4	1.6	2.6	3.1	3.5	4.0
Hadron PID	1.7	1.6	1.5	1.4	1.6	1.8
p_T acceptance	5.9	5.6	1.2	2.3	3.1	1.9
Backgrounds	1.1	0.9	0.8	0.8	0.7	0.7
Fit model	0.2	0.2	0.2	0.2	0.4	0.4
Sum η-dependent	9.3	8.0	5.7	5.8	6.6	7.3
Total	11.0	10.0	8.2	8.3	8.9	9.4
			Ratio 13/7			
Source	$2.0< \eta <2.5$	$2.5< \eta <3.0$	$3.0< \eta <3.5$	$3.5< \eta <4.0$	$4.0< \eta <4.5$	$4.5< \eta <5.0$
MC statistics	8.3	3.1	4.0	3.1	3.6	6.4
Tracking efficiency	4.4	3.7	2.7	2.2	2.1	2.2
Trigger	4.7	3.3	2.9	3.1	3.4	5.1
Sum η dependent	10.5	5.8	5.6	4.9	5.4	8.5
Total	11.0	6.8	6.6	6.0	6.4	9.1

13 Results

In this chapter, the b-hadron production cross-sections are presented and compared with the theory model using the fixed-order next-to-leading log framework (FONLL) [12]. The differential cross-sections and their ratios are measured as a function of η and then summed up to the integrated cross-sections.

13.1 Determination of the b-hadron production cross-sections

The differential b-hadron production cross-sections at 7 TeV and 13 TeV centre-of-mass energies are shown in Fig. 13.1, where the black error bars refer to the statistical uncertainties and the blue bars have the systematic uncertainties added in quadrature. The solid red curve indicates the theoretical prediction from the FONLL model with the $\pm 1\sigma$ uncertainty represented by the grey-shaded band. It should be noted that the presented results deviate from the cross-sections published in Ref. [1]. The reason for this is that the interaction of the charged particles with the material of the vertex locator was not perfectly modelled in the simulation used for the results in Ref. [1]. This lead to a wrong evaluation of the reconstruction and selection efficiencies. The model was corrected and an erratum of the measurement will be submitted soon. The results presented in this thesis are determined using the simulation with the corrected model.

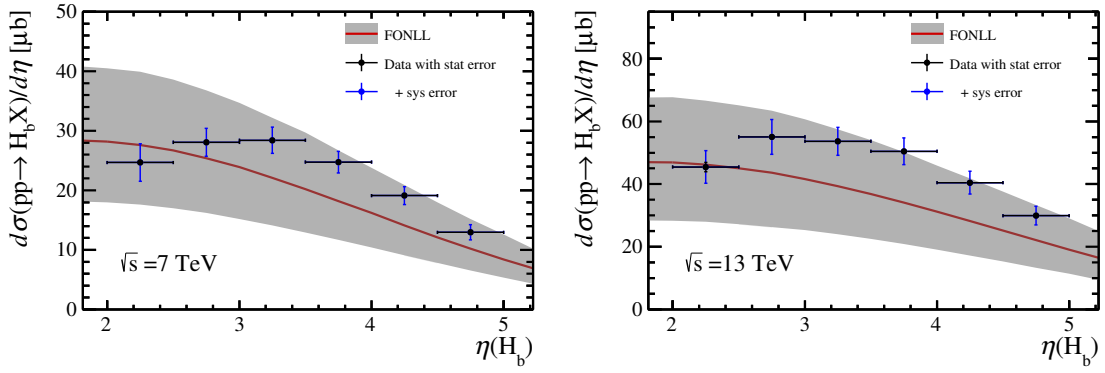

Figure 13.1: The differential b-hadron production cross-sections, $\sigma(pp \to H_b X)$, as a function of η, at (left) 7 TeV and (right) 13 TeV center-of-mass energies, where H_b is a hadron that contains a specific quark, either a b or a $\bar{b}$. The black error bars show the statistical uncertainties only, and the blue bars have the systematic uncertainties added in quadrature. The solid red line gives the theoretical prediction from the FONLL model [12], while the shaded band outlines the $\pm 1\sigma$ uncertainty on the prediction.

For both energies, it can be seen that the theoretical uncertainties are much larger than the systematically dominated experimental uncertainties and the data is compatible with

the theory within the uncertainties. At both centre-of-mass energies, the shapes in η are modelled by the theory in the medium and upper η-range where the cross-section gradually decreases. The observed drop in cross-sections at low η is not described by the theory model. Apart from this first bin in η, the data lies above the central value of the theory prediction but well within the theoretical uncertainties. The statistical uncertainty of the 13 TeV data is higher due to the smaller dataset but still small compared to the fully dominating systematics.

The ratio of cross-sections for 13 TeV/7 TeV is presented in Fig. 13.2, where the theoretical expectation is predicted with less uncertainty because major contributions, such as uncertainties on the normalisation and factorisation scale, cancel in the ratio. The experimental uncertainties decrease only marginally. In general, the central values of the data are slightly above the theory prediction but compatible within uncertainties and a good agreement of the shapes is observed. Only the ratio in the second bin in η is not compatible with the theory model within $\pm1\sigma$ of the uncertainties.

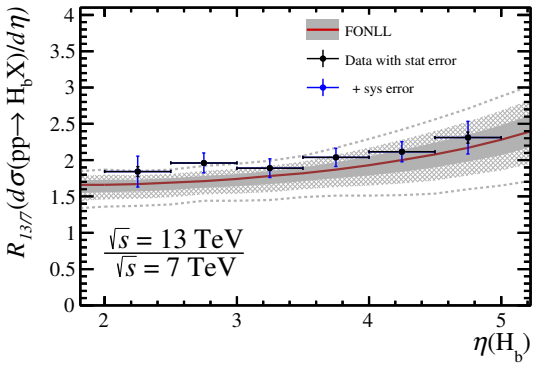

Figure 13.2: The differential b-hadron production cross-section ratio for 13 TeV/7 TeV as a function of η. The black error bars show the statistical uncertainties only, and the blue bars have the systematic uncertainties added in quadrature. The solid red line gives the theoretical prediction from the FONLL model [12], while the solid-shaded band gives the estimated uncertainty on the predictions at $\pm1\sigma$, the cross-hatched band at $\pm2\sigma$, and the dashed line at $\pm3\sigma$.

The absolute values of the b-hadron production cross-sections and their ratios are tabulated for the six bins of η in Table 13.1, where the first uncertainty is statistical and the second is systematic. The integrated cross-sections in the covered pseudorapidity range between between 2 and 5 are compared with the theory expectation in Table 13.2 which are compatible with each other within the uncertainties. The integrated cross-section at a centre-of-mass energy of 7 TeV is 69.0 ± 0.3 (stat) $\pm$ 6.1 (syst) µb with the theory expectation of 62^{+28}_{-22} µb and the integrated cross-section at 13 TeV is 137.5 ± 1.1 (stat) $\pm$ 12.8 (syst) µb with the theory value of 111^{+51}_{-44}. The ratio of integrated cross-sections is 2.03 ± 0.02 (stat) $\pm$ 0.15 (syst) compared to the expectation of $1.79^{+0.21}_{-0.15}$.

These results represent the measured b-hadron production cross-section in the LHCb acceptance. Using the general-purpose MC event generator Pythia 8, the measured cross-sections can be extrapolated to the entire solid angle. However, this calculation is completely dependent on the Pythia extrapolation into a region that cannot be assessed with the

Table 13.1: Absolute b-hadron production cross-sections in proton-proton collisions at centre-of-mass energies of 7 TeV and 13 TeV and their ratio as a function of η. The first uncertainty is statistical and the second is systematic.

η	7 TeV [μb]	13 TeV [μb]	Ratio 13/7
$2.0 < 2.5$	$12.3 \pm 0.2 \pm 1.6$	$22.7 \pm 0.7 \pm 2.5$	$1.84 \pm 0.07 \pm 0.20$
$2.5 < 3.0$	$14.0 \pm 0.1 \pm 1.2$	$27.5 \pm 0.4 \pm 2.8$	$1.96 \pm 0.03 \pm 0.13$
$3.0 < 3.5$	$14.2 \pm 0.1 \pm 1.1$	$26.8 \pm 0.4 \pm 2.2$	$1.89 \pm 0.03 \pm 0.12$
$3.5 < 4.0$	$12.4 \pm 0.1 \pm 0.9$	$25.2 \pm 0.4 \pm 2.1$	$2.04 \pm 0.03 \pm 0.12$
$4.0 < 4.5$	$9.6 \pm 0.1 \pm 0.7$	$20.2 \pm 0.3 \pm 1.8$	$2.12 \pm 0.04 \pm 0.14$
$4.5 < 5.0$	$6.5 \pm 0.1 \pm 0.6$	$15.0 \pm 0.5 \pm 1.4$	$2.31 \pm 0.08 \pm 0.21$

Table 13.2: Integrated b-hadron production cross-sections in proton-proton collisions at centre-of-mass energies of 7 TeV and 13 TeV and their ratio from 2 to 5 in pseudorapidity. The first uncertainty is statistical and the second is systematic.

integrated in $2 < \eta < 5$	7 TeV [μb]	13 TeV [μb]	Ratio 13/7
data	$69.0 \pm 0.3 \pm 6.1$	$137.5 \pm 1.1 \pm 12.8$	$2.03 \pm 0.02 \pm 0.15$
FONLL prediction [12]	62^{+28}_{-22}	111^{+51}_{-44}	$1.79^{+0.21}_{-0.15}$

LHCb detector. Hence, the related uncertainties of the extrapolation are not known but they are assumed to be much larger than the uncertainties of the measured cross-sections in the accessible η range. The extrapolated total b-hadron production cross-sections in the entire solid angle in proton-proton collisions at 7 TeV and 13 TeV centre-of-mass energies are approximately ≈280 μb and ≈540 μb, respectively.

13.2 Contributions of the charm-hadron decay modes to the b-hadron production cross-section

In this section, the measured b-hadron production cross-section is broken down into the contributions from the individual b-hadron species with their subsequent decays into the related charm-hadron final states. As B^0 and B^+ mesons decay into both D^0 and D^+ mesons, these charm-hadron contributions can only be associated to the summed production cross-sections of B^0 and B^+ mesons. The contributions from the D_s^+ and Λ_c^+ decay modes are directly related to the production cross-section of B_s^0 mesons and Λ_b^0 hadrons, respectively. In principle, these contributions can be used to extract the hadronisation fractions of a b-quark into the related b-hadron species, but this will be done in a future analysis. For this analysis, only the relative occurrences of the charm-hadron modes are needed to evaluate the systematic uncertainties in Chap. 12. Tables 13.3 and 13.4 give the fractional contributions from the charm-hadron final states to the differential b-hadron production cross-section for 7 TeV and 13 TeV centre-of-mass energies, respectively. In Fig. 13.3, their absolute contributions are drawn stacked upon each other.

The uncertainties given refer only to the statistical uncertainties. The production of B^+ and B^0 mesons with the subsequent D^0 decay mode is by far, with about 50% of the total, the main contributor to the cross-section and the D^+ mode sums up to about 20%. Λ_b^0 hadrons with the Λ_c^+ decay mode form about 20% of the total and the B_s^0 production is the lowest with about 10%. At 13 TeV, this does not change significantly.

Table 13.3: Fractional contributions of the individual charm-hadron decay modes to the differential b-hadron production cross-sections as a function of η at a centre-of-mass energy of 7 TeV. The uncertainties refer to the statistical uncertainties only.

mode	$2.0 < \eta < 2.5$	$2.5 < \eta < 3$	$3.0 < \eta < 3.5$	$3.5 < \eta < 4$	$4.0 < \eta < 5.5$	$4.5 < \eta < 5$
D^0 [%]	52.8 ± 0.9	54.5 ± 0.4	53.5 ± 0.5	53.7 ± 0.4	53.5 ± 0.4	54.8 ± 0.5
D^+ [%]	16.8 ± 0.4	19.2 ± 0.2	18.5 ± 0.2	18.8 ± 0.1	20.0 ± 0.2	20.7 ± 0.5
D_s^+ [%]	6.7 ± 0.5	7.2 ± 0.2	6.9 ± 0.2	7.3 ± 0.2	9.1 ± 0.3	7.1 ± 0.5
Λ_c^+ [%]	23.7 ± 1.3	19.1 ± 0.3	21.1 ± 0.3	20.2 ± 0.2	17.4 ± 0.3	17.5 ± 0.5

Table 13.4: Fractional contributions of the individual charm-hadron decay modes to the differential b-hadron production cross-sections as a function of η at a centre-of-mass energy of 13 TeV. The uncertainties refer to the statistical uncertainties only.

mode	$2.0 < \eta < 2.5$	$2.5 < \eta < 3$	$3.0 < \eta < 3.5$	$3.5 < \eta < 4$	$4.0 < \eta < 5.5$	$4.5 < \eta < 5$
D^0 [%]	54.0 ± 1.6	53.4 ± 0.7	54.2 ± 1.0	54.5 ± 1.0	52.3 ± 0.8	51.2 ± 1.3
D^+ [%]	20.2 ± 1.2	19.9 ± 0.5	19.6 ± 0.5	18.4 ± 0.5	18.9 ± 0.6	20.7 ± 1.4
D_s^+ [%]	8.5 ± 2.0	6.9 ± 0.5	6.0 ± 0.3	7.9 ± 0.6	8.2 ± 0.7	8.5 ± 1.8
Λ_c^+ [%]	17.3 ± 1.6	19.9 ± 0.9	20.2 ± 0.9	19.3 ± 0.6	20.6 ± 0.9	19.7 ± 1.8

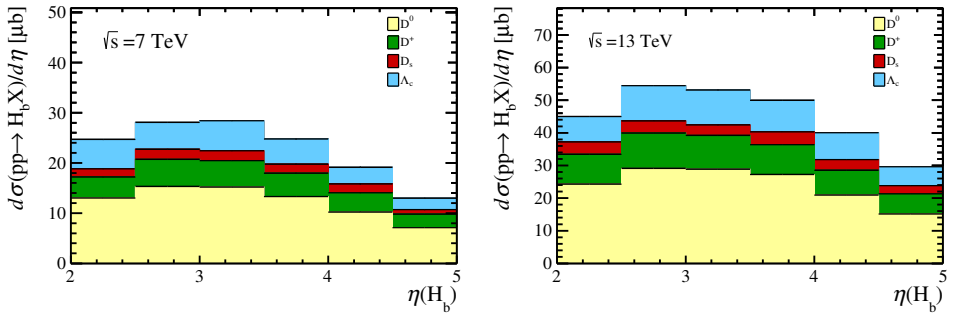

Figure 13.3: Differential cross-sections for the production of a b-hadron broken down into the contributions from the individual charm-hadron final states, as a function of η at centre-of-mass energies of (left) 7 TeV and (right) 13 TeV. The combined cross-sections for the production of B^0 and B^+ mesons with the subsequent decay into D^0 mesons are given by the beige areas and with the subsequent decay into D^+ mesons by the green areas. The red areas correspond to the production cross-section of B_s^0 mesons with the subsequent decay into D_s^+ mesons and the light blue areas to the Λ_b^0-hadron cross-section with the subsequent decay into Λ_c^+ hadrons.

14 Conclusion

This first part of the thesis presents the measurement of the b-hadron production cross-sections in proton-proton collisions at centre-of-mass energies of 7 TeV and 13 TeV and their ratio as a function of the b-hadron pseudorapidity. Semileptonic decays of b hadrons are used where the final-state charm hadrons and muons are reconstructed and additional particles such as neutrinos are left undetected. The analysed data samples at 7 TeV and 13 TeV have been collected during the years 2011 and 2015, respectively, by the LHCb experiment and correspond to integrated luminosities of $\mathcal{L} = 284\ pb^{-1}$ and $\mathcal{L} = 4.60\ pb^{-1}$. Experimentally, the cross-sections are measured with the background-subtracted and efficiency-corrected number of signal yields divided by the luminosities and branching fractions. The signal yields of the reconstructed charm hadrons are determined in a simultaneous fit to the invariant mass and logarithmic impact parameter distributions of the selected signal candidates. The fit is used to identify combinatorial background and charm hadrons that originate directly from the proton-proton interaction vertex and not from a long-lived b hadron. Backgrounds from randomly combined charm hadrons and muons and real b-hadron decays into two charmed hadrons are subtracted from these yields whereas contributions from falsely identified muons are negligible. The efficiencies of the reconstruction and selection process are evaluated using fully simulated signal samples and additional data-driven methods for the trigger, hadronic particle identification and track reconstruction efficiencies and the efficiencies of the selection criteria on the occupancy of the detector. These are determined using well-known calibration samples that have a high signal-to-background ratio.

Reconstructing about 450'000 and 90'000 semileptonic b-hadron decays in the 7 TeV and 13 TeV datasets, respectively, the integrated b-hadron production cross-sections in the LHCb forward acceptance, between 2 and 5 in pseudorapidity, are determined to be $69.0 \pm 0.3 \pm 6.1\,\mu b$ and $137.5 \pm 1.1 \pm 12.8\,\mu b$, where the first uncertainty is statistical and the second is systematic in nature. The differential results as a function of the pseudorapidity, η, show good agreement with theoretical predictions using fixed-order next-to-leading logarithmic (FONLL) [12] calculations within the uncertainties. Due to correlated theoretical uncertainties, the ratio of cross-sections at 13 TeV and 7 TeV is predicted with less uncertainty and the measurement shows a good agreement within the uncertainties.

The precision of the presented analysis is dominated by systematic uncertainties, of which the leading contributions are the uncertainties on the transverse momentum acceptance of the charm-plus-muon system, the luminosity determination, the track reconstruction and trigger efficiencies and the finite statistics of the simulated events. Hence, the analysis can be improved with larger samples of simulated events that are tuned better in terms of transverse momentum spectra to properly reflect the p_{T} acceptance. Especially the simulated kinematics of the baryon decays deviates from real data. Due to the tight trigger requirements at 7 TeV, the trigger efficiency changes more steeply at low transverse

momenta and pseudorapidities than at 13 TeV which leads to larger uncertainties due to the finite binning scheme. However, during the 13 TeV data-taking period, the trigger system was operated with a dedicated configuration that granted more computational capabilities. This was not possible during the nominal 7 TeV run. The 7 TeV results confirm the less precise previous LHCb measurement [24] using the D^0 decay mode only which depended on the b-quark hadronisation fraction into B^0 and B^+, measured at LEP.

Cross-section measurements of heavy-flavour production have also been performed in similar analyses at LHCb using b-hadron decays to charmonia [67]. The charm-hadron production cross-section has been measured with prompt charm mesons [69]. All of them show a similar agreement of the ratios of cross-sections with theory models[1]. The fact that the production cross-sections can be predicted to the recently unexplored high centre-of-mass energy of 13 TeV to this accuracy shows that the QCD processes are very well described. This is a great success of the underlying theory model.

With an instantaneous luminosity of $4 \cdot 10^{32}\,\mathrm{cm}^{-2}\mathrm{s}^{-1}$ during LHCb Run II, the b-hadron production rate within the LHCb acceptance is approximately 50 kHz that allows never-reached high-precision measurements of Standard Model parameters. One of these parameters is the CP-violating phase ϕ_s in the relatively rare decay $B_s^0 \to \phi\phi$. Using previously collected data at 7 TeV and 8 TeV proton-proton collisions, the measurement of CP violation in $B_s^0 \to \phi\phi$ decays is presented in the following second part of this thesis.

[1] The pusblished results in Ref. [67] and [69] were evaluated with a wrong model of the material interaction. An erratum will be submitted soon.

Part II:
Measurement of CP violation in $B_s^0 \to \phi\phi$ decays

15 Introduction

The large number of b hadrons produced in the LHCb acceptance allows for the study of decay modes that occur rarely, but offer great sensitivity to deviations from Standard-Model predictions. One of the key goals of LHCb is the measurement of the CP-violating phase ϕ_s in the decay channel $B_s^0 \to J/\psi\,\phi$, in which time-dependent CP violation arises from the interference between the direct decay and the decay after mixing of the b meson. Since meson mixing in the Standard Model proceeds via suppressed box diagrams, it is very sensitive to new heavy degrees of freedom contributing to the loop corrections. Due to the fact that only virtual particles are exchanged in the loops, the mass scale of these New-Physics contributions can be much higher than the actual accessible energy scale. Within a relative uncertainty of ~ 7 %, the LHCb Run I result [70] is compatible with Standard-Model expectations. It is the goal of the coming years to further improve the statistical sensitivity of the ϕ_s ($J/\psi\,\phi$) measurement and put more stringent limits on possible new effects. In parallel, channels are investigated that offer a different dependence on New Physics through quantum loops of different types. The decay $B_s^0 \to \phi\phi$ is such a channel. Unlike in the $B_s^0 \to J/\psi\,\phi$ mode, where the B_s^0 meson decay is described by a tree-level amplitude, the decay $B_s^0 \to \phi\phi$ can only proceed via a rare gluonic or electroweak penguin process, a loop diagram. Thus, this decay channel is not only sensitive to New-Physics contributions in flavour mixing which is mediated by the electroweak interaction in the SM, but additionally to possible new effects in the quantum corrections of the loop-suppressed decay amplitude. Therefore, the observed CP-violating phase $\phi_s(\phi\phi)$ provides a different way to test the presence of new phenomena, with the drawback that the decay occurs more rarely. At LHCb, a first measurement has been conducted with the 2011 dataset in Ref. [71], but due to the small number of signal, it was only possible to obtain limits on the allowed parameter range. The 2012 dataset that provides twice the integrated luminosity, is included in the following.

The second part of this thesis presents the measurement of CP violation in the decay $B_s^0 \to \phi\phi$ using the combined datasets from 2011 and 2012. The CP violation parameters, the phase $\phi_s(\phi\phi)$ and the parameter of direct CP violation or CP ciolation in mixing, $|\lambda_{\mathrm{CP}}|$, are extracted. The measurement has been published in Phys. Rev. D 90, 052011 [6] and the author was one of the main contributors. It is organised as follows: Chapter 16 presents a theoretical overview of time-dependent CP violation and reviews the resulting decay rates of the B_s^0 and $\overline{B}_s^0$ mesons. Chapter 17 comprises the analysis strategy to perform the CP-violation measurement. Chapter 18 sketches the reconstruction and selection of the signal decay and possible background contributions are investigated. Chapter 19 shows the measurement of the decay-time resolution and in Chap. 20, acceptance effects of the detector are determined, namely decay-time and angular acceptances. Chapter 21 describes methods to determine the initial production flavour of the B_s^0 meson. After describing the fit procedure in Chap. 22 and discussing the systematic uncertainties in Chap. 23, the final results are presented in Chap. 24, followed by a concluding discussion in Chap. 25.

16 Introduction to the theoretical framework of CP violation

This chapter presents a short overview of CP violation in the b-meson system. Time-dependent CP violation in the interference between the direct decay and the decay after mixing of the B_s^0 meson into its anti-meson $\overline{B}_s^0$ can arise through the introduction of a complex phase ϕ_s. CP violation in $B_s^0 \to \phi\phi$ decays is presented in detail.

16.1 Measurement of complex phase differences

In the Standard Model, CP violation is introduced by a complex phase in the CKM matrix as it was shown in Chap. 2. Defining a general complex amplitude as $A = |A|\, e^{i\phi}$, the phase ϕ cancels when taking the absolute square $A^*A = |A|^2\, e^{i(\phi-\phi)} = |A|^2$. Therefore, CP violation cannot be observed with single decay amplitudes. In the amplitude of a b-meson decay into a final state f, $A(B \to f)$, the phase consists of a weak phase, ϕ, that changes sign under CP transformation, $\overline{A} = A(\overline{B} \to \overline{f})$, and a strong phase, δ, that does not change sign:

$$A = |A|\, e^{i(\phi+\delta)}, \qquad\qquad \overline{A} = |A|\, e^{i(-\phi+\delta)}.$$

The two phases phase originate from different processes of the decay. In the sum of single amplitudes, $A = A_1 + A_2$, the phases are still present in the interference terms

$$\begin{aligned} |A|^2 &= |A_1 + A_2|^2 \\ &= |A_1|^2 + |A_2|^2 + 2\,|A_1 A_2| \cos(\Delta\phi + \Delta\delta) \end{aligned} \tag{16.1}$$

and the CP-transformed amplitude $\overline{A}$ is computed as

$$\begin{aligned} \left|\overline{A}\right|^2 &= \left|\overline{A}_1 + \overline{A}_2\right|^2 \\ &= |A_1|^2 + |A_2|^2 + 2\,|A_1 A_2| \cos(-\Delta\phi + \Delta\delta). \end{aligned} \tag{16.2}$$

Although the phases depend on the choice of convention, the phase difference is an observable quantity. Additionally, it should be noted that due to the even cosine function, the strong phase difference is needed to measure the weak phase difference. Thus, CP violation can only be measured in the interference of two amplitudes when there are two phases of which one flips sign under CP transformation. The weak phases are related to the phases of the CKM matrix elements. An example where direct CP violation occurs is in $B^0 \to K^+\pi^-$ and $\overline{B} \to K^-\pi^+$ decays [72] that exhibit different decay amplitudes $A \neq \overline{A}$. For each of them, the tree-level decay amplitude on the left-hand side of Fig. 16.1 interferes with the loop-induced penguin amplitude on the right. Since they involve different CKM

elements and thus different weak phases, CP violation can be measured. However, the strong phases originating from QCD processes and involved gluons are hard to calculate in penguin diagrams and therefore, the result is difficult to interpret in terms of CKM angles.

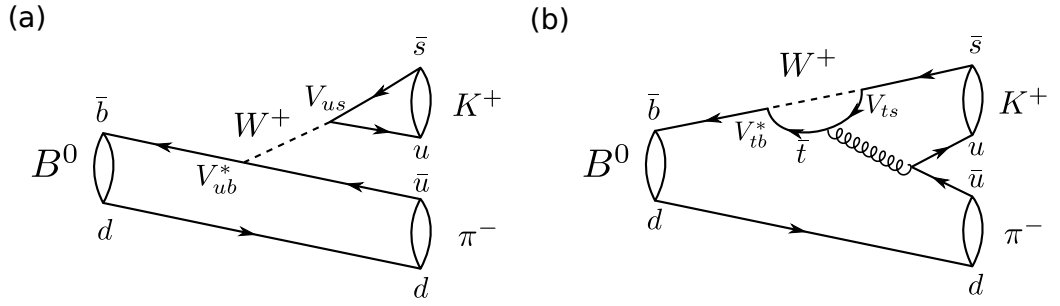

Figure 16.1: (a) Tree-level and (b) penguin Feynman diagram of the decay $B^0 \to K^+ \pi^-$.

16.2 Flavour-changing neutral currents

The quark transition in the tree-level diagram of the $B^0 \to K^+ \pi^-$ decay, shown in Fig. 16.1(a), proceeds via a charged current. Quark transitions without charge exchange, as it is the case for the penguin amplitude drawn in Fig. 16.1(b), are very interesting to study because these are not allowed in tree-level amplitudes. As the net charge does not change in these processes, they are called flavour-changing neutral currents (FCNC) and only proceed via a loop diagram. Figure 16.2 (a) shows the $b \to s$ transition in the Standard Model in which a $W^\pm$ boson is emitted and an up-type quark is exchanged.

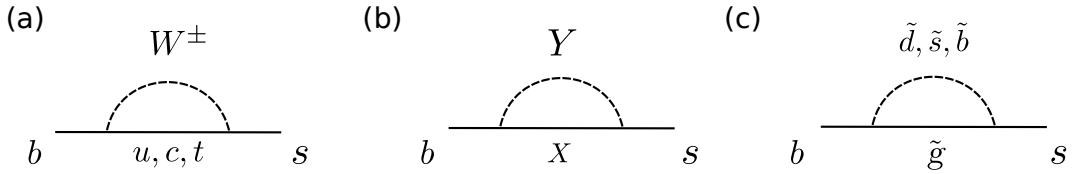

Figure 16.2: The skeleton $b \to s$ transition, a flavour-changing neutral current, in (a) the Standard Model; (b) with generic New Physics and (c) a possible MSSM amplitude with gluinos and squarks.

The Standard-Model amplitude, A, for a $b \to s$ transition is determined by the sum of all possible up-type quark flavours in the loop. Due to the high top mass, it is dominated by the top quark. However, this contribution is suppressed by four powers of the weak

coupling constant and two powers of the CKM element, $V_{ts} \approx 0.04$. Hence, even suppressed small New-Physics amplitudes might compete with it. Since the particles in the loop, as the W boson, are created virtually, new particles can contribute to the loop diagrams that are much heavier than the b-meson energy scale. It should be noted that the SM top quark is already much heavier. Figure 16.2 (b) shows possible Beyond-the-Standard-model (BSM) processes with model-independent generic particles X and Y and (c) gluinos and squarks from the MSSM model that might contribute to the overall $b \to s$ transition. Since these have not been confirmed in other experimental results, their amplitudes must be tiny but the fact that the SM amplitude is also suppressed makes FCNC processes so interesting. The New-Physics amplitude, A_{N}, can have a sizeable effect. Even if the absolute amplitude is small compared to the overwhelming SM amplitude, A_{SM}, it still appears in the interference terms of the absolute square of the total amplitude

$$|A|^2 = |A_{\mathrm{SM}} + A_{\mathrm{N}}|^2 = |A_{\mathrm{SM}}|^2 + A_{\mathrm{SM}}A_{\mathrm{N}}^* + A_{\mathrm{SM}}^* A_{\mathrm{N}} + |A_{\mathrm{N}}|^2 \tag{16.3}$$

that are sensitive to phase differences of the amplitudes. For this reason, phase differences are particularly sensitive to New-Physics contributions.

16.2.1 Mixing of neutral b mesons

Flavour-changing neutral currents occur in the mixing process of neutral mesons. Meson mixing describes the possible transitions from one meson-flavour state to the other through flavour-changing neutral currents. In the B_s^0 system, it is dominated by the so-called box diagrams shown in Fig. 16.3.[1]

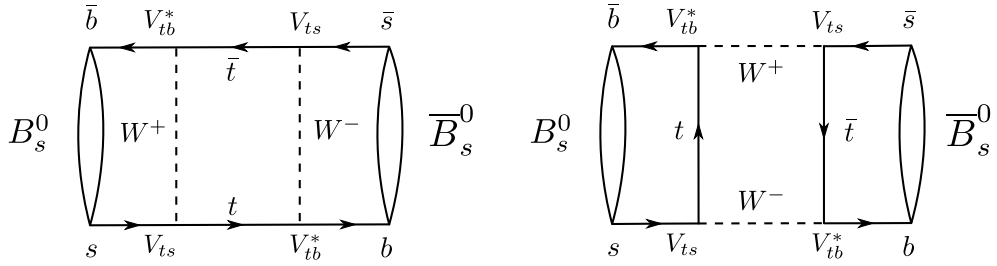

Figure 16.3: Leading-order B_s^0 mixing diagrams in the Standard Model.

The time-development of the initially-produced flavour states $|B_s^0\rangle$ and $|\overline{B}_s^0\rangle$ can be computed with a phenomenological time-dependent Schrödinger equation [73]

$$-\frac{\partial}{\partial t}\begin{pmatrix} |B_s^0\rangle \\ |\overline{B}_s^0\rangle \end{pmatrix} = \left(\mathbf{M} - \tfrac{\mathbf{i}}{\mathbf{2}}\mathbf{\Gamma}\right)\begin{pmatrix} |B_s^0\rangle \\ |\overline{B}_s^0\rangle \end{pmatrix} \tag{16.4}$$

with the hermitian mass matrix $\mathbf{M}$ and the hermitian decay matrix $\mathbf{\Gamma}$ in the Hamiltonian. The diagonal entries describe the masses and decay widths of the states and the off-diagonal

[1] The contributions from penguin diagrams are neglected.

elements are responsible for the transitions between them. M_{12} refers to the short-distance effects given in Fig. 16.3 whereas Γ_{12} describes long-distance effects where the mixing proceeds via real on-shell particles such as a pion pair. In the b-meson system, mixing is dominated by the short-distance effects and $|M_{12}| \gg |\Gamma_{12}|$. Assuming equal masses and decay widths of the particle and anti-particle according to the CPT theorem, it follows that $M_{11} = M_{22} = m_s$, $M_{21} = M_{12}^*$, $\Gamma_{11} = \Gamma_{22} = \Gamma_s$ and $\Gamma_{21} = \Gamma_{12}^*$. The phase of M_{12} is defined as the mixing phase

$$\phi_{\mathrm{M}} = \arg(M_{12}) \tag{16.5}$$

that is determined by the CKM elements V_{ts} and V_{tb}, $\phi_{\mathrm{M}} = \arg(V_{tb}V_{ts}^*)^2$ [74], as can be seen in the box diagram in Fig. 16.3.

The matrices are diagonalised and the eigenvalues are the masses, $M_{\mathrm{L/H}}$, and the decay widths, $\Gamma_{\mathrm{L/H}}$, so that the mass states are expressed as linear combinations of the flavour states

$$\begin{aligned} |B_{\mathrm{L}}\rangle &= p|B_s^0\rangle + q|\overline{B}_s^0\rangle \\ |B_{\mathrm{H}}\rangle &= p|B_s^0\rangle - q|\overline{B}_s^0\rangle \end{aligned}$$

with the normalisation condition $|p|^2 + |q|^2 = 1$. These parameters are related to the flavour eigenbasis by

$$\begin{aligned} m_s &= \frac{M_{\mathrm{H}} + M_{\mathrm{L}}}{2}, & \Gamma_s &= \frac{\Gamma_{\mathrm{L}} + \Gamma_{\mathrm{H}}}{2} \\ \Delta m_s &= M_{\mathrm{H}} - M_{\mathrm{L}}, & \Delta\Gamma_s &= \Gamma_{\mathrm{L}} - \Gamma_{\mathrm{H}}, \end{aligned}$$

where Δm_s is the mass difference and $\Delta\Gamma_s$ is decay width difference of the mass states. Experimentally, the most precise measurement of $\Delta m_s = 17.63 \pm 0.11\,\mathrm{ps}^{-1}$ [75], has been performed by LHCb using $B_s^0 \to D_s^-\pi^+$ decays. Using $B_s^0 \to J/\psi\,\phi$ and $B_s^0 \to J/\psi\,\pi^+\pi^-$ decays, Γ_s and $\Delta\Gamma_s$ have been measured at LHCb as $0.661 \pm 0.007\,\mathrm{ps}^{-1}$ and $0.106 \pm 0.013\,\mathrm{ps}^{-1}$, respectively [76]. The ratio of q/p is related to the off-diagonal matrix elements and can be approximated by expanding in Γ_{12}/M_{12} as [74]

$$\frac{q}{p} = \sqrt{\frac{M_{12}^* - \frac{i}{2}\Gamma_{12}^*}{M_{12} - \frac{i}{2}\Gamma_{12}}} \overset{|M_{12}| \gg |\Gamma_{12}|}{\approx} -e^{-\phi_{\mathrm{M}}}. \tag{16.6}$$

The mass states develop in time with

$$\begin{aligned} |B_{\mathrm{L}}\rangle(t) &= e^{-(iM_{\mathrm{L}} + \Gamma_{\mathrm{L}}/2)t}|B_{\mathrm{L}}\rangle \\ |B_{\mathrm{H}}\rangle(t) &= e^{-(iM_{\mathrm{H}} + \Gamma_{\mathrm{H}}/2)t}|B_{\mathrm{H}}\rangle, \end{aligned}$$

and the flavour states can be written as

$$\begin{aligned} |B_s^0\rangle(t) &= \frac{1}{2p}\left(e^{-(iM_{\mathrm{L}} + \Gamma_{\mathrm{L}}/2)t}|B_{\mathrm{L}}\rangle + e^{-(iM_{\mathrm{H}} + \Gamma_{\mathrm{H}}/2)t}|B_{\mathrm{H}}\rangle\right) \\ |\overline{B}_s^0\rangle(t) &= \frac{1}{2q}\left(e^{-(iM_{\mathrm{L}} + \Gamma_{\mathrm{L}}/2)t}|B_{\mathrm{L}}\rangle - e^{-(iM_{\mathrm{H}} + \Gamma_{\mathrm{H}}/2)t}|B_{\mathrm{H}}\rangle\right). \end{aligned} \tag{16.7}$$

Inserting the mass eigenstates, the amplitude to observe an initially-produced B_s^0 in the same flavour, in the so-called un-mixed state, at time t is computed as

$$\begin{aligned}\langle B_s^0|B_s^0(t)\rangle &= e^{-i(m_s-i\Gamma_s/2)t}\left[\cosh\frac{\Delta\Gamma_s t}{4}\cos\frac{\Delta m_s t}{2} - i\sinh\frac{\Delta\Gamma_s t}{4} sin\frac{\Delta m_s t}{2}\right] \\ &\overset{\Delta\Gamma_s\ll\Gamma}{\approx} e^{-i(m_s-i\Gamma_s/2)t}\ \cos\frac{\Delta m_s t}{2}\end{aligned} \tag{16.8}$$

and the amplitude that it is in the mixed state is

$$\begin{aligned}\langle \overline{B}_s^0|B_s^0(t)\rangle &= e^{-i(m_s-i\Gamma_s/2)t}\ \frac{q}{p}\left[-\sinh\frac{\Delta\Gamma_s t}{4}\cos\frac{\Delta m_s t}{2} - i\cosh\frac{\Delta\Gamma_s t}{4} sin\frac{\Delta m_s t}{2}\right] \\ &\overset{\Delta\Gamma_s\ll\Gamma}{\approx} e^{-i(m_s-i\Gamma_s/2)t}\ \frac{q}{p}\ i\sin\frac{\Delta m_s t}{2}.\end{aligned} \tag{16.9}$$

This is the reason why Δm_s is also called the mixing frequency. In the mixed amplitude, complex phases in the ratio p/q and in $i = e^{i\pi/2}$ are introduced. The CP-conjugate mixing amplitude is given by

$$\langle B_s^0|\overline{B}_s^0(t)\rangle \overset{\Delta\Gamma_s\ll\Gamma}{\approx} e^{-i(m_s-i\Gamma_s/2)t}\ \frac{p}{q}\ i\sin\frac{\Delta m_s t}{2}. \tag{16.10}$$

Comparing the CP-conjugate amplitudes, the sign of the strong phase difference $i = e^{i\pi/2}$ stays the same whereas the ratio q/p flips, so its phase is related to the weak phase, hence called the mixing phase ϕ_{M}.

16.3 Introduction to CP violation

There are three different types of CP violation that can, however, occur at the same time.

Direct CP violation

Direct CP violation, often called CP violation in decay, appears when the decay rates of the CP-conjugate processes $\Gamma(X \to f)$ and $\Gamma(\overline{X} \to \bar{f})$ with particle X and final CP-eigenstate f are not equal. It is defined by unequal decay amplitudes, $A_f = A(X \to f)$ and $\overline{A}_{\bar{f}} = A(\overline{X} \to \bar{f})$:

$$\left|\frac{\overline{A}_{\bar{f}}}{A_f}\right| \neq 1. \tag{16.11}$$

As mentioned before, direct CP violation occurs, for example, in $B^0 \to K^+\pi^-$ decays, first measured at Babar [72].

CP violation in mixing

CP violation in mixing of neutral mesons, X^0 and $\overline{X}^0$, is related to different transition probabilities $\Gamma(X^0 \to \overline{X}^0)$ and $\Gamma(\overline{X}^0 \to X^0)$. This leads to an excess of particles of one flavour when assuming no direct CP violation but equal X^0-$\overline{X}^0$ production. Using q and p

as introduced before, it is realised when

$$\frac{|q|}{|p|} \neq 1. \tag{16.12}$$

CP violation in mixing can be measured in semileptonic $B^0 \to X l^+ \mu\nu$ decays but the Standard-Model expectation of $\mathcal{O}(10^{-4})$ is very small.

CP violation in interference of mixing and decay

CP violation through interference between the decay and the decay after mixing is only possible when the two mixing states, X^0 and $\overline{X}^0$, can decay into the same final CP eigenstate, $f_{\rm CP}$, with the eigenvalue $\eta_{\rm CP} = \pm 1$. The amplitudes where X^0 directly decays into the final state, $X^0 \to f_{\rm CP}$, and where it first mixes, $X^0 \to \overline{X}^0 \to f_{\rm CP}$, interfere as it is illustrated for the B_s^0 meson with the red and blue colors in Fig. 16.4. The strong and weak mixing phases, $\delta_{\rm M} = \pi/2$ and $\phi_{\rm M}$, are the ones obtained from Eqs. 16.9 and 16.10 and the decay phases, $\phi_{\rm D}$ and $\delta_{\rm f}$, are decay-specific. This kind of CP violation was first discovered in the B^0 system in the decay $B^0 \to J/\psi\, K_s^0$.

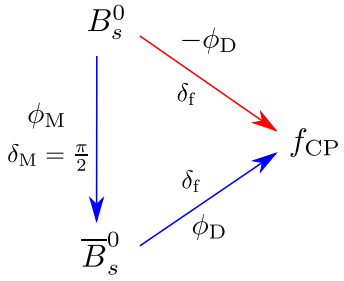

Figure 16.4: Illustration of interfering amplitudes (red and blue) contributing to CP violation in interference between the direct decay $B_s^0 \to f_{\rm CP}$, and the decay after mixing, $B_s^0 \to \overline{B}_s^0 \to f_{\rm CP}$.

Writing the decay amplitude of the decay $X^0 \to f_{\rm CP}$ as

$$A_{f_{\rm CP}} = |A_{f_{\rm CP}}|\, e^{i(\delta_f - \phi_{\rm D})} \tag{16.13}$$

with the strong phase $\delta_{\rm f}$ and the weak phase $\phi_{\rm D}$, the conjugate amplitude is written as

$$\overline{A}_{f_{\rm CP}} = \eta_{\rm CP} \overline{A}_{\bar{f}_{\rm CP}} = \eta_{\rm CP}\, |A_{f_{\rm CP}}|\, e^{i(\delta_{\rm f} + \phi_{\rm D})}. \tag{16.14}$$

Denoting the complex parameter

$$\lambda_{\rm CP} = \frac{q}{p} \frac{\overline{A}_{f_{\rm CP}}}{A_{f_{\rm CP}}} \approx -\eta_{\rm CP} e^{-i(\phi_{\rm M} - 2\phi_{\rm D})}, \tag{16.15}$$

CP violation through interference between the decay and the decay after mixing is defined by

$$Im(\lambda_{\rm CP}) \neq 0. \tag{16.16}$$

Both phases ϕ_{M} and ϕ_{D} depend on the convention of the CKM matrix but the ratio λ_{CP} does not. Its phase can be expressed as the phase difference

$$\phi_s = \phi_{\mathrm{M}} - 2\phi_{\mathrm{D}}, \tag{16.17}$$

which is an observable quantity. Experimentally, CP violation through interference between the decay and the decay is measured by determining the time-dependent decay asymmetry

$$a(t) = \frac{\Gamma(\overline{X} \to f_{\mathrm{CP}})(t) - \Gamma(X \to f_{\mathrm{CP}})(t)}{\Gamma(\overline{X} \to f_{\mathrm{CP}})(t) + \Gamma(X \to f_{\mathrm{CP}})(t)}. \tag{16.18}$$

16.3.1 Time-dependent decay rate for $B_s^0 \to f_{\mathrm{CP}}$

When B_s^0 and $\overline{B}_s^0$ mesons decay into the final CP eigenstate f_{CP} and no CP violation in mixing is assumed ($\frac{|q|}{|p|} = 1$), the time-dependent decay rates are written as [74],

$$\begin{aligned}\frac{d\Gamma(B_s^0 \to f_{\mathrm{CP}})}{dtN_f} &= |A_{\mathrm{CP}}|^2 \; e^{-\Gamma_s t}\frac{1}{1+C}\Bigg[\cosh\frac{\Delta\Gamma_s t}{2} \; + \; D\eta_{\mathrm{CP}} \; \sinh\frac{\Delta\Gamma_s t}{2} \\ &\qquad + C \; \cos(\Delta m_s t) \; - \; S\eta_{\mathrm{CP}} \; \sin(\Delta m_s t)\Bigg], \end{aligned} \tag{16.19}$$

$$\begin{aligned}\frac{d\Gamma(\overline{B}_s^0 \to f_{\mathrm{CP}})}{dtN_f} &= |A_{\mathrm{CP}}|^2 \; e^{-\Gamma_s t}\frac{1}{1+C}\Bigg[\cosh\frac{\Delta\Gamma_s t}{2} \; + \; D\eta_{\mathrm{CP}} \; \sinh\frac{\Delta\Gamma_s t}{2} \\ &\qquad - C \; \cos(\Delta m_s t) \; + \; S\eta_{\mathrm{CP}} \; \sin(\Delta m_s t)\Bigg], \end{aligned} \tag{16.20}$$

with the decay amplitude $A_{\mathrm{CP}} = A(B_s^0 \to f_{\mathrm{CP}})$ and a time-dependent normalisation factor N_f. The terms C, S and D are defined as

$$C = \frac{1-|\lambda_{\mathrm{CP}}|^2}{1+|\lambda_{\mathrm{CP}}|^2}, \qquad S = -\frac{2|\lambda_{\mathrm{CP}}|}{1+|\lambda_{\mathrm{CP}}|^2} \; \sin\phi_s, \qquad D = -\frac{2\,|\lambda_{\mathrm{CP}}|}{1+|\lambda_{\mathrm{CP}}|^2} \; \cos\phi_s. \tag{16.21}$$

The difference between the two decay rates is introduced by a non-trivial CP-violating phase ϕ_s that is obtained from the measured time-dependent decay asymmetry. The decay rates are basically exponential decay functions that are modulated by the mixing oscillation with the frequency Δm_s and the amplitude $\sin\phi_s$. For the considered decays, $|\lambda_{\mathrm{CP}}|$ is expected to be close to one as no direct CP violation is assumed to occur for the considered decays. As the CP-violating phase ϕ_s is sensitive to New-Physics contributions to the loop-suppressed mixing and decay amplitudes, it is the main physics observable of the presented analysis.

16.3.2 CP-violating phase ϕ_s in $B_s^0 \to J/\psi\,\phi$ and $B_s^0 \to J/\psi\,\pi^+\pi^-$ decays

In the tree-level diagram of the decays $B_s^0 \to J/\psi\,\phi$ and $B_s^0 \to J/\psi\,\pi^+\pi^-$, shown in Fig. 16.5, the $b \to c$ transition proceeds via the emittance of a W boson. The $c\bar{c}$ quark pair hadronises to become a J/ψ and the $s\bar{s}$ final state forms a ϕ meson or an $f_{0/2}$ resonance that can

decay into two pions.

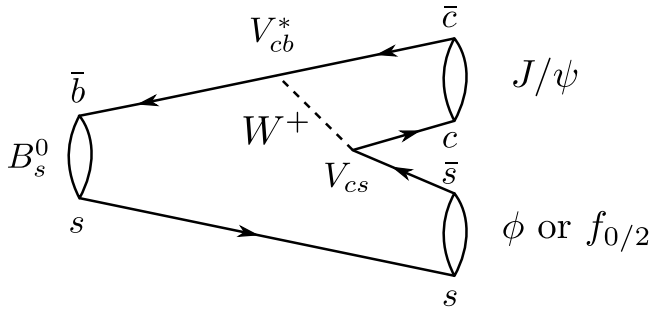

Figure 16.5: Tree-level Feynman diagram of the decays $B_s^0 \to J/\psi\,\phi$ and $B_s^0 \to J/\psi\, f_{0/2}(\to \pi^+\pi^-)$.

Neglecting higher-order penguin diagrams, the decay amplitude, A_f, is proportional to the CKM matrix elements V_{cs} and V_{cb}^* that do not have a complex phase in the chosen convention. Therefore, the observable CP-violating phase difference, $\phi_s(J/\psi\,\phi) = \phi_{\rm M} - 2\phi_{\rm D}(J/\psi\,\phi) = 2\ \arg(V_{ts}^* V_{tb}) - 2\ \arg(V_{cb} V_{cs}^*)$ is equal to $-2\beta_s$. In a combined analysis of these decay modes, the CP-violating phase is determined as $\phi_s(J/\psi\,\phi) = 0.01 \pm 0.07 \pm 0.01$ rad [76] which is compatible with the Standard-Model expectation value of $\phi_s^{\rm SM}(J/\psi\,\phi)$ = -0.0363 ± 0.0013 rad [22].

16.4 CP violation in $B_s^0 \to \phi\phi$ decays

In parallel to the afore-described measurements, other decay modes are investigated that offer a different dependence on New-Physics contributions through additional quantum loops. The decay $B_s^0 \to \phi\phi$ can only proceed via a rare penguin process, a loop diagram that is given in Fig. 16.6. The penguin can be formed by a gluonic loop in (a) where the top quark emits a gluon that splits into an $s - \bar{s}$ quark pair. It can also proceed via an electroweak penguin diagram, shown in (b), where the top quark emits a Z or a γ boson.

Thus, the measurement of CP violation in this decay channel is not only sensitive to New-Physics contributions in mixing, but additionally to possible new effects in the quantum corrections of the loop-suppressed decay amplitude that is mediated via a gluon, a Z boson or a γ. Therefore, the observed CP-violating phase $\phi_s(\phi\phi)$ differs from $\phi_s(J/\psi\,\phi)$ and is sensitive to the presence of additional new phenomena as it is sketched in Fig. 16.7. Considering the CKM matrix elements for this decay, the weak phase $\phi_{\rm D}$ is related as $\phi_{\rm D}(\phi\phi) = \arg(V_{tb}^* V_{ts})$ which are exactly the same elements present in the mixing diagram in Fig. 16.3. For this reason, the Standard-Model expectation value for the CP-violating phase $\phi_s(\phi\phi)$, further simply denoted as ϕ_s, vanishes. A calculation using QCD factorisation

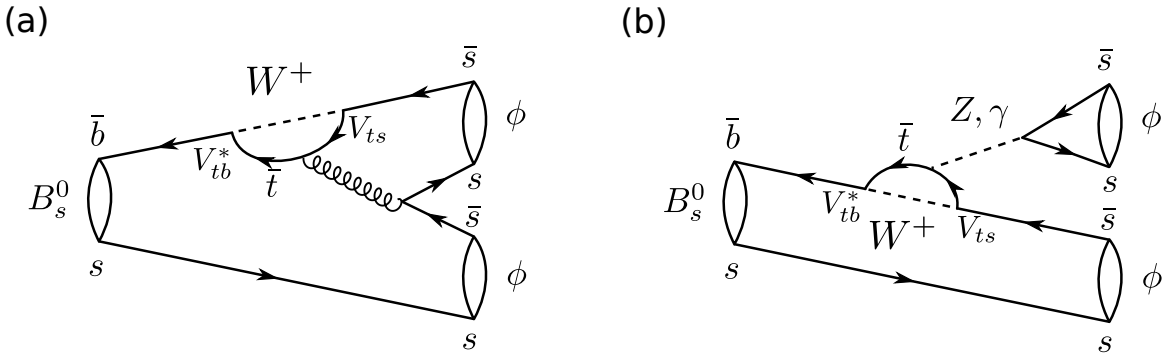

Figure 16.6: Loop-induced Feynman diagram of the penguin decay $B_s^0 \to \phi\phi$ via the emission of a (a) gluon and (b) a Z or a γ boson.

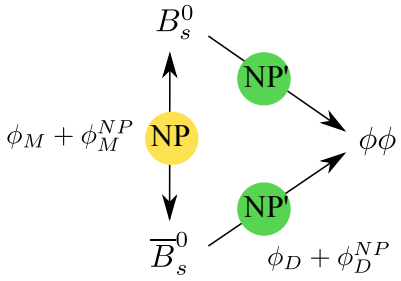

Figure 16.7: Illustration of CP violation in interference between the direct decay $B_s^0 \to \phi\phi$, and the decay after mixing, $B_s^0 \to \overline{B}_s^0 \to \phi\phi$ with possible New-Physics contributions to (yellow) the box-diagram of mixing and (green) the penguin diagram of the decay.

gives a theoretical upper limit on the SM value of 0.02 [77, 78]:

$$\phi_s^{\mathrm{SM}}(\phi\phi) = \phi_{\mathrm{M}} - 2\phi_{\mathrm{D}}(\phi\phi) = 0.00 \pm 0.02. \tag{16.22}$$

Any significant observed CP violation, larger than the theoretical uncertainty of 0.02, would indicate the existence of new particles and couplings [79–81].

16.4.1 Determination of the CP eigenstates of the final state $\phi\phi$

The general decay rates for a B_s^0 and $\overline{B}_s^0$ meson into a final CP eigenstate f_{CP} are given in Eq.s 16.19 and 16.20. In the decay $B_s^0 \to \phi\phi$, a pseudo-scalar meson with spin 0 decays into two vector mesons with spin 1 (P-wave state). To conserve the initial spin $\mathbf{J} = 0$, the final-state mesons can have a relative angular momentum l of 0, 1 and 2. The final CP

eigenvalue η_{CP} is related to the angular momentum via

$$\eta_{\mathrm{CP}} = (\eta_\phi)^2 \cdot (-1)^l = (-1)^l. \tag{16.23}$$

Thus, the final state is not a pure CP eigenstate but a mixture of CP-even ($l = 0,\ 2$) and CP-odd ($l = 1$) eigenstates that have to be separated in an angular analysis. Each angular momentum is related to an angular polarisation as it is shown in Fig. 16.8. $A_0(t)$ corresponds to the longitudinal polarisation of the mesons. $A_\perp(t)$ and $A_{||}(t)$ are related to the transverse polarisations, where for $A_\perp$, the polarisation vectors are perpendicular and for $A_{||}$, they are parallel. At time t = 0, the CP-even part is formed by A_0 and $A_{||}$ and the CP-odd part by $A_\perp$.

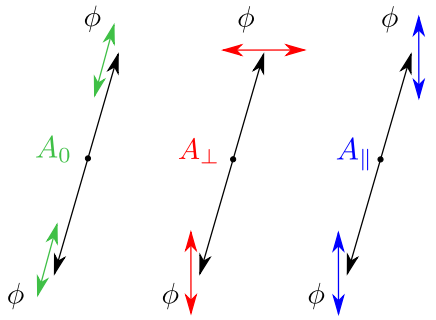

Figure 16.8: Illustration of the angular amplitudes A_0, $A_\perp$ and $A_{||}$ referring to the relative angular momentum l of 0, 1, 2.

In the experiment, the ϕ mesons are reconstructed in the decay $\phi \to K^+K^-$. The decay topology is described in a basis of three angles where the observable amplitudes are independent of the choice of the basis. The so-called helicity basis, $(\theta_1, \theta_2, \Phi)$, is defined in Fig. 16.9. The K^+ momentum in the $\phi_{1,2}$ rest frame, and the parent $\phi_{1,2}$ momentum in the rest frame of the B_s^0 meson span the two ϕ-meson decay planes. $\theta_{1,2}$ is the angle between the K^+ momentum in the $\phi_{1,2}$-meson rest frame and the parent $\phi_{1,2}$ momentum in the B_s^0 rest frame. Φ is the angle between the two ϕ-meson decay planes and $\hat{n}_{1,2}$ is the unit vector normal to the decay plane of the $\phi_{1,2}$ meson. The angles θ_1 and θ_2 correspond to the angle between the K^+ and the flight direction of the ϕ meson in the rest frame of the ϕ meson. In this analysis, the choice of which ϕ meson is used to determine θ_1 and which is used to determine θ_2 is randomised.

Using the helicity basis, the total decay amplitude $A(t, \theta_1, \theta_2, \Phi)$ is written as the summed amplitude of the angular eigenstates as [82]

$$\begin{aligned} A(t, \theta_1, \theta_2, \Phi) = \quad & A_0(t)\ \cos\theta_1\ \cos\theta_2 \\ & + \frac{A_{||}(t)}{\sqrt{2}}\ \sin\theta_1\ \sin\theta_2 \cos\Phi + i\ \frac{A_\perp(t)}{\sqrt{2}}\ \sin\theta_1\ \sin\theta_2 \sin\Phi. \end{aligned} \tag{16.24}$$

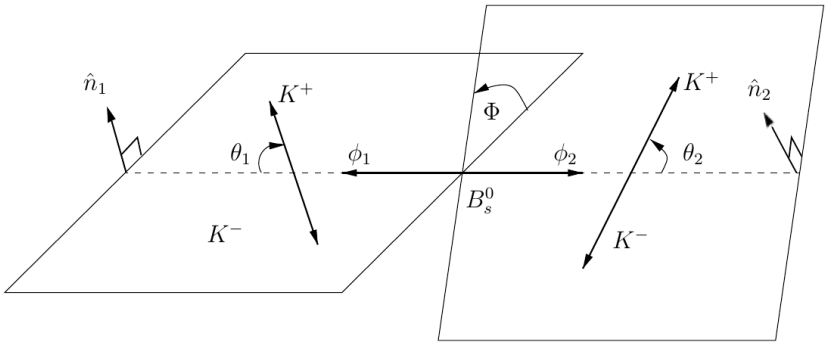

Figure 16.9: Definition of the decay angles of the decay $B_s^0 \to \phi\phi$ in the helicity basis, taken from Ref. [2].

The total differential decay rate is computed as the absolute square of the decay amplitude

$$\frac{\mathrm{d}\Gamma}{\mathrm{dt}\ \mathrm{dcos}\theta_1\ \mathrm{dcos}\theta_2\ \mathrm{d}\Phi} \propto |A(t,\theta_1,\theta_2,\Phi)|^2 = \sum_{i=1}^{6} \mathrm{K}_i(t)\ \mathrm{f}_i(\theta_1,\theta_2,\Phi), \tag{16.25}$$

where the six terms are composed of three squared angular amplitudes and three interference terms. The time-dependent functions $\mathrm{K}_i(t)$ are similar to the decay rates of Eqs. 16.19 and 16.20 and are given by

$$K_i(t) = N_i e^{-\Gamma_s t}\frac{1}{1+C}[c_i\cos(\Delta m_s t) + d_i\sin(\Delta m_s t) + a_i\cosh(\frac{1}{2}\Delta\Gamma_s t) + b_i\sinh(\frac{1}{2}\Delta\Gamma_s t)]. \tag{16.26}$$

The functions $\mathrm{f}_i(\theta_1,\theta_2,\Phi)$ are purely geometrical angular functions. All the coefficients are given in Table 16.1, where the strong phase differences are defined as $\delta_1 := \delta_\perp - \delta_\parallel$ and $\delta_2 := \delta_\perp - \delta_0$ and $\delta_{2,1} = \delta_2 - \delta_1 = \delta_\parallel$. The coefficients C, S and D are defined as above. To compute the decay rate of a $\overline{B}_s^0$ decaying into two ϕ mesons, the coefficients c_i and d_i are replaced by $-c_i$ and $-d_i$, respectively.

16.4.2 Contribution from K^+K^- in an S-wave state

Experimentally, the $B_s^0 \to \phi\phi$ decay is reconstructed in the most abundant ϕ-meson decay mode into two kaons leading to a final state with four kaons. However, the B_s^0 decay can also proceed via a non-resonant mode or a different intermediate resonance like the $f_0(980)$ for which the kaon pair is in a spin-0 state. This S-wave component has to be disentangled from the P-wave state in the angular analysis. Besides the S-wave component, defined by a $B_s^0 \to \phi(K^+K^-)_S$ decay where one kaon pair is in an S-wave state, both pairs can also be simultaneously found in an S-wave state leading to an SS-wave component, $B_s^0 \to (K^+K^-)_S(K^+K^-)_S$. The additional contributions of the S-wave and SS-wave

Table 16.1: Coefficients of the time-dependent terms and angular functions used in Eq.s 16.25 and 16.26. Amplitudes are defined at $t = 0$.

i	N_i	a_i	b_i	c_i	d_i	f_i
1	$\|A_0\|^2$	1	D	C	$-S$	$4\cos^2\theta_1\cos^2\theta_2$
2	$\|A_\parallel\|^2$	1	D	C	$-S$	$\sin^2\theta_1\sin^2\theta_2(1+\cos 2\Phi)$
3	$\|A_\perp\|^2$	1	$-D$	C	S	$\sin^2\theta_1\sin^2\theta_2(1-\cos 2\Phi)$
4	$\|A_\parallel\|\|A_\perp\|$	$C\sin\delta_1$	$S\cos\delta_1$	$\sin\delta_1$	$D\cos\delta_1$	$-2\sin^2\theta_1\sin^2\theta_2\sin 2\Phi$
5	$\|A_\parallel\|\|A_0\|$	$\cos\delta_{2,1}$	$D\cos\delta_{2,1}$	$C\cos\delta_{2,1}$	$-S\cos\delta_{2,1}$	$\sqrt{2}\sin 2\theta_1\sin 2\theta_2\cos\Phi$
6	$\|A_0\|\|A_\perp\|$	$C\sin\delta_2$	$S\cos\delta_2$	$\sin\delta_2$	$D\cos\delta_2$	$-\sqrt{2}\sin 2\theta_1\sin 2\theta_2\sin\Phi$

amplitudes, A_S and A_{SS}, to the total decay amplitude are given by [82]

$$A_{S/SS}(t,\theta_1,\theta_2,\Phi) = \frac{A_S(t)}{\sqrt{3}}\,(\cos\theta_1+\cos\theta_2) + \frac{A_{SS}(t)}{3}. \tag{16.27}$$

After adding these terms to the signal P-wave contribution, the total decay rate

$$\frac{\mathrm{d}\Gamma}{\mathrm{dt}\ \mathrm{dcos}\theta_1\ \mathrm{dcos}\theta_2\ \mathrm{d}\Phi} \propto |A(t,\theta_1,\theta_2,\Phi)|^2 = \sum_{i=1}^{15} \mathrm{K}_i(t)\ \mathrm{f}_i(\theta_1,\theta_2,\Phi) \tag{16.28}$$

exhibits 15 terms: the 6 P-wave terms for which the coefficients were given previously in Table 16.1, the S-wave and SS-wave terms with interferences between them in lines 7-9 of Table 16.2, the interference terms of SS-wave and P-wave terms in lines 10-12 and the interference terms of S-wave and P-wave terms in lines 13-15. In the following, the expression $B_s^0 \to \phi\phi$ denotes both the P-wave and the S-wave and SS-wave contributions and their interferences to the decay. The S-wave and SS-wave contributions are simply referred to as the S-wave contribution. Only if necessary, the components will be distinguished distinctly.

Defining the flavour of the meson as $q = 1$ for a B_s^0 meson and $q =$ -1 for a $\overline{B}_s^0$ meson, the total decay rate is defined as the sum of the decay rates of the produced B_s^0 and $\overline{B}_s^0$ mesons:

$$s(t,\Omega|\vec{a}) = \frac{(1+q)}{2}\frac{\mathrm{d}\Gamma(B_s^0\to\phi\phi)}{\mathrm{d}t\mathrm{d}\Omega} + \frac{(1+q)}{2}\frac{\mathrm{d}\Gamma(\overline{B}_s^0\to\phi\phi)}{\mathrm{d}t\mathrm{d}\Omega}, \tag{16.29}$$

where $\vec{a}$ is the set of physics parameters. The total differential decay rates of the produced B_s^0 and $\overline{B}_s^0$ mesons are also denoted as $\mathcal{P}_{B_s^0}(t,\Omega|\vec{a})$ and $\mathcal{P}_{\overline{B}_s^0}(t,\Omega|\vec{a})$, implying that these are normalised PDFs.

Table 16.2: Coefficients of the time-dependent terms and angular functions used in equation 16.28. Amplitudes are defined at $t = 0$.

i	N_i	a_i	b_i	c_i	d_i	f_i
7	$\lvert A_{SS}\rvert^2$	1	D	C	$-S$	$\frac{4}{9}$
8	$\lvert A_S\rvert^2$	1	$-D$	C	S	$\frac{4}{3}(\cos\theta_1 + \cos\theta_2)^2$
9	$\lvert A_S\rvert\lvert A_{SS}\rvert$	$C\cos(\delta_S - \delta_{SS})$	$S\sin(\delta_S - \delta_{SS})$	$\cos(\delta_{SS} - \delta_S)$	$D\sin(\delta_{SS} - \delta_S)$	$\frac{8}{3\sqrt{3}}(\cos\theta_1 + \cos\theta_2)$
10	$\lvert A_0\rvert\lvert A_{SS}\rvert$	$\cos\delta_{SS}$	$D\cos\delta_{SS}$	$C\cos\delta_{SS}$	$-S\cos\delta_{SS}$	$\frac{8}{3}\cos\theta_1\cos\theta_2$
11	$\lvert A_\parallel\rvert\lvert A_{SS}\rvert$	$\cos(\delta_{2,1} - \delta_{SS})$	$D\cos(\delta_{2,1} - \delta_{SS})$	$C\cos(\delta_{2,1} - \delta_{SS})$	$-S\cos(\delta_{2,1} - \delta_{SS})$	$\frac{4\sqrt{2}}{3}\sin\theta_1\sin\theta_2\cos\Phi$
12	$\lvert A_\perp\rvert\lvert A_{SS}\rvert$	$C\sin(\delta_2 - \delta_{SS})$	$S\cos(\delta_2 - \delta_{SS})$	$\sin(\delta_2 - \delta_{SS})$	$D\cos(\delta_2 - \delta_{SS})$	$-\frac{4\sqrt{2}}{3}\sin\theta_1\sin\theta_2\sin\Phi$
13	$\lvert A_0\rvert\lvert A_S\rvert$	$C\cos\delta_S$	$-S\sin\delta_S$	$\cos\delta_S$	$-D\sin\delta_S$	$\frac{8}{\sqrt{3}}\cos\theta_1\cos\theta_2$ $\times(\cos\theta_1 + \cos\theta_2)$
14	$\lvert A_\parallel\rvert\lvert A_S\rvert$	$C\cos(\delta_{2,1} - \delta_S)$	$S\sin(\delta_{2,1} - \delta_S)$	$\cos(\delta_{2,1} - \delta_S)$	$D\sin(\delta_{2,1} - \delta_S)$	$\frac{4\sqrt{2}}{\sqrt{3}}\sin\theta_1\sin\theta_2$ $\times(\cos\theta_1 + \cos\theta_2)\cos\Phi$
15	$\lvert A_\perp\rvert\lvert A_S\rvert$	$\sin(\delta_2 - \delta_S)$	$-D\sin(\delta_2 - \delta_S)$	$C\sin(\delta_2 - \delta_S)$	$S\sin(\delta_2 - \delta_S)$	$-\frac{4\sqrt{2}}{\sqrt{3}}\sin\theta_1\sin\theta_2$ $\times(\cos\theta_1 + \cos\theta_2)\sin\Phi$

Mass-dependent interference of S- and P-wave amplitudes

In the afore-described total differential decay rate, the mass dependence of the individual amplitudes A_i is neglected for simplicity. However, the P-wave signal contribution is larger for kaon pairs with an invariant mass that is closer to the known ϕ-meson mass. The S-wave component is assumed to be rather uniform in the di-kaon mass. Hence, also the interference of S- and P-wave amplitudes must be smaller as a consequence. This could be accounted for by parameterising the mass dependence of the amplitudes in the angular PDF. Instead, this analysis is performed in intervals of the di-kaon mass of the ϕ-meson candidates which gives rise to effective coupling factors, $C_{\rm SP}$, of the S- and P-wave amplitudes. The effect of using a finite m_{KK} range, $[\mu_l, \mu_h]$, can be incorporated through making the substitutions [83]

$$\begin{aligned} |A_i(\mu)|^2 \to \int_{\mu_l}^{\mu_h} |A_i(\mu)|^2 \mathrm{d}\mu \quad &\to \int_{\mu_l}^{\mu_h} |a_i g_i(\mu)|^2 \mathrm{d}\mu \quad \text{for } \; i \in \{\|, \perp, 0, S, SS\}, \\ A_i^*(\mu) A_j^*(\mu) \to \int_{\mu_l}^{\mu_h} A_i^*(\mu) A_j^*(\mu) \mathrm{d}\mu \quad &\to \int_{\mu_l}^{\mu_h} a_i g_i^*(\mu) a_j g_j(\mu) \mathrm{d}\mu \qquad \text{for } \; i \neq j, \end{aligned} \tag{16.30}$$

where the functions $g_i(\mu)$ are normalised to the mass interval, $\int_{\mu_l}^{\mu_h} g_i(\mu)\mathrm{d}\mu = 1$, and the coefficients refer to the integrated amplitudes over the mass interval, $a_i = \int_{\mu_l}^{\mu_h} A_i(\mu)\mathrm{d}\mu$. The effective coupling parameter $C_{\rm SP}$ and its phase $\theta_{\rm SP}$ are defined by the equation

$$\int_{\mu_l}^{\mu_h} g_{\rm P}^*(\mu) g_{\rm S}(\mu) \mathrm{d}\mu \equiv C_{\rm SP} e^{i\theta_{\rm SP}}. \tag{16.31}$$

Due to the resonant structure of the P-wave component, $g_{\rm P}(\mu)$ is known to be a Breit-Wigner function. The non-resonant production of a kaon pair decreases gradually with the mass due to reduction of the available phase space, but within a small mass interval, the mass dependence of the S-wave component is assumed to be uniform:

$$g_{\rm P}(\mu) = \sqrt{\frac{\Gamma_\phi/2}{\Delta\lambda}} \cdot \frac{1}{\mu - \mu_\phi + i\Gamma_\phi/2}, \tag{16.32}$$

$$g_{\rm S}(\mu) = \sqrt{\frac{1}{\Delta\mu}}, \tag{16.33}$$

where

$$\Delta\lambda = \tan^{-1}\frac{2(\mu_h - \mu_\phi)}{\Gamma_\phi} - \tan^{-1}\frac{2(\mu_l - \mu_\phi)}{\Gamma_\phi}. \tag{16.34}$$

Whereas the mass dependence of the P-wave component is fully described by the Breit-Wigner, the amplitude and the phase of the S-wave component can be different for each mass interval. Thus, the S-wave and SS-wave amplitudes and phases have to be determined for each mass interval separately.

The effective coupling parameter $C_{\rm SP}$ becomes one for a very small mass region, but this would lead to an increasing number of independent S-wave parameters. The coupling factors for a single wide ϕ-meson mass region and when dividing it into a lower and an

upper region are given in Table 16.3. When assuming that the S-wave component originates from the decay of the $f_0(980)$ meson, the mass dependence of the S-wave amplitude can be parameterised by a Flatté function that was shown to be suitable in Ref. [84]. The resulting coupling factors are slightly smaller and are tabulated in the third column.

Table 16.3: Coupling factors between the S-wave and P-wave based on a flat S-wave model and a Flatté function describing the $f_0(980)$ resonance.

	C_{SP}	
$m_{K^+K^-}$ Range [MeV/c^2]	flat S-wave	$f_0(980)$
$[994.455, 1044.455]$	0.36	0.34
$[994.455, 1019.455]$	0.69	0.63
$[1019.455, 1044.455]$	0.69	0.68

16.5 New-Physics contributions to ϕ_s

As already mentioned, physics effects beyond the description of the Standard Model can be introduced by additional contributions to the box diagram of B_s^0 mixing in Fig. 16.3 and to the loop-induced penguin diagram of Fig. 16.6. New phenomena manifest themselves in changing the magnitude of the mixing phase ϕ_{M} and the weak decay phase ϕ_{D}, respectively. This can be parameterised in a largely model-independent way through the introduction of an additional phase $\phi_{\mathrm{s}}^{\Delta}$. As a consequence, the Standard-Model expectation ϕ_s^{SM} is shifted as [73]

$$\phi_s = \phi_s^{\mathrm{SM}} + \phi_{\mathrm{s}}^{\Delta}. \tag{16.35}$$

In the decay mode $B_s^0 \to J/\psi\,\phi$, the CP-violating phase $\phi_s(J/\psi\,\phi)$ has been determined to be compatible with the SM expectation [76] which sets strong limits on New-Physics contributions in mixing. However, the CP-violating phase $\phi_s(\phi\phi)$ in the decay $B_s^0 \to \phi\phi$ is sensitive to deviations of the SM mixing and decay amplitudes such that a significant non-trivial value might indicate New-Physics contributions to the decay amplitudes. Within the framework of Supersymmetry, Ref. [80] indicates considerably larger CP asymmetries for $B_s^0 \to \phi\phi$ decays than for $B_s^0 \to J/\psi\,\phi$ decays due to contributions from squarks and gluinos to the flavour-changing $b \to s$ transition. A model-independent analysis is performed in Ref. [81]. This direct sensitivity to New Physics contributions represents a strong incentive to determine $\phi_s(\phi\phi)$.

16.6 Experimental status of $B_s^0 \to \phi\phi$ decays

In 2008, the CDF Collaboration presented the first evidence for the $B_s^0 \to \phi\phi$ decay and measured a branching ratio of $\mathcal{B}(B_s^0 \to \phi\phi)$ of $(14^{+6}_{-5}(\mathrm{stat}) \pm 6(\mathrm{syst})) \times 10^{-6}$ [85]. The polarisation amplitudes were determined as $|A_0|^2 = 0.348 \pm 0.041 \pm 0.021$, $|A_{\|}|^2 = 0.287 \pm 0.043 \pm 0.011$ and $|A_{\perp}|^2 = 0.365 \pm 0.044 \pm 0.027$ [86]. Measurements of triple product asymmetries of the decay angle distributions that are sensitive to CP violation, revealed central values of A_u = -0.007 $\pm$ 0.064 $\pm$ 0.018 and $A_v = 0.120 \pm 0.064 \pm 0.016$ of which the latter deviates from Standard-Model expectations of zero, but with large uncertainties [86].

The first measurement of the CP-violating phase $\phi_s(\phi\phi)$ has been performed at LHCb with the 7 TeV dataset collected in 2011. Due to limited statistics of 880 signal decays, it was only possible to obtain limits on the allowed parameter range. The phase is measured to be in the large interval $[-2.46, -0.76]$ rad at a 68% confidence level [71]. The polarisation amplitudes are determined as $|A_0|^2$= 0.365 ± 0.022 ± 0.012 and $|A_\perp|^2$= 0.291 ± 0.024 ± 0.010 [87] [2]. The measured central values of the triple product asymmetries of A_u = -0.055 ± 0.036 ± 0.018 and A_v = 0.010 ± 0.036 ± 0.018 are in agreement with those reported by the CDF Collaboration and consistent with the hypothesis of CP conservation [87].

16.7 Simulated event samples

As described in Sec. 3.5, fully simulated $B_s^0 \to \phi\phi$ decays are needed to optimise the signal selection and assess reconstruction artefacts of the detector. The generated samples of simulated decays consist of in total four million events that are equally distributed over the 7 TeV and 8 TeV centre-of-mass energies of the LHC Run I data and magnet-up and magnet-down configurations. These are restricted to the P-wave signal component with both of the ϕ mesons in the spin-1 state. The physics parameters used for the MC generator are tabulated in Table 16.4. The polarisation amplitudes are set to the values measured by the CDF Collaboration [86] and no CP violation is generated.

Table 16.4: Values of the physics parameters used in the generation of the fully simulated decay samples.

Parameter	Value
$\lvert A_0\rvert^2$	0.348
$\lvert A_\parallel\rvert^2$	0.287
$\lvert A_\perp\rvert^2$	0.365
δ_0	0.0
$\delta_\parallel$	2.71 rad
$\delta_\perp$	2.39 rad
ϕ_s	0.0 rad

[2] The amplitude $|A_\parallel|^2$is given by $|A_\parallel|^2$= $(1-|A_0|^2-|A_\perp|^2)$

17 Analysis Strategy

The CP violation parameters, ϕ_s and $|\lambda_{\rm CP}|$, in $B_s^0 \to \phi\phi$ decays are obtained from the measured time-dependent decay asymmetry of the B_s^0 and $\overline{B}_s^0$ mesons. Due to five possible polarisation amplitudes, the theoretical $B_s^0 \to \phi\phi$ decay rates, introduced in Chap. 16, are given by the sum of 15 terms of which 10 are interference terms. Each term can be split into a time-dependent function $K_i(t)$ and a geometrical angular-dependent function $\mathrm{f}_i(\theta_1, \theta_2, \Phi)$:

$$\frac{\mathrm{d}\Gamma}{\mathrm{dt}\ \mathrm{dcos}\theta_1\ \mathrm{dcos}\theta_2\ \mathrm{d}\Phi} \propto |A(t, \theta_1, \theta_2, \Phi)|^2 = \sum_{i=1}^{15} \mathrm{K}_i(t)\ \mathrm{f}_i(\theta_1, \theta_2, \Phi). \tag{17.1}$$

The time-dependent parts, $K_i(t)$, are formed by exponential decay functions modulated by the B_s^0 oscillation frequency. The first term is exemplary given by

$$K_1(t) \propto \quad e^{-\Gamma_s t} \Big[\ q\ \frac{1 - |\lambda_{\rm CP}|^2}{1 + |\lambda_{\rm CP}|^2} \cos(\Delta m_s t)\ +\ q\ \frac{2|\lambda_{\rm CP}|}{1 + |\lambda_{\rm CP}|^2} \sin\phi_s \sin(\Delta m_s t) \tag{17.2}$$

$$+\ \cosh(\frac{1}{2}\Delta\Gamma_s t)\ -\ \frac{2|\lambda_{\rm CP}|}{1 + |\lambda_{\rm CP}|^2} \cos\phi_s \sinh(\frac{1}{2}\Delta\Gamma_s t)\ \Big], \tag{17.3}$$

where q denotes the initial flavour of the Bs meson at production[1]. In order to extract ϕ_s and $|\lambda_{\rm CP}|$, the theoretical decay rates are fitted simultaneously to the measured B_s^0 and $\overline{B}_s^0$ decay-time and angular distributions. The measurement is performed in the following steps:

- The two ϕ mesons are reconstructed using their most abundant decay modes into a charged kaon pair. The calorimeter signals are processed by the hardware trigger system to find hadrons with large transverse momenta that are later identified as kaons with the RICH detectors. The B_s^0 signal candidates are selected by exploiting the characteristic decay topology of b mesons that decay significantly away from the primary vertex. Combinatorial background is identified in a fit to the invariant mass distribution of the B_s^0 signal candidates. Background contributions from other b-hadron decays occur when a pion or a proton track is falsely identified as a kaon. Their absolute yields are investigated by explicitly reconstructing these background decays.

- The finite resolution of the decay-time measurement leads to a dilution of the B_s^0-$\overline{B}_s^0$ oscillation which has to be correctly modelled in the fit. The decay-time resolution of the detector depends on the kinematics of the final-state particles and is extracted from fully simulated signal events.

[1] $q = 1$ refers to a B_s^0 and $q = -1$ for a $\overline{B}_s^0$

- Due to the reconstruction and selection process and the detector acceptance, the measured decay-time and angular distributions deviate from the actual distributions. The decay-time acceptance describes the efficiency of reconstructing and selecting the signal decays as a function of the decay time and is determined using the well-known calibration channel $B_s^0 \to D_s^- \pi^+$. The angular acceptance corresponds to the geometrical efficiency of the detector as a function of the decay angles and is obtained from fully simulated signal events.

- To determine the B_s^0-$\overline{B}_s^0$ oscillation in time, the knowledge of the initial production flavour, q, of the reconstructed b meson is essential. This information is determined by so-called tagging algorithms that exploit characteristic signatures of the hadronisation process of the signal b quark and the other $\bar{b}$ quark from the produced $b\bar{b}$ pair. The reliability of the tagging algorithms further dilutes the measured oscillation amplitude. This tagging dilution is measured on calibration samples for which the initial flavour is given by the charge of the reconstructed decay.

- The CP parameters are extracted using a four-dimensional $(t, \theta_1, \theta_2, \Phi)$ unbinned maximum likelihood fit to the decay-time and angular distributions of the B_s^0 signal candidates where the detector effects are taken into account. The pre-determined background contributions are subtracted on a statistical basis using the sFit technique described in Sec. 4.2.

18 Reconstruction and selection of the $B_s^0 \to \phi\phi$ signal decays

The proton-collision data samples used in this analysis correspond to $1.1\,\text{fb}^{-1}$ of integrated luminosity at a centre-of-mass energy of 7 TeV and $2.0\,\text{fb}^{-1}$ at 8 TeV that were collected in 2011 and 2012, respectively. The reconstruction of the decay $B_s^0 \to \phi\phi$ is based on the reconstruction of four hadron tracks that are identified as kaons and combined to a common vertex. In order to suppress background from prompt particles, the characteristic decay topology of b mesons is exploited. After applying a loose selection to the recorded events, a multi-variate analysis technique is used to further isolate the signal.

18.1 Trigger strategy

The hardware trigger uses information from the electromagnetic and hadronic calorimeters to select hadrons with large transverse momenta. In this so-called level-0 hadron trigger (L0Hadron), an event is accepted when the combined transverse energy, E_T, measured in the electromagnetic and hadronic showers, is larger than 3.5 GeV.

Events that satisfy the L0Hadron trigger requirements are processed in the first stage of the high-level trigger (Hlt1), in which tracks are reconstructed and their momenta are measured. All recorded tracks passing any set of Hlt1-trigger requirements are accepted.

In the second stage of the high-level trigger (Hlt2), a dedicated set of trigger requirements is used to explicitly reconstruct ϕ-meson decays into two kaons. This so-called *inclusive* ϕ trigger (Hlt2IncPhi) exploits the particle identification information from the RICH detectors and combines two kaons from a common vertex.

However, due to the low efficiencies of both the L0Hadron and the Hlt2IncPhi trigger requirements ($\sim$12% [88]), an additional strategy is followed. If the event does not satisfy the L0Hadron trigger requirements, it is still accepted if any other level-0 trigger decision has been taken for a different track of the rest of the event. In case of a negative Hlt2IncPhi response, the signal tracks are required to satisfy the topological three-body trigger requirements. As described in Sec. 3.2.5, topological trigger lines partially reconstruct b-hadron decays from few tracks. Events for which the corrected mass of the partially reconstructed B_s^0 candidate is between $4\,\text{GeV}/c^2$ and $7\,\text{GeV}/c^2$, are selected.

In total, there are four disjoint ways an event is recorded, depending on the decisions of the L0Hadron and the Hlt2IncPhi triggers. If the L0Hadron trigger decision is negative, further referred to as 'not L0Hadron', any other level-0 trigger decision is required to be taken for the rest of the event. For a negative Hlt2IncPhi response, denoted as 'not Hlt2IncPhi', the event is required to satisfy the three-body topological trigger.

The four trigger categories are:

- L0Hadron and Hlt2IncPhi
- (not L0Hadron) and Hlt2IncPhi
- L0Hadron and (not Hlt2IncPhi)
- (not L0Hadron) and (not Hlt2IncPhi).

18.2 Selection criteria to isolate the $B_s^0 \to \phi\phi$ decay

To select the $B_s^0 \to \phi\phi$ signal candidates, the loose kinematic selection requirements of Table 18.1 are applied to the recorded data. These were chosen such that they efficiently select simulated signal decays. As described in Sec. 3.3, the b-hadron decay topology with its displaced secondary vertices is exploited by applying selection criteria on the impact parameter and the transverse momenta that discriminate against prompt particles. The transverse momentum of each kaon track is required to be larger than 400 MeV/c and the product of the two ϕ-meson transverse momenta must exceed 2 GeV$^2/c^2$. The selection criterion on the $\chi^2_{\rm IP}$ value of 25 favours displaced b-hadron decay vertices[1]. The invariant di-kaon mass, m_{KK}, is required to be within a ± 25 MeV/c^2 mass window around the known ϕ mass, $m_\phi^{\rm PDG}$. The χ^2 value of the reconstruction fit of the ϕ-meson and B_s^0 vertices, divided by the number of degrees of freedom, $n_{\rm dof}$, is demanded to be less than 15. The particle identification information provided by the RICH detectors is exploited by applying a very loose selection criterion on the difference of logarithmic likelihoods to separate kaons from pions of $\Delta\log\mathcal{L}_{K-\pi} > -5$.

Table 18.1: Summary of the loose kinematic selection requirements to select the $B_s^0 \to \phi\phi(\to K^+K^-K^+K^-)$ signal candidates.

parameter	selection criterion
track p_T	> 400 MeV/c
ϕ^1 p_T $\times$ ϕ^2 p_T	> 2 GeV$^2/c^2$
track $\chi^2_{\rm IP}$	> 25
$\lvert m_{KK} - m_\phi^{\rm PDG}\rvert$	< 25 MeV/c^2
ϕ vertex $\chi^2/n_{\rm dof}$	< 15
B_s^0 vertex $\chi^2/n_{\rm dof}$	< 15
track $\Delta\log\mathcal{L}_{K-\pi}$	> -5

Figure 18.1 shows the invariant four-kaon mass distribution after applying this loose set of selection requirements to the recorded datasets. The B_s^0 signal peak at the known mass of 5366.82 MeV/c^2 [19] on top of a large combinatorial background component is visible.

To further isolate the signal candidates, a dedicated multi-variate analysis technique using a boosted decision tree (BDT) [89] is applied. For each event, the BDT combines

[1] The $\chi^2_{\rm IP}$ value that is related to the significance of the impact parameter, and the $\Delta\log\mathcal{L}_{X-\pi}$ value have been defined in Sec. 3.3

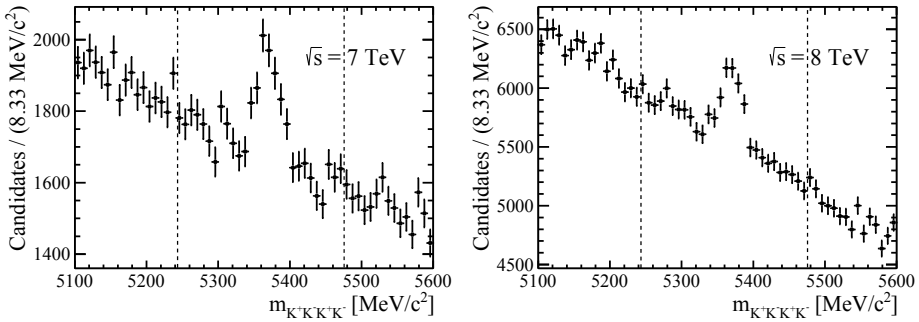

Figure 18.1: Invariant four-kaon mass distribution of the B_s^0 signal candidates after the loose selection for the (left) 7 TeV and (right) 8 TeV data. Events with an invariant mass outside the window of $\pm 120\,\mathrm{MeV}/c^2$ around the known B_s^0 mass serve as the combinatorial background sample for the BDT training.

several observables with separation power to a dimensionless response in an optimised way. A schematic view of a simple decision tree is given in Fig. 18.2. Starting from the root node, a series of binary decisions is applied using the discriminating variables xi, xj and so on, until a configurable break-condition is fulfilled and the event is classified as signal-like (S) or background-like (B). The splitting conditions at each node are obtained from pure signal and background samples in a process called *training*. The advantage of a decision tree compared to a cut-based selection is that the selection criteria are applied in a multi-dimensional grid of the input variables. Hence, it can consider higher-dimensional correlations.

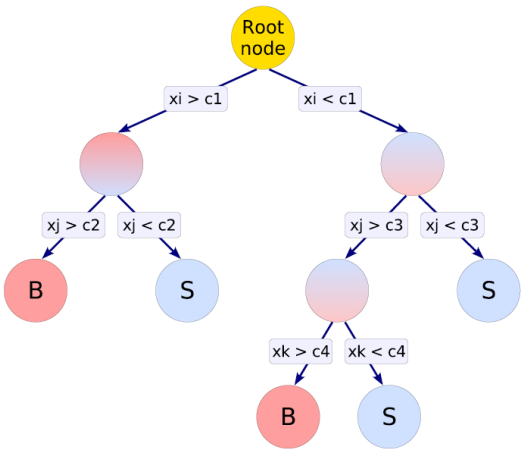

Figure 18.2: Schematic view of a decision tree, taken from Ref. [90].

However, simple decision trees are known to be unstable such that small changes in the training sample can lead to large changes in the splitting criteria, and thus in the resulting separation [89]. Therefore, a method that typically trains thousands of decision trees and combines their outputs has been developed in Ref. [91]. The first decision tree is trained

to provide the largest separation power. After training it, event weights are computed that are larger when the event is misclassified by the decision tree and ends up in the wrong category. The second decision tree is trained with the weighted dataset. Previously misclassified events are thus considered as more important and new weights are computed. Repeating this procedure, misclassified events get increasingly higher weights with each tree which is called *boosting*, hence the method is referred to as a boosted decision tree. At the same time, different weights are assigned to the trees that become smaller for every consecutive tree. After the training process, each tree is applied to data and provides a response, +1 or -1, depending if the event is classified as signal or background, respectively. The responses of all trees, weighted according to the tree weights, are summed up and divided by the sum of all tree weights. The resulting weighted mean of the tree responses is the final response of the boosted decision tree. The BDT has been found to be very efficient and robust to changes of the input samples.

To describe the signal sample, simulated and fully reconstructed $B_s^0 \to \phi\phi$ events are used in the training. To mimic the background sample in the training, data is used for which the invariant four-kaon mass is outside a mass window of $\pm 120\,\mathrm{MeV}/c^2$ around the known B_s^0 mass, as indicated in Fig. 18.1. Due to different run conditions leading to a different event composition, a separate BDT is trained for each of the two centre-of-mass energies. The discriminating variables used to train the BDT are the following:

- B_s^0 vertex reconstruction fit χ^2 value per number of degrees of freedom.
- The pseudorapidity, η, of the B_s^0 candidate and of each ϕ candidate, and the maximum and minimum η of the kaon tracks.
- The minimum ProbNN_K variable of the kaon tracks. This is a particle identification variable that is evaluated with neural networks[1].
- The cosine of the pointing angle between the direction of the momentum and the flight direction of the B_s^0 candidate.
- The logarithmic transverse momentum, $\log(p_\mathrm{T})$, of the B_s^0 candidate, each ϕ candidate, and the maximum and minimum $\log(p_\mathrm{T})$ of the kaon tracks. The logarithm is used as the separation power is larger in the low-momentum range.
- The maximum track reconstruction fit χ^2 value per number of degrees of freedom[2].
- The p_T cone asymmetry, $a_{p_\mathrm{T},\mathrm{cone}}$, for each kaon track. It describes the spatial isolation of the kaon track from other high-p_T tracks. It is defined as the difference between the transverse momentum of the kaon track, ${p_\mathrm{T}}^\mathrm{K}$, and the summed transverse momenta of the other tracks, ${p_\mathrm{T}}^\mathrm{other}$, in a cone of radius $\mathrm{r} = \sqrt{(\Delta\Phi)^2 + (\Delta\eta)^2} = 1\,\mathrm{rad}$ around the kaon track, divided by the sum:

$$a_{p_\mathrm{T},\mathrm{cone}} = \frac{{p_\mathrm{T}}^\mathrm{K} - {p_\mathrm{T}}^\mathrm{other}}{{p_\mathrm{T}}^\mathrm{K} + {p_\mathrm{T}}^\mathrm{other}},$$

[1] The ProbNN_X variable has been described in Sec. 3.2.4.
[2] The track χ^2 per degree of freedom has been described in Sec. 3.2.1

where ${p_{\mathrm{T}}}^{\mathrm{other}}$ is still defined with respect to the beam axis, not with respect to the kaon track axis. Random combinations of tracks tend to pass the vertex criteria when their trajectories are very close to each other. Thus, randomly combined tracks tend to have a smaller p_{T} cone asymmetry. In $B_s^0 \to \phi\phi$ decays, the two kaon pairs are, on average, well separated as the ϕ mesons have larger transverse momenta in opposite directions.

The particle identification performance of the RICH detectors depends on the number of tracks in the event which is known to be underestimated in simulation. As the number of hits in the Scintillating Pad Detector is a good proxy of the global track multiplicities, weights are assigned to the simulated events such that the distribution of the number of hits in the Scintillating Pad Detector agrees with the data[3].

The distributions of the discriminating variables for the 7 TeV and 8 TeV signal and background samples are shown in Appendix B.1. It also includes the correlation matrix between the input variables for the simulated $B_s^0 \to \phi\phi$ 8 TeV events. Among these, the variables with the largest discriminating power are the cosine of the pointing angle, the B_s^0 vertex χ^2/n_{dof} value, the track χ^2/n_{dof} value and the transverse momenta.

The performance of the BDT training is limited by statistical fluctuations of the input samples. If these are too large, the BDT might falsely identify them as characteristic signatures of the signal or the background. This symptom is called *overtraining*. In order to test the reliability of the BDT, the signal sample is randomly split into two halves. The first half, the training sample, is used to train the BDT which is tested with the other half, the test sample. If the BDT is not overtrained, the distributions of the BDT output values are the same for the training and the test samples. Figure 18.3 shows the distributions of the BDT response of the signal and the background, both for the training and the test samples. A good agreement is seen between them indicating that the BDT is not overtrained. The background and signal samples show well-separated BDT responses with asymmetric peaks at around -0.5 for the background and 0.3 for the signal. It is only in the tails where they overlap.

The selection criterion on the BDT response is chosen such that the figure of merit, $S/\sqrt{S+B}$, is maximal, where S denotes the expected number of signal candidates and B the expected number of background events. Figure 18.4 shows the selection efficiencies of the signal and background samples and the figure of merit as a function of the cut value on the BDT response. For the figure of merit, the number of signal candidates before the BDT selection is estimated from the observed number of events in the previous 7 TeV analysis [71], in which a tighter pre-selection was used. This number is corrected for the higher efficiency of the loose selection in this analysis and extrapolated to the higher luminosity collected at 8 TeV. The number of background events is obtained from a fit to the invariant four-kaon mass distribution shown in Fig. 18.1 where the B_s^0 candidates is described by a Gaussian function and the background by an exponential function. For the 7 TeV dataset, this results in the estimated number of signal and background events of

[3] To determine the data distribution without combinatorial background, a tighter pre-selection is applied to the data and the resulting invariant four-kaon mass distribution of the B_s^0 candidates is described by a Gaussian function for the B_s^0 signal and an exponential function for the remaining background. The fit result is used to determine the corresponding distribution of the data using the ${}_s\mathcal{P}lot$ technique described in Sec. 4.2.

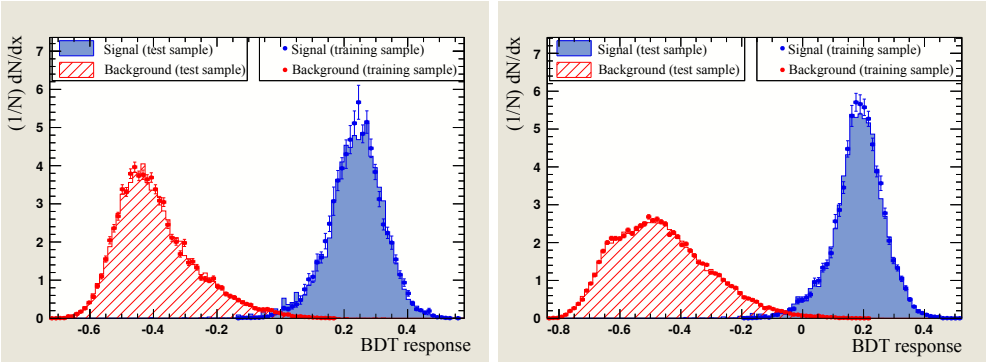

Figure 18.3: Distributions of the BDT response for the (left) 7 TeV and (right) 8 TeV signal and background samples, drawn in blue and red, respectively. The shaded areas refer to the BDT response for the test samples and the points for the training samples.

1500 and 53500, respectively. The corresponding numbers for the 8 TeV dataset are 3000 and 149500. Using these values, the figure of merit is maximum for the cut values of 0.1261 and 0.0532 on the BDT response for the 7 TeV and 8 TeV data, respectively. After applying the selection criteria on the BDT response, B_s^0 candidates are additionally rejected when their decay time is less than 0.3 ps. This affects only a very small fraction of the events but it reduces the systematic uncertainties of the decay-time acceptance in the region of very low decay times.

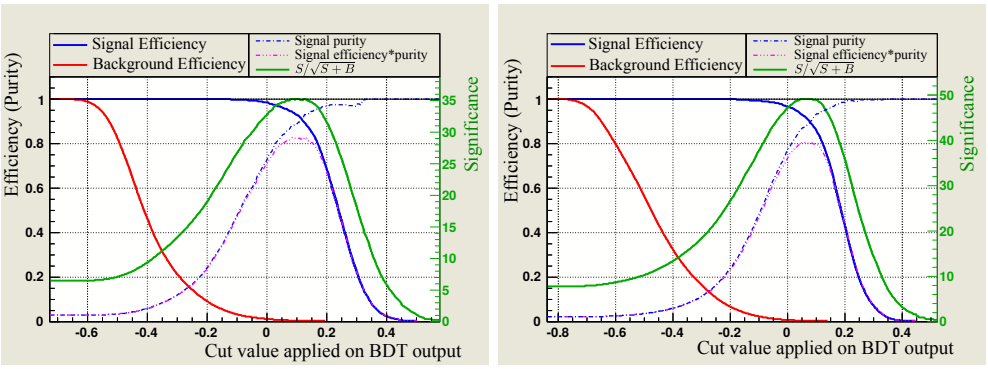

Figure 18.4: Signal selection efficiency (blue, solid line), background selection efficiency (red, solid line), signal purity (dash-dotted blue line), signal efficiency multiplied by the purity (dash-dotted purple line) and significance (green, solid line) of the (left) 7 TeV BDT and (right) 8 TeV BDT, with expected number of signal (background) events of 1500 (53500) for the 7 TeV dataset and 3000 (149500) for the 8 TeV dataset.

The invariant mass distribution of one of the selected ϕ-meson candidates, after applying the BDT selection, is shown in Fig. 18.5, separately for the 7 TeV and 8 TeV datasets. Figure 18.6 shows the invariant mass distribution of the selected B_s^0 candidates, again for 7 TeV and 8 TeV, respectively. They exhibit clean signal peaks at the known ϕ-meson and

B_s^0 masses with small combinatorial background contributions. However, among these candidates, there is still a small background contribution from b-hadron decays that cannot be distinguished from the signal decays. This will be investigated in the following section.

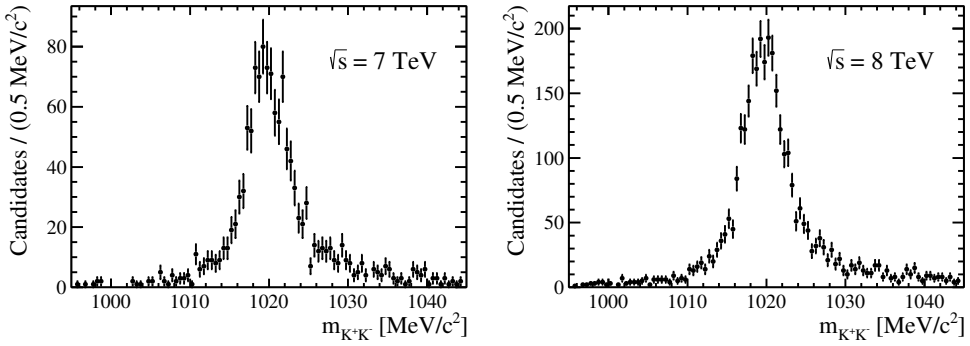

Figure 18.5: Invariant mass distribution of one of the ϕ-meson signal candidates after applying the BDT-based selection to the (left) 7 TeV and (right) 8 TeV datasets.

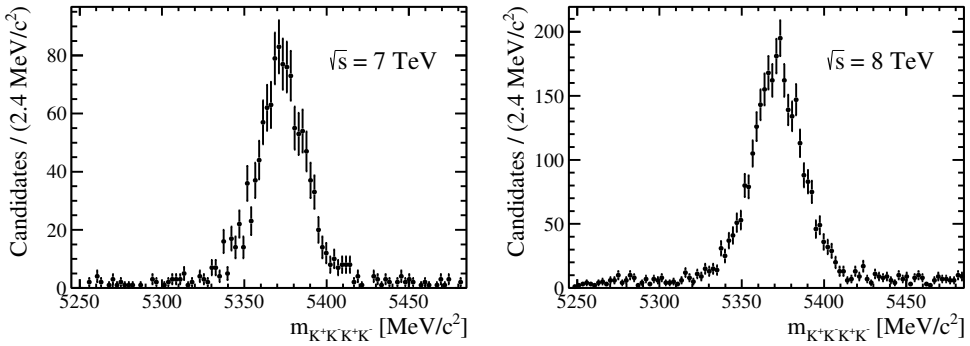

Figure 18.6: Invariant mass distribution of the B_s^0 signal candidates after applying the BDT-based selection to the (left) 7 TeV and (right) 8 TeV datasets.

18.3 Background from falsely identified b-hadron decays

Apart from a small combinatorial background component, other b-hadron decays contribute to the selected B_s^0 candidates when one of the final-state tracks is falsely identified as a kaon. The baryonic channel $\Lambda_b^0 \to \phi K p$ is reconstructed as signal when the proton is misidentified as a kaon. In the same way, the decay mode $B^0 \to \phi K^{*0}(\to K\pi)$ is reconstructed as signal when the pion is misidentified as a kaon. To determine their contributions, these decays are explicitly reconstructed. Background contributions from other b-hadron decays such as $B_{(s)}^0 \to \phi\pi\pi$ and $B^\pm \to \phi K^\pm$ decays have been found to be negligible as they involve the simultaneous misidentification of two pions and fail to fulfil the kinematic selection requirements, respectively. The measured yields and mass shapes

of the background contributions are then fixed in a fit to the invariant four-kaon mass distribution to obtain the number of B_s^0 signal candidates.

18.3.1 Background contribution from $\Lambda_b^0 \to \phi K p$ decays

To estimate the contribution from $\Lambda_b^0 \to \phi K p$ decays to the selected datasets, the selected B_s^0 candidates are reconstructed under the hypothesis that one of the four final-state particles is a proton. As described in Sec. 3.3.1, the invariant b-hadron mass is obtained from the summed four-momenta of the final-state particles. Whereas the three-momenta are measured with the detector, the known masses of the daughter particles are inserted into the four-momenta according to the particle hypothesis provided by the particle identification system. Instead of inserting the kaon mass, one track is assigned the proton mass. In the following, the B_s^0 candidates are simply said to be reconstructed as $\Lambda_b^0 \to \phi K p$. The track for which the mass hypothesis is changed is the one with the lowest ProbNN_K value. The resulting invariant mass distribution of the system gets distorted and shifted to larger values compared to the four-kaon hypothesis. The effect on the $B_s^0 \to \phi\phi$ signal mass shape is determined by reconstructing simulated signal decays under the varied particle hypothesis on the left-hand side of Fig. 18.7. It is described by a Crystal Ball function[4]. The invariant mass distribution of the selected $B_s^0 \to \phi\phi$ candidates from data, reconstructed in the same way as $\Lambda_b^0 \to \phi K p$, is shown in the centre and on the right, separately for the two centre-of-mass energies. A fit using a Crystal Ball function for the distorted $B_s^0 \to \phi\phi$ shape and a Gaussian function for the small Λ_b^0 peak yields contributions of 52 ± 19 and 51 ± 29 $\Lambda_b^0 \to \phi K p$ decays among the selected 7 TeV and 8 TeV datasets, respectively. These events are the background from falsely identified Λ_b^0 decays.

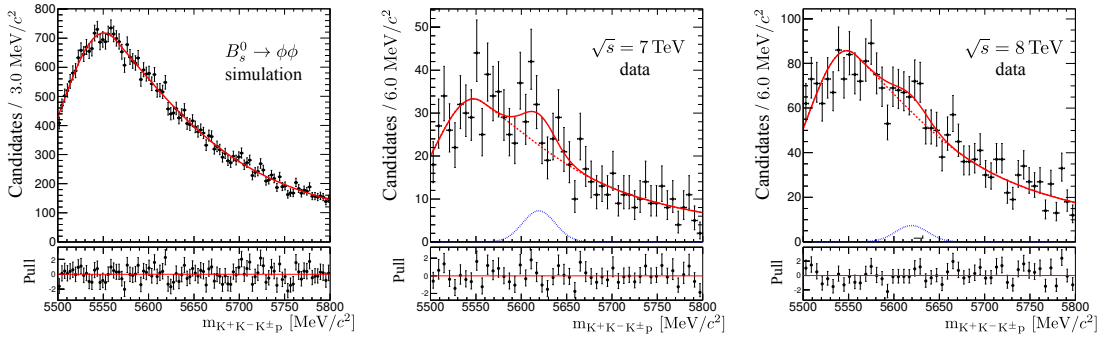

Figure 18.7: Invariant mass distribution of (left) simulated 8 TeV $B_s^0 \to \phi\phi$ signal events, reconstructed under the mass hypothesis of $\Lambda_b^0 \to \phi K p$. The fit model is a Crystal Ball function. Invariant mass distribution of (centre) 7 TeV and (right) 8 TeV $B_s^0 \to \phi\phi$ signal candidates reconstructed under the mass hypothesis of $\Lambda_b^0 \to \phi K p$. The $B_s^0 \to \phi\phi$ signal component, drawn as a red dotted line, is modelled by a Crystal Ball function, the $\Lambda_b^0 \to \phi K p$ component is described by a Gaussian function, given by the blue dotted line, and the red line refers to the total fit.

[4]The Crystal Ball function is a Gaussian-like function with asymmetric widths and a long tail that flattens out. It has been introduced in Sec. 12.3.7.

18.3.2 Background contribution from $B^0 \to \phi K^{*0}(\to K\pi)$ decays

The contribution from $B^0 \to \phi K^{*0}$ decays to the selected B_s^0 candidates is smaller than the Λ_b^0 contribution and cannot be determined in the same way because the background peak is not visible in the mass distribution of the data reconstructed as $B^0 \to \phi K^{*0}$. Therefore, the background yields are determined with a different approach in which a dedicated ϕK^{*0} selection is applied to data and simulated events.

For the ϕK^{*0} selection, the loose signal selection requirements of Table 18.1 are modified for the track with the smallest ProbNN_K value: the difference of the logarithmic likelihood is set in favour of the pion, $\Delta\mathcal{L}_{K-\pi} < -5$. Both selections are applied to data and simulated $B^0 \to \phi K^{*0}$ decays that result in $B^0 \to \phi K^{*0}$ event yields that are defined as follows:

- $N_{\text{MC, }\phi K^{*0}}$: number of selected $B^0 \to \phi K^{*0}$ decays of the simulated $B^0 \to \phi K^{*0}$ sample using the ϕK^{*0} selection
- $N_{\text{MC, }\phi\phi}$: number of selected $B^0 \to \phi K^{*0}$ decays of the simulated $B^0 \to \phi K^{*0}$ sample using the loose $\phi\phi$ selection
- $N_{\text{data, }\phi K^{*0}}$: number of selected $B^0 \to \phi K^{*0}$ decays in data using the ϕK^{*0} selection
- $N_{\text{data, }\phi\phi}$: number of selected $B^0 \to \phi K^{*0}$ decays in data using the loose $\phi\phi$ selection. It should be noted that this number corresponds to the background yield after the loose $\phi\phi$ selection and it cannot be obtained directly from data.

In simulated events, the $B^0 \to \phi K^{*0}$ yields using both selections can be easily obtained from the information which decay has been generated (MC truth). In data, the $B^0 \to \phi K^{*0}$ yield after the ϕK^{*0} selection is determined in the following but the corresponding number of decays after the $\phi\phi$ selection cannot be extracted from data because the contribution is too small.

The assumption is that the ratio of selection efficiencies of the loose cut-based $\phi\phi$ selection to the ϕK^{*0} selection is the same in data and simulation such that the ratios of event yields are equal:

$$\frac{N_{\text{data, }\phi\phi}}{N_{\text{data, }\phi K^{*0}}} = \frac{N_{\text{MC, }\phi\phi}}{N_{\text{MC, }\phi K^{*0}}}. \tag{18.1}$$

After having determined the yields $N_{\text{MC, }\phi\phi}$, $N_{\text{MC, }\phi K^{*0}}$, and $N_{\text{data, }\phi K^{*0}}$, the unknown yield $N_{\text{data, }\phi\phi}$ can be calculated from Eq. 18.1.

The number of selected decays in the simulated $B^0 \to \phi K^{*0}$ event sample are determined to be $N_{\text{MC, }\phi K^{*0}} = 196606 \pm 443$ and $N_{\text{MC, }\phi\phi} = 1070 \pm 33$. The invariant mass distribution of the $B^0 \to \phi K^{*0}$ candidates from the combined 7 TeV and 8 TeV datasets, reconstructed as $B^0 \to \phi K^{*0}$ and selected with the ϕK^{*0} selection, is shown in Fig. 18.8. The fit model consists of the sum of two Gaussian functions for the $B^0 \to \phi K^{*0}$ signal component and an exponential function for the combinatorial background. The fit yields $N_{\text{data, }\phi K^{*0}} = 6972 \pm 141$ selected $B^0 \to \phi K^{*0}$ decays. Hence, the missing number of $B^0 \to \phi K^{*0}$ decays in data when applying the loose $\phi\phi$ selection is computed as $N_{\text{data, }\phi\phi} = 38 \pm 2$.

In order to obtain the $B^0 \to \phi K^{*0}$ yields after the full BDT selection, $N_{\text{data, }\phi\phi\text{ BDT}}$, the BDT is applied to the simulated $B^0 \to \phi K^{*0}$ decay sample and the relative yields before and after the BDT, $N_{\text{MC, }\phi\phi\text{ loose}}$ and $N_{\text{MC, }\phi\phi\text{ BDT}}$, are used to correct the number

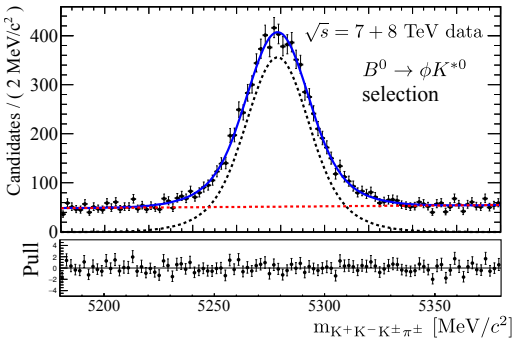

Figure 18.8: Invariant mass distribution of the $B^0 \to \phi K^{*0}$ signal candidates from the combined 7 TeV and 8 TeV datasets using the ϕK^{*0} selection. The data is represented by the black points, the $B^0 \to \phi K^{*0}$ signal is described by the sum of two Gaussian functions and drawn with a black dotted line. The combinatorial background model is an exponential function, represented by the red dotted line. The total fit is given by the blue line.

of events seen in data:

$$N_{\text{data, }\phi\phi\text{ BDT}} = \frac{N_{\text{MC, }\phi\phi\text{ BDT}}}{N_{\text{MC, }\phi\phi\text{ loose}}} \cdot N_{\text{data, }\phi\phi\text{ loose}}. \tag{18.2}$$

Inserting the determined numbers results in the final $B^0 \to \phi K^{*0}$ background yields after the $\phi\phi$ BDT selection of 7.3 ± 0.4 and 17.8 ± 0.9 for the 7 TeV and 8 TeV datasets, respectively. Figure 18.9 shows the invariant mass distribution of the $B_s^0 \to \phi\phi$ candidates after the full BDT selection for the combined 7 TeV and 8 TeV datasets, reconstructed under the mass hypothesis of $B^0 \to \phi K^{*0}$. In the fit, the combined $B^0 \to \phi K^{*0}$ yields are fixed to the determined values and the shape is a Gaussian function. The $B_s^0 \to \phi\phi$ signal shape is a Crystal Ball function.

18.4 Determination of the number of $B_s^0 \to \phi\phi$ signal decays

The extracted yields of the falsely identified b-hadron decays are used to determine the remaining number of $B_s^0 \to \phi\phi$ signal decays after the BDT selection. This is done using a fit to the invariant four-kaon mass distribution. The $B_s^0 \to \phi\phi$ signal component is modelled by the sum of two Gaussian functions and the combinatorial background by an exponential function. The shapes of the misidentified b-hadron components, reconstructed as $B_s^0 \to \phi\phi$, are Crystal Ball functions, whose parameters are determined with fully simulated and reconstructed decays. Fixing the extracted b-hadron background yields and the shape parameters, the fit to the invariant mass distribution of the selected $B_s^0 \to \phi\phi$ candidates is shown in Fig. 18.10, separately for the 7 TeV and 8 TeV datasets. The fit model agrees well with the data without significant deviating structures in the pull distributions[5]. The yields of the B_s^0 signal are found to be 1185 ± 35 and 2765 ± 57 for the 7 TeV and 8 TeV datasets,

[5]The pull of a fit has been defined in Chap. 9.

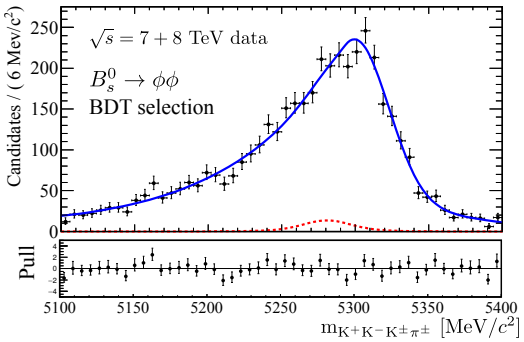

Figure 18.9: Invariant mass distribution of the $B_s^0 \to \phi\phi$ candidates after the full BDT selection for the combined 7 TeV and 8 TeV datasets, reconstructed with the mass hypothesis of $B^0 \to \phi K^{*0}$. In the fit, the $B^0 \to \phi K^{*0}$ yield is fixed to the sum of the numbers computed in the text. The $\phi\phi$ shape is a Crystal Ball function and the $B^0 \to \phi K^{*0}$ component is described by a Gaussian function, shown as a red dotted line. The total fit given by the blue line.

respectively. This is approximately 4.1% of the number of $B_s^0 \to J/\psi\,\phi$ signal decays found in the same combined dataset in Ref. [6]. The fit results are used to assign sWeights to the selected events according to the invariant four-kaon mass. When the sWeights are applied to the events, the background contributions are subtracted on a statistical basis as described in Sec. 4.2. This will be exploited in the fit for the $B_s^0 \to \phi\phi$ physics parameters in Chap. 24.

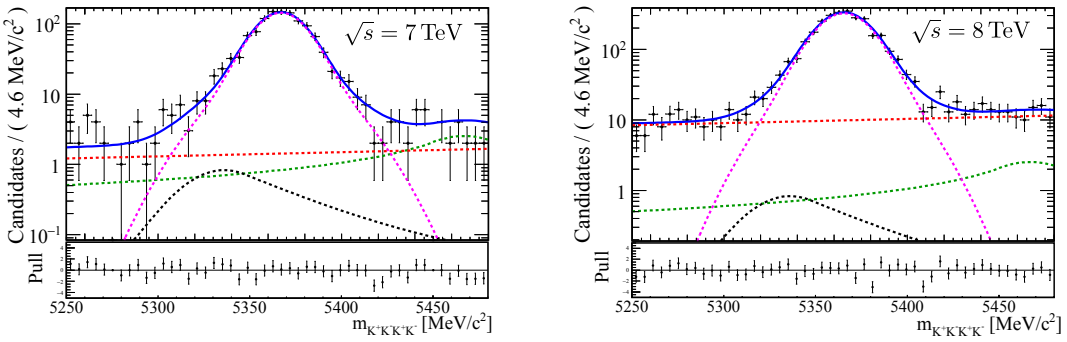

Figure 18.10: Fit to the invariant mass distributions of the $B_s^0 \to \phi\phi$ signal candidates of the (left) 7 TeV and (right) 8 TeV datasets. The data is represented by the black points. Superimposed are the results of the total fit (blue solid line). The $B_s^0 \to \phi\phi$ signal component is described by the sum of two Gaussian functions (purple dashed curve) and the combinatorial background function is an exponential function (red dashed line). The shapes of the $B^0 \to \phi K^{*0}$ (black dashed line) and the $\Lambda_b^0 \to \phi p K^-$ (green dashed line) background components are Crystal Ball functions whose parameters are determined with fully simulated events. The yields are fixed to the values determined in the previous section.

19 Determination of the decay-time resolution

The CP parameters ϕ_s and $|\lambda_{\rm CP}|$ are extracted from the time-dependent decay asymmetry of the B_s^0 and $\overline{B}_s^0$ mesons. Due to the finite decay-time resolution, the observed B_s^0-$\overline{B}_s^0$ oscillation gets diluted which has to be correctly modelled in the fit. The decay-time resolution depends on the number of final-state particles and their kinematics and is in general different for different decays. In this chapter, the decay-time resolution is determined with simulated and fully reconstructed signal decays.

19.1 Determination of the average decay-time resolution

The decay-time resolution is measured with simulated and fully reconstructed signal decays by computing the difference between the reconstructed and the generated decay time, which is referred to as the decay-time error. The distributions of the decay-time error for simulated 7 TeV and 8 TeV $B_s^0 \to \phi\phi$ signal events is shown in Fig. 19.1. Clean peaks around zero can be seen which are described by the sum of two Gaussian functions. The fit values of the 7 TeV widths are $\sigma_1 = 30.4 \pm 0.5$ fs and $\sigma_2 = 60.0 \pm 1.1$ fs for the first and second Gaussian functions, respectively. The fraction of the first Gaussian is found to be 0.658 ± 0.020. The corresponding values for the 8 TeV simulation are $\sigma_1 = 31.6 \pm 0.5$ fs and $\sigma_2 = 63.3 \pm 1.1$ fs and a fraction of 0.639 ± 0.020.

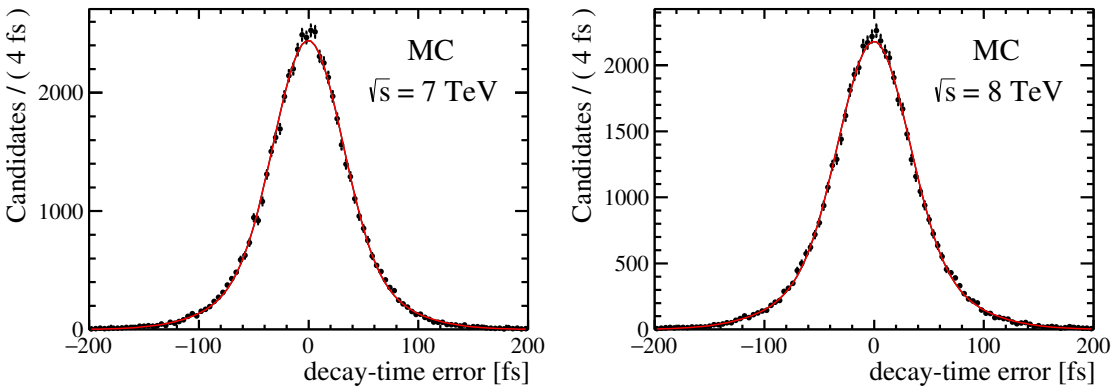

Figure 19.1: Distribution of the decay-time error, computed as the difference between the reconstructed decay time and the generated decay time, of simulated (left) 7 TeV and (right) 8 TeV $B_s^0 \to \phi\phi$ events. Superimposed are the results of a fit using the sum of two Gaussian functions, given by the red line.

19.2 Decay-time resolution model

In the fit for the $B_s^0 \to \phi\phi$ physics parameters, the effect of a finite decay-time resolution is incorporated with a resolution model, $R(t-t')$, of the difference of the reconstructed decay time t and the true decay time t'. The time-dependent decay rate of the produced B_s^0, $\mathcal{P}_{B_s^0}(t)$, is convoluted with the resolution model

$$(\mathcal{P}_{B_s^0} \otimes R)(t) = \int_{-\infty}^{\infty} \mathcal{P}_{B_s^0}(t')\,\mathrm{R}(t-t')\mathrm{d}t', \tag{19.1}$$

which leads to an an effective dilution, $\mathcal{D}$, of the observable CP asymmetry. The dilution to the amplitude of an oscillation with frequency Δm_s is obtained by taking the Fourier transform of the resolution function [92, 93]

$$\mathcal{D}(\Delta m_s) = \frac{2}{\sqrt{\pi}} \int_0^{\infty} R(\delta_t)\cos(-\Delta m_s \delta_t)\ \mathrm{d}\delta_t, \tag{19.2}$$

where $\delta_t = t - t'$. Using a sum of Gaussian functions as the resolution model, $\mathcal{D}$ reduces to

$$\mathcal{D} = \sum_j f_j\ \exp(-\Delta m_s^2 \sigma_{j,t}^2/2), \tag{19.3}$$

where f_j is the fraction of the j^{th} Gaussian and $\sigma_{j,t}$ is the width of the j^{th} Gaussian. The equivalent effective single-Gaussian resolution, $\sigma_{\mathrm{eff},t}$, is computed with

$$\sigma_{\mathrm{eff},t} = \frac{\sqrt{-2\log\mathcal{D}}}{\Delta m_s}. \tag{19.4}$$

which describes the effective decay-time resolution in the measurement of the phase ϕ_s.

Using these equations, the dilutions for the simulated 7 TeV and 8 TeV events are 0.762 $\pm$ 0.005 and 0.738 $\pm$ 0.005, respectively. They yield effective resolutions of 41.4 $\pm$ 0.5 fs and 43.9 $\pm$ 0.5 fs.

19.3 Determination of the event-dependent decay-time resolution

As described in Sec. 3.3, the decay time is reconstructed from the b-meson flight distance and the momentum. Since the quality of the reconstruction depends on various event properties such as occupancies and the decay time itself, the decay-time resolution is different for every event. Therefore, a per-event decay-time resolution model is applied during the fit for the $B_s^0 \to \phi\phi$ physics parameters. For each event i, the uncertainties on the global kinematic fit [94] of the track momenta and the decay vertex is used to provide an estimate of the uncertainty of the decay time, the so-called per-event decay-time error δ_i. However, the absolute scale of this estimate has to be calibrated to the measured effective resolution. Therefore, the simulated signal events are split into equi-statistical slices of δ. For each slice, a single Gaussian function is fitted to the difference between the

reconstructed decay time and the generated decay time to determine the actual effective resolution $\sigma_{\text{eff}}(\delta)$ according to Eq.s 19.3 and 19.4. A single Gaussian function is used because the statistics in each slice is smaller. The dependence on δ is modelled by a linear function

$$\sigma_{\text{eff}}(\delta) = q_0 + q_1\delta. \tag{19.5}$$

Figure 19.2 shows the measured effective resolution in 19 bins of the per-event decay time error for simulated 7 TeV and 8 TeV $B_s^0 \to \phi\phi$ decays. Except for the first bin, the effective resolution is well-described by the linear fit. The calibration parameters of the per-event

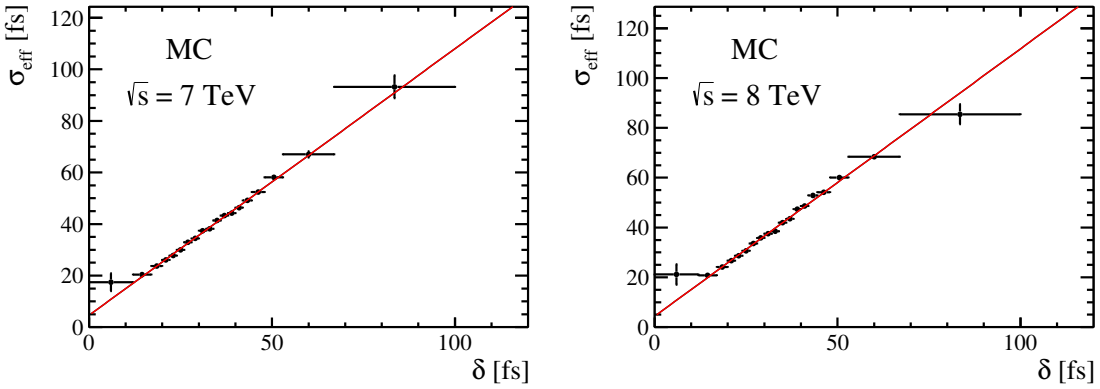

Figure 19.2: Determined effective time resolution for equal-statistics bins of the estimated per-event decay time error δ for (left) 7 TeV and (right) 8 TeV simulated events. Also plotted is the result of a linear fit.

decay time error are given in Table 19.1. In the fit for the $B_s^0 \to \phi\phi$ physics parameters, the calibrated per-event decay-time error is taken as the width of the single-Gaussian resolution model. Uncertainties due to possible differences of the decay-time resolution in simulation and real data are taken into account as a systematic uncertainty in Chap. 23.

Table 19.1: 7 TeV and 8 TeV calibration parameters of the estimated per-event decay time error, obtained from a linear fit, according to Eq. 19.5, to the measured effective resolution, shown in Fig. 19.2.

	7 TeV	8 TeV
q_0	4.5 ± 0.4 fs	4.3 ± 0.4 fs
q_1	1.036 ± 0.013	1.076 ± 0.014

20 Determination of the detector acceptance corrections

Due to reconstruction and selection artefacts and the geometrical coverage of the detector, the measured distributions of the decay time and the helicity angles get distorted and deviate from the actual distributions. Therefore, the decay-time and angular acceptances have to be correctly modelled in the fit. In this chapter, the decay-time acceptance is obtained from the well-known calibration channel $B_s^0 \to D_s^-(\to K^+K^-\pi^-)\pi^+$ that has a very similar decay topology and the angular acceptance is extracted from fully simulated signal decays.

20.1 Definition of the detector acceptance

The selection criteria to isolate B_s^0 signal decays exploit the long lifetime such that the flight distance from the production to the decay vertex can usually be resolved. Decays in which the final-state kaons appear to originate from the proton-proton interaction point, are rejected to suppress background. However, these selection criteria also reject signal B_s^0 decays with very small decay times. Geometrically, the detector is not a homogeneous object, but built from different sub-components with well-defined sensitive areas. The detector acceptance, ε_{acc}, describes the efficiency of selecting the signal decays as a function of the decay time t and the helicity angles Ω. It is defined as the decay-time and angular-dependent ratio of the number of reconstructed and selected particles, N_{acc}, to the number of produced signal particles, N_{tot},

$$\varepsilon_{\text{acc}}(t,\Omega) = \frac{N_{\text{acc}}(t,\Omega)}{N_{\text{tot}}(t,\Omega)}. \tag{20.1}$$

In data, the total number of produced B_s^0 mesons is not known but the shape of the acceptance is obtained by comparing the measured distribution with the expected theoretical decay rate, $s(t,\Omega|\vec{a})$, defined in Sec.16.4.2. This is done in a binned way in intervals of the decay time and the decay angles and $s(t,\Omega|\vec{a})$ is integrated over the decay-time and angular range covered by the bin i:

$$\varepsilon_{\text{acc}}(t_i,\Omega_i) \;\propto\; \frac{N_{\text{acc}}(t_i,\Omega_i)}{N_{\text{acc,tot}} \int\limits_{\Omega_i} \mathrm{d}\Omega \int\limits_{t_i} \mathrm{d}t \; s(t,\Omega|\vec{a})}, \tag{20.2}$$

where $N_{\text{acc}}(t_i,\Omega_i)$ is the number of reconstructed and selected events within bin i. As this ratio is normalised to the total number of reconstructed and selected events, $N_{\text{acc,tot}}$, it does not correspond to the absolute detector acceptance, but only to the relative acceptance. However, for the analysis, only the shape is of importance. It should also be noted that

this definition depends on the inserted set of physics parameters $\vec{a}$ and the assumed physics model for the undistorted shapes in t and Ω. The detector acceptance is assumed to factorise into the decay-time and the angular acceptance, $\varepsilon_{\text{acc}}(t,\Omega) = \varepsilon_{\text{acc}}(t)\varepsilon_{\text{acc}}(\Omega)$. The impact of neglecting correlations between the angular and decay-time acceptances has been found to be negligible for $B_s^0 \to J/\psi\,\phi$ decays [70] by determining the angular acceptance in different regions of the decay time.

20.2 Determination of the decay-time acceptance correction

The physics parameters of the theoretical $B_s^0 \to \phi\phi$ decay rate are part of this analysis and are yet to be measured. Therefore, they cannot be used to obtain the detector acceptance. Instead, the topologically similar channel $B_s^0 \to D_s^+(\to K^+K^-\pi^+)\,\pi^-$, for which two final-state kaons are simply replaced by two pions, is used as a control mode to model the time acceptance. The advantages of this decay are the excellent signal-to-background ratio, the larger number of events and the well-measured parameters of the decay rates.

20.2.1 Selection of $B_s^0 \to D_s^-\pi^+$ signal decays

In order to match the decay topologies of the two decay modes, the event selection to isolate the $B_s^0 \to D_s^-\pi^+$ signal is designed to be as close as possible to the $B_s^0 \to \phi\phi$ signal selection. The same four trigger categories as the signal, described in Chap. 18, are used to record the data. Except for the particle identification requirements for the two pions, the loose selection criteria of Table 18.1 are applied. A new BDT without the ProbNN_K variable is trained with the simulated $B_s^0 \to \phi\phi$ signal sample and applied to the data. Since the charm meson has a finite lifetime itself, it decays, on average, significantly away from the B_s^0 decay vertex. Therefore, a selection criterion on the maximum D_s^+ decay time of 1 ps is enforced.[1] Due to the different hadron masses of the kaons and pions, the kinematic distributions are slighlty different for the two modes. In order to ensure a kinematic agreement, the $B_s^0 \to D_s^-\pi^+$ events are assigned weights such that the distribution of the minimum transverse momentum of the four tracks agrees with the one observed for $B_s^0 \to \phi\phi$ decays.

20.2.2 Validation of the procedure and results

The decay rate when averaging over B_s^0 and $\overline{B}_s^0$ mesons and neglecting contributions from mixing, is a simple exponential function with the lifetime τ. It is inserted into Eq. 20.2 to determine the decay-time acceptance. Instead of computing the integrals of the theoretical decay rates by hand, a different, technically more simple approach is followed. Events are generated according to the theoretical decay-time-dependent $B_s^0 \to D_s^-\pi^+$ decay rate. Detector and reconstruction effects are not included, hence the generated decay-time distribution is not diluted and the set of events is also called a *pseudo dataset*. The decay-time acceptance is determined by comparing this generated decay-time distribution with the one measured in data. Resolution effects of the decay-time of the selected $B_s^0 \to D_s^-\pi^+$

[1] It should be noted that the B_s^0 decay vertex is defined by the combined vertex of the prolongated charm-hadron trajectory and the pion track.

candidates are neglected because they are negligible for the acceptance. The decay-time acceptance is computed with[2]

$$\varepsilon_{\text{acc}}(t_i) \;\propto\; \frac{N_{\text{acc}}(t_i)}{N_{\text{gen}}/\tau \int\limits_{t_i} \exp(-t/\tau)\ \mathrm{d}t}, \tag{20.3}$$

where N_{gen} is the number of generated events and $N_{\text{acc}}(t_i)$ is the number of selected events in data or simulation that fall into the decay-time bin i. The two distributions are normalised to unity as a convention. In the fit for the physics parameters, the decay-time acceptance, as defined here, is multiplied to the theoretical decay rates and the resulting product is normalised to serve as a probability density.

Fully simulated decays are used to validate that the decay-time acceptances in $B_s^0 \to D_s^- \pi^+$ and $B_s^0 \to \phi\phi$ decays agree with each other. The lifetimes used to generate the pseudo datasets are the same as those for the fully simulated decays. The different kinematic selection criteria for each of the four trigger categories give rise to individual decay-time acceptances which are determined separately. The simulated 8 TeV decay-time acceptances for the signal channel $B_s^0 \to \phi\phi$ and the re-weighted control mode $B_s^0 \to D_s^- \pi^+$, denoted as 'K-RW', are shown for the four trigger categories in Fig. 20.1. As the absolute scale depends on the number of generated events of the pseudo dataset, only the relative acceptance is shown. Since B_s^0 candidates with a decay time less than 0.3 ps are rejected in addition to the BDT selection, the decay-time acceptance are not shown for values below 0.3 ps. At small decay times, the efficiency steeply rises from zero and reaches a plateau at the maximum efficiency. The agreement between the simulated acceptances in the signal and the control mode is satisfactory, especially in the two trigger categories that provide most of the B_s^0 signal decays, namely (L0Hadron and Hlt2IncPhi) and (not L0Hadron and Hlt2IncPhi). The observed differences will be taken into accounted as a systematic uncertainty in Chap. 23. The decay-time acceptances of the control mode $B_s^0 \to D_s^- \pi^+$ for the 7 TeV and 8 TeV datasets, separately for the four trigger categories, are given in Fig. 20.2. In the fit for the $B_s^0 \to \phi\phi$ physics parameters, the decay-time dependent decay rates are corrected for by the decay-time acceptance in the corresponding bin of these histograms.

[2] The decay time t of the $B_s^0 \to D_s^- \pi^+$ candidates in the numerator refers to the reconstructed decay time and the decay time t used to generate the pseudo datasets in the denominator corresponds to the true decay time. Differences of the reconstructed and the true decay time are neglected for the decay-time acceptance.

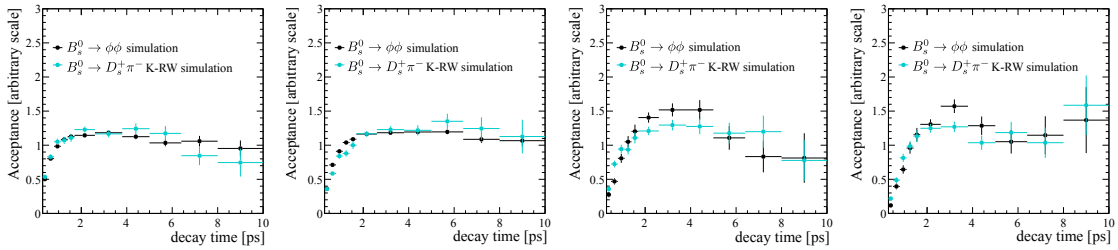

Figure 20.1: Simulated decay-time acceptances for the signal channel $B_s^0 \to \phi\phi$, shown by the black points, and the control mode $B_s^0 \to D_s^-\pi^+$, given by the cyan points obtained from fully simulated 8 TeV decays. Weights have been assigned to the $B_s^0 \to D_s^-\pi^+$ events such that the distribution of the minimum transverse momentum of the four tracks agrees with the one from $B_s^0 \to \phi\phi$ decays. From left to right, the acceptances are shown for the trigger categories (L0Hadron and Hlt2IncPhi), (not L0Hadron and Hlt2IncPhi), (L0Hadron and not Hlt2IncPhi) and (not L0Hadron and not Hlt2IncPhi), defined in Chap. 18.

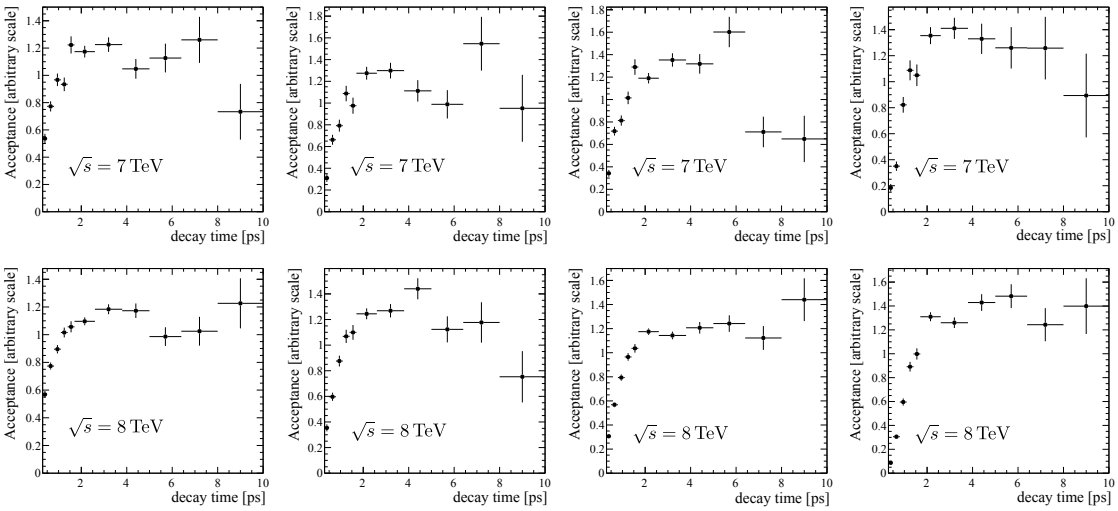

Figure 20.2: Decay-time acceptance of the control mode $B_s^0 \to D_s^-\pi^+$, obtained from the (first row) 7 TeV and (second row) 8 TeV datasets. Weights have been assigned to the events such that the distribution of the minimum transverse momentum of the four tracks agrees with the one from $B_s^0 \to \phi\phi$ decays. From left to right, the acceptances are shown for the trigger categories (L0Hadron and Hlt2IncPhi), (not L0Hadron and Hlt2IncPhi), (L0Hadron and not Hlt2IncPhi) and (not L0Hadron and not Hlt2IncPhi), defined in Chap. 18.

20.3 Determination of the angular acceptance correction

The angular acceptance is obtained from fully simulated $B_s^0 \to \phi\phi$ signal decays. Since these events have been generated with geometrical selection criteria applied to reduce the

computational effort, the total number of generated events is not accessible either. As it was done for the decay-time acceptance, a pseudo dataset is generated according to the theoretical decay rates and the angular acceptance is determined by comparing the reconstructed angular distributions from simulation with the generated distributions:

$$\varepsilon_{\text{acc}}(\Omega_i) \;\propto\; \frac{N_{\text{acc}}(\Omega_i)}{N_{\text{gen}} \int \mathrm{d}t \int\limits_{\Omega_i} \mathrm{d}\Omega \; s(t, \Omega|\vec{a})}, \tag{20.4}$$

where N_{gen} is the number of generated events of the pseudo-dataset and $s(t, \Omega|\vec{a})$ is integrated over the full true decay time and the corresponding Ω_i range in bin i. The physics parameters that are used to generate the pseudo dataset are the same as the ones that were used for the fully simulated $B_s^0 \to \phi\phi$ signal decays.

The one-dimensional projections of the three-dimensional angular acceptance are drawn in Fig. 20.3. Since the absolute scale depends on the number of generated events of the pseudo dataset, only the relative acceptance is shown. The shape is flat in the angle Φ, but the acceptance drops towards $\cos\theta_i \to \pm\, 1$ which is due to the selection requirements on the transverse momenta of the kaons. For small opening angles, the kaons move along the flight direction of the B_s^0 meson and thus, have small transverse momenta which fail the selection criteria.

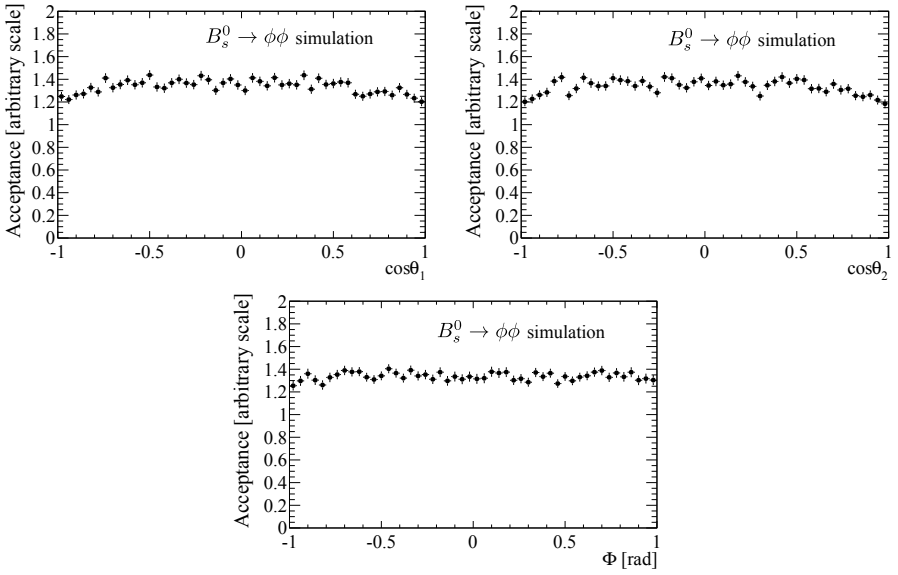

Figure 20.3: One-dimensional projections of the three-dimensional angular acceptance for the $B_s^0 \to \phi\phi$ signal decay, obtained from fully simulated 8 TeV signal decays. It is determined by the ratio of the reconstructed angular distributions to the theoretical distributions, generated with a pseudo dataset. As it depends on the number of generated events, the scale is arbitrary and only the shape is of importance.

20.3.1 Treatment of the angular acceptance correction

The angular acceptance is used to assign weights to each of the 15 angular terms of the theoretical decay rate, described in Sec. 16.4.2. This so-called method of normalisation weights is reviewed in detail in Refs. [95] and [96]. Resolution effects of the decay angles have been found to be negligible in previous studies with $B_s^0 \to J/\psi\,\phi$ decays [97] and are neglected in the complete analysis.

The maximum likelihood fit procedure has been reviewed in Sec. 4.1 and the corresponding signal PDF $s(t, \Omega|\vec{a})$ has been introduced in Eq. 16.29[3] as the sum of the decay rates of the produced B_s^0 and $\overline{B}_s^0$ mesons. As this PDF does not include resolution effects, t and Ω refer to the true decay time and decay angles. Denoting $S(t, \Omega|\vec{a})$ as the unnormalised signal PDF and correcting it for the angular acceptance, the process of maximising the logarithmic likelihood function, $\mathcal{L}$, is equal to determining the root of the derivative

$$\frac{\partial}{\partial a_j} \log \mathcal{L} = \frac{\partial}{\partial a_j} \sum_e^{N_{\rm ev}} \log \frac{S(t_e, \Omega_e|\vec{a})\ \varepsilon_{\rm acc}(\Omega_e)}{\int\int S(t, \Omega|\vec{a})\ \varepsilon_{\rm acc}(\Omega)\ {\rm d}t{\rm d}\Omega} = 0, \tag{20.5}$$

where t_e and Ω_e correspond to the reconstructed decay time and decay angles of the event e. Differences between the reconstructed and the true values are neglected in the determination of the acceptance. The number of events is denoted by $N_{\rm ev}$ and a_j is the j^{th} parameter of the set of physics parameters, $\vec{a}$. Using the logarithmic identity, $\log(S\ \varepsilon_{\rm acc})$ $= \log(S) + \log(\varepsilon_{\rm acc})$, and the fact that the acceptance does not depend on the set of parameters $\vec{a}$, the equation is further simplified to

$$\frac{\partial}{\partial a_j} \log \mathcal{L} = \frac{\partial}{\partial a_j} \sum_e^{N_{\rm ev}} \log \frac{\sum_i^{15} K_i(t_e|\vec{a}) f_i(\Omega_e)}{\sum_i^{15} \int K_i(t|\vec{a}){\rm d}t\ \int f_i(\Omega)\varepsilon_{acc}(\Omega){\rm d}\Omega} = 0, \tag{20.6}$$

where $K_i(t|\vec{a})$ is the time-dependent and $f_i(\Omega)$ the angular-dependent part of the PDF of a B_s^0 or a $\overline{B}_s^0$ meson. The angular part $f_i(\Omega)$ does not depend on the physics parameters and hence, the integral factorises. For each of the 15 terms, the normalisation of the angular function f_i, corrected for the acceptance, is given by the normalisation weight

$$\xi_i = \int f_i(\Omega)\varepsilon_{\rm acc}(\Omega){\rm d}\Omega. \tag{20.7}$$

It should be noted that the uncorrected weights vanish for the interference terms, $i = 4, 5, 6, 9\text{-}15$, and are given by $32/9\pi$ for the pure squared amplitudes, $i = 1, 2, 3, 7, 8$. They are independent from the physics parameters and thus, can be determined before the fit. Due to kinematic selection criteria, the acceptance does not only depend on the angles, but also on kinematic observables such as momenta and impact parameters. Denoting the set of these observables as $\vec{z}$, the normalization weights are written as

$$\xi_i = \int \frac{\int f_i(\Omega)\ \varepsilon_{\rm acc}(\Omega, \vec{z})\ s(t, \Omega, \vec{z}|\vec{a})\ {\rm d}\vec{z}}{s(t, \Omega|\vec{a})} {\rm d}\Omega, \tag{20.8}$$

where $s(t, \Omega|\vec{a}) = \int s(t, \Omega, \vec{z}|\vec{a}){\rm d}\vec{z}$, with $s(t, \Omega, \vec{z}|\vec{a}){\rm d}\vec{z}{\rm d}\Omega$ as the probability that a simulated

[3] $s(t, \Omega|\vec{a}) = \frac{(1+q)}{2} \frac{{\rm d}\Gamma(B_s^0 \to \phi\phi)}{{\rm d}t{\rm d}\Omega} + \frac{(1+q)}{2} \frac{{\rm d}\Gamma(\overline{B}_s^0 \to \phi\phi)}{{\rm d}t{\rm d}\Omega}$, where q = 1 for a B_s^0 meson and q = -1 for a $\overline{B}_s^0$ meson

event is generated with observables $(\Omega, \vec{z})$ within the range $[\Omega, \Omega + \mathrm{d}\Omega]$ and $[\vec{z}, \vec{z} + \mathrm{d}\vec{z}]$. Using fully simulated decays, the integral is approximated by the sum over all generated events and the normalisation weight can be written as [96]

$$\begin{aligned} \xi_i \simeq & \frac{1}{N_{\mathrm{gen}}} \sum_{e}^{N_{\mathrm{gen}}} \frac{f_i(\Omega_e)\varepsilon(t_e, \Omega_e, z_e)}{s(t_e, \Omega_e|\vec{a})}, \\ = & \frac{1}{N_{\mathrm{gen}}} \sum_{e}^{N_{\mathrm{acc}}} \frac{f_i(\Omega_e)}{s(t_e, \Omega_e|\vec{a})}, \end{aligned} \tag{20.9}$$

where N_{gen} is the number of generated events and N_{acc} is the number of reconstructed and selected events. In the first of the two equations, the efficiency for each individual event, $\varepsilon(t_e, \Omega_e, z_e)$, is one when the event is accepted and zero when it is rejected. It should be noted that the overall number of generated events factors out in the process of maximising the likelihood.

The angular acceptance weights, normalised to $9/(32\pi)$, calculated with the 7 TeV and 8 TeV simulated datasets are tabulated in Table 20.1. As expected, the values are close to one and zero, respectively, with only small deviations from the case without acceptance correction. Possible differences between the angular acceptance observed in simulation and real data are corrected for in the next subsection.

Table 20.1: Angular acceptance weights, computed with fully simulated 7 TeV and 8 TeV events with Eq. 20.9. These will be corrected for differences seen in simulation and data in the next subsection.

acc. weight	7 TeV $[9/(32\pi)]$	8 TeV $[9/(32\pi)]$
ξ_1	0.973 ± 0.006	0.973 ± 0.006
ξ_2	1.009 ± 0.006	1.017 ± 0.006
ξ_3	1.015 ± 0.004	1.024 ± 0.004
ξ_4	0.000 ± 0.007	0.004 ± 0.008
ξ_5	0.015 ± 0.008	0.004 ± 0.008
ξ_6	0.000 ± 0.006	-0.007 ± 0.006
ξ_7	1.006 ± 0.005	1.001 ± 0.005
ξ_8	0.997 ± 0.007	0.984 ± 0.007
ξ_9	-0.026 ± 0.020	-0.017 ± 0.020
ξ_{10}	-0.017 ± 0.010	-0.005 ± 0.010
ξ_{11}	-0.015 ± 0.011	0.012 ± 0.011
ξ_{12}	-0.010 ± 0.009	0.015 ± 0.009
ξ_{13}	-0.018 ± 0.018	-0.021 ± 0.018
ξ_{14}	-0.009 ± 0.014	0.012 ± 0.015
ξ_{15}	0.001 ± 0.011	-0.001 ± 0.011

20.3.2 Correction for differences between simulated and real acceptances

Possible deviations of the angular acceptance in simulation and real data can arise from differences between distributions of kinematic variables. These can be due to reconstruction effects as well as the choice of the physics parameters that were used to generate the simulated events. In order to reduce the differences, an iterative re-weighting method is performed according to Ref. [98]. Weights are assigned to the simulated events such that distributions of the BDT response and the transverse momenta of the ϕ mesons agree with the data. Additionally, differences of the theoretical decay rates when inserting the fitted physics parameters from data and the parameters used to generate the simulated events, $\vec{a}_{\mathrm{MC}}$, are corrected for. This is done iteratively because the decay kinematics depends on the physics parameters. The iterative method is performed as follows. The normalisation weights of Table 20.1 are applied in a preliminary fit to the data and a set of fitted $B_s^0 \to \phi\phi$ physics parameters, $\vec{a}_0$, is extracted. In a first re-weighting procedure, the simulated events are assigned weights such that the distribution of the BDT response agrees with the data. After that, another set of weights, $w(\Omega)$, is applied that corrects for the difference of the angular signal PDF, $s(\Omega|\vec{a})$, for the fitted set of physics parameters and the generated set of parameters of the simulated events:

$$w_0(\Omega) = \frac{s(\Omega|\vec{a}_0)}{s(\Omega|\vec{a}_{\mathrm{MC}})}. \tag{20.10}$$

Finally, the simulated events are re-weighted with two-dimensional histograms such that the transverse momenta of the two ϕ mesons agree with the data. Thus, the simulated events are re-weighted three times and then used to obtain new normalisation weights, $\vec{\xi}$(iter. 1). These are applied in a second fit to the data which result in a new set of physics parameters, $\vec{a}_1$. Using this new set, the sequential re-reweighting of the theoretical decay rates and the ϕ momenta is repeated and a third set of normalisation weights $\vec{\xi}$(iter. 2) and physics parameters $\vec{a}_2$ is determined. In each iteration, new estimates of the normalisation weights and physics parameters are computed until changes per iteration become small. Following this procedure, the normalisation weights are given in Table. 20.2. As the values of the second iteration remain almost unchanged compared to the first iteration, they will be used for the nominal fit of the $B_s^0 \to \phi\phi$ physics parameters in Chap. 24.

The re-weighting procedure is repeated using the transverse momentum distributions of the B_s^0 candidates instead of the BDT response to re-weight the simulation in the first step. This has a negligible effect on the normalisation weights. Therefore, differences of the transverse momentum distributions of the B_s^0 candidates in simulation and data are irrelevant for the angular acceptance.

Table 20.2: Angular acceptance weights computed with fully simulated 7 TeV and 8 TeV events after correcting for differences in the BDT response of simulated events and data. This is done using the iterative method described in the text. The weights of iteration 2 will be used in the nominal fit to the $B_s^0 \to \phi\phi$ physics parameters in Chap. 24.

	7 TeV $[9/(32\pi)]$			8 TeV $[9/(32\pi)]$	
acc. weight	iter. 1	iter. 2		iter. 1	iter. 2
ξ_1	0.980	0.980		0.982	0.982
ξ_2	1.004	1.004		1.010	1.011
ξ_3	1.010	1.010		1.016	1.016
ξ_4	0.001	0.001		0.005	0.005
ξ_5	0.016	0.016		0.002	0.002
ξ_6	0.001	0.0001		–0.006	–0.006
ξ_7	1.006	1.006		1.001	1.001
ξ_8	1.000	1.000		0.990	0.990
ξ_9	–0.020	–0.020		–0.005	–0.005
ξ_{10}	–0.017	–0.018		–0.003	–0.003
ξ_{11}	–0.014	–0.014		0.010	0.011
ξ_{12}	–0.009	–0.009		0.015	0.015
ξ_{13}	–0.014	–0.014		–0.008	–0.008
ξ_{14}	–0.009	–0.008		0.015	0.015
ξ_{15}	–0.002	0.001		0.003	–0.003

21 Determination of the initial B_s^0 production flavour

The knowledge of the initial flavour states of the B_s^0 mesons is crucial to determine the B_s^0-$\overline{B}_s^0$ oscillations in time and measure the CP asymmetry. The determination of the initial B_s^0 production flavour is called *flavour tagging*. It exploits characteristic signatures of the hadronisation process in the vicinity of the B_s^0 and the fact that b quarks are produced as quark anti-quark pairs. At LHCb, there are two different methods of flavour tagging, the *opposite-side* (OS) [99] and *same-side* (SS) [100] tagging algorithms that are illustrated in Fig. 21.1 and described in the following. The $b\bar{b}$-quark pair is produced at the proton-proton interaction point and the $\bar{b}$ quark hadronises to form the signal B_s^0 meson in the upper half. The corresponding b quark in the lower half can hadronise to any b hadron such as a B^- meson.

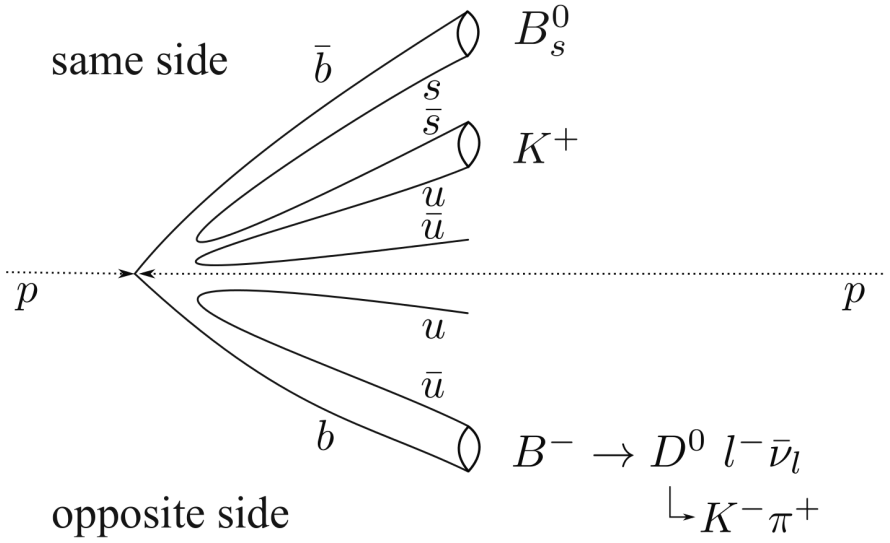

Figure 21.1: Illustration of the flavour-tagging algorithms to determine the initial production flavour of the signal $\overline{B}_s^0$. The same-side tagging algorithm is shown in the upper half and the opposite-side tagging algorithm in the lower half.

- The **opposite-side** tagging algorithm obtains the flavour of the signal B_s^0 from the decay of the other b hadron. This is possible when the final-state particles of the decay exhibit flavour-specific charges such as in semileptonic decays. In the case shown here, the flavour of the b quark is determined by the charge of the lepton l

and the kaon originating from the D^0 decay. The combined information forms the so-called opposite-side tagging decision.

- The **same-side** tagging algorithm profits from the fact that the s quark of the signal B_s^0 meson is produced together with an $\overline{s}$ quark. As sketched in the upper half of Fig. 21.1, it forms a hadron, with a probability of about 50% a kaon, in the vicinity of the B_s^0. Hence, the flavour of the $\overline{b}$ quark is defined by the charge of the $\overline{s}$-quark hadron. The combined information forms the so-called same-side tagging decision.

The flavour-tagging decision, q, provided by the taggers is defined as $q = 1$ for a tagged B_s^0, $q = -1$ for a $\overline{B}_s^0$ and $q = 0$ for an untagged b meson. The tagging efficiency, ε_{tag}, is defined by the ratio between the events, for which the tagging algorithms are able to deliver a tagging decision, N_{tagged}, and the total number of events N_{tot}:

$$\varepsilon_{\text{tag}} = \frac{N_{\text{tagged}}}{N_{\text{tot}}}. \tag{21.1}$$

The reliability of the tagging decision is described by the mistag probability, ω_{tag}, which is the probability that the algorithm has assigned the wrong flavour. A value of 0.5 corresponds to a random tagging decision. The largest source of wrong tag assignments is the possibility of either of the b mesons to oscillate into its anti-particle state. Due to the hadronic environment, it can also happen that uninvolved hadrons are associated with the signal meson. At LHCb, the typical mistag probability is of the order of 40%. If both algorithms provide a tagging decision, they are combined by weighting the individual decisions according to their mistag probabilities as described in Ref. [99]. If the tagging decisions are the same, the combined mistag probability, ω_{com}, is computed with

$$\omega_{\text{com}} = \left(1 \; - \; \frac{1 \; - \; \omega_{\text{ss}} \; - \; \omega_{\text{os}} \; + \; \omega_{\text{ss}}\omega_{\text{os}}}{1 \; - \; \omega_{\text{os}} \; - \; \omega_{\text{ss}} \; + \; 2\omega_{\text{ss}}\omega_{\text{os}}}\right), \tag{21.2}$$

where ω_{os} and ω_{ss} are the mistag probabilities from the opposite-side and the same-side tagging algorithms, respectively. When the two decisions are different, the tag that is determined with the smaller mistag probability, $\omega_<$, is chosen as the combined tagging decision and ω_{com} is calculated with

$$\omega_{\text{com}} = \left(1 \; - \; \frac{\omega_>(1 \; - \; \omega_<)}{\omega_>(1 \; - \; \omega_<) + \omega_<(1 \; - \; \omega_>)}\right), \tag{21.3}$$

where $\omega_>$ is the larger mistag probability of the two.

In the time-dependent decay rate of the B_s^0, introduced in Sec. 16.4.2, the mistag probability results in a dilution, $\mathcal{D}_{\text{tag}}$, of the observable B_s^0-$\overline{B}_s^0$ oscillation amplitude. It is related to the mistag probability via $\mathcal{D}_{\text{tag}} = (1 - 2\ \omega_{\text{tag}})$. Due to the dilution of the oscillation amplitude, the sensitivity to ϕ_s decreases, which is reflected in a reduced statistical power of the signal sample. The so-called effective tagging power is related to the mistag probability and the dilution via $\mathcal{P}_{\text{tag}}^{\text{eff}} = \varepsilon_{\text{tag}}\ D_{\text{tag}}^2$. It corresponds to the fraction of events which can be used in the measurement assuming no mistag probability. Considering a per-event determination of the mistag probabilities, the event-by-event dilution $\mathcal{D}_{\text{tag}}^{\text{ev}}$ and

the effective tagging power are computed with

$$\mathcal{D}_{\text{tag}}^{\text{ev}} = \sqrt{\frac{1}{N_{\text{tagged}}} \sum_{i=1}^{N_{\text{tagged}}} (1-2\omega_{\text{tag,i}})^2}, \qquad \mathcal{P}_{\text{tag}}^{\text{eff}} = \frac{1}{N_{\text{tot}}} \sum_{i=1}^{N_{\text{tagged}}} (1-2\omega_{\text{tag,i}})^2.$$

During Run I, the typical effective tagging power at LHCb is approximately 3% to 5%.

21.1 Calibration of the tagging algorithms

Similar to the per-event time resolution, the tagging algorithms provide, for each event, an estimated mistag probability which is determined by a neural network based on the occurring kinematics and is denoted as ω_{est}. The estimate is calibrated with decays in which the b quark flavour is determined by the final-state charge. The calibration is performed by the flavour-tagging group at LHCb and details of the procedure can be found in Ref. [99]. For each tagging algorithm, the linear dependence of the measured true mistag probability in the calibration modes, ω_{true}, on the estimated mistag probability ω_{est}, is used to compute the calibrated mistag probability, ω_{C}. The uncertainties of the calibration are taken into account by expressing the true mistag probability as a linear function of the calibrated mistag probability,

$$\omega_{\text{true}}(\omega_{\text{C}}) = p_0 \pm \Delta p_0/2 + (p_1 \pm \Delta p_1/2) \cdot (\omega_{\text{C}} - \langle\omega_{\text{C}}\rangle), \tag{21.4}$$

where $\langle\omega_{\text{C}}\rangle$ is the average of the calibrated mistag probabilities for all events. In case of a perfect calibration, the parameter p_0 is equal to $\langle\omega_{\text{C}}\rangle$ and the slope p_1 is one. The performance of the tagging algorithms also depends on the determined tagging decision itself. Therefore, the B_s^0 and $\overline{B}_s^0$ mesons are calibrated separately, by using a (+) and (-) sign in Eq. 21.4, respectively. Hence, the resulting tagging dilution is different for B_s^0 and $\overline{B}_s^0$ mesons, denoted by $\mathcal{D}_{\text{tag}}$ and $\overline{\mathcal{D}}_{\text{tag}}$. The calibration parameters for each tagging algorithm are given in Table 21.1. Uncertainties refer to the combined statistical and systematic uncertainties.

Table 21.1: Calibration parameters used to relate the calibrated mistag probabilities of the opposite-side (OS) and same-side (SS) tagging algorithms with the true mistag probability for each B_s^0 candidate, from private communication with the flavour-tagging group at LHCb. Uncertainties refer to the combined statistical and systematic uncertainties

Dataset	p_0	p_1	$\langle\omega_{\text{C}}\rangle$	Δp_0	Δp_1
OS	0.373 ± 0.004	0.982 ± 0.035	0.367	0.014 ± 0.001	0.066 ± 0.012
SS	0.443 ± 0.005	0.976 ± 0.091	0.438	-0.0158 ± 0.0014	0.007 ± 0.022

21.2 Tagging performance for the $B_s^0 \to \phi\phi$ signal candidates

The tagged $B_s^0 \to \phi\phi$ signal candidates are classified into three tagging categories, depending on the opposite and same-side tagging decisions: OS-tagged (OST), SS-tagged (SST) and tagged by both (OST+SST). The performance of the flavour-tagging algorithms in the three tagging categories for the selected $B_s^0 \to \phi\phi$ candidates is given in Table 21.2, separately for the 7 TeV and 8 TeV datasets. The overall effective tagging power is given by the sum of the tagging power for the three categories as 5.33% and 5.44% for the 7 TeV and 8 TeV datasets, respectively.

Table 21.2: Tagging efficiency (ε_{tag}), event-by-event dilution ($\mathcal{D}_{\text{tag}}^{\text{ev}}$) and effective tagging power ($\mathcal{P}_{\text{tag}}^{\text{eff}}$), as estimated from the data. The quoted uncertainties refer the combined statistical and systematic uncertainties.

Dataset	ε_{tag} [%]	$\mathcal{D}_{\text{tag}}^{\text{ev}}$ [%]	$\mathcal{P}_{\text{tag}}^{\text{eff}}$ [%]
7 TeV OST	12.3 ± 1.0	31.6 ± 0.2	1.23 ± 0.10
8 TeV OST	14.5 ± 0.7	32.7 ± 0.3	1.55 ± 0.08
7 TeV SST	40.2 ± 1.4	15.2 ± 2.0	0.93 ± 0.25
8 TeV SST	33.1 ± 0.9	16.0 ± 1.6	0.85 ± 0.17
7 TeV OST+SST	26.0 ± 1.3	34.9 ± 1.1	3.17 ± 0.26
8 TeV OST+SST	27.5 ± 0.9	33.2 ± 1.2	3.04 ± 0.24

22 Description of the fit procedure

The $B_s^0 \to \phi\phi$ physics parameters are determined from a four-dimensional fit to the decay-time and angular distributions of the selected $B_s^0 \to \phi\phi$ signal candidates using an unbinned maximum likelihood fit. Background contributions are subtracted on a statistical basis using the sFit technique. This chapter summarises the composition of the signal PDF and describes the incorporation of resolution, acceptance and tagging effects. The fit method is validated with pseudo experiments and fully simulated $B_s^0 \to \phi\phi$ signal decays.

22.1 Implementation of constraints on measured physics parameters

The maximum likelihood fit procedure has been reviewed in Sec. 4.1, in which the likelihood function is defined as the product of the single-event probabilities of all events. The signal PDFs for B_s^0 and $\overline{B}_s^0$ mesons, $\mathcal{P}_{B_s^0}(t, \Omega|\vec{a}_{\rm phys})$ and $\mathcal{P}_{\overline{B}_s^0}(t, \Omega|\vec{a}_{\rm phys})$, have been introduced in Sec. 16.4.2. The parameters of the theoretical decay rates, $\vec{a}_{\rm phys}$, are referred to as the *physics* parameters. In order to correct the PDFs for reconstruction effects of the detector, additional parameters occur that are denoted as *nuisance* parameters, $\vec{a}_{\rm nuis}$. The complete set of parameters is given by $\vec{a} = (\vec{a}_{\rm phys}, \vec{a}_{\rm nuis})$. As the number of $B_s^0 \to \phi\phi$ signal decays is small, the data sample does not provide enough sensitivity to fit for all physics parameters. However, some of them have already been measured independently from this analysis with other decay channels. In the fit, the already known physics and nuisance parameters are constrained within their measured uncertainties using a method called *Gaussian constraints*. For each of the constrained parameters, the signal PDF is modified by multiplying it with a Gaussian function:

$$\mathcal{P}(t, \Omega|\vec{a}) \to \mathcal{P}(t, \Omega|\vec{a}) \cdot \prod_{i=1}^{N_{\rm con}} \frac{1}{\sqrt{2\pi}\sigma_{\rm i,meas}} e^{\frac{-(a_i - a_{\rm i,meas})^2}{2\sigma^2_{\rm i,meas}}}, \tag{22.1}$$

where $N_{\rm con}$ is the number of constrained parameters, $a_{\rm i,meas}$ is the measured value of the i^{th} parameter and $\sigma_{\rm i,meas}$ is its uncertainty. The effect on the negative logarithm of the likelihood function is an additional term

$$-\log\mathcal{L} = -\sum_{e=1}^{N_{\rm ev}} \left\{ \log\mathcal{P}(t_e, \Omega_e|\vec{a}) - \sum_{i=1}^{N_{\rm con}} \frac{(a_i - a_{\rm i,meas})^2}{2\sigma^2_{\rm i,meas}} \right\}, \tag{22.2}$$

where constant normalisation terms are omitted. In this way, the negative logarithmic likelihood increases quadratically with the deviation of the fitted parameter a_i from the measured value $a_{\rm i,meas}$, which makes it less likely. Since the constrained parameters are allowed to be varied within their measured uncertainties, the computed uncertainties of the physics parameters include the uncertainties due to variations of the constrained parameters.

Hence, these uncertainties do not have to be considered as systematic uncertainties. The parameters that are constrained in the fit are described in the following sections. These are the B_s^0 mixing parameters and the nuisance parameters describing the decay-time resolution and the calibration of the mistag probabilities.

22.2 Description of the signal PDF

The decay-time and angular-dependent signal PDFs of B_s^0 and $\overline{B}_s^0$ mesons decaying into two ϕ mesons are formed by the sum of 15 terms of which each can be separated into a time-dependent part $\mathrm{K}_i(t)$ and an angular-dependent function $\mathrm{f}_i(\Omega)$. The combined differential decay rate, $s(t, \Omega, \mathcal{D}_{\mathrm{tag}}, q|\vec{a}_{\mathrm{phys}})$, of the produced B_s^0 and $\overline{B}_s^0$ mesons is written as

$$s(t, \Omega, \mathcal{D}_{\mathrm{tag}}, q|\vec{a}_{\mathrm{phys}}) = \frac{1 + q\mathcal{D}_{\mathrm{tag}}}{2}\ \mathcal{P}_{B_s^0}(t, \Omega|\vec{a}_{\mathrm{phys}}) + \frac{1 + q\overline{\mathcal{D}}_{\mathrm{tag}}}{2}\ \mathcal{P}_{\overline{B}_s^0}(t, \Omega|\vec{a}_{\mathrm{phys}}), \qquad (22.3)$$

where q is the tagging decision and $\overset{(-)}{\mathcal{D}}_{\mathrm{tag}}$ is the tagging dilution of the produced B_s^0 and $\overline{B}_s^0$ mesons, respectively. The set of physics parameters is formed by $\vec{a}_{\mathrm{phys}} = (\phi_s,\, \Gamma_s,\, \Delta\Gamma_s,\, \Delta m_s,\, |A_0|^2,\, |A_\parallel|^2,\, |A_\perp|^2,\, \delta_\parallel,\, \delta_\perp,\, \delta_0,\, |A_S|^2,\, |A_{SS}|^2,\, \delta_S,\, \delta_{SS})$. The difference of the heavy and light mass eigenstates of the B_s^0 meson, Δm_s, is obtained from measurements at LHCb using $B_s^0 \to D_s^- \pi^+$ decays [75]. The decay width, Γ_s, and the difference of decay widths, $\Delta\Gamma_s$, have been extracted in a combined analysis from $B_s^0 \to J/\psi\,\phi$ and $B_s^0 \to J/\psi\,\pi^+\pi^-$ decays [76]. Table 22.1 shows their measured values that are constrained in the fit within their uncertainties using Gaussian constraints. The correlation of 0.1 between the fitted values of Γ_s and $\Delta\Gamma$ is taken into account by multiplying a multi-variate Gaussian function to the PDF, instead of two simple Gaussian functions.

Table 22.1: Summary of the known B_s^0 mixing parameters, Δm_s, Γ_s and $\Delta\Gamma_s$. In the fit for the $B_s^0 \to \phi\phi$ physics parameters, they are constrained to these values using Gaussian constraints. The correlation of 0.1 between Γ_s and $\Delta\Gamma_s$ is taken into account in the fit.

parameter	constrained value
Γ_s [ps^{-1}]	0.661 ± 0.007 [76]
$\Delta\Gamma_s$ [ps^{-1}]	0.106 ± 0.013 [76]
Δm_s [ps^{-1}]	17.768 ± 0.024 [75]

The sum of the P-wave polarisation amplitudes are defined such that they sum up to unity, $|A_0|^2 + |A_\parallel|^2 + |A_\perp|^2 = 1$, and only $|A_0|^2$ and $|A_\perp|^2$ are determined in the fit. As the absolute phases are not observable quantities but only phase differences, the phases can be re-defined in order to minimise correlations between the phases. The relation between the strong phases is expressed by fitting the differences $\delta_1 = \delta_\perp - \delta_\parallel$ and $\delta_2 = \delta_\perp - \delta_0$, where δ_0 is zero in the chosen convention.

The number of $B_s^0 \to \phi\phi$ signal candidates have been determined in Chap. 18 in a fit to the invariant four-kaon mass distribution. This fit is used to assign sWeights to each

event, as described in Sec. 4.2. Therefore, the fit method to extract the $B_s^0 \to \phi\phi$ physics parameters is an unbinned maximum likelihood fit using the sFit technique. It simplifies the fitting procedure drastically as the background does not have to be modelled in terms of decay time and decay angles.

22.2.1 S-wave parameters for small di-kaon mass intervals

In order to account for a dependence of the S-wave parameters on the invariant di-kaon mass of the ϕ-meson candidates, m_ϕ, the invariant di-kaon mass distribution is divided into two regions as described in Sec. 16.4.2: below the known ϕ-meson mass, $m_\phi^{\rm PDG}$ and above. For two final-state ϕ mesons, this leads to four bins in the two-dimensional mass grid. However, two of these bins are symmetric and are joined into one bin as the particles are identical. The three bins are defined as follows:

- M_{Q1}: $\left(m_{\phi_1} < m_\phi^{\rm PDG}\ \&\ m_{\phi_2} < m_\phi^{\rm PDG}\right)$
- M_{Q2}: $\left(\ (m_{\phi_1} < m_\phi^{\rm PDG}\ \&\ m_{\phi_2} > m_\phi^{\rm PDG})\ ||\ (m_{\phi_1} > m_\phi^{\rm PDG}\ \&\ m_{\phi_2} < m_\phi^{\rm PDG})\ \right)$
- M_{Q3}: $\left(m_{\phi_1} > m_\phi^{\rm PDG}\ \&\ m_{\phi_2} > m_\phi^{\rm PDG}\right)$

M_{Q1} corresponds to the region for which both ϕ-meson candidates have invariant masses smaller than the known ϕ mass. M_{Q2} refers to the case that one ϕ-meson candidate has an invariant mass smaller than the known ϕ mass and one larger, and in the third region M_{Q3}, both ϕ-meson candidates have invariant masses larger than the known ϕ mass. The effective coupling factor, $C_{\rm SP}$, between the S-wave and P-wave amplitudes for the chosen mass intervals has been determined in Sec. 16.4.2 as 0.69.

22.3 Implementation of reconstruction effects

Reconstruction effects that have to be taken into account are the dilution due to imperfect tagging algorithms, the finite decay-time resolution and the decay-time and angular acceptance corrections. As already mentioned in Sec. 20.3, resolution effects of the decay angles are neglected in this analysis because their impact has been found to be negligible.

22.3.1 Dilution due to tagging

The tagging dilution, $\overset{(-)}{\mathcal{D}}_{\rm tag} = (1 - 2\,\overset{(-)}{\omega}_{\rm C})$, is already included in the combined differential decay rate of Eq. 22.3, where $\overset{(-)}{\omega}_{\rm C}$ refers to the calibrated mistag probability of the produced B_s^0 and $\overline{B}_s^0$ mesons, respectively. As discussed in Chap. 21, the uncertainties on the calibrated mistag probability are taken into account with the calibration parameters, p_0, Δp_0, p_1, Δp_1 and $\langle\omega_{\rm C}\rangle$, which are given for each tagging category in Table 21.1. In the fit, the parameters p_0, p_1, Δp_0 and Δp_1 are constrained to their determined values within their uncertainties, separately for the opposite-side and the same-side tagged events. The parameter $\langle\omega_{\rm C}\rangle$ is fixed to its pre-determined value. When both tagging algorithms provide a tagging decision, they are combined according to Eq.s 21.2 and 21.3 as described in Chap. 21.

22.3.2 Acceptance and resolution effects

The signal PDF $\mathcal{P}_{B_s^0}(t, \Omega|\vec{a})$ does not include detector acceptance and resolution effects such that differences between the reconstructed decay time t and the true decay time t' are not taken into account. The reconstruction effects are incorporated in the fit by multiplying the signal PDF with the acceptance, $\varepsilon_{\text{acc}}(t.\Omega)$, and convoluting it with the resolution function $R(t - t', \delta|q_0, q_1)$

$$\mathcal{P}_{B_s^0}(t, \Omega|\vec{a}) \;\rightarrow\; \frac{\varepsilon_{\text{acc}}(t, \Omega) \cdot \mathcal{P}_{B_s^0}(t, \Omega|\vec{a}) \otimes R(t, \delta|q_0, q_1)}{\int \varepsilon_{\text{acc}}(t, \Omega) \cdot \mathcal{P}_{B_s^0}(t, \Omega|\vec{a}) \otimes R(t, \delta|q_0, q_1) \mathrm{d}t \mathrm{d}\Omega}, \tag{22.4}$$

where the resulting PDF has to be re-renormalised. The resolution is modelled by a single Gaussian function with mean zero and the width $\sigma_{\text{eff}}(\delta) = q_0 + q_1\delta$. The parameters q_0 and q_1 to calibrate the estimated per-event decay-time error δ are given in Table 19.1. In the fit, the calibration parameters are constrained to their values within their uncertainties, separately for the 7 TeV and 8 TeV datasets. The decay-time acceptance histograms have been determined in Sec. 20.2 and are shown in Fig. 20.2. They are applied by directly multiplying the signal PDF with the acceptance $\varepsilon_{\text{acc}}(t)$ in the corresponding bin of the histograms. The angular acceptance weights, ξ_i, given in Table 20.1, are used to re-normalise the angular functions $f_i(\Omega)$ to correct for the angular acceptance:

$$\mathcal{P}_{B_s^0}(t, \Omega|\vec{a}) \;\rightarrow\; \frac{\varepsilon_{\text{acc}}(t) \cdot \mathcal{P}_{B_s^0}(t, \Omega|\vec{a}) \otimes R(t, \delta|q_0, q_1)}{\int \varepsilon_{\text{acc}}(t) \cdot \sum_i^{15} \xi_i \; K_{B_s^0,i}(t|\vec{a}) \otimes R(t, \delta|q_0, q_1) \mathrm{d}t} \tag{22.5}$$

Both of the acceptances are fixed to their determined values and their uncertainties are used to estimate the relevant systematic uncertainties.

22.4 Implementation of a simultaneous fit in subsets of the dataset

In order to take into account differences in the run conditions and detector effects, the complete dataset is split into several subsets that are distinguished by:

- two centre-of-mass energies of 7 TeV and 8 TeV
- four trigger categories, defined in Chap. 18
- three regions M_{Q1}, M_{Q2} and M_{Q3} of the invariant di-kaon mass of the two ϕ-meson candidates, just defined before in Sec. 22.2.1
- three tagging categories OS-tagged (OST), SS-tagged (SST) and tagged by both (OST+SST)

The CP parameters, ϕ_s and $|\lambda_{\text{CP}}|$, and the P-wave polarisation amplitudes and phases are shared between the subsets. The resolution and acceptance parameters are specific for each centre-of-mass energy, where the decay-time acceptance additionally depends on the trigger category. Due to the dependence of the S-wave and SS-wave parameters on the invariant di-kaon mass, they are determined independently for each of the three

regions of the invariant di-kaon mass of the two ϕ-meson candidates. The effective coupling factor, C_{SP}, is fixed to 0.69 for all of three regions. The tagging calibration parameters are determined independently for the two tagging categories, OST and SST. When a B_s^0 candidate is tagged by both algorithms, they are combined as described before. A summary of all fit parameters and their treatment in the fit is given in Table 22.2. In total, 33 parameters are determined in the fit of which 15 are constrained within their measured uncertainties. The remaining 18 parameters are the CP parameters, ϕ_s and $|\lambda_{\mathrm{CP}}|$, the P-wave polarisation amplitudes and phases and the S-wave parameters of the three mass regions of the two ϕ-meson candidates.

Table 22.2: Summary of the fit parameters and their treatment in the fit to the $B_s^0 \to \phi\phi$ signal decays. The fourth column indicates for which subsets of the data they are determined independently.

	parameter	treatment	specific for subset
physics parameters	ϕ_s, $\lvert\lambda_{\mathrm{CP}}\rvert$, $\lvert A_0\rvert^2$, $\lvert A_\perp\rvert^2$, δ_1, δ_2	free	shared between subsets
	Γ_s, $\Delta\Gamma_s$, Δm_s	constrained	
	$\lvert A_\parallel\rvert^2$	(1-$\lvert A_0\rvert^2$-$\lvert A_\perp\rvert^2$)	
	$\delta_\perp$	δ_2	
	$\delta_\parallel$	$\delta_2 - \delta_1$	
S-wave	$\lvert A_S\rvert^2$, $\lvert A_{SS}\rvert^2$, δ_S, δ_{SS}	free	M_{Q1}, M_{Q2}, M_{Q3}
	C_{SP}	fixed	
time resolution	q_0, q_1	constrained	7 TeV, 8 TeV
time acceptance	$\varepsilon(t)$	fixed	7 TeV, 8 TeV and trigg. cat.
ang. acceptance	ξ_i, $i = 1 - 15$	fixed	7 TeV, 8 TeV
tagging	p_0, p_1, Δp_0, Δp_1,	constrained	OST and SST
	$\langle\omega_{\mathrm{C}}\rangle$	fixed	

22.5 Validation of the fitting procedure

In order to validate the constructed maximum likelihood fit method, in particular the handling of the uncertainties and the likelihood normalisations, it is tested with pseudo experiments. In these so-called *toy studies*, events are generated according to the signal PDFs, including the parameterisation of the dilutions and acceptance effects. The fit is applied to these pseudo datasets and the fitted parameters are compared with the generated values. To validate the fitting procedure, samples are generated with a larger number of events than observed in data in order to identify even small effects in the fit procedure. One thousand sets of simulations are performed, each with 48000 signal events that are equally distributed over the subsets. The generated values of the physics parameters are the same as in the nominal result that will be discussed in Chap. 24. Several values are chosen for the CP-violating phase ϕ_s, but no dependence is found. The CP parameter $|\lambda_{\mathrm{CP}}|$ is generated with a value of 1.0 and the S-wave and SS-wave amplitudes are set to 0.05 for all regions. The obtained pull, the deviation of the fitted parameter from the

generated value, divided by the estimated statistical uncertainty, allows for an evaluation of both the fit value and the estimated uncertainty. For a successful fit procedure, the mean is distributed around zero with a width of unity. The pull distributions of the $B_s^0 \to \phi\phi$ physics parameters that are not constrained in the fit are shown in Figs. 22.1 and 22.2. All of them exhibit a Gaussian-shaped peak with means and widths that are compatible with zero and one, respectively. Thus, the generated values are correctly recovered and their statistical uncertainties properly computed.

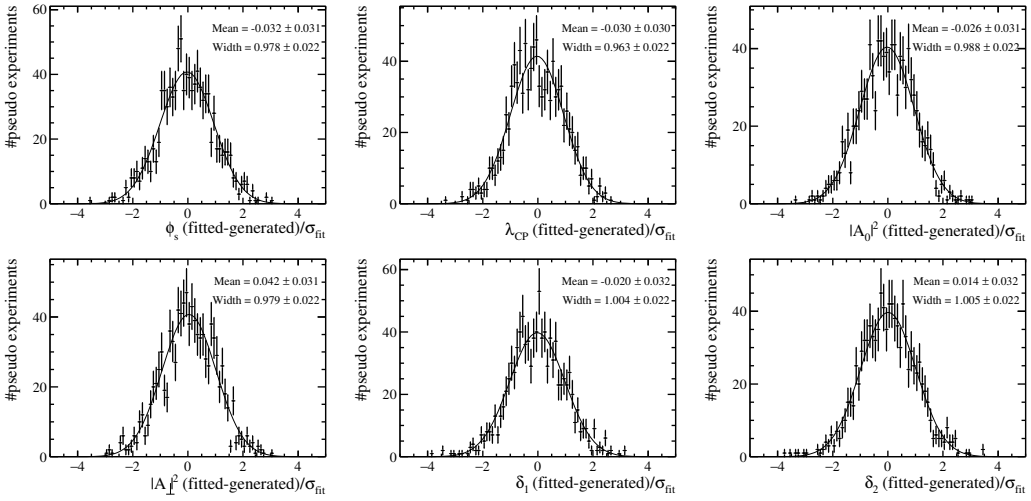

Figure 22.1: Pull distributions of ϕ_s $|\lambda_{\mathrm{CP}}|$, and the P-wave polarisation amplitudes and phases, obtained from 1000 pseudo experiments with 48000 generated events each. The fit functions are Gaussian functions.

22.5.1 Sensitivity study

When generating the pseudo experiments with the same number of events as observed in data, toy studies provide an estimate of the statistical uncertainties of the fitted parameters. Figure 22.3 shows the distributions of the uncertainties of the CP parameters, ϕ_s and $|\lambda_{\mathrm{CP}}|$, and the P-wave polarisation amplitudes and phases, obtained from 2000 pseudo experiments. For each toy dataset, the number of generated events corresponds to the number of selected $B_s^0 \to \phi\phi$ signal decays in data. The distribution over the subsets is chosen accordingly. The expected sensitivities for the CP parameters ϕ_s and $|\lambda_{\mathrm{CP}}|$ are 0.15(1) rad and 0.06(1), respectively. This is comparable with the observed statistical uncertainties that will be compared to the expected sensitivities in Sec. 24.1.1.

22.5.2 Validation with fully simulated events

Another way to validate the fitting procedure is to test it with fully simulated $B_s^0 \to \phi\phi$ signal decays. Since the simulation includes the modelling of the kinematics of the related particles and the reconstruction of the decay with the detector, the correct extraction of the physics parameters also confirms the calculation of the helicity angles and the

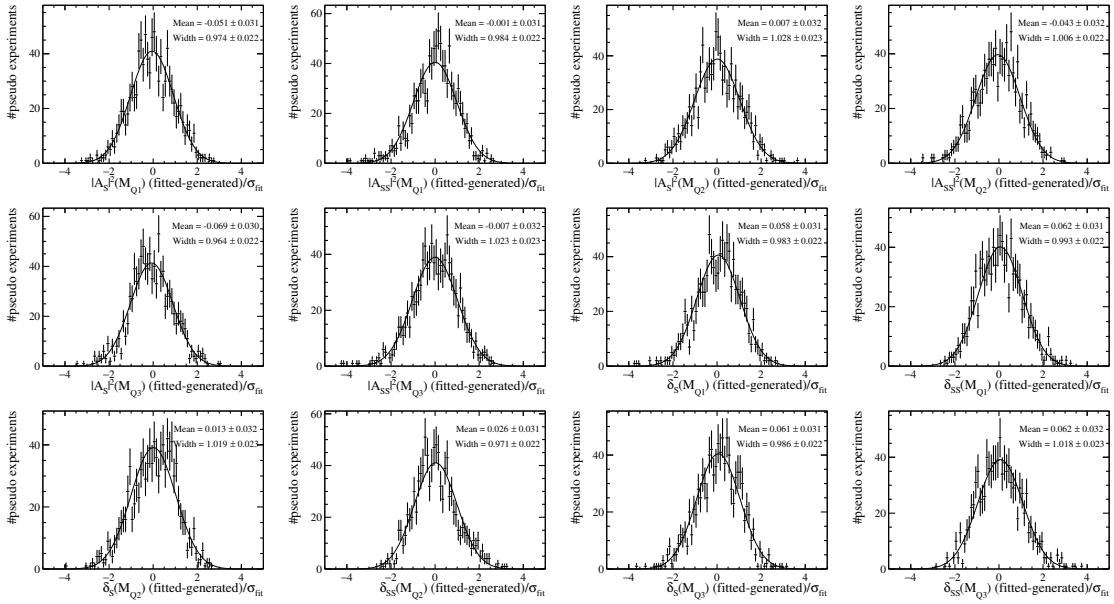

Figure 22.2: Pull distributions of the S-wave and SS-wave amplitudes and phases for the three mass regions of the ϕ-meson candidates, obtained from 1000 pseudo experiments with 48000 generated events each. The fit functions are Gaussian functions.

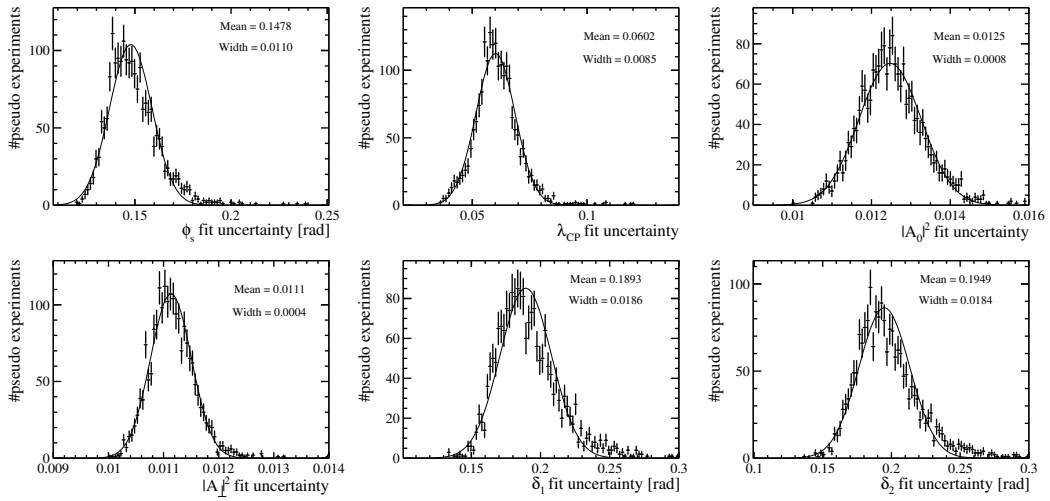

Figure 22.3: Distributions of the fitted uncertainties of the CP parameters, ϕ_s and $|\lambda_{\rm CP}|$, and the P-wave polarisation amplitudes and phases, obtained from 2000 pseudo experiments. Each generated dataset contains the same number of $B_s^0 \to \phi\phi$ signal events as observed in data. The distributions are fitted with a Gaussian function.

implementation of the acceptance corrections. To perform this validation, the decay-time acceptance has been extracted from the simulated events and no iterative re-weighting procedure is applied for the angular normalisation weights. Flavour tagging is performed using an average mistag probability for all b-meson candidates. Since the S-wave amplitudes are not generated for the simulated events, they are fixed to zero. The decay width, Γ_s, and difference of the decay widths, $\Delta\Gamma_s$, are fixed to the generated values as well as the value of the B_s^0-$\overline{B}_s^0$ oscillation frequency Δm_s. The results of the fit to the fully simulated events are shown in Table 22.3. All fitted values are consistent with the generated values within statistical uncertainties.

Table 22.3: Comparison of generated and fitted physics parameters obtained from a fit to fully simulated $B_s^0 \to \phi\phi$ signal decays.

parameter	fit result	generated value
ϕ_s (rad)	-0.01 ± 0.02	0.0
$\lvert\lambda_{\rm CP}\rvert$	1.00 ± 0.01	1.0
$\lvert A_\perp\rvert^2$	0.365 ± 0.002	0.365
$\lvert A_0\rvert^2$	0.348 ± 0.002	0.348
δ_1 (rad)	-0.33 ± 0.03	-0.32
δ_2 (rad)	2.37 ± 0.03	2.39

23 Estimation of systematic uncertainties

The measurement of the $B_s^0 \to \phi\phi$ physics parameters is subject to various sources of systematic uncertainties that are summarised in Table 23.2 and described in detail in this chapter. As described previously, the uncertainties on the parameters that are constrained to their pre-determined values within their uncertainties do not have to be considered as systematic uncertainties as these uncertainties are taken into account by the statistical uncertainty of the fitted parameters.

23.1 Mass model

The number of $B_s^0 \to \phi\phi$ signal decays is obtained from a fit to the invariant four-kaon mass distribution of the selected B_s^0 candidates in Sec. 18.4. This result is used to compute sWeights that are applied in the fit for the $B_s^0 \to \phi\phi$ physics parameters to subtract the background components on a statistical basis. The systematic uncertainty due to the choice of the mass model is investigated by describing the signal with a single Gaussian function instead of the sum of two. The fitted signal yields decrease from 1185 ± 35 to 1134 ± 36 and from 2765 ± 57 to 2658 ± 56 B_s^0 candidates in the 7 TeV and 8 TeV datasets, respectively. The fit for the $B_s^0 \to \phi\phi$ physics parameters is repeated with the new set of sWeights and the differences of the fitted parameters from the nominal fit results are taken as the systematic uncertainties. In order to investigate the impact of the statistical uncertainties of the nominal yields, they are varied by $\pm 1\sigma$ and fixed in the mass fit to extract new sets of sWeights. The physics parameters are determined for each set of sWeights and the maximum deviations are taken as the systematic uncertainties. The uncertainties due to the statistical uncertainties of the signal yields and the uncertainties due to the choice of the mass model are added in quadrature (see Table 23.2).

23.2 Background estimation

The uncertainties on the background yields from $B^0 \to \phi K^{*0}$ and $\Lambda_b^0 \to \phi K p$ decays, determined in Sec. 18.3, lead to additional uncertainties of the signal yields and the sWeights. The fits to the invariant four-kaon mass distribution of the selected B_s^0 candidates are repeated with varied background yields, by $\pm 1\sigma$ of the given uncertainties, for each of the components individually or simultaneously. The largest deviations of the fitted parameters from the nominal results are taken as the systematic uncertainties (see Table 23.2).

23.3 Decay-time resolution

The calibration parameters, q_0 and q_1, of the per-event decay-time resolution are not fixed to their determined values, but only constrained within their uncertainties. Therefore, their

uncertainties are included in the statistical uncertainty of the fitted physics parameters. Additional uncertainties arise from the fact that the calibration relies on fully simulated events and differences between simulated and real decay-time resolutions have been found to be of the order of 5 fs for previous analyses with $B_s^0 \to J/\psi\,\phi$ decays [2, 95]. As a systematic check, an average resolution model is applied with a single Gaussian function and the effective width obtained in Sec. 19.1. It is conservatively varied by 10 fs, upwards and downwards, which results in negligible changes of the fitted physics parameters. Therefore, no systematic uncertainty due to the decay-time resolution is assigned.

23.4 Decay-time acceptance

Systematic uncertainties on the decay-time acceptance correction arise from differences of the acceptances in the signal channel and the control mode $B_s^0 \to D_s^-\pi^+$. Pseudo experiments are used to evaluate them. Events are generated according to the decay-time acceptance determined from simulated $B_s^0 \to \phi\phi$ signal decays, but the acceptance correction that is applied in the fit for the physics parameters is the one obtained from simulated $B_s^0 \to D_s^-\pi^+$ events. In this way, the impact of applying the deviating acceptance correction is simulated. Two thousand datasets are generated, each with the same number of signal events as observed in data, and the resulting differences of the mean of the fitted physics parameters from the generated values are taken as the systematic uncertainties (see Table 23.2).

Uncertainties due to the choice of the binning scheme of the acceptance histograms are analysed by increasing the number of bins to 18. As it does not have an effect on the fit results, no additional systematic uncertainty is assigned.

23.5 Angular acceptance

The systematic uncertainties on the angular acceptance correction arise from the finite statistics of the simulated events and a possible dependence on the trigger and tagging categories. Differences between acceptances in simulation and data have been corrected for in Sec. 20.3 and no further systematic uncertainty is assigned.

Due to the finite statistics of the simulated event sample, the angular acceptance weights are subject to statistical uncertainties. The resulting impact on the physics parameters is estimated by varying the set of acceptance weights according to the uncertainties. Each acceptance weight is varied by a random number that is Gaussian distributed around zero with the uncertainty taken as the width. Correlations between the normalisation weights are taken into account. The set of acceptance weights is varied 1000 times and used in fits to the data, each at a time. For each fitted physics parameter, the distribution of the difference between the resulting fit value from the nominal result is described by a Gaussian function and the width is taken as the systematic uncertainty.

The acceptance weights have been determined globally for the 7 TeV and 8 TeV datasets. However, they can also depend, in general, on the tagging and the trigger categories. A different relative occupancy of these categories can lead to differences of the weights. Therefore, the acceptance weights are computed separately for all individual subsets of the dataset. No dependency on the trigger categories is found, but a small effect is observed

for the three tagging categories. The three sets of weights are sequentially applied in the fit and the maximum deviations of the fitted physics parameters from the nominal values are taken as the systematic uncertainties.

The systematic uncertainties due to the statistical uncertainties of the normalisation weights and the dependence of the weights on the tagging categories are added in quadrature. The resulting systematic uncertainties are dominated by the statistical uncertainties of the normalisation weights and are significant for all physics parameters (see Table 23.2).

23.6 Fit bias

The fitting procedure has been validated in Sec. 22.5 with pseudo experiments that are generated with a large number of events. The generated values of the fit parameters are correctly recovered. However, this may not be the case for the smaller number of signal events available in real data. Therefore, the toy studies are repeated with generating the same number of $B_s^0 \to \phi\phi$ signal decays as observed in data. The remaining difference between the mean of the fitted values from the generated parameters reveals a so-called systematic fit bias due to the finite number of signal events. The distributions of the fitted physics parameter values, obtained from 2000 pseudo experiments, is shown in Fig. 23.1. The mean of the fitted parameters and the generated values for the toy datasets are given in Table 23.1. For each fitted parameter, the difference between the mean of the fitted value from the generated parameter is taken as the systematic uncertainty. For most of the parameters, the fit bias is negligible but it is significant for the phases δ_1 and δ_2 (see Table 23.2).

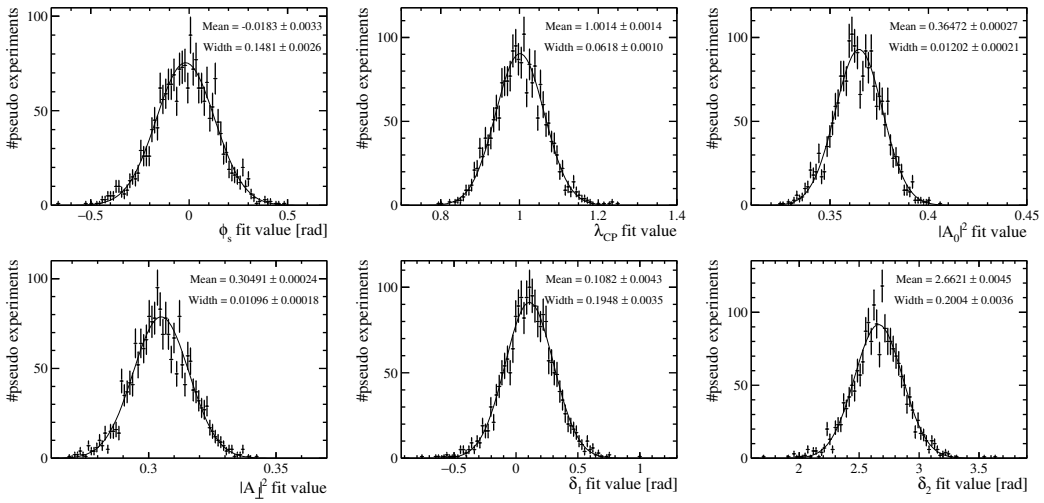

Figure 23.1: Distributions of the fitted values of ϕ_s, $|\lambda_{\rm CP}|$, and the P-wave polarisation amplitudes and phases, obtained from 2000 pseudo experiments. Each generated dataset contains the same number of signal events as observed in data. The fit functions are Gaussian functions.

Table 23.1: Comparison of the generated values and the mean of the fitted values of ϕ_s, $|\lambda_{\mathrm{CP}}|$, and the P-wave polarisation amplitudes and phases, obtained from 2000 pseudo experiments. Each generated dataset contains the same number of signal events as observed in data.

parameter	mean of the fitted values	generated value
ϕ_s [rad]	-0.0183 ± 0.0033	-0.02
$\lvert\lambda_{\mathrm{CP}}\rvert$	1.0014 ± 0.0014	1.0
$\lvert A_0\rvert^2$	0.3647 ± 0.0003	0.365
$\lvert A_\perp\rvert^2$	0.3049 ± 0.0002	0.305
δ_1 [rad]	0.108 ± 0.004	0.13
δ_2 [rad]	2.662 ± 0.005	2.65

23.7 Effective coupling of of S-wave and P-wave amplitudes

The computation of the effective coupling factors, C_{SP}, of the S- and P-wave amplitudes has been presented in Sec. 16.4.2. The dependence of the S-wave amplitude on the invariant di-kaon mass of the S-wave amplitude is parameterised by a uniform distribution which corresponds to the non-resonant production of kaon pairs. However, the kaons can also originate from an intermediate resonance state with spin 0 such as the $f_0(980)$ meson that can be modelled by a Flatté function. Table 16.3 shows the slightly deviating coupling factors with this parameterisation. When applying these values, the resulting changes of the fitted physics parameters are negligible and no systematic uncertainty is assumed.

23.8 Summary of the systematic uncertainties

The systematic uncertainties on the physics parameters of the $B_s^0 \to \phi\phi$ decay are summarised in Table 23.2. The total uncertainty is formed by the squared sum of the individual uncertainties. It is largely dominated by the uncertainties on the acceptance corrections. The overall systematic uncertainties for the CP parameters, ϕ_s and $|\lambda_{\mathrm{CP}}|$, are 0.03 rad and 0.03, respectively.

Table 23.2: Summary of the systematic uncertainties on the CP parameters, ϕ_s and $|\lambda_{\mathrm{CP}}|$, and the P-wave polarisation amplitudes and phases of the $B_s^0 \to \phi\phi$ decay. Entries marked as '–' correspond to no measurable effect.

parameter	mass model	angular acc.	fit bias	time acc.	background	total
ϕ_s [rad]	–	0.02	–	0.02	–	0.03
$\lvert\lambda_{\mathrm{CP}}\rvert$	0.02	0.02	–	–	0.01	0.03
$\lvert A_0\rvert^2$	–	0.007	–	0.005	–	0.009
$\lvert A_\perp\rvert^2$	–	0.004	–	0.003	–	0.005
δ_1 [rad]	0.03	0.02	0.02	0.02	0.01	0.05
δ_2 [rad]	0.04	0.02	0.01	0.05	0.01	0.07

24 Results

This chapter presents the fit results of the $B_s^0 \to \phi\phi$ physics parameters using 3950 $B_s^0 \to \phi\phi$ signal candidates that have been selected from the combined dataset recorded at centre-of-mass energies of 7 TeV and 8 TeV. The fit method applied to the decay-time and angular distributions of the B_s^0 and $\overline{B}_s^0$ mesons has been described in Chap. 22.

24.1 Extraction of the physics parameters

The results of the fitted $B_s^0 \to \phi\phi$ physics parameters are given in Table 24.1, where the first uncertainties refer to the statistical and the second to the systematic uncertainties. The $\star$ symbol indicates that the B_s^0 mixing parameters, Γ_s, $\Delta\Gamma_s$ and Δm_s, are constrained to their already known values in the fit, as discussed in Chap. 22. The fitted values of the CP parameters, ϕ_s and $|\lambda_{\rm CP}|$, are $-0.17 \pm 0.15 \pm 0.03$ rad and $1.04 \pm 0.07 \pm 0.03$, respectively, which is compatible with Standard-Model predictions, and thus no CP violation can be claimed. The measured values of $|A_\perp|^2$ and $|A_0|^2$ are compatible with the results of the previous LHCb measurement [71]. The fitted values of the S-wave and SS-wave parameters

Table 24.1: Results of the fitted $B_s^0 \to \phi\phi$ physics parameters. The $\star$ symbol indicates that the B_s^0 mixing parameters, Γ_s, $\Delta\Gamma_s$ and Δm_s have been constrained to their pre-determined values as discussed in Chap. 22.

parameter	best fit value
ϕ_s (rad)	$-0.17 \pm 0.15 \pm 0.03$
$\lvert\lambda_{CP}\rvert$	$1.04 \pm 0.07 \pm 0.03$
$\lvert A_\perp\rvert^2$	$0.304 \pm 0.013 \pm 0.005$
$\lvert A_0\rvert^2$	$0.365 \pm 0.012 \pm 0.009$
δ_1 (rad)	$0.12 \pm 0.23 \pm 0.05$
δ_2 (rad)	$2.67 \pm 0.23 \pm 0.07$
Γ_s (ps^{-1}) $\star$	0.662 ± 0.005
$\Delta\Gamma_s$ (ps^{-1}) $\star$	0.104 ± 0.009
Δm_s (ps^{-1}) $\star$	17.774 ± 0.024

for the three regions of the invariant di-kaon mass of the two ϕ mesons are shown in Table 24.2, where $|A_S|^2$and $|A_{SS}|^2$are in the range from 0.00 to 0.02 but consistent with zero within the large uncertainties. In $B_s^0 \to J/\psi\,\phi$ decays, the S-wave contribution has been measured to be within 2-3% relative to the summed P-wave amplitudes [4].

The correlation matrix is given in Table 24.3 for a fit with shared S-wave and SS-wave parameters between all subsets of the data. This is done for illustration purposes, but the correlations are almost identical when defining them separately for the regions. The largest correlations are observed between the amplitudes $|A_\perp|^2$and $|A_0|^2$, between the strong phase differences δ_1 and δ_2 and between the amplitude $|A_{SS}|^2$and its phase δ_{SS}. The determined correlations are verified with pseudo experiments that are generated with the same number of signal events as observed in data. It should be noted that the CP violation parameters ϕ_s and $|\lambda_{\rm CP}|$ are hardly correlated to any other parameter.

Table 24.2: Results of the fitted S-wave and SS-wave parameters for the three regions of the invariant di-kaon mass of the two ϕ mesons. M_{Q1} refers the region where both invariant di-kaon masses are smaller than the known ϕ-meson mass, M_{Q2} the region with one smaller and one larger, and M_{Q3} indicates the region with both invariant di-kaon masses larger than the known ϕ-meson mass.

region	$\lvert A_S\rvert^2$	δ_S (rad)	$\lvert A_{SS}\rvert^2$	δ_{SS} (rad)
M_{Q1}	0.006 ± 0.011	-0.37 ± 0.55	0.009 ± 0.013	-3.12 ± 1.30
M_{Q2}	0.005 ± 0.009	2.77 ± 0.41	0.004 ± 0.011	-2.14 ± 0.68
M_{Q3}	0.001 ± 0.002	-2.46 ± 2.28	0.021 ± 0.021	0.54 ± 0.53

Table 24.3: Correlation matrix associated with the fit result using shared S- and SS-wave parameters for the complete dataset. This is done for illustration purposes.

	$\lvert A_\perp\rvert^2$	$\lvert A_0\rvert^2$	$\lvert A_{SS}\rvert^2$	$\lvert A_S\rvert^2$	δ_{SS}	δ_S	δ_1	δ_2	Δm_s	ϕ_s	$\lvert\lambda_{\rm CP}\rvert$
$\lvert A_\perp\rvert^2$	1.00	–0.48	0.01	0.07	0.00	0.01	–0.04	0.01	0.00	–0.13	–0.01
$\lvert A_0\rvert^2$		1.00	–0.02	–0.14	–0.03	0.01	0.05	0.02	–0.01	0.07	0.03
$\lvert A_{SS}\rvert^2$			1.00	0.18	**0.59**	0.01	0.04	0.07	–0.01	–0.03	–0.18
$\lvert A_S\rvert^2$				1.00	0.21	0.01	0.01	0.06	0.01	–0.03	–0.25
δ_{SS}					1.00	–0.02	0.03	0.06	–0.01	–0.06	–0.21
δ_S						1.00	0.40	0.42	0.07	–0.07	–0.16
δ_1							1.00	**0.95**	0.14	–0.20	–0.27
δ_2								1.00	0.14	–0.20	–0.28
Δm_s									1.00	0.02	–0.03
ϕ_s										1.00	0.12
$\lvert\lambda_{\rm CP}\rvert$											1.00

24.1.1 Comparison with expected sensitivities

The expected sensitivities of the $B_s^0 \to \phi\phi$ physics parameters have been obtained in Sec.22.5.1 by generating toy studies with the same number of events as observed in data. Table 24.4 compares the fitted statistical uncertainty of the parameters from data with the mean of the uncertainty values obtained from the toy studies. Except for the phases, they agree well within the uncertainties of the mean. As it can be seen in Fig.22.3, the uncertainty distributions of the phases have asymmetric shapes with tails towards larger values that cover the fitted uncertainties observed in data.

Table 24.4: Comparison of the observed statistical uncertainty and the expected sensitivity obtained from 2000 pseudo experiments, each generated with 3950 events corresponding to the number of selected $B_s^0 \to \phi\phi$ signal decays in data.

parameter	measured uncertainty	expected sensitivity
ϕ_s (rad)	0.15	0.15(1)
$\lvert\lambda_{\rm CP}\rvert$	0.07	0.06(1)
$\lvert A_0\rvert^2$	0.013	0.0125(8)
$\lvert A_\perp\rvert^2$	0.012	0.0111(4)
δ_1 (rad)	0.23	0.19(2)
δ_2 (rad)	0.23	0.19(2)

24.2 Determination of the likelihood shape

The statistical uncertainties on the fitted parameter are only estimated accurately when the logarithm of the likelihood function exhibits a parabolic shape around the minimum as a function of this parameter. Therefore, a scan of the logarithmic likelihood is performed for the CP-violating phase ϕ_s that is shown in Fig. 24.1. At each point in the scan, the likelihood is minimised with respect to all the other physics parameters. A parabolic shape is observed at the fit value that deviates only for significantly smaller phases that are more than 3 standard deviations away from the minimum. Hence, the estimation of the uncertainty is correct.

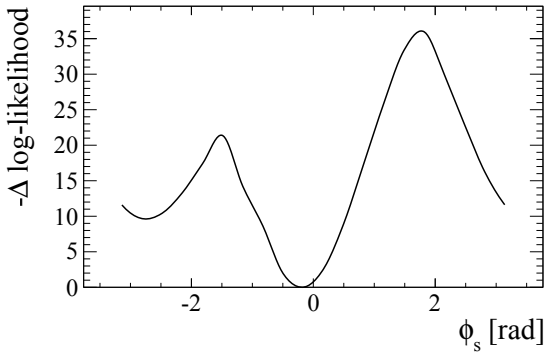

Figure 24.1: Profile log-likelihood scan for the ϕ_s parameter.

24.3 Projections of the measured distributions and fitted PDFs

Figure 24.2 shows the measured distributions of the decay time and the three helicity angles of the $B_s^0 \to \phi\phi$ signal candidates. Superimposed are the one-dimensional projections of the fitted total decay rate and the CP-even and CP-odd components, together with the sum of the S-wave and SS-wave components. The projections are corrected for decay-time and angular acceptance effects. The decay-time projections exhibit clear steps due to

the binned decay-time acceptance corrections. For illustration purposes, the acceptance histograms with the fine binning are chosen to draw the projections. The total fit agrees with the data except for one bin in the distribution of $\cos\theta_2$ which is probably a statistical fluctuation. It should be noted that the angles θ_1 and θ_2 are symmetric as the two related ϕ mesons are chosen randomly and the deviation in the same bin of the distribution of $\cos\theta_1$ is smaller.

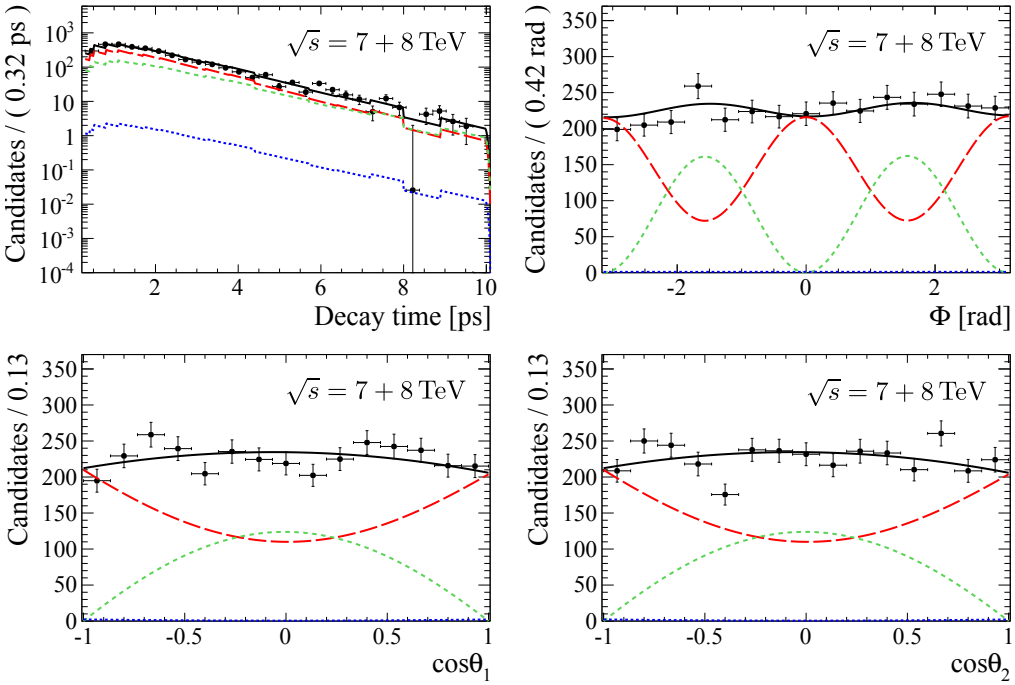

Figure 24.2: Distributions of the (top left) decay time, (top right) helicity angle Φ and cosine of the helicity angles (bottom left) θ_1 and (bottom right) θ_2 of the $B_s^0 \to \phi\phi$ signal candidates, shown as black point. The black solid lines represent the one-dimensional projections of the best fit of the total differential decay rate. The CP-even P-wave component is shown by the red long-dashed line, the CP-odd P-wave component by the green short-dashed line and the combined S-wave and SS-wave component is given by the blue dotted lines. The steps in the decay-time projection of the PDF are due to the binned decay-time acceptance histogram.

25 Discussion and Outlook

The second part of this thesis presents the measurement of time-dependent CP violation in $B_s^0 \to \phi\phi$ decays which can arise from the interference between the direct decay and the decay after mixing of the B_s^0 meson. The analysed proton-proton collision data samples at centre-of-mass energies of 7 TeV and 8 TeV have been collected during the years 2011 and 2012, respectively, by the LHCb experiment and correspond to an integrated luminosity of $\mathcal{L} = 3.0\,\text{fb}^{-1}$. The signal decay is reconstructed in the most abundant decay mode of the ϕ meson into a charged kaon pair. Background contributions from random combinations and falsely identified b-hadron decays are determined in a fit to the invariant four-kaon mass distribution of the B_s^0 candidates. In total 3950 $B_s^0 \to \phi\phi$ signal decays are found in the combined dataset. The fitting procedure that is applied to determine the physics parameters of the theoretical decay rate is a four-dimensional unbinned maximum likelihood fit to the decay time and the decay angles, defined in the helicity basis. The pre-determined background contributions are subtracted on a statistical basis using the sFit technique. The angular fit is needed to disentangle the polarisation amplitudes of the final state that are related to CP-even and CP-odd eigenstates. Each kaon pair can also be produced in an S-wave state that corresponds to the non-resonant decay mode. To perform a measurement of the time-dependent CP asymmetry, information of the initial B_s^0 production flavour is used. The effective decay-time resolutions are determined with fully simulated signal decays to be 41.1 fs and 43.9 fs for the 7 TeV and 8 TeV datasets, respectively. Acceptance effects due to reconstruction and selection artefacts and the geometrical coverage of the detector are corrected for. The decay-time acceptance is determined with the topologically similar decay $B_s^0 \to D_s^-(\to K^+K^-\pi^-)\pi^+$ and the angular acceptance is obtained from fully simulated signal decays. In the fit, the B_s^0 mixing parameters, Γ_s, $\Delta\Gamma_s$ and Δm_s are constrained to their previously-measured values within their uncertainties. The CP-violating phase, ϕ_s, and CP-violation parameter, $|\lambda_{\text{CP}}|$, are determined to be

$$\begin{aligned} \phi_s &= -0.17 \pm 0.15\ (\text{stat}) \pm 0.03\ (\text{syst})\,\text{rad}, \\ |\lambda_{\text{CP}}| &= 1.04 \pm 0.07\ (\text{stat}) \pm 0.03\ (\text{syst}), \end{aligned}$$

which is compatible with Standard-Model predictions of $\phi_s^{\text{SM}} = 0.00 \pm 0.02\,\text{rad}$ and $|\lambda_{\text{CP}}|^{\text{SM}} = 1$ [77, 78]. Thus, no evidence for CP violation can be claimed.

This is the first determination of the CP parameters in $B_s^0 \to \phi\phi$ decays. The time-dependent CP-violation measurements in $B_s^0 \to J/\psi\,\phi$ and $B_s^0 \to J/\psi\,\pi^+\pi^-$ decays [76] that are only sensitive to New-Physics contributions in mixing also do not reveal deviation from Standard-Model predictions [76]. Therefore, physics beyond the Standard Model is not found either in the B_s^0 mixing process or in the $\bar{b} \to s\bar{s}\bar{s}$ penguin decay amplitude.

The accuracy of the presented analysis is largely dominated by the statistical uncertainties and the prevailing systematic uncertainties are due to the acceptance corrections. At the moment, the measurement of CP violation in $B_s^0 \to \phi\phi$ decays is performed with the

additional dataset collected at 13 TeV centre-of-mass energies during 2015 and 2016, which provides approximately the same number of B_s^0 candidates. Studies are ongoing to reduce the differences observed in the decay-time acceptance in the control channel $B_s^0 \to D_s^- \pi^+$ using a more optimised kinematic re-weighting of the BDT response as suggested in Ref. [101]. The leading uncertainties on the angular acceptance weights is due to the limited statistics of the fully simulated events. These uncertainties can be reduced, if necessary, by generating a significantly larger amount of simulated events .

The polarisation amplitudes are found to be different for tree-level and penguin-induced decays in Ref. [102]. Therefore, the magnitude of CP violation and contributions from New-Physics phenomena can be different for each polarisation. In $B_s^0 \to J/\psi\,\phi$ decays, the CP parameters have been determined separately for each polarisation amplitude in Ref. [70]. The polarisation-dependent fitted parameters are compatible with the nominal values within the uncertainties. In $B_s^0 \to \phi\phi$ decays, various penguin topologies, gluonic and electroweak, contribute to the decay and a separate measurement of the CP parameters might reveal CP violation in the individual polarisations. However, the dataset used in this analysis is too small to allow for the measurement of additional amplitudes.

Until the end of the ongoing LHC Run II, the LHCb experiment will record an additional dataset that corresponds to approximately $6\,\text{fb}^{-1}$ of integrated luminosity. Despite the higher b-hadron production cross-section at the centre-of-mass energy of 13 TeV, the expected ϕ_s sensitivity of 0.11 rad is not within the range of the theoretical uncertainty of 0.02.

So far none of the other key measurements at LHCb has found a significant deviation from Standard-Model predictions and most of them are statistically limited. An exception is the measurement of the CP-averaged observables in $B^0 \to K^{*0}\mu^+\mu^-$ decays that reveal differences with predictions based on the Standard Model at the level of 3.4 standard deviations [103]. In order to collect significantly larger datasets, the LHCb detector will undergo a major upgrade before the LHC Run III. It will be operated at a five times higher instantaneous luminosity of $2 \cdot 10^{33}\,\text{cm}^{-2}\text{s}^{-1}$ and the data will be recorded without hardware trigger requirements with a 40 MHz readout system. Since dedicated hadron triggers suffer from large inefficiencies, the triggerless readout will largely improve the reconstruction and selection efficiency of the $B_s^0 \to \phi\phi$ final state with four hadrons. With the future LHCb dataset, corresponding to an estimated integrated luminosity of $50\,\text{fb}^{-1}$, the sensitivity of ϕ_s is expected to be comparable to the theoretical uncertainty. This will set stringent limits on possible new effects beyond the Standard Model.

In order to cope with the high readout rates and occupancies, parts of the LHCb tracking detectors and the particle identification system are upgraded. The main tracking device, currently formed by the Inner and the Outer Tracker, will be replaced by a single technology using scintillating fibres that are read out with Silicon Photomultipliers. The following last part of this thesis presents performance measurements of prototype modules of this Scintillating Fibre tracker, which are obtained from a dedicated test-beam campaign at the SPS facility at CERN.

Part III:
Performance of the LHCb upgrade Scintillating Fibre tracker

26 Introduction

At the LHC, protons collide at a bunch-crossing rate of 40 MHz at the maximum instantaneous luminosity of $\mathcal{L} = 2 \cdot 10^{34}\,\mathrm{cm}^{-2}\mathrm{s}^{-1}$ [23]. However, at the LHCb collision point, the luminosity is intentionally tuned to a lower value of $\mathcal{L} = 4 \cdot 10^{32}\,\mathrm{cm}^{-2}\mathrm{s}^{-1}$ by focusing the beam less strongly compared to ATLAS and CMS[1] and slightly separating the colliding beams. This is done to reduce the average number of visible proton-proton interactions per bunch crossing, μ, to 1.4 which simplifies the association of the displaced heavy-flavour hadron decay vertices to the production vertices. Moreover, the occupancy of the current detector at higher luminosities would be too high and large backgrounds from randomly combined tracks would make it very difficult to isolate the rare heavy-flavour hadron decays of interest. Besides the smaller number of proton-proton collisions, the maximum readout rate of the front-end electronics of 1 MHz limits the hardware trigger rate, and thus the data that can be processed in the software trigger. During LHC Run I, the LHCb experiment performed some very interesting measurements, but no significant evidence was found for the breakdown of the Standard-Model description in the observed energy range within the current uncertainties. Some of the results indicate possible new effects but the uncertainties are statistically limited. Thanks to the higher b-hadron production cross-section at 13 TeV and the longer run period, the collected amount of b-hadron decays of LHC Run II is expected to be almost four times as large as the currently available number of decays from Run I. However, the resulting statistical precisions of the key analyses will not reach the range of the theoretical uncertainties. Significantly larger datasets are needed to confirm the observed deviations from the Standard Model.

Therefore, the LHCb detector will be upgraded during the Long Shutdown 2, from the end of 2018 until the end of 2020. After that, it will be operated at a five times higher instantaneous luminosity of $\mathcal{L} = 2 \cdot 10^{33}\,\mathrm{cm}^{-2}\mathrm{s}^{-1}$ and the data will be recorded without a hardware trigger system at the full collision rate of 40 MHz. This will allow for the application of a full software trigger for every single event, and results in significantly higher trigger efficiencies for a wide range of decay channels. The upgraded LHCb detector is designed to collect a dataset corresponding to an integrated luminosity of at least $50\,\mathrm{fb}^{-1}$. As it is currently particularly difficult to design an efficient dedicated hadron trigger system, the triggerless readout will largely improve the reconstruction and selection efficiencies of decays with purely hadronic final states. The resulting trigger efficiency of $B_s^0 \to \phi\phi(\to K^+K^-K^+K^-)$ decays is estimated to be approximately a factor of 4 higher than in Run I [104]. Taking into account the factor five of the instantaneous luminosity allows for a final sensitivity of the CP-violating phase ϕ_s ($B_s^0 \to \phi\phi$) of 0.026 [105]. This is almost as small as the theoretical uncertainty of 0.02. The LHCb upgrade will set stringent limits on possible New-Physics contributions in various decay channels.

The full readout every 25 ns implies that all front-end electronics and parts of the sensitive elements of the LHCb detector have to be replaced. Due to the larger instantaneous

[1] At LHCb, $\beta^* = 3$ compared to a β^* value less than 1 at the collision points of ATLAS and CMS.

luminosity, the average number of visible proton-proton interactions per bunch crossing increases to $\mu = 5.2$ [106]. The large track multiplicities in the detector, the necessity to reconstruct several primary vertices and the 40 MHz readout rate require an upgrade of the complete tracking system. Currently, the main tracking stations consist of a silicon-based Inner Tracker and an Outer Tracker built with 5 mm straw tubes. The stations will be replaced by a single uniform technology using scintillating fibres with a diameter of 250 µm that are read out by Silicon Photomultiplier arrays with a similar pitch. The granular design will allow for the reconstruction of the large number of tracks. In order to cope with the new run conditions, the new tracker has to fulfil challenging requirements. Besides the 40 MHz readout rate, the single-hit detection efficiency is required to be about 99%, even when taking radiation effects after collecting $50\,\mathrm{fb}^{-1}$ of integrated luminosity into account. The spatial resolution of single hits in the bending plane of the magnet must be less than 100 µm [106][2]. In order to confirm that the Scintillating Fibre Tracker (SciFi) meets these requirements, prototype modules have been tested in a dedicated test-beam campaign at the SPS accelerator at CERN. Part III of this thesis presents the measurements of the light yield, the cluster size, the attenuation length and the detector performance parameters, the spatial resolution and the single-hit efficiency.

It is organised as follows: Chapter 27 briefly reviews the LHCb upgrade and the technology used for the SciFi tracker. Chapter 28 describes the experimental setup of the test-beam campaign. Chapter 29 presents the results of the performance tests, followed by a conclusion in Chap. 30.

[2] A better resolution would not help due to multiple scattering before the tracking stations

27 The LHCb upgrade Scintillating Fibre Tracker (SciFi)

During the LHCb upgrade, various parts of the detector will be replaced. This chapter briefly summarises the major changes and describes the technology used for the new main tracking stations, the Scintillating Fibre Tracker (SciFi).

27.1 The LHCb upgrade

Besides the necessary upgrade of the front-end electronics to allow for a 40 MHz readout rate, several subsystems of the LHCb detector will be replaced. The layout shown in Fig. 3.2 remains almost unchanged except that the first muon station, the scintillating pad and the preshower detector will be removed as they were mainly needed for the hardware trigger system. New technologies will be used for the complete track reconstruction system. Instead of a silicon strip detector, the VELO will be upgraded to a pixel detector with the first sensitive pixels at a radial distance of 5.1 mm from the proton beam. The Tracker Turicensis, located before the LHCb dipole magnet will be replaced by a highly-granular silicon micro-strip detector with an improved coverage of the LHCb acceptance [106]. The new system is called the Upstream Tracker. The current main tracking stations behind the magnet, composed of the Inner and Outer Tracker, will be replaced with the Scintillating Fibre Tracker. The overall structure of the two RICH detectors will remain but the photon detectors are replaced with commercial multi-anode photomultipliers with external readout electronics.

27.2 The Scintillating Fibre detector

The current Outer Tracker is constructed from 5 mm wide straw tubes and can cope with a maximum occupancy of 25% without a loss in track-finding efficiency [106]. In order to meet the upgrade requirements, the parts close to the beam pipe would have to be replaced as well as the readout electronics of the IT and the OT. Therefore, it was decided to choose a new single technology over the whole area of 5 m $\times$ 6 m. The new SciFi tracking detector will be built from 2.5 m long scintillating fibres with a diameter of 250 µm that are read out by Silicon Photomultiplier (SiPM) arrays. A sketch of the SciFi tracker is shown in Fig. 27.1. A charged particle within the LHCb detector acceptance will traverse in total 12 planes of the SciFi that are tilted by $\pm 5^\circ$ with respect to the vertical axis to provide two-dimensional spatial resolution. The highest resolution is achieved in the bending plane of the magnet, perpendicular to the fibres in order to precisely measure the track momenta. The highest expected occupancy is 2-3% without including noise hits. The conceptual design of this tracking detector is described in the Tracker Technical Design Report [106].

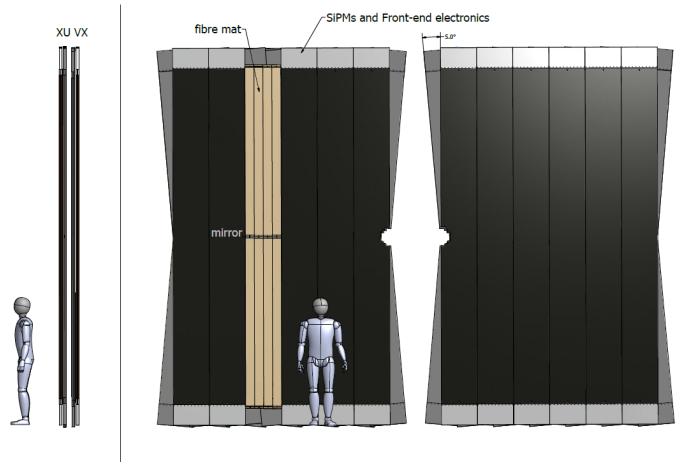

Figure 27.1: Sketch of the Scintillating Fibre tracker.

The requirements on the new SciFi tracking detector are the following:

- The single-hit detection efficiency should be about 99% while limiting the rate of noise hits well below the signal rate.
- The spatial resolution must be less than 100 µm.
- In order to reduce multiple scattering, the radiation length, X/X_0, is required to be less than 1% per SciFi plane.
- The readout rate of the front-end electronics is 40 MHz.
- Despite an expected radiation dose of up to 35 kGy, the detector should allow for an efficient operation up to an integrated luminosity of 50 fb^{-1}.

27.2.1 Scintillating fibres

Scintillating fibres consist of a plastic scintillator core made of polystyrene that serves as the active element of the tracker and two cladding layers with different refractive indices. When charged particles traverse the fibres, photons are emitted isotropically in the core. Due to the two claddings, the critical angle is increased and 5.3% of the photons are trapped in the fibre. The core is doped with two scintillating dyes to improve the efficiency of the scintillation mechanism. The primary dye absorbs the energy from the base polystyrene material[1] and the second dye is a wavelength shifter. It absorbs the emission of the primary dye and emits photons at a longer wavelength for which re-absorption in the fibre is less likely to occur [106]. The travelled distance when the probability has dropped to 1/e that the photon has not been absorbed according to Beer-Lambert's law is referred to as the attenuation length. Due to different geometrical paths in the fibre and a wavelength-dependent absorption, the observed attenuation length is typically expressed as having short and long components. The long component varies between 3 m and 4 m

[1] via the Förster resonant energy transfer

for the used fibres. At the fibre end towards the beam pipe, a mirror is mounted that reflects the photons. At the other end, they are detected with the SiPMs where typically 15 - 20 photons are observed when taking detection efficiencies into account. As shown in Fig. 27.2, a SciFi fibre mat is formed by six layers of fibres that are densely packed in a hexagonal structure. Including the glue that holds the fibres together, the thickness of the mat is 1.45 mm and the width is cut to 130.6 mm. The length of the fibres is 2424 mm.

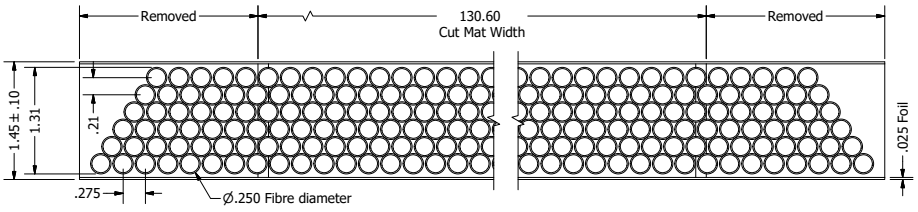

Figure 27.2: Sketch of a cross-section through a SciFi fibre mat consisting of six layers of scintillating fibres, taken from Ref. [8].

27.2.2 Module design

A single SciFi module that covers the full vertical length of 5 m is formed by 4×2 fibre mats that are glued to each other as indicated in Fig. 27.1. The grey parts on the upper and the lower end of the module correspond to the readout boxes in which the Silicon Photomultiplier arrays and the front-end electronics are mounted. To provide mechanical stability with small material budget, the mats are sandwiched between two 19.7 mm thick layers of Nomex[2] honey-comb material with a $200\,\mathrm{g\,m^{-2}}$ carbon-fibre reinforced polymer skin at the outside. The radiation length, X/X_0, of each module is 0.99%. The production procedure is described in the Engineering Design Review (EDR) Report [107].

27.2.3 Silicon Photomultipliers (SiPM)

SiPM arrays with high granularity are used as photodetectors for the SciFi due to their high photon-detection efficiency (PDE) in a large wavelength range, the large signal per photon, as well as the capability to detect single photons. A single SiPM channel consists of multiple pixels that are connected in parallel. Each of the pixels is an avalanche photodiode operated in Geiger mode. When a photon is absorbed by the pixel, an electron is excited into the conductance band. Due to the applied operation voltage, the electron travels into a high potential region which then triggers an avalanche process. The output charge per pixel avalanche divided by the single-electron charge is referred to as the *gain*. The output of one channel is the sum of the charges from all fired pixels. When the number of photons is much smaller than the total number of pixels, the probability that multiple photons fall into the same pixel is very low such that the number of incident photons can be approximated by the number of fired pixels. Hence, the output is measured in units

[2]Nomex is a registered trademark of E.I. du Pont de Nemours and Company (DuPont).

of *photo-electrons* (p.e.), *i.e.* detected photons. In the following, the observed number of photo-electrons is also referred to as the collected charge or the light yield.

The breakdown voltage corresponds to the minimum voltage at which an avalanche process can be released by a free electron. Depending on the manufacturing process, it varies between 20V and 100V. There are three main sources of noise for the SiPMs: dark noise, after-pulsing and optical cross-talk between pixels. Dark noise refers to an avalanche which is induced by thermally excited electrons. The dark-noise rate depends on the temperature and the operation voltage. As dark noise increases strongly after irradiation, the SiPMs need to be cooled down to $-40\,^{\circ}\mathrm{C}$ for the SciFi in order to reduce the rate to an acceptable level. After-pulses are delayed avalanche processes released by trapped charge that are caused by impurities in the crystal structure of the silicon. Additional noise in SiPM channels originates from cross-talk between pixels due to infra-red photons causing the neighbouring pixel to fire. This will increase the signal amplitude, but it will also enhance low-amplitude dark noise of single pixels that will appear like a low-amplitude signal. The difference between the operation voltage and the break-down voltage is the so-called *over-voltage*. SiPMs operated at a high over-voltage will have a higher gain and PDE, but the noise rate will also increase.

The SciFi custom SiPM array comprises 128 channels, each containing on the order of 100 pixels with a channel-to-channel pitch of 250 µm. The vertical height is 1.5 mm such that it covers the full six-layer fibre mat. Due to the manufacturing technology, each array is a combination of two 64-channel dies. Figure 27.3 shows pictures of a package that has been produced by the industrial manufacturer Hamamatsu (2015 model). Single pixels and the insensitive gap of 250 µm between the dies are visible. Four SiPM arrays will be mounted on each fibre mat. When operated at 3.5V over-voltage, the PDE of the SiPMs (2015 model) is up to 50% with a cross-talk probability of about 10% and an after-pulse rate of about 5% [108].

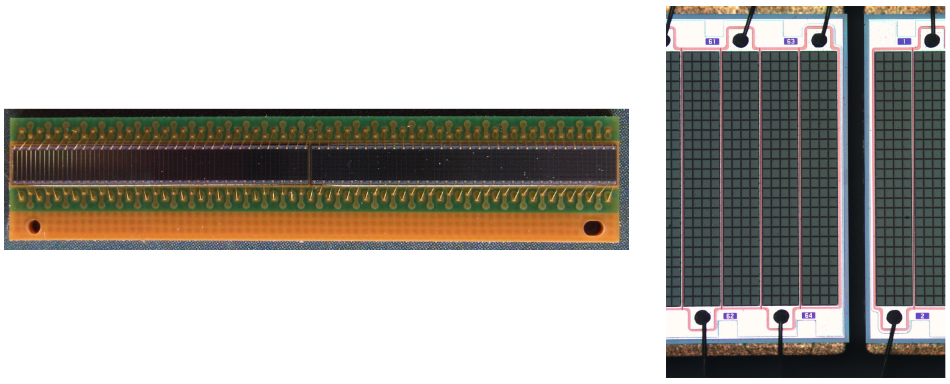

Figure 27.3: (Left) Picture taken with a microscope of a SiPM array produced by the industrial manufacturer Hamamatsu (2015 model). (Right) Close-up picture of the central region where the gap between the two dies can be seen, both pictures taken from Ref. [108].

27.2.4 Clustering

As indicated in Fig. 27.4(a), there is no one-to-one correspondence between fibres and SiPM channels. Instead, the photons from a single fibre are shared between two SiPM channels. In order to separate signal from noise, pre-defined thresholds will be applied

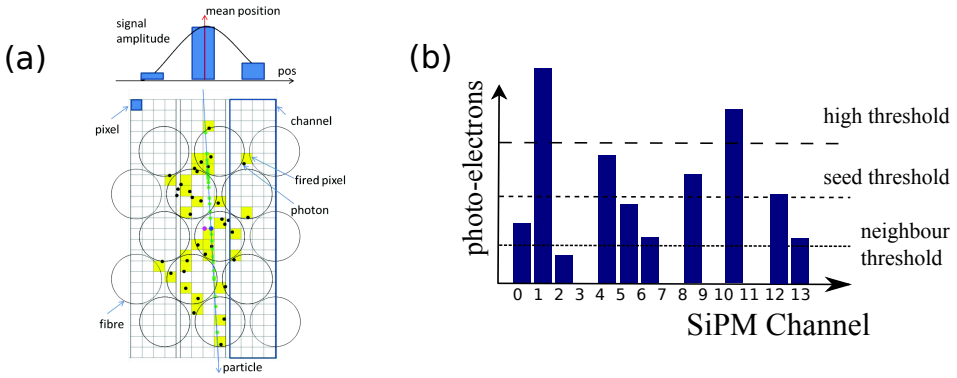

Figure 27.4: (a) Illustration of the cross-section of the fibre mat with a traversing particle, taken from Ref. [106]. The yellow square-shaped boxes correspond to the fired pixels. The emitted light spreads over several SiPM channels. (b) Clustering of neighbouring channels using three thresholds.

in the front-end electronics that reject low-amplitude signals. A cluster is composed of few neighouring channels for which the collected charge exceeds the so-called neighbour threshold as sketched in Fig. 27.4(b). At least one of the related cluster channels is required to exceed the so-called seed threshold. The overall collected charge in one cluster has to be larger than the sum threshold. If the cluster is composed of only one channel, it is additionally required to pass the high threshold. Channel 2 in Fig. 27.4(b) is not included in the first cluster as its signal falls below the neighbour threshold. The one-channel cluster at channel 8 is not accepted as the signal does not exceed the high threshold. The last cluster might be rejected when the total collected charge does not exceed the sum threshold. The cluster size corresponds to the number of related channels of the cluster.

Dependence of the SciFi detector performance on the clustering

The main performance parameters of the SciFi detector are the spatial resolution and the single-hit detection efficiency. The number of photons emitted in a scintillating fibre follows a Poissonian distribution and the absorption of photons along the path in the fibre is a statistical process. Despite multiple layers of scintillating fibres, this can result in a low number of photons arriving at the photo-detectors, for a small fraction of the hits. This leads to an inefficient detector response when the collected charges in the SiPM channels do not exceed the thresholds. The precision of the mean of the cluster position profits from large light yields as the related channels can be weighted accordingly. Therefore, after having minimised the fraction of insensitive regions and having chosen the pitches of the fibres and the SiPM channels, the performance parameters are dominated by the

number of observed photons and the thresholds used to suppress dark-noise avalanches. The cluster size is relevant for the occupancy of the detector and should be small.

27.2.5 Readout electronics

The SiPM arrays are read out by the low-Power ASIC for the sCintillating FIbres traCker, shortly referred to as the PACIFIC. The current-sensitive ASIC provides a configurable fast shaper to cut the long tails of the SiPM signals so that 90% of the charge is integrated within 10 ns [109]. Two interleaved gated integrators are used for each channel to reduce the integration dead time to be almost zero. After the integration, the analogue signal is further digitised to 2-bit pulse-height information using three comparators with configurable thresholds. This reduces efficiently the required data bandwidth while keeping sufficient tracking information. Although the exact amplitude information is missing after the digitisation, the channels can be weighted according to the thresholds their signal have passed and failed. These weights correspond to the pre-determined mean collected charge, $\bar{q}_{\text{thr}}$, of the SiPM channels for that particular threshold pattern. The barycentre position of the cluster is then computed from the hit positions x_i with

$$\bar{x}_{\text{PAC}} = \frac{\sum_i \bar{q}_{\text{thr},i} x_i}{\sum_i \bar{q}_{\text{thr},i}}. \tag{27.1}$$

The clustering is performed directly by the digital front-end electronics that provides a highly efficient suppression of single hits from dark noise. Only the cluster positions are transferred further which reduces the data volume drastically.

27.3 Radiation effects on the SciFi detector

Radiation effects after collecting an integrated luminosity of $50\,\text{fb}^{-1}$ represent one of the major challenges of the SciFi detector. Two sources of radiation effects are relevant: the ionising radiation from primary charged particles and the non-ionising damage caused by interactions with neutrons that are emitted as secondary particles in the calorimeters and are then backscattered to the SciFi detector. The maximum dose from ionising particles of 35 kGy is absorbed by the fibres in the region near the beam pipe. This ionisation dose modifies the polystyrene matrix and leads to an increase of attenuation and to a reduced attenuation length. The expected reduction of the observed light yield is 40% [106]. At the outer fibre ends and close to the SiPM arrays, the ionising radiation drops to a moderate dose of 40 to 80 Gy that has no effect on the SiPMs. However, the secondary neutrons that hardly interact with the fibre material due to the low mass of its atoms, do interact with the silicon atoms of the SiPMs. This results in an increase of the dark noise hits which occur proportionally to the neutron fluence that reaches up to 13×10^{11} $n_{\text{eq}}/\,\text{cm}^2$ [106]. To reduce the dark noise, the SiPM arrays are cooled down to $-40\,^{\circ}\text{C}$, for which the 1 p.e. dark-noise rate will reach on the order of tens of MHz per channel. Together with pixel cross-talk, this will produce dark signals larger than 1 p.e. Therefore, the foreseen thresholds to be applied for the SciFi detector are 1.5 p.e. for the neighbour, 2.5 p.e. for the seed, 4.0 p.e for the sum and 4.5 p.e. for the high threshold, but these values will be studied further. This will limit the noise-cluster rate to an acceptable level.

28 Description of the test-beam setup

In order to study the expected detector performance, SciFi prototype modules have been brought to the SPS facility at CERN in October 2014 and May 2015. Beam tests have been done with a mixed-particle beam. This chapter describes the test-beam setup and the strategy to perform the measurements.

28.1 The SPS accelerator and the CERN test-beam facilities

The Super Proton Synchrotron (SPS) accelerator accelerates protons to a maximum centre-of-mass energy of 450 GeV. In the North Area Test Beam Facilities[1] of CERN in Prévessin, France, the proton beams can be directed on a primary target[2] where a secondary beam of pions (≈20 %), protons (≈60 %), muons (≈10 %) and some electrons is produced. Particles are further selected to have a momentum of about 180 GeV/c. The secondary beam is produced in debunched spills with a duration of 4 s to 5 s and approximately $10 \cdot 10^6$ particles. The time between spills varies from 30 s to 60 s. The beam profile can be configured and was chosen to have horizontal and vertical widths of 5 mm and 13 mm, respectively, in order to cover the width of one 64-channel SiPM die.

28.2 Description of the SciFi prototype modules

The SciFi prototype modules used in the test-beam campaign have the same structure as the SciFi modules but are built from one fibre mat only. A sketch of the module design is shown in Fig. 28.1 where the honey-comb support structure and the carbon foil at the outside can be seen. The modules have not been exposed to irradiation prior to the test. Two SiPM arrays per module are mounted on the right end of the fibre mat covering the central half.

The properties of the used modules are listed in Table 28.1. The HD modules and the Slayer module have been produced using the same manufacturing process as the nominal SciFi module. The scintillating fibres of type SCSF-78 were produced by the industrial manufacturer Kuraray in the year 2015. The HD modules are early prototypes with five layers of fibres that are only used to determine the attenuation length. Their mirrors have been removed which simplifies the measurement due to the uncertainties of the reflectivity of the mirror. The Slayer module is built from six layers of fibres and serves as the device-under-test (DUT). The pitch between the fibres is 275 µm for both types of modules. The fourth module has been assembled with an alternative technique where the first fibre layer is aligned using a coverlay technique with a Kapton substrate. This type of

[1] The test-beam took place in the experimental hall EHN1 on the H8 beamline.
[2] The target used is the T4 target.

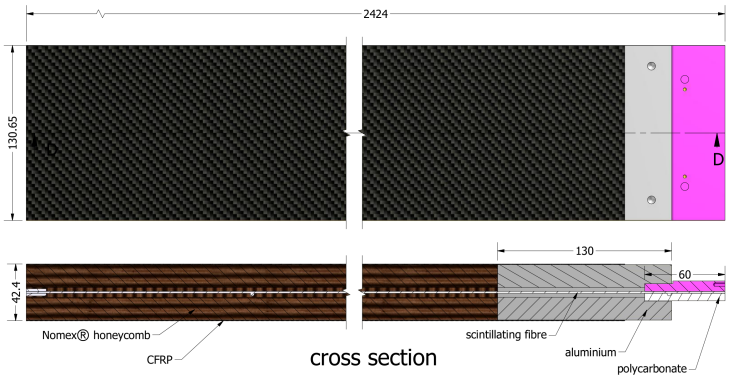

Figure 28.1: Top view and cross-section of a SciFi prototype module, taken from Ref. [8].

module will not be used in the future. The used SiPM arrays are provided by the company Hamamatsu (2014 model) and they are operated at room temperature.

Table 28.1: SciFi prototype modules used in the test-beam campaign. The Slayer module serves as the major DUT.

name	layers	width / cm	x-pitch / µm	feature	test-beam date
HD1	5	7	275	no mirror	Oct '14 & May '15
HD2	5	13.0	275	no mirror	Oct '14 & May '15
Slayer	6	13.0	275	mirrored	May '15
Coverlay	6	13.0	280	Kapton coverlay	Oct '14 & May '15

28.3 Readout electronics

During the test-beam campaign, the PACIFIC design was still in an early-prototype stage, and was not suitable to be used in the test-beam to characterise the mat performance. Instead, an upgraded version of the electronic system designed for the PEBS experiment [110] is used. The system uses a 32-channel analogue ASIC called SPIROC [111] to read out the SiPM arrays. The SPIROC contains a slow shaper with a configurable peaking time of 50-200 ns. The sampled signal of each channel is saved in an analogue buffer and the 32 channels are read out and digitised sequentially by an external 12-bit ADC[3]. The data are transferred to a PC via a USB connection. The shaping time is chosen to be 200 ns during the test-beam campaign such that the signal amplitude is less sensitive to the sampling time. The 12-bit information allows for the measurement of the observed number of photo-electrons in the SiPM channels but the readout rate of the large number of channels is limited to several kHz due to the slow USB 2.0 protocol. The slow data rate

[3]The signal of each channel is serially-multiplexed to the output. The multiplexed analogue output is subsequently digitised by an external 12-bit ADC and then packed in the FPGA.

suffices for the test-beam measurement and the expected 2-bit response of the PACIFIC can be simulated offline. The weights, $\bar{q}_{\text{thr}}$, used for the barycentre position of Eq. 27.1 are determined using the full 12-bit analogue information from the SPIROC readout: collected charges per channel passing the comparator levels of 1.5 p.e., 2.5 p.e. and 4.5 p.e are found to be optimally weighted by the factors $\bar{q}_{1.5} = 2$ p.e., $\bar{q}_{2.5} = 4$ p.e. and $\bar{q}_{4.5} = 12$ p.e. These numbers refer to the case when the particle traverses the module at a distance of 240 cm to the SiPM arrays. In the following, the resulting barycentre position using these weights is referred to as the PACIFIC-like weighted mean position.

Charge-weighted position

When making use of the full charge information, the charge-weighted mean position of the particle track is defined by

$$\bar{x}_{\text{Q}} = \frac{\sum_i q_i x_i}{\sum_i q_i}, \tag{28.1}$$

where the sum refers to the sum over the related channels and q_i is the collected charge of the channel x_i.

28.4 Calibration of the output signal per photo-electron

In order to measure the number of photo-electrons released in the SiPM channels, the digital output value has to be calibrated. This is done by injecting pulsed light directly into the fibre mat in dedicated calibration runs between spills. The change of the digitised SiPM signals of a single channel is shown in Fig. 28.2. As the number of photons incident on single channels is a statistical process, the distribution is a spectrum of several equi-distant photo-peaks that are described by the sum of Gaussian functions with equal distances between them. This distance defines the gain per photo-electron. The first peak is not a photo-peak but corresponds to the pedestal. The offset of the pedestal peak that is determined by the mean of the digitised signals in dark calibration runs without light injection, has been subtracted here.

28.5 Setup

The experimental test-beam setup is shown in Fig. 28.3. The four SciFi prototype modules are placed on a table next to each other and the beam traverses the fibres perpendicular to the fibre mat. Two SiPM arrays are mounted to the end of the module at the inner region of the fibre mat where the beam traverses the fibres. A so-called test-beam telescope is installed downstream of the beam at a distance of about 20 cm. It is a well-known track reconstruction detector with high spatial resolution that provides a reference track which is compared to the found hits in the DUT. During the test-beam campaign, the TimePix3 telescope [112] was used. It has been developed as part of the LHCb VELO Upgrade project and consists of eight layers of silicon hybrid pixel detectors. The pixels of a size of $55 \times 55\,\mu\text{m}$ are arranged in a $14\,\text{mm} \times 14\,\text{mm}$ matrix. Each layer is tilted to $9\,^\circ$ in both horizontal and vertical axes to optimise the spatial resolution. Usually, the DUT is placed in the centre of the telescope where the best pointing resolution of $1.54(11)\,\mu\text{m}$ is achieved.

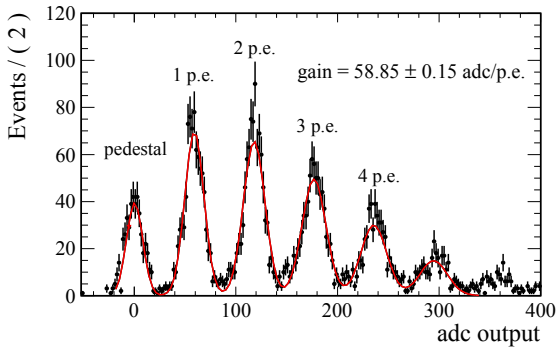

Figure 28.2: Distribution of the digital output value of one SiPM channel when injecting pulsed light directly onto the fibre mat. The fit function is a sum of six equi-distant Gaussian functions. The distance corresponds to the gain, the digital output per photo-electron.

At the position of the SciFi modules, about 70 cm from the telescope centre, the resolution of the track reconstruction is estimated to be about 12 µm which is negligible compared to the resolution of the SciFi.

The coincidence of signals from three 2 cm^2 plastic scintillators are used as the trigger signals for both the readout electronics and the telescope. The scintillators are placed as shown in Fig. 28.3 to make sure that the beam particle has traversed the SciFi prototype modules and the complete TimePix telescope.

The table, on which the SciFi modules are mounted to, can be moved horizontally such that the beam traverses the modules at different positions along the module. This allows for the measurement of the module performance for different distances the photons have to travel from the incident beam particle to the SiPM arrays. Additionally, the modules can be rotated around the axis along the fibres to a maximum angle of 30 °. At an angle of 0°, the beam traverses the fibre mat perpendicularly. The angular dependence of the module performance is determined because the path length of the beam particles, and thus the number of emitted photons, depends on the angle between the beam and the surface vector of the fibre mat.

The hits in the TimePix telescope are used to reconstruct the particle tracks that are extrapolated to the position of the SciFi modules. Hence, the spatial resolution is obtained from the residual between the extrapolated TimePix track and the track position determined in the SciFi module. The single-hit efficiency is determined from the fraction of TimePix tracks for which a correctly reconstructed SciFi cluster is found. The performance is determined only for the regions that are covered by SiPM channels. Inactive regions such as gaps between the dies and arrays are excluded from the measurement. Inefficiencies due to insensitive areas will be simulated in complete detector simulations of the SciFi tracker.

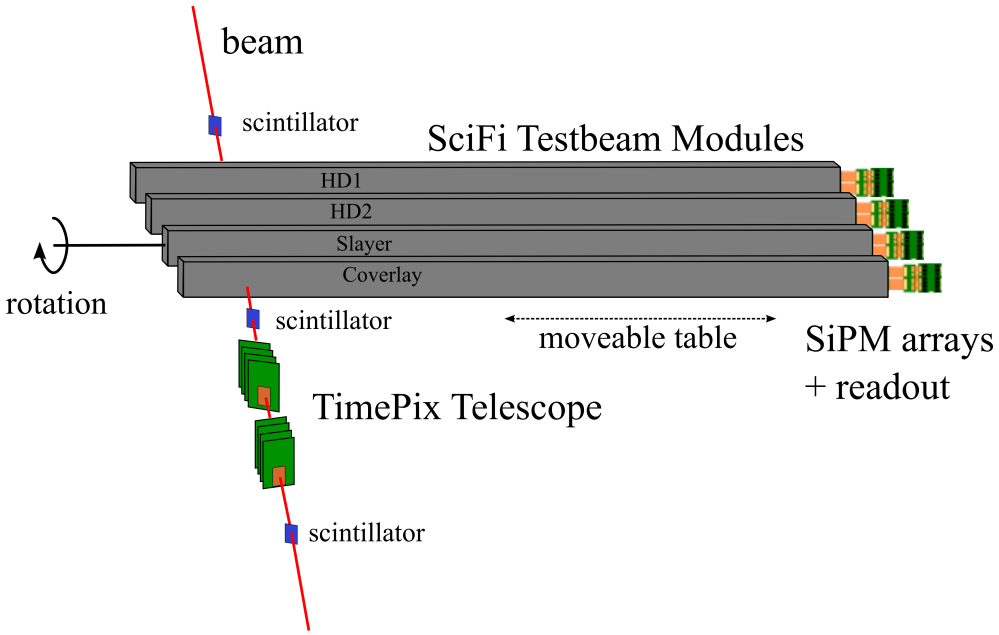

Figure 28.3: Sketch of the test-beam setup during May 2015. In October 2014, only the HD and the Coverlay modules were tested.

29 Measurement of the performance of SciFi prototype modules

Using data of the afore-described test-beam setup, this chapter presents the performance results of the SciFi prototype modules. The light yield, cluster size, spatial resolution and single-hit efficiency are measured at three different distances of the beam to the SiPM arrays. The angular dependence of the performance is obtained by rotating the module around the axis along the fibres to three angles.

29.1 Description of the measurement

The SciFi prototype performance is determined with the DUT, the Slayer module, at three different distances of the beam to the SiPM arrays: (1) when the beam traverses the module almost directly at the mirror (distance to SiPM $\sim$ 240 cm), (2) at the centre of the module (distance to SiPM $\sim$ 120 cm), and (3) at a distance of 50 cm to the SiPM arrays. At the LHCb experiment, a large fraction of the particles pass through the tracking stations close to the beam pipe due to the η-dependence of the production mechanism. This corresponds to a distance of about 240 cm to the SiPMs. In order to obtain the angular dependence of the module performance, the measurements are repeated at the two outer positions at a distance of 240 cm and 50 cm to the SiPM arrays while rotating the module around the axis along the fibres to 10 ° and 20 °. At an angle of 0°, the beam traverses the module perpendicular to the fibre mat. In the following, the angle is simply referred to as the angle of the module, implying that it is the angle between the surface vector of the fibre mat and the beam direction. At LHCb, the average angle between the particle and the surface vector of the tracking stations is small for the inner modules but can reach 20° for few tracks. At each distance of the beam to the SiPM arrays and each angle of the module, between 100k and 600k triggered events are collected.

As described in the previous section, a coincidence of the three scintillators is used as a trigger signal to make sure that the signal track has traversed all four SciFi modules and the TimePix telescope. However, due to the large number of particles in the beam and the long shaping time of the readout electronics of 200 ns used for the SiPM signals, it can happen that multiple tracks are reconstructed in the SciFi modules. These might have traversed the module shortly before the signal particle. As this can lead to ambiguities and to wrong assignments of TimePix tracks to SciFi clusters, several selection requirements are applied to the triggered events. Events are only accepted when the number of well-reconstructed TimePix tracks for a triggered event is exactly one. The excellent time resolution of the TimePix telescope would allow to distinguish consecutive tracks, but within 200 ns, these would appear as simultaneous for the SciFi modules with the used test-beam electronics. The reconstruction fit χ^2 value of the TimePix track, divided by the number of degrees of freedom is required to be less than 4 such that the required spatial resolution of 12 µm

for the reconstructed TimePix tracks is ensured. Except for the DUT, all Scifi modules are required to reconstruct exactly one cluster whose charge-weighted mean position is compatible with the extrapolated TimePix track within 0.5 mm. For all but the efficiency measurement, an event is rejected when the extrapolated TimePix track falls into insensitive areas of the DUT. Additional selection requirements for the individual analyses will be described in the respective section.

In the following, the set of thresholds applied for the clusters is shortly referred to by using the notation (neighbour, seed, sum) in units of photo-electrons. The high threshold is only used to simulate the 2-bit response of the PACIFIC and determine the reconstructed PACIFIC-like weighted mean position according to Eq. 27.1. The total number of collected events and the number of remaining events after applying the selection criteria are given in in Table 29.1 for the three distances of the beam to the SiPM arrays and the three angles of the module. The attenuation length is determined with the five-layer module HD1 because it has no mirror attached to the other end of the fibre mat. This simplifies the determination of the attenuation length. The module is moved along its length and 150k triggered events are collected in finer steps.

Table 29.1: Collected datasets to measure the performance of the six-layer SciFi prototype module. The number of selected events corresponds to the number when applying the selection criteria described in the text and forming clusters using the set of thresholds of (1.5, 2.5, 4.0) that are foreseen for the operation in LHCb. The angle refers to the angle between the surface vector of the module and the beam.

distance beam to SiPM	angle	total number of events	number of selected events
240 cm	0°	440000	120000
	10°	500000	130000
	20°	670000	180000
120 cm	0°	830000	310000
50 cm	0°	460000	200000
	10°	140000	60000
	20°	400000	180000

29.2 Determination of the light yield

The light yield of a reconstructed cluster corresponds to the collected charge of the related cluster channels observed in the SiPM arrays when the beam particle traverses the fibre mat. The amplitudes presented in the following are not corrected for cross-talk between pixels or saturation of the pixels. The used cluster algorithm introduces a shift of the observed light yield to higher values. Therefore, the thresholds are tuned to the low values of (1.5, 1.5, 1.5). In the case of a missing cluster in the DUT, a light yield of zero photo-electrons is taken into account. If multiple clusters are found in the DUT, the cluster is considered whose charge-weighted mean is closest to the reconstructed TimePix track. Figure 29.1 shows the light yield distributions of the clusters of all selected events for tracks at the

three different distances to the SiPMs. The angle between the surface vector of the module and the beam direction is 0°. The corresponding distributions at angles of 10° and 20° can be found in Appendix C.

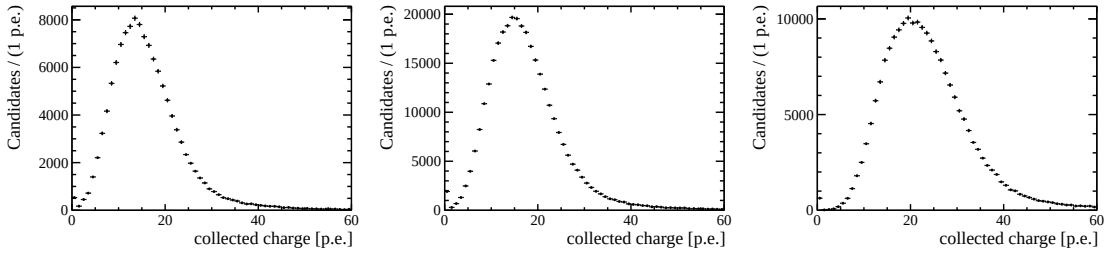

Figure 29.1: Light yield distributions of clusters found in the DUT of all accepted events for tracks at a distance of (a) 240 cm, (b) 120 cm and (c) 50 cm from the SiPM arrays. The angle between the surface vector of the module and the beam is 0°. The light yields are not corrected for crosstalk.

Due to the various possible path lengths through the circular-shaped cross-section of the active scintillator fibres in the fibre mat, the distribution deviates from the expected Landau shape observed in flat planar scintillating detectors. Therefore, no functional form is found that describes the light yield for different conditions and the light yield distribution is evaluated using the mean and the median for comparison. These are prone to the shift introduced by the threshold cuts. The mean and median of the light yield distributions at the three distances of the beam to the SiPMs and the three angles of the module are given in Table 29.2. The dominant systematic uncertainty on the absolute light light is due to an imperfect alignment of the SiPM arrays in this test-beam with respect to the fibre mat. It is estimated by determining the light yield for all illuminated channels separately and the width of the resulting distribution of the means is taken as the uncertainty. The mean of the light yield for tracks at a distance of 50 cm to the SiPMs is about 23.9 p.e. Due to the photon absorption along the fibre, the mean light yield at a distance of 240 cm to the SiPM arrays decreases to 16.3 p.e. This is compatible with the expected light yield of 16.6 p.e. [106]. The decrease in light yield with the distance from the beam to the SiPMs is smaller than what is naively expected for an attenuation length of about 350 cm. This is due to the mirror that is attached to the other fibre end. Reflected photons that were emitted at a distance of 240 cm from the SiPMs have to travel almost the same distance as the direct photons. Only a small fraction is lost due to the imperfect reflectivity of the mirror. Light that is emitted from particle tracks close to the SiPM into the direction of the mirror, has to travel almost twice the distance compared to the direct photons and is therefore lost for the most parts. The increase in path length through the fibre mat at an angle of the module is also reflected in higher light yields but the naive $\cos^{-1}(\theta)$ dependence for flat planar scintillators is not confirmed due to the various possible ways of traversing the circular cross-section of the fibres. After the collection of 50 fb^{-1} of collision data, the light yield of the modules will reduce by about 40% due to an increase of photon absorption in the fibres. This leads to an expected light of about 10 p.e.

Table 29.2: Mean and median of the light yield distribution for tracks at a distance of 240 cm, 120 cm and 50 cm from the SiPM arrays and angles between the surface vector of the module and the beam direction. The light yields are not corrected for crosstalk.

	angle	240 cm	120 cm	50 cm
mean light yield [p.e.]	0°	16.3 ± 0.4	17.5 ± 0.4	23.9 ± 0.5
	10°	17.6 ± 0.4	–	23.8 ± 0.5
	20°	19.1 ± 0.4	–	26.7 ± 0.5
median light yield [p.e.]	0°	15.0 ± 0.3	16.3 ± 0.4	22.3 ± 0.5
	10°	16.3 ± 0.4	–	22.1 ± 0.5
	20°	17.7 ± 0.4	–	24.9 ± 0.5

29.2.1 Determination of the cluster size

The cluster size is determined by the number of related channels of the cluster. As it is the case for the light yield, the mean cluster size depends on the applied cluster thresholds. Two sets of thresholds are applied in the following: the low values of (1.5, 1.5, 1.5) that hardly introduce a shift of the observed light yield and the set of thresholds (1.5, 2.5, 4.0) that is foreseen for the LHCb upgrade detector. When no cluster is found in the DUT, the event is rejected. Figure 29.2 shows the normalised cluster size distributions of all selected clusters using the two sets of threshold for tracks at the three distances to the SiPM arrays. The angle between the surface vector of the module and the beam direction is 0°. The difference between the distributions using the two sets of thresolds is only visible for very large cluster sizes and clusters with only one channel because the higher sum threshold rejects clusters with small light yields. The corresponding distributions at angles of 10° and 20° using the set of thresholds (1.5, 2.5, 4.0) are attached to Appendix C.

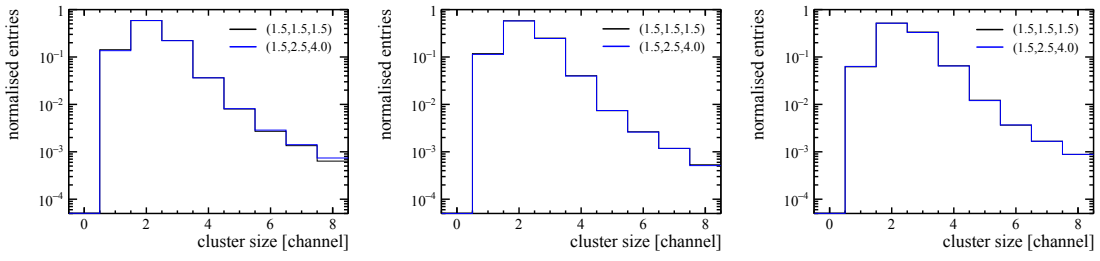

(a) (b) (c)

Figure 29.2: Normalised cluster size distributions of all clusters found in the DUT of all accepted events when applying the set of thresholds (1.5, 1.5, 1.5) and (1.5, 2.5, 4.0) (foreseen for the LHCb upgrade detector) for tracks at a distance of (a) 240 cm, (b) 120 cm and (c) 50 cm to the SiPM arrays. The angle of the module with respect to the beam is 0°.

The mean cluster sizes when applying either of the two sets of thresholds at all distances and angles are given in Table 29.3. For tracks at a distance of 240 cm to the SiPMs and a module angle of 0°, the mean cluster size is found to be 2.2 channels. For smaller distances of the beam to the SiPMs, the mean cluster size slightly increases to 2.5. The mean cluster size increases with the angle between the surface vector of the module and the beam direction, as expected from geometrical considerations, to 2.5 and 3.0 for 10° and 20°, respectively.

Table 29.3: Mean cluster size for tracks at a distance of 240 cm, 120 cm and 50 cm to the SiPM arrays and angles between the surface vector of the module and the beam when applying either of the two sets of thresholds, (1.5, 1.5, 1.5) or (1.5, 2.5, 4.0).

	angle	240 cm	120 cm	50 cm
mean cluster size [channel]	0°	2.2	2.3	2.5
	10°	2.5	–	2.7
	20°	3.0	–	3.3

For about 1.4% of the events, the cluster exceeds a size of four channels. This is larger than what is expected from the geometrical path of the particle track through the fibre mat. The responsible mechanisms are assumed to be cross-talk between fibres and secondary particles produced in the mat. The cross-talk between fibres is suspected to occur because a large fraction of the emitted light from the primary dye is not captured in the fibre and enters the next fibre. In order to reduce this mechanism, titanium dioxide has been added to the glue that keeps the mat together, but the layer might be too thin to block 100% of the light. The mean cluster size as a function of the light yield is shown in Fig. 29.3 for tracks at a distance of 240 cm to the SiPMs for the three angles of the module. The dependence of the cluster size on the light yield can be described by a straight line that is rather independent of the angle of the module. This observation is compatible with the assumption that large cluster sizes are due to cross-talk between fibres that occurs more often when more light is emitted.

29.3 Measurement of the attenuation length

The attenuation length is obtained from data collected with the HD1 module during the test-beam in October 2014 . The light yield of this module is measured in a finer position scan over the length of the module with smaller data samples. As it was done for the light yield measurement, the thresholds are tuned to lower values in order to avoid introducing a shift to larger collected charges. Due to the missing mirror, the light yield is even smaller and the set of thresholds is set to (0.5, 1.5, 1.5). The light yield as a function of the distance from the beam to the SiPM arrays is shown in Fig. 29.4. At each distance, the width and position of the particle beam is configured such that it covers the whole width of one SiPM array and the signal distributes equally over all channels. Hence, a possible mis-alignment of the SiPM array with respect to the fibre mat is averaged out and the

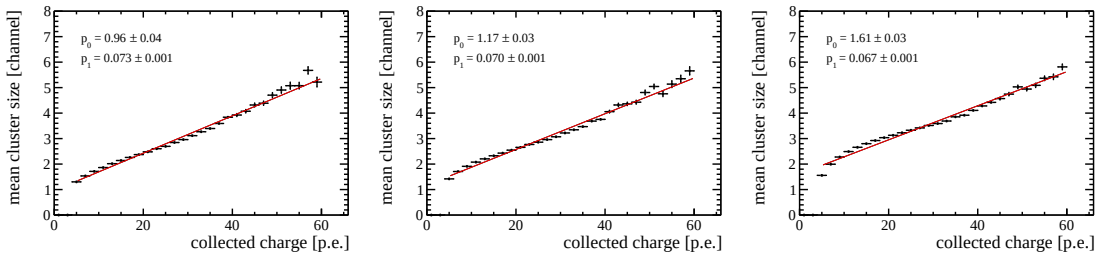

(a) (b) (c)

Figure 29.3: Mean cluster size as a function of the collected charge for tracks at a distance of 240 cm to the SiPM arrays and an angle of the module of (a) 0°, (b) 10°, and (c) 20°. The fit function is a straight line with offset p_0 and slope p_1.

light yields relative to each other are assumed to be measured with small uncertainties on the order of 1%. Due to the long and the short components of the attenuation length, Λ_S and Λ_L, the light yield is modelled by the sum of two exponential functions according to Beer-Lambert's law

$$N(x) = N_S \exp(-x/\Lambda_S) + N_L \exp(-x/\Lambda_L), \tag{29.1}$$

where N_S and N_L are the light yields of each component at a distance of zero. The fit, shown in Fig. 29.4(a), yields a short component of 53 ± 24 cm and a long component of 356 ± 41 cm. The industrial producer (Kuraray) suggests to measure the long component only in a single exponential fit, defined in the range from 1 m to 2.5 m, where the contribution from the short component is negligible. This is the case for tracks at a distance of 240 cm to the SiPMs and particles traversing the SciFi modules near the proton beam at LHCb, thus the long component is typically defined as the attenuation length. The corresponding single exponential fit is shown in Fig. 29.4(b) which reveals an attenuation length of 326 ± 11 cm. The determined attenuation lengths are compatible with measurements of ∼300-350 cm that were performed in the laboratory by directly shining light into the fibres and measuring the light intensity at the end of the fibre. For the SciFi detector, the attenuation length should be larger than 350 cm.

29.4 Determination of the spatial hit resolution

In order to determine the spatial hit resolution, the residuals of the SciFi cluster positions with respect to the reconstructed TimePix tracks are calculated. The width of the residual distribution, σ_{res}, is determined by the uncertainty of the extrapolated TimePix track, σ_{tr}, and the spatial resolution of the SciFi module, σ_{SciFi}, that are added in quadrature as

$$\sigma_{res} = \sqrt{\sigma_{tr}^2 + \sigma_{SciFi}^2} \approx \sigma_{SciFi}. \tag{29.2}$$

Due to the negligible track resolution from the TimePix telescope compared to the module resolution, the residual width can be identified with the spatial resolution of the SciFi

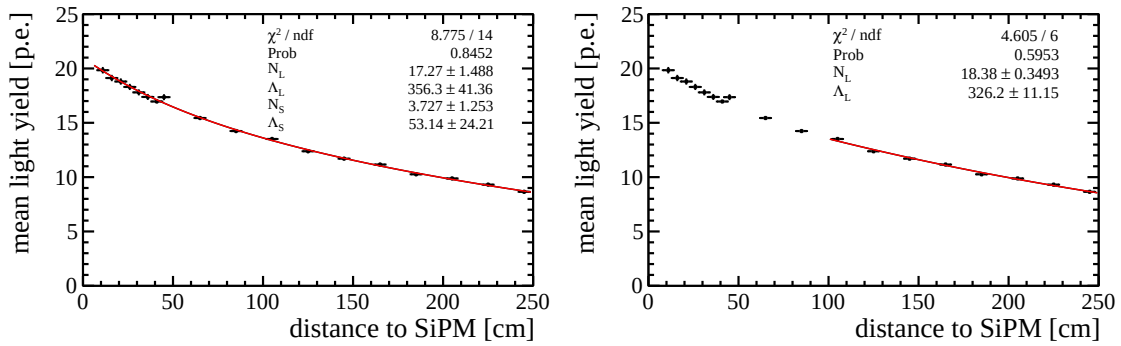

(a) (b)

Figure 29.4: Mean light yield measured in the HD1 module as a function of the distance from the beam to the SiPM arrays. The fit model is (a) a sum of two exponential functions and (b) a single exponential, defined in the range from 1 m to 2.5 m, where Λ_S and Λ_L refer to the short and long components of the attenuation length. The angle between the surface vector of the module and the beam is 0°.

module to a good approximation.

Clusters are determined using the set of thresholds (1.5, 2.5, 4.0) that are foreseen for the LHCb upgrade detector. The residual distributions using the charge-weighted mean and the PACIFIC-like weighted mean as the SciFi cluster position are shown in Fig. 29.5. The distance of the beam to the SiPMs is 240 cm and the angle between the surface vector of the module and the beam is 0°. The corresponding residual distributions for tracks at a distance of 120 cm and 50 cm to the SiPMs are given in Appendix C. The distributions are modelled by the sum of two Gaussian functions with inner and outer widths, σ_1 and σ_2, weighted with their fractions f and $(1 - f)$. The effective resolution, σ_{eff}, is determined as the weighted squared sum of the widths

$$\sigma_{\text{eff}} = \sqrt{f \cdot \sigma_1^2 + (1 - f) \cdot \sigma_2^2}. \tag{29.3}$$

Table 29.4 shows the measured effective spatial resolutions of the DUT for tracks at the three distances of the beam to the SiPMs and the three angles of the module. Whereas the charge-weighted clustering benefits from an increase of total light yield, the resolution stays constant over the module when applying the PACIFIC-like weighting. It is slightly worse for tracks near the SiPM arrays because the weights used for the PACIFIC-like clustering have been optimised for tracks at a distance of 240 cm. For tracks at a distance of 240 cm to the SiPMs and a module angle of 0°, the spatial resolutions using the charge-weighted and the PACIFIC-like weighted mean position are determined as 70.2 ± 0.9 µm and 77.2 ± 1.3 µm, respectively. This is better than the requirement on the SciFi tracker of 100 µm. Simulations predicted a spatial resolution of 60 µm for a light yield of 15 p.e. [106].

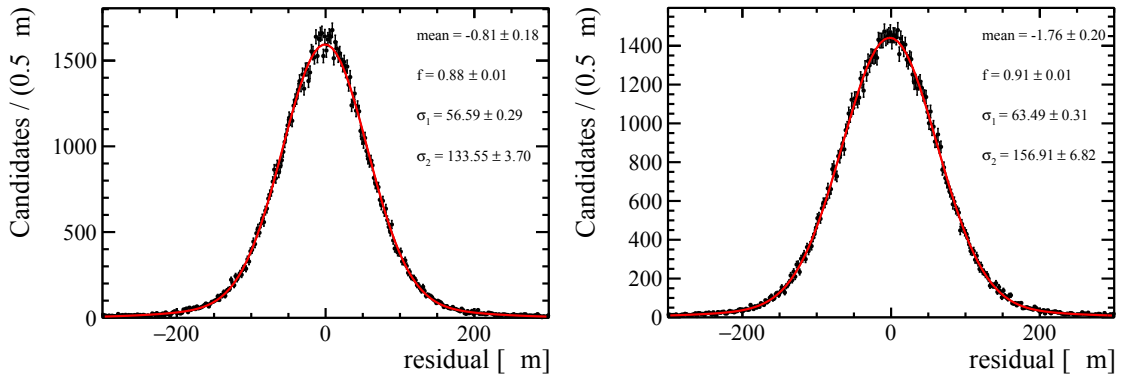

(a) (b)

Figure 29.5: Residual distributions of the SciFi cluster positions with respect to the reconstructed TimePix tracks using the (a) charge-weighted and (b) PACIFIC-like weighted mean position for tracks at a distance of 240 cm to the SiPMs. The angle between the surface vector of the module and the beam is 0°.

At an angle between the surface vector of the module and the beam, the resolution gets worse. The dependence of the resolution on light yield and cluster size is investigated in the following.

Table 29.4: Effective spatial resolution of the six-layer SciFi prototype module using the charge-weighted clustering, $\sigma_{\text{eff,Q}}$, and the PACIFIC-like weighted clustering, $\sigma_{\text{eff,PAC}}$, for tracks at a distance of 240 cm, 120 cm and 50 cm to the SiPM arrays and at three angles between the surface vector of the module and the beam. The track resolution of the TimePix telescope is neglected.

	angle	240 cm	120 cm	50 cm
$\sigma_{\text{eff,Q}}$ [µm]	0°	70.2 ± 0.9	69.5 ± 0.5	66.3 ± 0.6
	10°	74.0 ± 1.0	–	66.9 ± 1.0
	20°	83.7 ± 1.2	–	77.9 ± 1.0
$\sigma_{\text{eff,PAC}}$ [µm]	0°	77.2 ± 1.3	77.2 ± 0.8	80.8 ± 1.4
	10°	79.4 ± 1.2	–	77.0 ± 1.9
	20°	87.0 ± 1.6	–	84.5 ± 1.5

Figure 29.6 shows the effective spatial resolution using the charge-weighted mean position as a function of the light yield and the cluster size which are themselves correlated. The data refers to tracks at a distance of 240 cm to the SiPMs and a module angle of 0°. Figure 29.7 shows the corresponding spatial resolution using the PACIFIC-like weighted mean as the cluster position. For medium light yields between 8 and 25 photo-electrons, the effective resolution is rather constant between 60 µm and 70 µm and it rises for small light yields as expected. However, it also rises for large light yields. Figure 29.6(b) shows

the effective resolution in dependence of the cluster size. The resolution increases to 300 µm for cluster sizes larger than 4. Hence, large cluster sizes lead to less well-defined cluster positions and for this reason, the resolution increases for large light yields. The large outer width of the Gaussian functions might originate from large cluster sizes that are presumably caused by cross-talk between the fibres and the emission of delta rays. However, in this case the two outer width using the two charge-weighted and PACIFIC-like weighted mean position should be rather similar which is not observed. Clustering effects or other factors might also play a role. After the collection of 50 fb^{-1} of collision data and an expected light yield of about 10 p.e., the resolution using the PACIFIC-like weighted mean position will not change largely according to Figure 29.7 and will remain below 100 µm. Hence, the prototype module meets the requirements on the spatial resolution for the SciFi detector, even when taking radiation effects into account.

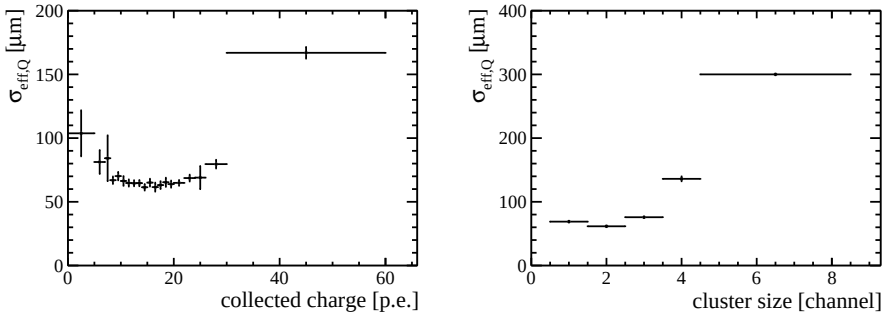

(a) (b)

Figure 29.6: The effective spatial resolution of the DUT using the charge-weighted mean cluster position as a function of (a) the light yield and (b) the cluster size for tracks at a distance of 240 cm to the SiPMs. The angle between the surface vector of the module and the beam is 0°.

29.5 Determination of the single-hit efficiency

The single-hit efficiency is obtained from the fraction of TimePix tracks for which a correctly reconstructed SciFi cluster is found. It depends on the applied set of cluster thresholds, but also on the tolerable distance from the cluster to the reference track. In the following, the neighbour threshold is fixed to 1.5 p.e. and the hit efficiency is determined for different seed thresholds. The sum threshold is not applied. Additionally, the single-hit efficiency is measured using the set of thresholds (1.5, 2.5, 4.0) that are foreseen for the LHCb upgrade detector. For the tolerable distance from the cluster to the reference track, two different values are investigated: (a) the residual between the SciFi cluster and the extrapolated TimePix track is less than the width of two channels which corresponds to a distance of about 7σ of the effective resolution and (b) the residual is less than the width of five channels. The efficiency is computed as a function of the channel ID to which the TimePix track is extrapolated to.

Figure 29.8 shows the single-hit efficiency as a function of the channel ID of the SiPM

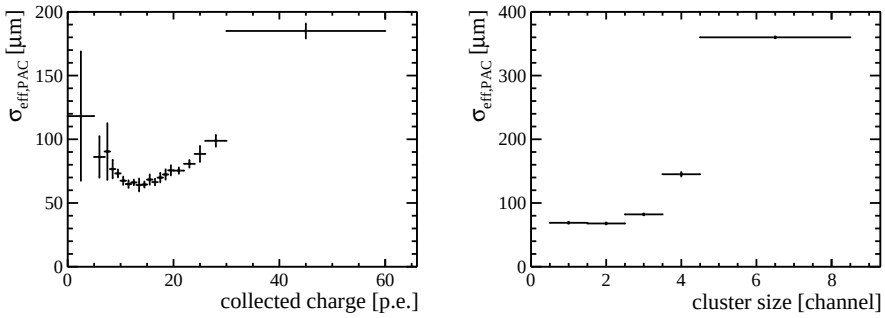

(a) (b)

Figure 29.7: The effective spatial resolution of the DUT using the PACIFIC-like weighted mean cluster position as a function of (a) the light yield and (b) the cluster size for tracks at a distance of 240 cm to the SiPMs. The angle between the surface vector of the module and the beam is 0°.

array for different seed thresholds for tracks at a distance of 240 cm from the SiPMs. In Fig. 29.8(a), the tolerable residual between the reconstructed SciFi cluster and the extrapolated TimePix track is two channels and in Fig. 29.8(b), the residual is less than five channels. The gap between the two dies is defined as the channel with ID 65. The angle between the surface vector of the module and the beam is 0°. The blue points refer to the set of thresholds foreseen for the operation in LHCb. For predicted tracks that fall into the gap of the SiPM array, the efficiency decreases to about 53% to 54%. It is not zero because the light is distributed over the neighbouring channels.

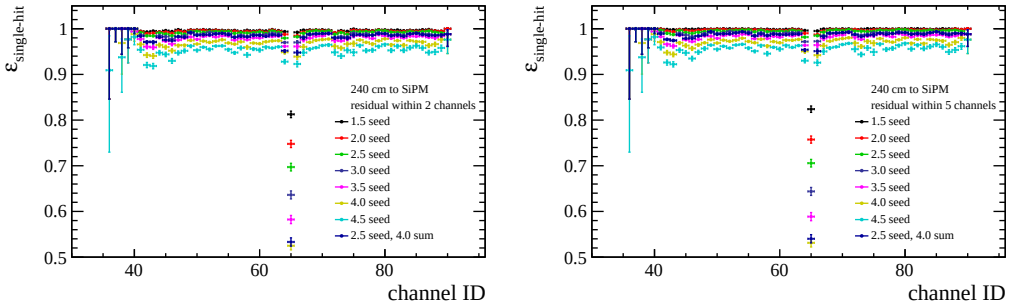

(a) (b)

Figure 29.8: Single-hit efficiency vs. SiPM channels ID for tracks at a distance of 240 cm to the SiPMs. The gap between the two dies of the SiPM arrays has the channel ID 65. The tolerable residual between the SciFi cluster and the extrapolated TimePix track is less than (a) 2 channels and (b) 5 channels. The angle between the surface vector of the module and the beam is 0°.

The single-hit efficiency at a significant distance away from the gap is determined by fitting a constant function to the efficiency plateau for channels with ID larger than 45

and less than 60. The fitted efficiencies are shown as a function of the seed threshold in Fig. 29.9(a) for a tolerable residual of two channels and in Fig. 29.9(b) for a tolerable residual of five channels. The values are listed in Table 29.5.

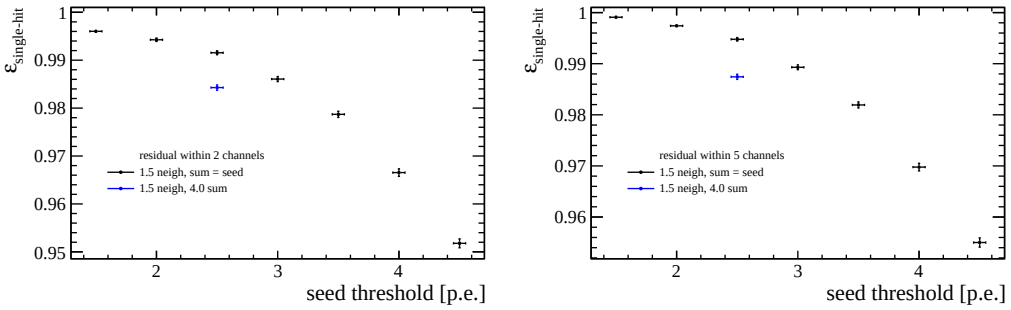

(a) (b)

Figure 29.9: Fitted single-hit efficiency for tracks at a distance of 240 cm to the SiPMs, obtained from a fit to the plateau for channels with ID larger than 45 and less than 60, significantly away from the gap. The blue points refer to the set of thresholds foreseen for the operation of the LHCb upgrade detector. The tolerable residual between the SciFi cluster and the extrapolated TimePix track is less than (a) 2 channels and (b) 5 channels. The angle between the surface vector of the module and the beam is 0°.

Table 29.5: The single hit efficiency for a given seed, neighbour and sum threshold for tracks at the mirror. The values in bold refer to the set of thresholds foreseen for the operation of the LHCb upgrade detector.

	$\varepsilon_{\text{single-hit}}$	
set of thresholds	residual within 2 channels	residual within 5 channels
(1.5, 1.5, 1.5)	$99.6 \pm 0.1\%$	$99.91 \pm 0.04\%$
(1.5, 2.0, 1.5)	$99.4 \pm 0.1\%$	$99.74 \pm 0.05\%$
(1.5, 2.5, 1.5)	$99.2 \pm 0.1\%$	$99.48 \pm 0.07\%$
(1.5, 3.0, 1.5)	$98.6 \pm 0.1\%$	$99.0 \pm 0.1\%$
(1.5, 3.5, 1.5)	$97.9 \pm 0.1\%$	$98.3 \pm 0.1\%$
(1.5, 4.0, 1.5)	$96.7 \pm 0.1\%$	$97.1 \pm 0.1\%$
(1.5, 4.5, 1.5)	$95.2 \pm 0.1\%$	$95.6 \pm 0.1\%$
(**1.5**, **2.5**, **4.0**)	$\mathbf{98.4 \pm 0.1\%}$	$\mathbf{98.8 \pm 0.1\%}$

For seed thresholds below 3.0 p.e., the single-fit efficiency is larger than 99% up to 99.91%. When applying the set of thresholds foreseen for the operation in LHC, the single-hit efficiency is $98.4 \pm 0.1\%$ for a tolerable residual of two channels and $98.8 \pm 0.1\%$ for a tolerable residual of five channels. The single-hit efficiency for the smaller tolerable residual of two channels is about 0.3% smaller compared to when residuals up to five channels are accepted. This difference presumably originates from a very small fraction of the particles that have scattered at the material of the SciFi modules. When expanding the

tolerable residual even further, the single-hit efficiency does not increase in this threshold region. In order to include clusters of particles that have scattered at the material but are reconstructed in the DUT, the single-hit efficiency of the SciFi module is defined for a tolerable residual between the SciFi cluster and the extrapolated TimePix track of five channels. The corresponding single-hit efficiencies for tracks at a distance of 120 cm and 50 cm to the SiPM arrays are given in Appendix C.

Table 29.6 lists the single-hit efficiencies using the set of thresholds foreseen for the operation of the LHCb upgrade detector for the three distances from the track to the SiPMs and the three angles between the surface vector of the module and the beam. The efficiency increases with the smaller distance from the track to the SiPM arrays because fewer clusters are rejected thanks to the higher light yield. Close to the SiPM arrays, the efficiency is almost 100%. For the same reason, the efficiency rises with the angle, and thus with the path length of the track through the fibre mat. The single-hit efficiency when

Table 29.6: The single-hit efficiency using the set of threshold foreseen for the operation of the LHCb upgrade detector for the six-layer SciFi prototype module for tracks at a distance of 240 cm, 120 cm and 50 cm from the SiPM arrays with angles between the surface vector of the module and the beam of 0°, 10° and 20°.

	angle	240 cm	120 cm	50 cm
$\varepsilon_{\text{single-hit}}$ [%]	0°	98.8 ± 0.1	99.3 ± 0.1	99.93 ± 0.05
	10°	99.6 ± 0.1	–	99.96 ± 0.02
	20°	99.6 ± 0.1	–	99.96 ± 0.01

applying the set of threshold foreseen for the operation of the LHCb upgrade detector is about 99% which is the requirement on the SciFi tracker. Improvements of the SiPMs have been made with the new 2016 models that lead to a higher light yield, and thus higher single-hit efficiency. New scintillating fibres produced during 2016 emit more light and have higher attenuation lengths. Both improvements lead to larger single-hit efficiencies. During the first period of LHCRun III when radiation effects do not play a role, the thresholds can be tuned to lower values in order to raise the single-hit efficiency. After the collection of $50\,\text{fb}^{-1}$ of collision data, the light yield of the modules will be reduced by about 40% which will lower the single-hit efficiency with the current choice of the set of thresholds. Recent irradiation studies of the SiPMs show smaller dark noise rates than expected. Therefore, the SciFi detector might be able to be operated with a lower set of thresholds.

30 Conclusion

The third part of this thesis presents the results of performance measurements of prototype modules of the LHCb upgrade Scinitillating Fibre Tracker (SciFi). The test-beam campaign took place at the SPS test-beam facilities at CERN with a mixed-particle beam with an energy of about 180 GeV. A prototype module consisting of six layers of scintillating fibres that has been assembled with the same techniques as the foreseen SciFi module, serves as the device-under-test. It has been brought to the test-beam along with three early prototype modules. The TimePix3 telescope is used to provide reference tracks that are extrapolated to the SciFi modules and compared with the reconstructed clusters in the detector. The absolute light yield collected by the Silicon Photomultiplier arrays, mounted to the end of the fibres, are obtained using a well-known data acquisition system. It allows to simulate the clustering process with three configurable thresholds that will be performed directly by the PACIFIC, the front-end electronics of the SciFi tracker. The test-beam is conducted at room temperature with modules that have not been exposed to irradiation prior to the test-beam.

Large datasets are collected at three different distances of the particle beam with respect to the SiPM arrays as photons get absorbed along the path through the fibres. At LHCb, most of the particles traverse the tracker in the inner part close to the beam pipe such that scintillating photons have to travel almost the full fibre length of 2.4 m before reaching the SiPM arrays. The angular dependence of the performance is obtained by rotating the module around the axis along the fibres to three angles between the surface vector of the fibre mat and the beam. At an angle of 0°, the beam traverses the fibre mat perpendicularly. The attenuation length of the scintillating fibres is measured with an early prototype with five layers of fibres that has no mirror attached to one end. The module is moved along its length in fine steps in order to obtain the light yield as a function of the distance of the beam to the SiPM arrays.

The mean of the collected light yield is found to be approximately 16.3 ± 0.4 photo-electrons for beam tracks that traverse the module at 2.4 m from the SiPM arrays. This is compatible with the expected light yield of 16.3 p.e. within uncertainties. The mean cluster size is 2.2 channels. A small fraction of the clusters is formed by more than four channels due to cross-talk between fibres and the emission of secondary particles in the scintillator. After the upgrade detector has collected a dataset corresponding to an integrated luminosity of at least $50\,\mathrm{fb}^{-1}$, the number of observed photons is expected to decrease by 40% due to radiation effects in the fibre caused by ionising radiation. This results in a remaining mean light yield of about 10 p.e.

The attenuation length is measured to be in the range of 326 cm to 356 cm, depending on the fit functions applied. This is consistent with measurements of single fibres in which light is directly shined into the fibre and the light intensity is determined at the end of the fibre.

The effective spatial resolution is determined to be $70.20 \pm 0.8\,\mu\mathrm{m}$ for clusters profiting

from the full light yield information and $77.23 \pm 1.3\,\mu\text{m}$ when using only the 2-bit threshold information as it is done for the SciFi tracker. The spatial resolution is determined to be rather constant between 60 µm and 70 µm for a light yield between 8 p.e. and 25 p.e. and about 100 µm below 5 p.e. Hence, with an expected light yield of 10 p.e. after collecting the integrated luminosity of $50\,\text{fb}^{-1}$ of collision data, the spatial resolution will presumably remain below 100 µm.

The single-hit detection efficiency for sensitive areas of the tracker is measured to be $98.8 \pm 0.1\%$ when forming clusters with the set of thresholds that are foreseen for the operation of the LHCb upgrade detector. These are designed to suppress thermal noise in the SiPMs that will emerge, due to non-ionising neutron irradiation, after the collection an integrated luminosity of $50\,\text{fb}^{-1}$. Studies are ongoing that investigate the benefits and disadvantages of cross-talk between fibres by changing the amount of titanium dioxide in the glue of the fibre mat. As the spatial resolution is already good enough, an increase of cross-talk might help to boost the single-hit efficiency.

The results of this test-beam campaign reveal that the SciFi modules meet the challenging upgrade requirements concerning the spatial resolution and the single-hit efficiency. Two test-beam campaigns followed in November 2015 and January 2017 in order to measure the performance of a module whose fibre mat has been irradiated to the dose expected for the lifetime of the upgrade detector. New mats with improved light yield and better performing SiPM arrays were used. Moreover, the PACIFIC readout system has been operated. These results are documented in Ref. [113]. In future test-beam campaigns, irradiated SiPM arrays will be used that have to be cooled down to $-40\,^{\circ}\text{C}$ to limit the thermal noise rate.

Concluding remarks

Concluding remarks

This thesis covers measurements that have been performed with the LHCb Run I dataset, with recently collected data of Run II and describes the development of the LHCb upgrade detector that will be installed before Run III.

The first part of this thesis presents the determination of the b-hadron production cross-sections at 7 TeV and 13 TeV centre-of-mass energies. The copious production of b hadrons, together with charm hadrons, provides the basis for all LHCb measurements as the LHCb detector has been designed to study the decays of heavy-flavour hadrons. Since the production of heavy-flavour hadrons proceeds via gluon-fusion processes, the production rate and its kinematic dependence provides a test of the knowledge of perturbative Quantum Chromodynamics. Due to the unique forward design of the LHCb detector, the measurement probes gluons that have highly asymmetric momentum fractions. The integrated b-hadron production cross-sections in the LHCb forward acceptance, between 2 and 5 in pseudorapidity η, are determined to be $69.0 \pm 0.3 \pm 6.1\,\mu$b and $137.5 \pm 1.1 \pm 12.8\,\mu$b, where the first uncertainty is statistical and the second is systematic in nature. The absolute values and the η-dependence of the measured cross-sections agree with theoretical predictions using fixed-order next-to-leading logarithmic (FONLL) [12] calculations within the uncertainties. The ratio of cross-sections at 13 TeV and 7 TeV is predicted with less uncertainty because large theoretical uncertainties of the renormalisation and factorisation scales cancel, which allows for a more precise comparison to data. The good agreement of both the measured cross-sections and their ratio at the recently unexplored centre-of-mass energy of 13 TeV and 7 TeV is a great success of the underlying theory model.

The second part of this thesis presents a measurement that demonstrates the general idea of precision measurements at LHCb. The b-hadron decay $B_s^0 \to \phi\phi$ occurs rarely and only about 4000 signal decays are found in the LHCb Run I dataset because its decay amplitude is strongly suppressed in the Standard Model. However, it is very sensitive to new phenomena in quantum loops that might compete with the Standard-Model amplitude. Since the particles in the loop-suppressed processes are only created virtually, the decay is sensitive to new particles that are much heavier than the b-hadron energy scale. The impact of new heavy particles can be observed indirectly, even if they cannot be directly produced and detected by the ATLAS and CMS exeriments. The CP-violating phase is determined to be $\phi_s(B_s^0 \to \phi\phi) = -0.17 \pm 0.15\,(\text{stat}) \pm 0.03\,(\text{syst})\,\text{rad}$ which is compatible with Standard-Model predictions of $\phi_s^{\text{SM}} = 0.00 \pm 0.02\,\text{rad}$. This is the first measurement of the CP-violating phase in $B_s^0 \to \phi\phi$ decays. No evidence for contributions from new physics beyond the Standard Model is found. Together with the time-dependent CP-violation measurements in $B_s^0 \to J/\psi\,\phi$ and $B_s^0 \to J/\psi\,\pi^+\pi^-$ decays [76], no deviation from Standard-Model predictions can be concluded either in the B_s^0 mixing process or in the $\bar{b} \to s\bar{s}\bar{s}$ penguin decay amplitude.

The measured uncertainty of $\phi_s(B_s^0 \to \phi\phi)$ is large and it is dominated by the statistical uncertainty. Even with the number of b-hadron decays that are expected to be collected

during LHC Run II, the uncertainties of most of LHCb's key analyses in various decay modes will not decrease to the level of the theoretical uncertainties. As the collection rate of heavy-flavour hadron decays is currently limited by the readout rate of the front-end electronics of 1 MHz and the low instantaneous luminosity, the LHCb detector has to undergo a major upgrade to collect significantly larger numbers of decays. To exploit the physics potential of a larger luminosity and a readout rate of 40 MHz, parts of the LHCb detector will be replaced. The current main tracking stations will be replaced with a Scintillating Fibre Detector (SciFi). In order to show that the new SciFi tracking detector meets the challenging requirements, the performance of prototype modules is measured under real conditions with a particle beam. The spatial resolution is determined to be $77.2 \pm 1.3\,\mu\text{m}$ and the single-hit detection efficiency is measured as $98.8 \pm 0.1\%$, which meets the requirements of the LHCb upgrade detector. The upgraded detector will be installed during 2019 and 2020 and the data-taking will start with LHC Run III from the beginning of 2021. The resulting measurements will set stringent limits on possible new-physics effects. After the collection of $50\,\text{fb}^{-1}$ of collision data, the final expected sensitivity of the CP-violating phase $\phi_s(B_s^0 \to \phi\phi)$ is 0.026 [105] which is almost as small as the theoretical uncertainty of 0.02. The statistical precision of the corresponding phase in $B_s^0 \to J/\psi\,\phi$ decays could reach 0.009 compared to the current sensitivity of 0.05. The statistical uncertainties of the CP-averaged observables in $B^0 \to K^{*0}\mu^+\mu^-$ decays that reveal differences with predictions based on the Standard Model at the level of 3.4 standard deviations [103], are expected to decrease from 0.04 to 0.007.

In 2018, the next-generation B-factory Belle II is planned to start taking data with e^+e^- collisions provided by the upgraded collider SuperKEKB. The electrons and positrons will collide at a 40 times higher instantaneous luminosity compared to the previous KEK accelerator and about 1000 pairs of b mesons will be produced per second without background tracks. Belle II will be complementary to the exploration of flavour physics and the search for new physics beyond the Standard Model done by LHCb. Whereas the LHCb experiment exploits the higher production rate of b hadrons, the reconstruction of both the b meson and its anti-b-meson at Belle II allows for the determination of the kinematics of undetected particles such as neutrinos. Belle II and the new LHCb upgrade detector will open a new era of heavy-flavour physics and measure its parameters to an unprecedented precision.

Bibliography

[1] LHCb Collaboration, R. Aaij et al, *Measurement of the b-Quark Production Cross Section in 7 and 13 TeV pp Collisions*, Phys. Rev. Lett. **118** (2017) 052002.

[2] LHCb Collaboration, R. Aaij et al, *Search for CP Violation in the Decay $B_s^0 \to \phi\phi$ with the Full LHCb Run I Dataset*, LHCb-ANA-2014-035 (2014) .

[3] C. Langenbruch, *Measurement of the B_s^0 mixing phase in the decay $B_s^0 \to J/\psi\phi$ with the LHCb experiment*, PhD thesis, Heidelberg U., 2011.

[4] C. Linn, *Measurement of the CP-violating phase ϕ_s using $B_s \to J/\psi\phi$ and $B_s^0 \to J/\psi\pi^+\pi^-$ decays with the LHCb experiment*, PhD thesis, Heidelberg U., 2013-04-01.

[5] M. Kecke, *Time-integrated measurement of CP violation using $B_s^0 \to \phi\phi$ decays with the LHCb experiment*, Master thesis in the HD LHCb group.

[6] LHCb Collaboration, R. Aaij et al, *Measurement of CP violation in $B_s^0 \to \phi\phi$ decays*, Phys. Rev. D **90** (2014) 052011.

[7] LHCb Collaboration, S. S. et al, *Measurement of the b quark production cross-section in 7 and 13 TeV pp collisions*, LHCb-ANA-2016-040.

[8] R. Cavalcante et al, *LHCb Scintillating Fibre Tracker: Test Beam Report 2015*, Tech. Rep. LHCb-PUB-2015-025. CERN-LHCb-PUB-2015-025, CERN, Geneva, Nov, 2015.

[9] G. Aad et al, *Observation of a new particle in the search for the Standard Model Higgs boson with the ATLAS detector at the LHC*, Physics Letters B **716** (2012), no. 1 1 .

[10] S. Chatrchyan et al, *Observation of a new boson at a mass of 125 GeV with the CMS experiment at the LHC*, Physics Letters B **716** (2012), no. 1 30 .

[11] D. J. Gross and F. Wilczek, *Asymptotically free gauge theories. I*, Phys. Rev. D **8** (1973) 3633.

[12] M. Cacciari *et al.*, *Theoretical predictions for charm and bottom production at the LHC*, Journal of High Energy Physics **2012** (2012), no. 10 137.

[13] S. L. Glashow, *Partial-symmetries of weak interactions*, Nuclear Physics **22** (1961), no. 4 579 .

[14] A. Salam and J. Ward, *Electromagnetic and weak interactions*, Physics Letters **13** (1964), no. 2 168 .

[15] S. Weinberg, *A model of leptons*, Phys. Rev. Lett. **19** (1967) 1264.

[16] G. ALTARELLI, *The Standard Model of particle physics*, arXiv:hep-ph/0510281.

[17] G. Altarelli, *The Standard electroweak theory and beyond*, in *Phenomenology of gauge interactions. Proceedings, Summer School, Zuoz, Switzerland, August 13-19, 2000*, pp. 1–59, 2000. arXiv:hep-ph/0011078.

[18] T. Brock, Ian; Schorner-Sadenius, *Physics at the Terascale*, WILEY-VCH Verlag, 2011.

[19] C. P. et al. (Particle Data Group), *2016 review of particle physics*, Chin. Phys. C, 40, 100001 (2016) (2016).

[20] M. Kobayashi and T. Maskawa, *CP-Violation in the Renormalizable Theory of Weak Interaction*, Progress of Theoretical Physics **49** (1973), no. 2 652.

[21] L. Wolfenstein, *Parametrization of the Kobayashi-Maskawa Matrix*, Phys. Rev. Lett. **51** (1983) 1945.

[22] CKMfitter Group, J. Charles et al, *CP violation and the CKM matrix: Assessing the impact of the asymmetric B factories; updated results and plots available at: http://ckmfitter.in2p3.fr*, Eur. Phys. J. **C41** (2005), no. 1 1, arXiv:hep-ph/0406184.

[23] L. Evans and P. Bryant, *LHC Machine*, Journal of Instrumentation **3** (2008), no. 08 S08001.

[24] LHCb Collaboration, R. Aaij et al, *Measurement of* $\sigma(pp \to b\bar{b}X)$ *at* $\sqrt{s} = 7TeV$ *in the forward region*, Physics Letters B **694** (2010), no. 3 209 .

[25] LHCb collaboration, A. A. Alves Jr. *et al.*, *The LHCb detector at the LHC*, JINST **3** (2008) S08005.

[26] LHCb, *Speaker's bureau:*, Material for Presentations.

[27] LHCb, *LHCb VELO TDR: Vertex locator. Technical design report*, .

[28] R. E. Kalman, *A new approach to linear filtering and prediction problems*, Transactions of the ASME–Journal of Basic Engineering **82** (1960), no. Series D 35.

[29] T. L. collaboration, *Measurement of the track reconstruction efficiency at LHCb*, Journal of Instrumentation **10** (2015), no. 02 P02007.

[30] LHCb Collaboration, F. Archilli et al, *Performance of the Muon Identification at LHCb*, Journal of Instrumentation **8** (2013), no. 10 P10020.

[31] L. Collaboration, *Performance of the LHCb RICH Detector*, Eur. Phys. J. C (2013) 73:2431 (2013) .

[32] LHCb Collaboration, R. Aaij et al, *The LHCb trigger and its performance in 2011*, Journal of Instrumentation **8** (2013), no. 04 P04022.

[33] T. L. collaboration, *Precision luminosity measurements at LHCb*, Journal of Instrumentation **9** (2014), no. 12 P12005.

[34] T. Sjöstrand, S. Mrenna, and P. Skands, *A brief introduction to PYTHIA 8.1*, Comput. Phys. Commun. **178** (2008) 852, arXiv:0710.3820.

[35] D. J. Lange, *The EvtGen particle decay simulation package*, Nucl. Instrum. Meth. **A462** (2001) 152.

[36] Geant4 collaboration, S. Agostinelli *et al.*, *Geant4: A simulation toolkit*, Nucl. Instrum. Meth. **A506** (2003) 250.

[37] Geant4 collaboration, J. Allison *et al.*, *Geant4 developments and applications*, IEEE Trans. Nucl. Sci. **53** (2006) 270.

[38] R. J. Barlow, *Statistics: A guide to the use of statistical methods in the physical sciences*, Wiley Blackwell, 1989.

[39] F. James, *Minuit, function minimization and error analysis*, CERN long writeup D506.

[40] Y. Xie, *sFit: A method for background subtraction in maximum likelihood fit*, ArXiv e-prints (2009) arXiv:0905.0724.

[41] M. Pivk and F. R. Le Diberder, *sPlot: A statistical tool to unfold data distributions*, Nucl. Instrum. Meth. **A555** (2005) 356, arXiv:physics/0402083.

[42] M. Pivk and F. L. Diberder, *A statistical tool to unfold data distributions*, Nuclear Instruments and Methods in Physics Research Section A: Accelerators, Spectrometers, Detectors and Associated Equipment **555** (2005), no. 1-2 356 .

[43] O. Zenaiev et al, *Impact of heavy-flavour production cross sections measured by the LHCb experiment on parton distribution functions at low x*, The European Physical Journal C **75** (2015), no. 8 396.

[44] R. Gauld, J. Rojo, L. Rottoli, and J. Talbert, *Charm production in the forward region: constraints on the small-x gluon and backgrounds for neutrino astronomy*, JHEP **11** (2015) 009, arXiv:1506.0802.

[45] Heavy Flavor Averaging Group, Y. Amhis *et al.*, *Averages of b-hadron, c-hadron, and τ-lepton properties as of summer 2014*, arXiv:1412.7515, updated results and plots available at http://www.slac.stanford.edu/xorg/hfag/.

[46] LHCb Collaboration, R. Aaij et al, *Observation of the decay $B_c^+ \to B_s^0 \pi^+$*, Phys. Rev. Lett. **111** (2013) 181801.

[47] M. B. Voloshin, *Remarks on measurement of the decay $\Xi_b^- \to \Lambda_b \pi^-$*, arXiv (2015), 1510.05568.

[48] A. V. Manohar and M. B. Wise, *Inclusive semileptonic B and polarized Λ_b^0 decays from QCD*, Phys. Rev. **D49** (1994) 1310, arXiv:hep-ph/9308246.

[49] I. I. Bigi, M. A. Shifman, N. Uraltsev, and A. I. Vainshtein, *QCD predictions for lepton spectra in inclusive heavy flavor decays*, Phys. Rev. Lett. **71** (1993) 496, arXiv:hep-ph/9304225.

[50] I. I. Bigi, T. Mannel, and N. Uraltsev, *Semileptonic width ratios among beauty hadrons*, JHEP **09** (2011) 012, arXiv:1105.4574.

[51] CLEO Collaboration, A. Mahmood *et al.*, *Measurement of the B-meson inclusive semileptonic branching fraction and electron energy moments*, Phys. Rev. **D70** (2004) 032003, arXiv:hep-ex/0403053.

[52] BaBar Collaboration, B. Aubert *et al.*, *Measurement of the ratio* $\mathcal{B}(B^+ \to Xe\nu)/\mathcal{B}(B^0 \to Xe\nu)$, Phys. Rev. **D74** (2006) 091105, arXiv:hep-ex/0607111.

[53] Belle Collaboration, P. Urquijo *et al.*, *Moments of the electron energy spectrum and partial branching fraction of* $B \to X(c)e\nu$ *decays at Belle*, Phys. Rev. **D75** (2007) 032001, arXiv:hep-ex/0610012.

[54] CDF Collaboration, T. Aaltonen *et al.*, *Measurement of the* B_s *Lifetime in Fully and Partially Reconstructed* $B_s \to D_s^-(\phi\pi^-)X$ *Decays in* $\bar{p}-p$ *Collisions at* $\sqrt{s} = 1.96$ *TeV*, Phys. Rev. Lett. **107** (2011) 272001, arXiv:1103.1864.

[55] LHCb Collaboration, R. Aaij et al, *Measurement of the* $\overline{B}_s^0$ *meson lifetime in* $D_s^+\pi^-$ *decays*, Phys. Rev. Lett. **113** (2014), no. 17 172001, arXiv:1407.5873.

[56] CLEO Collaboration, S. Dobbs *et al.*, *Measurement of absolute hadronic branching fractions of D mesons and* $e^+e^- \to D\overline{D}$ *cross-sections at the* $\psi(3770)$, Phys. Rev. **D76** (2007) 112001, arXiv:0709.3783.

[57] BESIII Collaboration, M. Ablikim et al, *Measurements of absolute hadronic branching fractions of the* Λ_c^+ *baryon*, Phys. Rev. Lett. **116** (2016) 052001.

[58] Belle Collaboration, A. Zupanc *et al.*, *Measurement of the branching braction* $\mathcal{B}(\Lambda_c^+ \to pK^-\pi^+)$, Phys. Rev. Lett. **113** (2014), no. 4 042002, arXiv:1312.7826.

[59] P. Fahner, *Measurement of the branching ratio for the decay* $\Lambda_b^0 \to D^0 p\mu^-\bar{\nu}_\mu X$ *with the LHCb experiment*, 2015. Master thesis in the HD LHCb group.

[60] M. Cacciari, M. Greco, and P. Nason, *The* p_T *spectrum in heavy-flavour hadroproduction*, Journal of High Energy Physics **1998** (1998), no. 05 007.

[61] M. L. Mangano, *Two lectures on heavy quark production in hadronic collisions*, in *Heavy flavor physics: A probe of nature's grand design. Proceedings, 137th Course of the International School of Physics 'Enrico Fermi', Varenna, Italy, July 8-18, 1997*, pp. 95–137, 1997. arXiv:hep-ph/9711337.

[62] P. Nason, S. Dawson, and R. Ellis, *The total cross section for the production of heavy quarks in hadronic collisions*, Nuclear Physics B **303** (1988), no. 4 607 .

[63] M. Cacciari and M. Greco, *Large* p_T *hadroproduction of heavy quarks*, Nucl. Phys. **B421** (1994) 530, arXiv:hep-ph/9311260.

[64] V. V. Gligorov, *A single track HLT1 trigger*, Public CERN Note (2011), CERN-LHCb-PUB-2011-003.

[65] LHCb Collaboration, R. Aaij et al, *Measurement of the $B_s^0 \to D_s^{(*)+} D_s^{(*)-}$ branching fractions*, Phys. Rev. D **93** (2016) 092008.

[66] The LHCb Collaboration, R. Aaij et al, *Measurement of b hadron production fractions in 7 TeV pp collisions*, Phys. Rev. D **85** (2012) 032008.

[67] LHCb Collaboration, R. Aaij et al, *Measurement of forward J/ψ production cross-sections in pp collisions at $\sqrt{s} = 13TeV$*, Journal of High Energy Physics **2015** (2015), no. 10 172.

[68] T. Skwarnicki, *A study of the radiative cascade transitions between the Upsilon-prime and Upsilon resonances*, PhD thesis, Institute of Nuclear Physics, Krakow, 1986, DESY-F31-86-02.

[69] LHCb Collaboration, R. Aaij et al, *Measurements of prompt charm production cross-sections in pp collisions at $\sqrt{s} = 13TeV$*, Journal of High Energy Physics **2016** (2016), no. 3 159.

[70] LHCb Collaboration, R. Aaij et al, *Precision measurement of CP violation in $B_s^0 \to \mathrm{J}/\Psi K^+ K^-$ decays*, Phys. Rev. Lett. **114** (2015) 041801.

[71] LHCb Collaboration, R. Aaij et al, *First Measurement of the CP-Violating Phase in $B_s^0 \to \phi\phi$ Decays*, Phys. Rev. Lett. **110** (2013) 241802.

[72] BABAR Collaboration, B. Aubert et al, *Direct CP Violating Asymmetry in $B^0 \to K^+\pi^-$ Decays*, Phys. Rev. Lett. **93** (2004) 131801.

[73] CKMfitter Group, A. Lenz *et al.*, *Anatomy of new physics in B-$\overline{B}$ mixing*, Phys. Rev. D **83** (2011) 036004.

[74] I. Dunietz, R. Fleischer, and U. Nierste, *In pursuit of new physics with B_s decays*, Phys. Rev. D **63** (2001) 114015.

[75] LHCb Collaboration, R. Aaij et al, *Measurement of the $B_s^0 - \bar{B}_s^0$ oscillation frequency Δm_s in $B_s^0 \to D_s^-(3)\pi$ decays*, Phys. Lett. **B709** (2012) 177, arXiv:1112.4311.

[76] LHCb Collaboration, R. Aaij et al, *Measurement of CP violation and the B_s^0 meson decay width difference with $B_s^0 \to J/\psi K^+ K^-$ and $B_s^0 \to J/\psi\pi^+\pi^-$ decays*, Phys. Rev. D **87** (2013) 112010.

[77] M. Bartsch, G. Buchalla, and C. Kraus, *$B \to$ V(L) V(L) Decays at Next-to-Leading Order in QCD*, arXiv:0810.0249.

[78] H.-Y. Cheng and C.-K. Chua, *QCD factorization for charmless hadronic B_s decays revisited*, Phys. Rev. D **80** (2009) 114026.

[79] T. Moroi, *CP violation in B(d) $\to \phi$ K(S) in SUSY GUT with right-handed neutrinos*, Phys. Lett. **B493** (2000) 366, arXiv:hep-ph/0007328.

[80] Y. Shimizu, M. Tanimoto, and K. Yamamoto, *Supersymmetry contributions to CP violations in b$\to$s and b$\to$d transitions taking account of new data*, Phys. Rev. **D87** (2013), no. 5 056004, arXiv:1212.6486.

[81] S. Nandi and A. Kundu, *New physics in $b \to s\bar{s}s$ decay. II: Study of $B \to V(1)\ V(2)$ modes*, J. Phys. **G32** (2006) 835, arXiv:hep-ph/0510245.

[82] C.-W. Chiang and L. Wolfenstein, *Observables in the decays of $\boldsymbol{B}$ to two vector mesons*, Phys. Rev. D **61** (2000) 074031.

[83] F. Azfar et al, *Formulae for the analysis of the flavor-tagged decay $B_s \to J/\psi\phi$*, Journal of High Energy Physics **2010** (2010), no. 11 158.

[84] S. Flatté, *On the nature of 0+ mesons*, Physics Letters B **63** (1976), no. 2 228 .

[85] CDF Collaboration, D. Acosta et al, *Evidence for $B_s^0 \to \phi\phi$ Decay and Measurements of Branching Ratio and A_{CP} for $B^+ \to \phi K^+$*, Phys. Rev. Lett. **95** (2005) 031801.

[86] CDF Collaboration, T. Aaltonen et al, *Measurement of Polarization and Search for CP Violation in $B_s^0 \to \phi\phi$ Decays*, Phys. Rev. Lett. **107** (2011) 261802.

[87] LHCb Collaboration, R. Aaij et al, *Measurement of the polarization amplitudes and triple product asymmetries in the decay $B_s^0 \to \phi\phi$*, Physics Letters B **713** (2012), no. 4-5 369 .

[88] *Letter of Intent for the LHCb Upgrade*, Tech. Rep. CERN-LHCC-2011-001. LHCC-I-018, CERN, Geneva, Mar, 2011.

[89] B. P. Roe *et al.*, *Boosted decision trees as an alternative to artificial neural networks for particle identification*, Nuclear Instruments and Methods in Physics Research Section A: Accelerators, Spectrometers, Detectors and Associated Equipment **543** (2005), no. 2-3 577 .

[90] A. Hoecker *et al.*, *TMVA: Toolkit for Multivariate Data Analysis*, PoS **ACAT** (2007) 040, arXiv:physics/0703039.

[91] R. Schapire, *The boosting approach to machine learning: an overview*, MSRI Workshop on Nonlinear Estima- tion and Classification (2002).

[92] LHCb Collaboration, R. Aaij *et al.*, *Selections and lifetime measurements for exclusive $b \to J/\psi X$ decays with $J/\psi \to \mu^+\mu^-$ with 2010 data*, LHCb-ANA-2011-001 (2011).

[93] H.-G. Moser and A. Roussarie, *Mathematical methods for $B^0\bar{B}^0$ oscillation analyses*, Nuclear Instruments and Methods in Physics Research Section A: Accelerators, Spectrometers, Detectors and Associated Equipment **384** (1997), no. 2 491 .

[94] W. D. Hulsbergen, *Decay chain fitting with a Kalman filter*, Nuclear Instruments and Methods in Physics Research Section A: Accelerators, Spectrometers, Detectors and Associated Equipment **552** (2005), no. 3 566 .

[95] LHCb Collaboration, R. Aaij et al, *Tagged time-dependent analysis of $B_s^0 \to J/\psi K^+K^-$ and $B_s^0 \to J/\psi\pi^+\pi^-$ decays with 1.0 fb^{-1}*, LHCb-ANA-2012-067 (2013), Linked to LHCb-PAPER-2013-002.

[96] T. du Pree, M. H. M. Merk, and H. G. Raven, *Search for a Strange Phase in Beautiful Oscillations. oai:cds.cern.ch:1299931*, PhD thesis, Amsterdam, Vrije Universiteit, Amsterdam, 2010, Presented on 22 Oct 2010.

[97] LHCb Collaboration, R. Aaij et al, *Flavour tagged time-dependent angular analysis of $B_s^0 \to J/\psi K^+K^-$ decays in the low K^+K^- mass range*, .

[98] Y. Xie, *Iterative method to improve simulation-based detector efficiency description in angular analysis*, Tech. Rep. LHCb-INT-2013-010. CERN-LHCb-INT-2013-010, CERN, Geneva, Feb, 2013.

[99] LHCb Collaboration, R. Aaij et al, *Opposite-side flavour tagging of B mesons at the LHCb experiment*, The European Physical Journal C **72** (2012), no. 6 2022.

[100] LHCb Collaboration, R. Aaij et al, *A new algorithm for identifying the flavour of B_s^0 mesons at LHCb*, Journal of Instrumentation **11** (2016), no. 05 P05010.

[101] A. Rogozhnikov, *Reweighting with boosted decision trees*, Journal of Physics: Conference Series **762** (2016), no. 1 012036.

[102] X. Liu, W. Wang, and Y. Xie, *Penguin pollution in $B \to J/\psi V$ decays and impact on the extraction of the $B_s - \overline{B}_s$ mixing phase*, Phys. Rev. D **89** (2014) 094010.

[103] LHCb Collaboration, R. Aaij et al, *Angular analysis of the $B^0 \to K^{*0}\mu^+\mu^-$ decay using 3 fb^{-1} of integrated luminosity*, JHEP **02** (2016) 104, `arXiv:1512.0444`.

[104] *LHCb Trigger and Online Upgrade Technical Design Report*, Tech. Rep. CERN-LHCC-2014-016. LHCB-TDR-016, May, 2014.

[105] T. Gerson, *Updated sensitivity projections for the LHCb Upgrade*, Tech. Rep. LHCb-PUB-2013-015. CERN-LHCb-PUB-2013-015, CERN, Geneva, Sep, 2013.

[106] L. Collaboration, *LHCb Tracker Upgrade Technical Design Report*, Tech. Rep. CERN-LHCC-2014-001. LHCB-TDR-015, Feb, 2014.

[107] C. Joram *et al.*, *LHCb Scintillating Fibre Tracker Engineering Design Review Report: Fibres, Mats and Modules*, Tech. Rep. LHCb-PUB-2015-008. CERN-LHCb-PUB-2015-008, CERN, Geneva, Mar, 2015.

[108] A. K. Kuonen *et al.*, *LHCb Scintillating Fibre Tracker Engineering Design Review: Silicon Photomultipliers*, Tech. Rep. LHCb-INT-2016-019. CERN-LHCb-INT-2016-019, CERN, Geneva, Apr, 2016.

[109] X. Han, *LHCb upgrade: Development of a large scintillating fibre tracker*, in *2015 IEEE Nuclear Science Symposium and Medical Imaging Conference (NSS/MIC)*, pp. 1–5, Oct, 2015. doi: 10.1109/NSSMIC.2015.7581959.

[110] B. Beischer *et al.*, *A high-resolution scintillating fiber tracker with silicon photomultiplier array readout*, Nuclear Instruments and Methods in Physics Research Section A: Accelerators, Spectrometers, Detectors and Associated Equipment **622** (2010), no. 3 542 .

[111] S. Callier, C. D. Taille, G. Martin-Chassard, and L. Raux, *EASIROC, an Easy & Versatile ReadOut Device for SiPM*, Physics Procedia **37** (2012) 1569 .

[112] K. Akiba *et al.*, *The Timepix Telescope for High Performance Particle Tracking*, Nucl. Instrum. Meth. **A723** (2013) 47, `arXiv:1304.5175`.

[113] D. Mueller, *Performance studies of irradiated scintillating fibre modules and quality checks during serial production for the LHCb SciFi Tracker*, Master thesis in the HD LHCb group.

Appendix

A Part I: Measurement of the b-hadron production cross-section

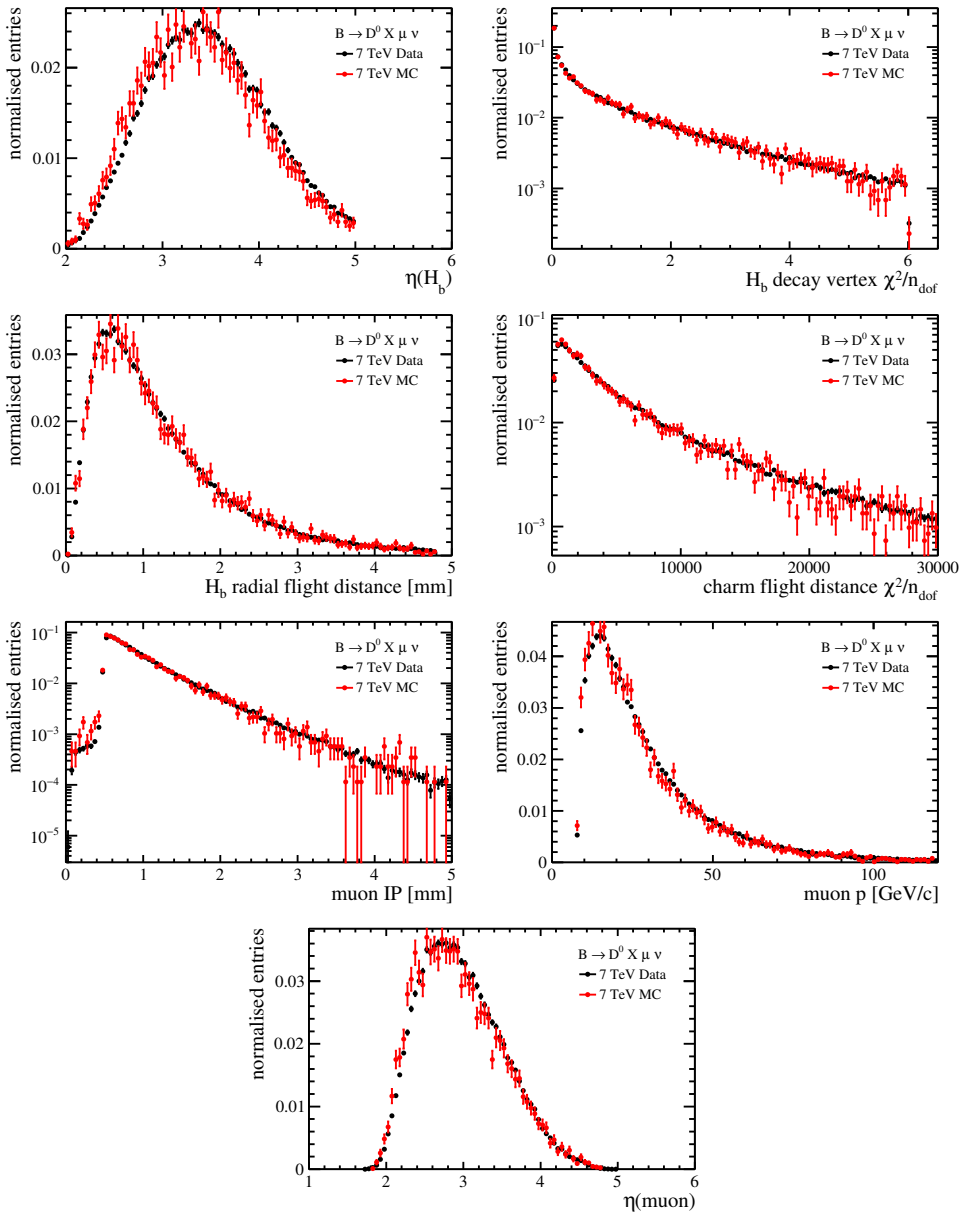

Figure A.1: Distributions of (top left) $\eta(B)$, B vertex χ^2, B radial flight distance, charm hadron flight distance χ^2 , muon IP, momentum and pseudorapidity from $B \to D^0 X \mu\nu$ decays in 7 TeV (black) data and (red) simulation.

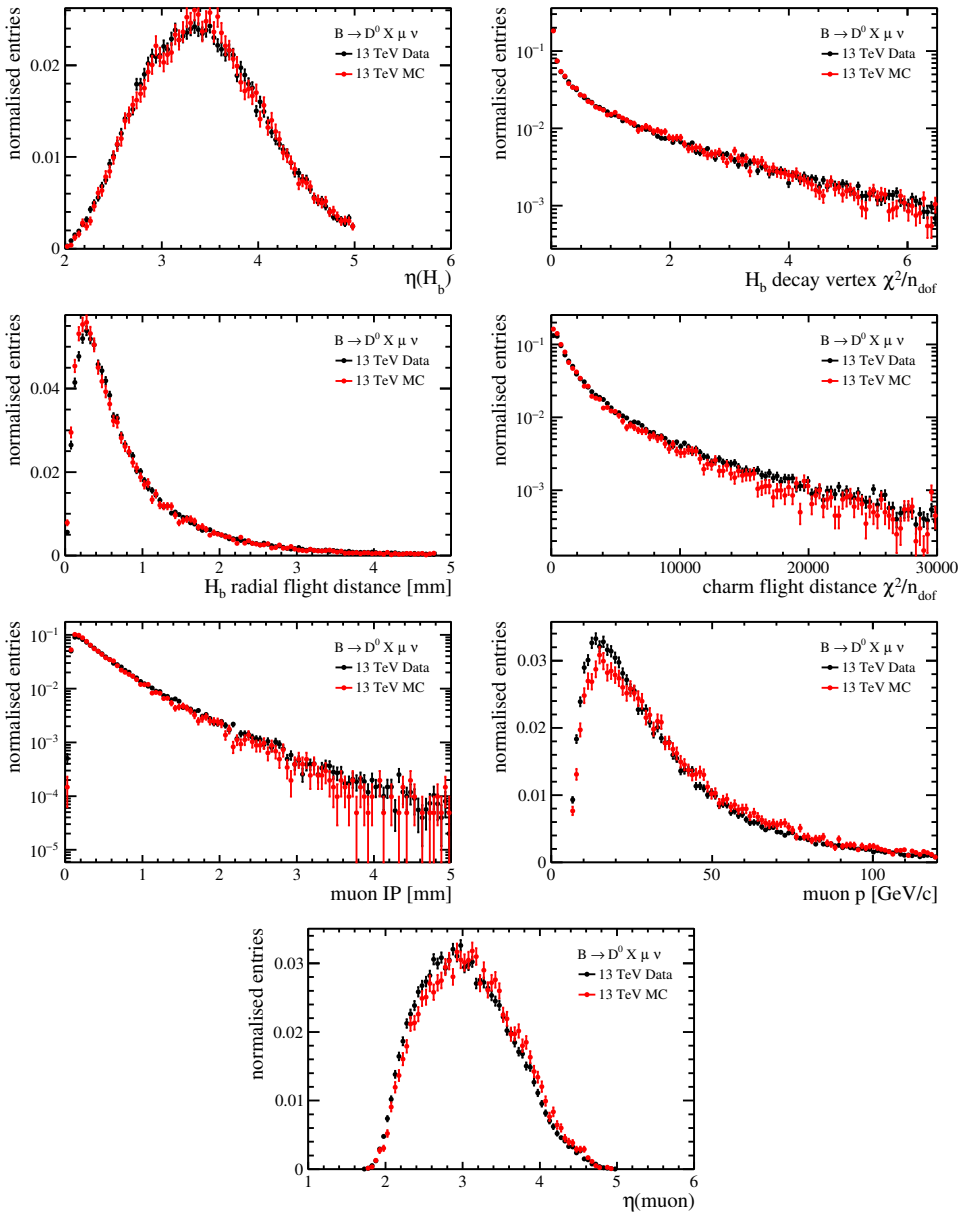

Figure A.2: Distributions of (top left) $\eta(B)$, B vertex χ^2, B radial flight distance, charm hadron flight distance χ^2 , muon IP, momentum and pseudorapidity from $B \to D^0 X \mu\nu$ decays in 13 TeV (black) data and (red) simulation.

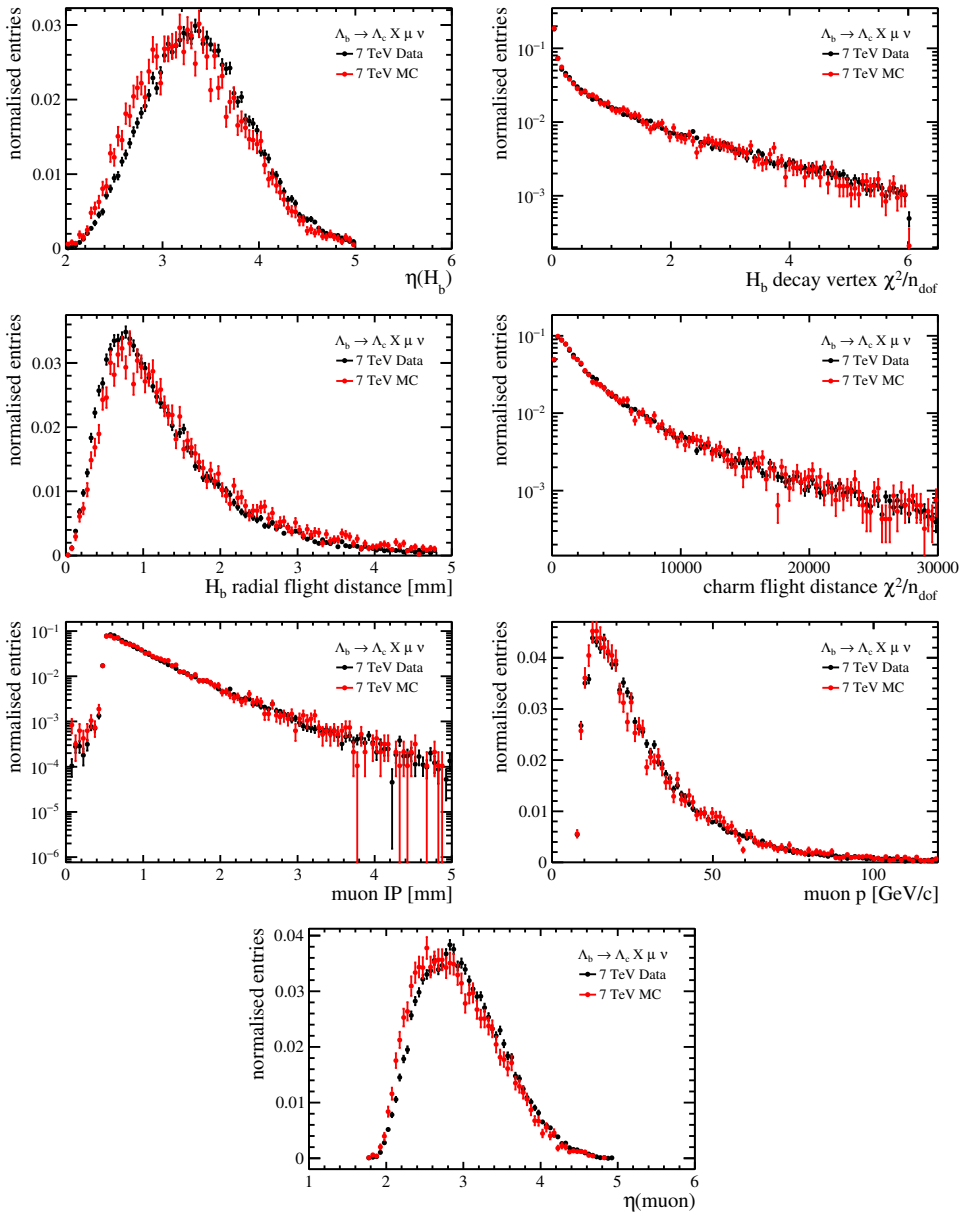

Figure A.3: Distributions of (top left) $\eta(\Lambda_b^0)$, Λ_b^0 vertex χ^2, Λ_b^0 radial flight distance, charm hadron flight distance χ^2 , muon IP, momentum and pseudorapidity from $\Lambda_b^0 \to \Lambda_c^+ X \mu\nu$ decays in 7 TeV (black) data and (red) simulation.

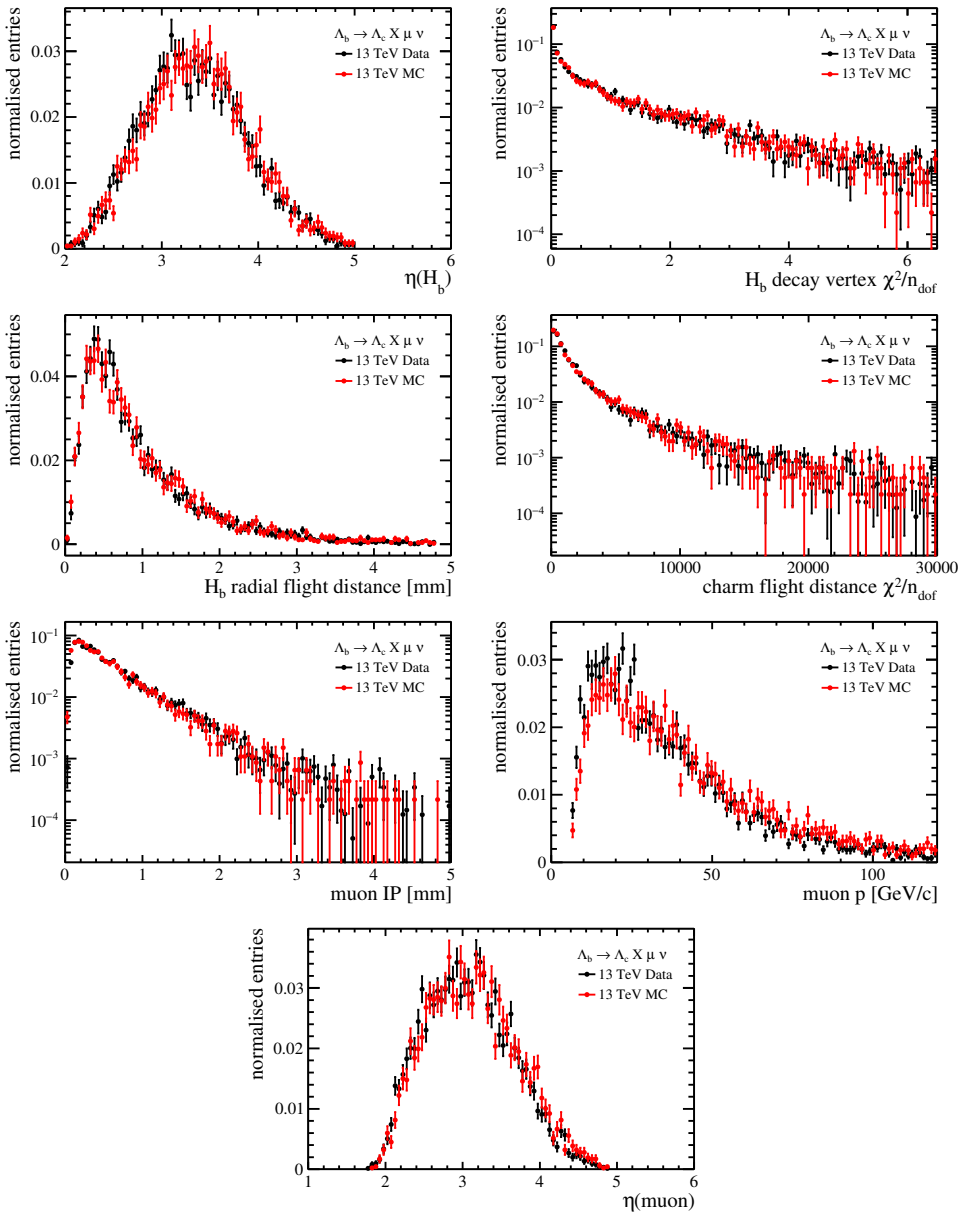

Figure A.4: Distributions of (top left) $\eta(\Lambda_b^0)$, Λ_b^0 vertex χ^2, Λ_b^0 radial flight distance, charm hadron flight distance χ^2 , muon IP, momentum and pseudorapidity from $\Lambda_b^0 \to \Lambda_c^+ X \mu\nu$ decays in 13 TeV (black) data and (red) simulation.

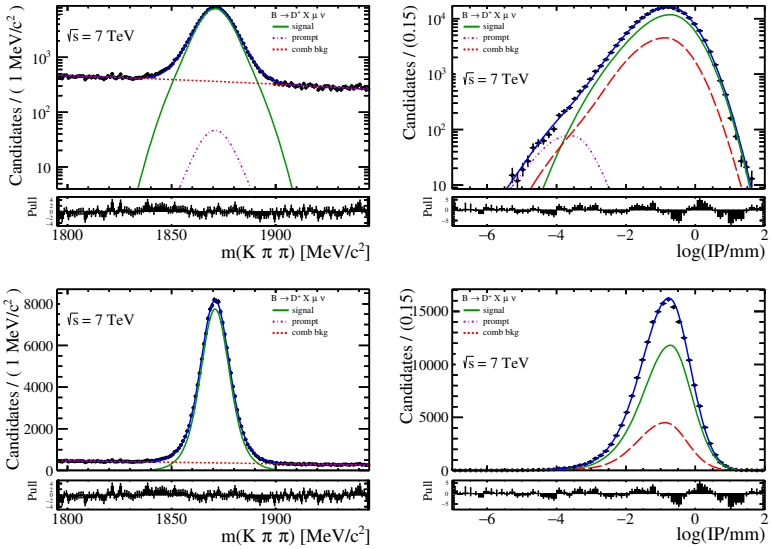

Figure A.5: Fit to the D^+ candidate invariant mass (left) and ln(IP/mm) (right) distributions in the pseudorapidity range 2 to 5 in data taken at a center-of-mass energy of 7 TeV. The black points show the data, the blue curves the total fit, the green curves the signal, the purple dashed curves charm from the primary, and the red dashed curves the combinatorial background.

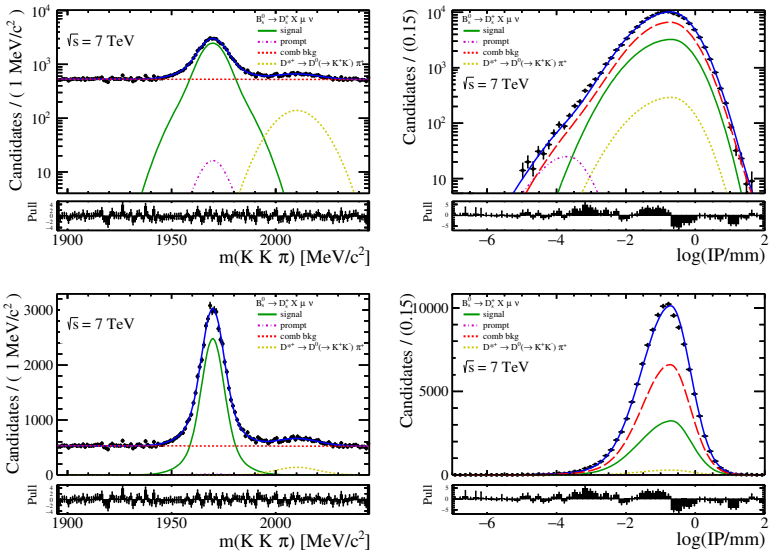

Figure A.6: Fit to the D_s candidate invariant mass (left) and ln(IP/mm) (right) distributions in the pseudorapidity range 2 to 5 in data taken at a center-of-mass energy of 7 TeV. The black points show the data, the blue curves the total fit, the green curves the signal, the purple dashed curves charm from the primary, and the red dashed curves the combinatorial background.

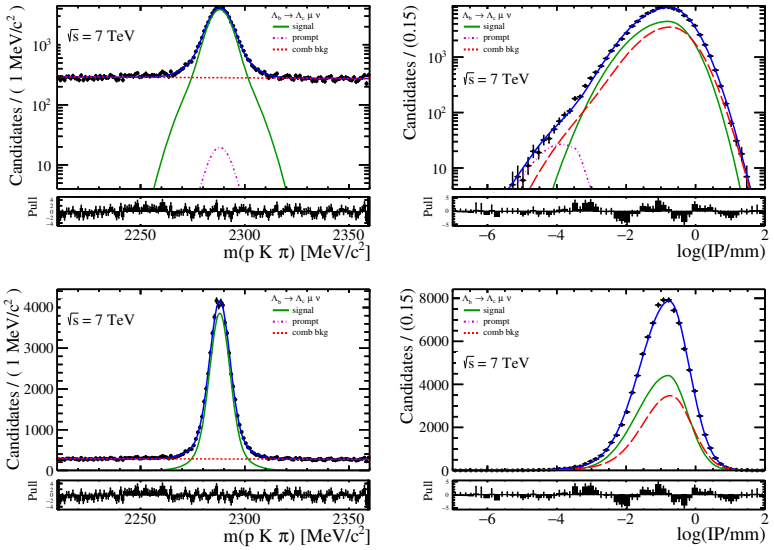

Figure A.7: Fit to the Λ_c candidate invariant mass (left) and ln(IP/mm) (right) distributions in the pseudorapidity range 2 to 5 in data taken at a center-of-mass energy of 7 TeV. The black points show the data, the blue curves the total fit, the green curves the signal, the purple dashed curves charm from the primary, and the red dashed curves the combinatorial background.

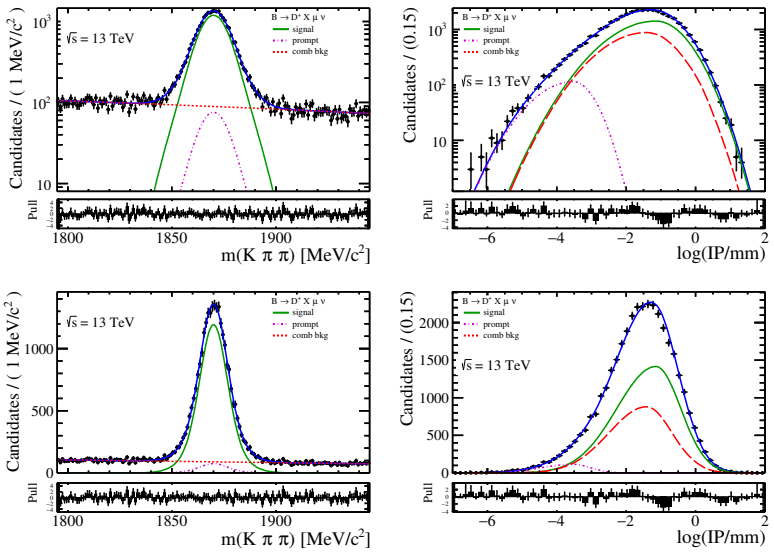

Figure A.8: Fit to the D^+ candidate invariant mass (left) and ln(IP/mm) (right) distributions in the pseudorapidity range 2 to 5 in data taken at a center-of-mass energy of 13 TeV. The black points show the data, the blue curves the total fit, the green curves the signal, the purple dashed curves charm from the primary, and the red dashed curves the combinatorial background.

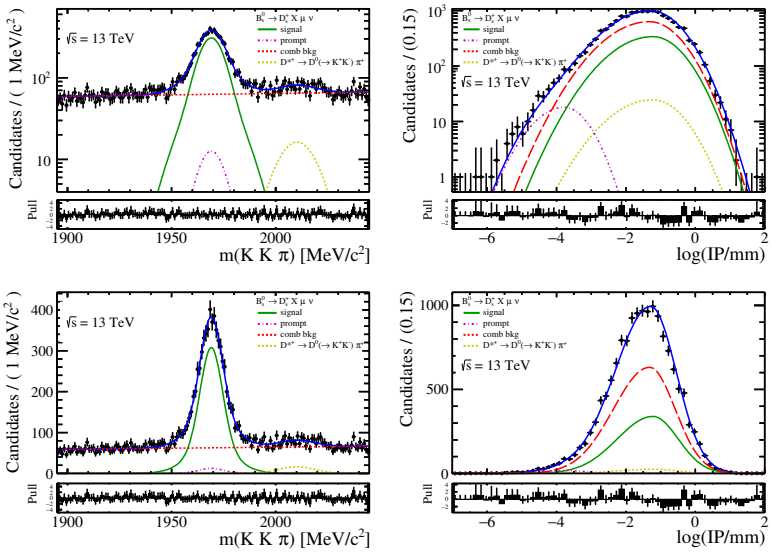

Figure A.9: Fit to the D_s candidate invariant mass (left) and ln(IP/mm) (right) distributions in the pseudorapidity range 2 to 5 in data taken at a center-of-mass energy of 13 TeV. The black points show the data, the blue curves the total fit, the green curves the signal, the purple dashed curves charm from the primary, and the red dashed curves the combinatorial background.

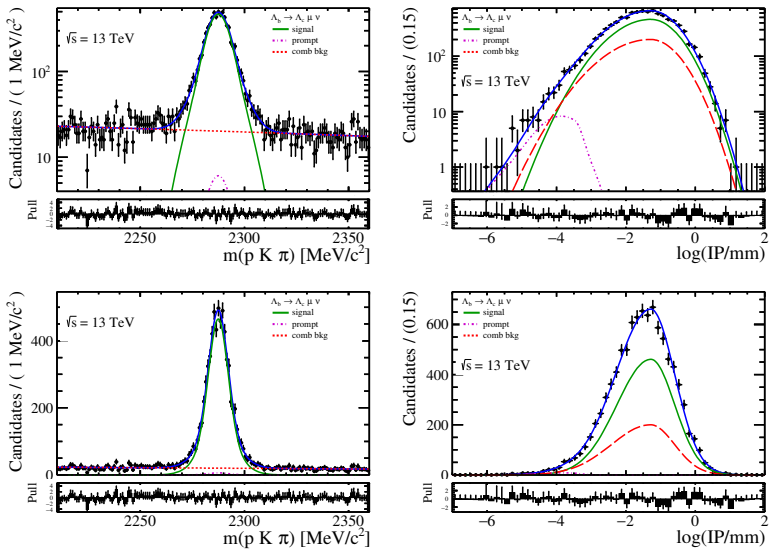

Figure A.10: Fit to the Λ_c candidate invariant mass (left) and ln(IP/mm) (right) distributions in the pseudorapidity range 2 to 5 in data taken at a center-of-mass energy of 13 TeV. The black points show the data, the blue curves the total fit, the green curves the signal, the purple dashed curves charm from the primary, and the red dashed curves the combinatorial background.

Table A.1: Fitted D^0 signal yields extracted in bins of $\eta(B^{0/+})$ and p_{T} (D^0 + μ) in the 7 TeV dataset.

p_{T} [GeV/c]	$2.0 < \eta < 2.5$	$2.5 < \eta < 3.0$	$3.0 < \eta < 3.5$	$3.5 < \eta < 4.0$	$4.0 < \eta < 4.5$	$4.5 < \eta < 5.0$
$0 < 2$	0.00 ± 0.50	52.18 ± 7.44	1164.04 ± 35.66	4211.49 ± 69.29	6320.14 ± 85.50	5859.94 ± 81.60
$2 < 4$	66.78 ± 8.44	3696.91 ± 63.12	15477.19 ± 129.74	20992.78 ± 152.57	15134.38 ± 130.14	5784.60 ± 81.66
$4 < 5$	290.85 ± 17.54	4933.81 ± 72.92	11225.32 ± 110.43	9800.03 ± 103.62	4207.37 ± 68.89	714.33 ± 28.61
$5 < 6$	581.54 ± 25.02	6016.12 ± 80.32	9688.03 ± 102.37	6911.13 ± 87.18	2443.25 ± 52.68	300.18 ± 19.10
$6 < 7$	911.45 ± 31.30	5933.66 ± 79.70	7270.12 ± 88.86	4491.47 ± 70.47	1345.50 ± 38.91	93.88 ± 10.76
$7 < 8$	1106.32 ± 34.40	4823.92 ± 72.07	5181.99 ± 75.05	2885.32 ± 56.52	718.89 ± 28.60	59.25 ± 8.11
$8 < 9$	1085.13 ± 34.10	3872.91 ± 64.49	3589.49 ± 62.53	1726.95 ± 43.53	388.68 ± 21.60	37.05 ± 6.37
$9 < 10$	1036.61 ± 33.38	2749.21 ± 54.42	2350.13 ± 50.71	1004.70 ± 33.47	202.57 ± 15.47	6.41 ± 3.07
$10 < 11$	864.41 ± 30.43	1996.31 ± 46.28	1503.70 ± 40.62	645.07 ± 26.72	112.73 ± 11.58	5.00 ± 1.67
$11 < 12$	720.87 ± 27.87	1492.09 ± 39.81	1002.01 ± 33.56	355.04 ± 20.10	59.55 ± 9.16	1.90 ± 1.42
$12 < 13$	552.66 ± 24.56	977.91 ± 32.76	698.50 ± 27.63	217.23 ± 15.55	28.17 ± 5.77	1.01 ± 1.00
$13 < 14$	399.80 ± 21.10	713.54 ± 27.86	450.39 ± 22.08	140.03 ± 12.69	20.61 ± 5.19	0.00 ± 0.50
$14 < 25$	1174.70 ± 35.77	1534.88 ± 40.82	822.50 ± 30.67	220.43 ± 22.42	17.00 ± 4.77	0.00 ± 0.50

Table A.2: Fitted D^+ signal yields extracted in bins of $\eta(B^{0/+})$ and p_{T} (D^+ + μ) in the 7 TeV dataset.

p_{T} [GeV/c]	$2.0 < \eta < 2.5$	$2.5 < \eta < 3.0$	$3.0 < \eta < 3.5$	$3.5 < \eta < 4.0$	$4.0 < \eta < 4.5$	$4.5 < \eta < 5.0$
$0 < 2$	0.00 ± 0.50	8.65 ± 3.01	294.38 ± 18.92	1160.43 ± 38.98	1983.29 ± 50.99	1905.20 ± 49.96
$2 < 4$	6.68 ± 2.90	1366.12 ± 40.59	6429.94 ± 89.03	9526.27 ± 110.44	6288.02 ± 91.68	2220.99 ± 54.94
$4 < 5$	118.56 ± 11.70	2727.04 ± 56.86	7366.57 ± 95.71	6929.16 ± 94.44	2991.85 ± 64.38	432.53 ± 24.95
$5 < 6$	230.56 ± 16.12	4000.30 ± 69.36	7733.67 ± 98.42	6002.09 ± 88.39	2067.30 ± 53.07	248.71 ± 18.12
$6 < 7$	462.77 ± 23.06	4469.20 ± 73.88	6616.49 ± 92.12	4671.98 ± 78.06	1425.84 ± 44.14	104.03 ± 12.96
$7 < 8$	590.57 ± 26.27	4230.40 ± 71.60	5206.02 ± 82.07	3114.70 ± 64.10	881.47 ± 34.37	55.96 ± 9.24
$8 < 9$	703.11 ± 29.02	3527.03 ± 66.13	3874.73 ± 70.83	2122.16 ± 52.64	540.53 ± 27.75	20.85 ± 5.80
$9 < 10$	695.94 ± 28.98	2830.45 ± 59.23	2849.68 ± 61.26	1321.90 ± 42.61	328.00 ± 20.79	8.48 ± 3.30
$10 < 11$	701.14 ± 29.06	2058.88 ± 51.11	1953.74 ± 49.97	936.93 ± 35.35	193.96 ± 16.05	6.48 ± 2.69
$11 < 12$	544.08 ± 25.77	1643.94 ± 45.34	1443.44 ± 42.67	542.56 ± 26.76	84.20 ± 10.88	5.99 ± 2.45
$12 < 13$	529.29 ± 25.36	1148.95 ± 38.39	858.73 ± 33.17	364.48 ± 21.43	55.72 ± 8.41	3.00 ± 1.73
$13 < 14$	376.75 ± 21.92	857.27 ± 32.68	636.35 ± 27.46	227.83 ± 18.12	38.78 ± 6.85	2.03 ± 1.43
$14 < 25$	1309.43 ± 39.65	2180.52 ± 51.32	1329.05 ± 41.69	358.33 ± 23.87	44.54 ± 7.86	2.98 ± 1.73

Table A.3: Fitted D_s^+ signal yields extracted in bins of $\eta(B_s^0)$ and p_{T} (D_s^+ + μ) in the 7 TeV dataset.

p_{T} [GeV/c]	$2.0 < \eta < 2.5$	$2.5 < \eta < 3.0$	$3.0 < \eta < 3.5$	$3.5 < \eta < 4.0$	$4.0 < \eta < 4.5$	$4.5 < \eta < 5.0$
$0 < 2$	0.00 ± 0.50	2.78 ± 1.73	84.17 ± 13.07	312.90 ± 29.06	484.72 ± 35.76	502.51 ± 33.70
$2 < 4$	7.92 ± 0.03	460.92 ± 30.99	1838.56 ± 70.31	2399.13 ± 80.86	1578.87 ± 64.02	445.96 ± 32.90
$4 < 5$	42.68 ± 9.72	868.91 ± 46.54	2077.16 ± 74.96	2029.34 ± 67.96	773.55 ± 42.57	94.89 ± 14.27
$5 < 6$	79.40 ± 15.11	1255.43 ± 56.71	2384.23 ± 75.24	1763.27 ± 62.82	532.94 ± 34.89	50.85 ± 8.90
$6 < 7$	155.77 ± 19.04	1239.38 ± 57.02	2064.99 ± 67.12	1240.74 ± 53.55	329.03 ± 26.32	13.05 ± 4.64
$7 < 8$	183.87 ± 22.17	1219.09 ± 53.11	1642.69 ± 57.86	1040.41 ± 45.67	194.80 ± 18.58	17.46 ± 0.34
$8 < 9$	226.60 ± 23.81	1099.21 ± 48.25	1170.45 ± 49.01	624.64 ± 36.72	108.56 ± 14.59	2.19 ± 1.72
$9 < 10$	245.17 ± 22.73	781.16 ± 41.15	790.11 ± 39.31	406.46 ± 27.89	54.12 ± 9.88	2.00 ± 1.41
$10 < 11$	217.87 ± 21.16	616.45 ± 34.20	550.53 ± 32.11	219.47 ± 18.97	41.92 ± 8.10	0.00 ± 0.50
$11 < 12$	200.63 ± 18.68	441.30 ± 28.86	378.53 ± 25.74	154.94 ± 17.58	12.71 ± 4.49	0.00 ± 0.50
$12 < 13$	145.94 ± 15.89	314.13 ± 23.31	258.82 ± 21.14	88.76 ± 12.61	13.27 ± 3.80	0.00 ± 0.50
$13 < 14$	107.04 ± 14.02	271.68 ± 20.90	173.97 ± 17.34	51.98 ± 8.66	5.29 ± 3.53	0.00 ± 0.50
$14 < 25$	392.64 ± 23.79	624.33 ± 30.43	325.60 ± 22.81	74.42 ± 11.24	4.78 ± 2.24	0.00 ± 0.50

Table A.4: Fitted Λ_c^+ signal yields extracted in bins of $\eta(\Lambda_b^0)$ and p_{T} $(\Lambda_c^+ + \mu)$ in the 7 TeV dataset.

p_{T} [GeV/c]	$2.0 < \eta < 2.5$	$2.5 < \eta < 3.0$	$3.0 < \eta < 3.5$	$3.5 < \eta < 4.0$	$4.0 < \eta < 4.5$	$4.5 < \eta < 5.0$
$0 < 2$	0.00 ± 0.50	1.97 ± 1.41	79.94 ± 11.91	359.51 ± 21.23	701.21 ± 31.99	570.12 ± 28.59
$2 < 4$	7.92 ± 3.96	441.01 ± 30.25	2279.24 ± 62.97	3361.82 ± 72.57	2157.47 ± 56.72	690.56 ± 30.62
$4 < 5$	46.61 ± 9.34	1017.23 ± 43.73	3026.66 ± 69.02	2738.49 ± 64.27	1019.65 ± 38.87	123.63 ± 13.57
$5 < 6$	125.20 ± 16.21	1551.85 ± 51.37	3325.60 ± 69.86	2657.37 ± 60.54	815.34 ± 33.42	65.07 ± 8.80
$6 < 7$	159.86 ± 18.11	1744.35 ± 52.26	3013.15 ± 64.89	2040.41 ± 52.70	524.66 ± 26.09	17.18 ± 5.09
$7 < 8$	237.32 ± 17.52	1641.82 ± 49.39	2318.14 ± 55.41	1303.11 ± 41.38	271.95 ± 18.89	15.65 ± 4.17
$8 < 9$	253.21 ± 20.22	1333.18 ± 43.85	1675.37 ± 46.40	813.28 ± 32.54	144.06 ± 13.18	1.96 ± 1.41
$9 < 10$	292.62 ± 20.64	985.32 ± 36.80	1129.52 ± 37.76	511.26 ± 25.09	61.47 ± 8.73	2.00 ± 1.41
$10 < 11$	226.61 ± 18.16	769.38 ± 31.91	703.36 ± 29.59	304.42 ± 19.86	31.76 ± 5.90	2.01 ± 1.42
$11 < 12$	170.35 ± 15.24	560.33 ± 26.73	524.77 ± 24.86	172.15 ± 14.61	22.40 ± 4.99	0.00 ± 0.50
$12 < 13$	154.91 ± 14.52	381.77 ± 21.91	314.58 ± 19.46	113.66 ± 11.79	11.03 ± 3.32	0.00 ± 0.50
$13 < 14$	121.38 ± 13.04	260.44 ± 17.20	196.63 ± 15.61	53.44 ± 7.97	5.51 ± 2.49	0.00 ± 0.50
$14 < 25$	342.59 ± 20.58	564.35 ± 25.84	346.51 ± 20.10	70.56 ± 9.44	4.00 ± 2.00	0.00 ± 0.50

Table A.5: Fitted D^0 signal yields extracted in bins of $\eta(B^{0,+})$ and p_{T} $(D^0 + \mu)$ in the 13 TeV dataset.

p_{T} [GeV/c]	$2.0 < \eta < 2.5$	$2.5 < \eta < 3.0$	$3.0 < \eta < 3.5$	$3.5 < \eta < 4.0$	$4.0 < \eta < 4.5$	$4.5 < \eta < 5.0$
$0 < 2$	0.00 ± 0.50	16.78 ± 4.39	391.90 ± 23.50	1331.37 ± 61.26	1572.31 ± 53.62	1300.27 ± 48.56
$2 < 4$	30.43 ± 5.83	1136.34 ± 37.16	3951.80 ± 71.26	4830.99 ± 81.29	3404.80 ± 70.11	1393.42 ± 55.13
$4 < 5$	91.94 ± 10.64	1511.03 ± 41.92	2719.28 ± 57.90	2403.20 ± 60.43	1133.79 ± 39.40	238.34 ± 16.54
$5 < 6$	220.29 ± 17.43	1789.79 ± 47.90	2360.67 ± 55.99	1745.19 ± 48.42	698.01 ± 30.94	80.85 ± 9.78
$6 < 7$	289.66 ± 17.63	1594.25 ± 45.86	1859.73 ± 48.94	1245.68 ± 41.08	408.08 ± 22.55	38.19 ± 7.07
$7 < 8$	388.98 ± 20.61	1353.78 ± 41.76	1449.29 ± 44.11	916.26 ± 33.23	222.16 ± 16.03	19.52 ± 5.12
$8 < 9$	320.61 ± 19.92	1078.73 ± 36.10	984.78 ± 36.06	543.11 ± 28.55	139.84 ± 12.87	9.61 ± 3.62
$9 < 10$	292.76 ± 21.74	828.28 ± 31.63	681.79 ± 28.26	354.58 ± 24.84	103.06 ± 10.55	4.54 ± 2.27
$10 < 11$	280.76 ± 18.18	617.13 ± 31.29	517.48 ± 27.14	265.49 ± 18.40	45.51 ± 7.64	3.99 ± 2.00
$11 < 12$	193.51 ± 14.63	465.94 ± 23.10	346.58 ± 19.33	154.45 ± 13.07	40.10 ± 6.60	2.76 ± 2.14
$12 < 13$	202.14 ± 18.28	336.63 ± 19.03	260.68 ± 19.42	112.07 ± 11.39	22.74 ± 5.44	0.00 ± 0.50
$13 < 14$	151.04 ± 12.79	246.56 ± 16.18	177.07 ± 16.51	69.27 ± 9.46	10.34 ± 3.92	1.00 ± 1.00
$14 < 25$	537.03 ± 24.18	733.68 ± 28.12	443.04 ± 21.90	164.51 ± 13.83	30.00 ± 5.80	1.00 ± 1.00

Table A.6: Fitted D^+ signal yields extracted in bins of $\eta(B^{0,+})$ and p_{T} $(D^+ + \mu)$ in the 13 TeV dataset.

p_{T} [GeV/c]	$2.0 < \eta < 2.5$	$2.5 < \eta < 3.0$	$3.0 < \eta < 3.5$	$3.5 < \eta < 4.0$	$4.0 < \eta < 4.5$	$4.5 < \eta < 5.0$
$0 < 2$	0.00 ± 0.50	0.00 ± 0.50	66.16 ± 11.61	235.34 ± 27.08	369.52 ± 29.32	284.93 ± 22.49
$2 < 4$	4.00 ± 2.24	221.68 ± 16.75	887.47 ± 40.26	1270.82 ± 50.83	865.56 ± 38.07	311.98 ± 22.13
$4 < 5$	8.12 ± 3.69	410.68 ± 22.98	984.49 ± 46.63	811.38 ± 35.08	398.22 ± 25.71	58.14 ± 15.90
$5 < 6$	53.60 ± 8.12	632.96 ± 38.59	1060.98 ± 41.55	821.81 ± 35.27	310.72 ± 21.72	44.81 ± 8.95
$6 < 7$	81.64 ± 9.66	680.54 ± 30.00	937.88 ± 36.17	626.76 ± 31.91	188.19 ± 17.00	28.57 ± 6.76
$7 < 8$	87.84 ± 10.69	630.98 ± 28.23	740.18 ± 33.47	525.13 ± 36.98	135.33 ± 13.96	6.93 ± 2.92
$8 < 9$	113.44 ± 12.08	573.92 ± 26.09	555.16 ± 29.49	356.51 ± 22.42	116.32 ± 12.11	7.52 ± 3.43
$9 < 10$	115.07 ± 11.71	433.81 ± 24.57	440.75 ± 26.69	257.41 ± 18.19	60.39 ± 9.16	2.60 ± 1.83
$10 < 11$	118.11 ± 11.77	301.87 ± 21.74	406.07 ± 23.83	197.94 ± 15.87	34.87 ± 6.70	2.85 ± 1.74
$11 < 12$	97.76 ± 10.84	296.45 ± 18.95	231.91 ± 19.35	135.10 ± 12.87	31.30 ± 6.06	0.89 ± 0.06
$12 < 13$	83.08 ± 9.79	208.86 ± 31.02	174.15 ± 20.26	79.03 ± 10.23	22.33 ± 5.17	0.00 ± 0.50
$13 < 14$	70.59 ± 9.71	160.79 ± 14.05	119.94 ± 13.08	50.78 ± 8.37	12.89 ± 4.21	0.00 ± 0.50
$14 < 25$	273.81 ± 21.28	464.78 ± 26.40	352.14 ± 21.74	122.83 ± 13.66	13.88 ± 4.10	0.00 ± 0.50

Table A.7: Fitted D_s^+ signal yields extracted in bins of $\eta(B_s^0)$ and p_{T} ($D_s^+ + \mu$) in the 13 TeV dataset.

p_{T} [GeV/c]	$2.0 < \eta < 2.5$	$2.5 < \eta < 3.0$	$3.0 < \eta < 3.5$	$3.5 < \eta < 4.0$	$4.0 < \eta < 4.5$	$4.5 < \eta < 5.0$
$0 < 2$	0.00 ± 0.50	1.19 ± 1.14	6.76 ± 3.43	30.62 ± 11.90	67.33 ± 13.29	57.76 ± 13.89
$2 < 4$	0.79 ± 0.84	33.63 ± 7.84	111.99 ± 8.97	299.43 ± 26.19	193.40 ± 20.43	58.51 ± 13.10
$4 < 5$	6.55 ± 2.66	85.71 ± 12.24	213.49 ± 21.67	181.70 ± 22.05	101.87 ± 14.04	16.67 ± 5.42
$5 < 6$	7.71 ± 4.61	144.15 ± 17.56	223.41 ± 21.42	169.54 ± 17.71	70.86 ± 10.97	4.99 ± 2.88
$6 < 7$	22.92 ± 6.02	153.59 ± 16.64	249.43 ± 21.80	137.79 ± 16.93	39.56 ± 7.65	0.00 ± 0.69
$7 < 8$	30.81 ± 7.46	167.59 ± 17.52	205.29 ± 19.09	157.65 ± 20.11	29.18 ± 6.99	0.00 ± 0.50
$8 < 9$	44.39 ± 0.11	135.97 ± 16.01	144.16 ± 16.56	94.29 ± 12.12	24.41 ± 5.98	0.98 ± 0.03
$9 < 10$	30.18 ± 7.21	102.78 ± 12.56	101.66 ± 16.31	79.24 ± 11.77	20.44 ± 5.66	0.43 ± 0.31
$10 < 11$	41.31 ± 7.93	77.45 ± 12.61	77.41 ± 11.90	41.57 ± 7.96	10.71 ± 3.77	1.00 ± 1.00
$11 < 12$	20.27 ± 6.71	80.20 ± 10.76	54.50 ± 8.84	25.42 ± 5.88	0.00 ± 135.73	0.00 ± 0.50
$12 < 13$	11.91 ± 4.15	50.45 ± 8.54	43.15 ± 7.69	28.36 ± 6.29	2.65 ± 0.16	0.00 ± 0.50
$13 < 14$	24.25 ± 5.61	27.34 ± 6.52	31.26 ± 7.10	7.57 ± 3.05	1.96 ± 1.41	0.00 ± 0.50
$14 < 25$	85.79 ± 11.67	125.57 ± 48.63	79.68 ± 11.27	27.76 ± 6.98	1.87 ± 1.42	0.00 ± 0.50

Table A.8: Fitted Λ_c^+ signal yields extracted in bins of $\eta(\Lambda_b^0)$ and p_{T} ($\Lambda_c^+ + \mu$) in the 13 TeV dataset.

p_{T} [GeV/c]	$2.0 < \eta < 2.5$	$2.5 < \eta < 3.0$	$3.0 < \eta < 3.5$	$3.5 < \eta < 4.0$	$4.0 < \eta < 4.5$	$4.5 < \eta < 5.0$
$0 < 2$	0.00 ± 0.50	0.00 ± 0.50	11.00 ± 3.87	30.82 ± 6.29	51.45 ± 8.03	49.97 ± 8.83
$2 < 4$	0.00 ± 0.50	30.95 ± 6.83	165.52 ± 15.91	305.22 ± 19.02	229.30 ± 17.50	61.93 ± 8.95
$4 < 5$	3.89 ± 2.00	75.25 ± 9.22	282.89 ± 18.26	280.78 ± 19.18	103.99 ± 11.93	20.02 ± 4.81
$5 < 6$	8.32 ± 3.36	163.48 ± 14.26	360.42 ± 21.64	272.68 ± 18.58	97.46 ± 10.99	9.56 ± 3.20
$6 < 7$	18.38 ± 4.51	183.48 ± 15.40	378.61 ± 22.29	258.93 ± 17.73	59.76 ± 8.51	5.79 ± 2.46
$7 < 8$	24.78 ± 5.54	203.78 ± 15.87	287.16 ± 18.50	178.38 ± 14.72	43.77 ± 7.22	3.00 ± 1.73
$8 < 9$	33.75 ± 6.73	183.18 ± 14.34	213.17 ± 15.63	108.71 ± 11.79	30.38 ± 5.77	0.99 ± 0.99
$9 < 10$	28.81 ± 6.47	160.35 ± 14.00	174.43 ± 13.98	83.20 ± 9.60	8.16 ± 3.04	0.00 ± 0.50
$10 < 11$	23.95 ± 5.59	106.37 ± 13.30	121.91 ± 12.05	53.30 ± 7.55	11.87 ± 3.47	0.00 ± 0.50
$11 < 12$	27.28 ± 6.05	85.67 ± 10.24	88.30 ± 9.86	31.26 ± 6.02	4.00 ± 2.00	0.00 ± 0.50
$12 < 13$	22.17 ± 5.54	68.87 ± 9.21	54.27 ± 7.65	17.06 ± 4.40	1.19 ± 0.80	0.00 ± 0.50
$13 < 14$	14.94 ± 4.20	57.04 ± 7.91	40.80 ± 7.14	13.59 ± 3.76	0.98 ± 0.99	0.00 ± 0.50
$14 < 25$	94.16 ± 10.82	140.53 ± 12.62	93.67 ± 10.30	36.83 ± 6.20	1.94 ± 1.42	0.00 ± 0.50

A.1 Backgrounds

Table A.9: Relative number of fake muons in the decay $B \to D^0 X \mu\nu$ for the 7 TeV selection

$\eta(H_b)$	Relative number of fake muons
2 - 2.5	0.07 ± 0.01 %
2.5 - 3	0.05 ± 0.01 %
3 - 3.5	0.04 ± 0.01 %
3.5 - 4	0.04 ± 0.01 %
4 - 4.5	0.020 ± 0.004 %
4.5 - 5	0.018 ± 0.004 %

Table A.10: Relative number of fake muons in the decay $B \to D^{+}X\mu\nu$ for the 7 TeV selection.

$\eta(H_b)$	Relative number of fake muons
2 - 2.5	0.06 ± 0.01 %
2.5 - 3	0.08 ± 0.02 %
3 - 3.5	0.05 ± 0.01 %
3.5 - 4	0.04 ± 0.01 %
4 - 4.5	0.02 ± 0.01 %
4.5 - 5	0.04 ± 0.01 %

Table A.11: Relative number of fake muons in the decay $B_s \to D_s X\mu\nu$ for the 7 TeV selection.

$\eta(H_b)$	Relative number of fake muons
2 - 2.5	0.09 ± 0.02 %
2.5 - 3	0.001 ± 0.02 %
3 - 3.5	0.001 ± 0.02 %
3.5 - 4	0.04 ± 0.01 %
4 - 4.5	0.02 ± 0.02 %
4.5 - 5	0.02 ± 0.01 %

Table A.12: Relative number of fake muons in the decay $\Lambda_b \to \Lambda_c X\mu\nu$ for the 7 TeV selection.

$\eta(H_b)$	Relative number of fake muons
2 - 2.5	0.10 ± 0.02 %
2.5 - 3	0.10 ± 0.02 %
3 - 3.5	0.05 ± 0.01 %
3.5 - 4	0.03 ± 0.01 %
4 - 4.5	0.01 ± 0.01 %
4.5 - 5	0.01 ± 0.01 %

Table A.13: Relative number of fake muons in the decay $B \to D^{0}X\mu\nu$ for the 13 TeV selection.

$\eta(H_b)$	Relative number of fake muons
2 - 2.5	0.05 ± 0.02 %
2.5 - 3	0.04 ± 0.01 %
3 - 3.5	0.03 ± 0.01 %
3.5 - 4	0.04 ± 0.01 %
4 - 4.5	0.03 ± 0.01 %
4.5 - 5	0.02 ± 0.01 %

Table A.14: Relative number of fake muons in the decay $B \to D^+ X \mu\nu$ for the 13 TeV selection.

$\eta(H_b)$	Relative number of fake muons
2 - 2.5	0.06 ± 0.04 %
2.5 - 3	0.07 ± 0.02 %
3 - 3.5	0.05 ± 0.02 %
3.5 - 4	0.05 ± 0.02 %
4 - 4.5	0.001 ± 0.04 %
4.5 - 5	0.002 ± 0.09 %

Table A.15: Relative number of fake muons in the decay $B_s \to D_s X \mu\nu$ for the 13 TeV selection.

$\eta(H_b)$	Relative number of fake muons
2 - 2.5	0.003 ± 0.001 %
2.5 - 3	0.002 ± 0.05 %
3 - 3.5	0.09 ± 0.04 %
3.5 - 4	0.001 ± 0.04 %
4 - 4.5	0.001 ± 0.08 %
4.5 - 5	0.004 ± 0.30 %

Table A.16: Relative number of fake muons in the decay $\Lambda_b \to \Lambda_c X \mu\nu$ for the 13 TeV selection.

$\eta(H_b)$	Relative number of fake muons
2 - 2.5	0.08 ± 0.1 %
2.5 - 3	0.06 ± 0.03 %
3 - 3.5	0.001 ± 0.04 %
3.5 - 4	0.001 ± 0.05 %
4 - 4.5	0.002 ± 0.001 %
4.5 - 5	0.00 ± 0.001 %

Table A.17: Potential backgrounds from B^0 decays to two charm mesons with branching fractions taken from the PDG [19]. Modes without entries indicate channels whose branching fractions have not been measured.

decay mode	branching fraction	
$D^-\ D_s^+$	(7.2 ± 0.8) x 10^{-3}	[19]
$D^-\ D_s^{*+}$	(7.4 ± 1.6) x 10^{-3}	
$D^*(2010)^- D_s^+$	(8.0 ± 1.1) x 10^{-3}	
$D^*(2010)^- D_s^{*+}$	(1.77 ± 0.14) %	
$(\overline{D}\ +\overline{D}^*)(D\ +D^*)$ K	(3.68 ± 0.26) %	
$D^-\ D^+$	(2.11 ± 0.18) x 10^{-4}	
$D^\pm D^{*\mp}$	(6.1 ± 0.6) x 10^{-4}	
$D_{s,0/1}^{(*)+}\ \overline{D}^{(*)-}$	(1.8 ± 0.3) %	
$D_{1/2}^{*-}\ D_s^+$	–	
$D_{1/2}^{*-}\ D_s^{*+}$	–	
$D_s^{(*)+}\ D^{0/-}\ \pi^{0/-}\ (\pi^{0/-})$	–	
$D^{*+}\ D^{*-}$	–	

Table A.18: Potential backgrounds from B^+ decays to two charm mesons with branching fractions taken from the PDG [19]. Modes without entries indicate channels whose branching fractions have not been measured.

decay mode	branching fraction	
$\overline{D}^0\ D_s^+$	(9.0 ± 0.9) x 10^{-3}	[19]
$\overline{D}^0\ D_s^{*+}$	(7.6 ± 1.6) x 10^{-3}	
$\overline{D}^*(2007)^0 D_s^+$	(8.2 ± 1.7) x 10^{-3}	
$\overline{D}^*(2007)^0 D_s^{*+}$	(1.71 ± 0.24) %	
$D_s^{(*)+}\ \overline{D}^{**0}$	(2.7 ± 1.2) %	
$(\overline{D}\ +\overline{D}^*)\ (D\ +D^*)$ K	(4.05 ± 0.30) %	
$\overline{D}^0\ D^+$	(3.8 ± 0.4) x 10^{-4}	
$\overline{D}^0\ D^*(2010)^+$	(3.9 ± 0.5) x 10^{-4}	
$D^+\ \overline{D}^*(2007)^0$	(6.3 ± 1.7) x 10^{-4}	
$\overline{D}^*(2007)^0 D^*(2010)^+$	(8.1 ± 1.7) x 10^{-4}	
$D_{s,0/J}^{(*)+}\ \overline{D}^{(*)0}$	(2.4 ± 0.4) %	
$D_s^{(*)+}\ D^{0/-}\ \pi^{0/-}\ (\pi^{0/-})$	–	

Table A.19: Potential backgrounds from B_s^0 decays to two charm mesons with branching fractions taken from a recent LHCb measurement [65]. Modes without entries indicate channels whose branching fractions have not been measured.

decay mode	branching fraction
$D_s^{(*)+}\ D_s^{(*)-}$	(3.05 ± 0.41) % [65]
$D_{1/2}^{(*)-}\ D_s^{(*)+}$	–
$(D_s^{(*)-} + D_s^{(*)+})\ (D^{(*)0} + D^{(*)\pm})$ K	–
$D_s^{(*)-}\ D^{(*)+}$	–
$D^{(*)0}\ \overline{D}^{(*)0}\ f^0$	–
$D^{(*)0}\ \overline{D}^{(*)0}\ \phi$	–
$(D_s^{(*)+} + D^{(*)+})\ (D^- + D^+)$ K π	–

Table A.20: Potential backgrounds from Λ_b^0 decays to two charm mesons with branching fractions taken from the PDG [19]. Modes without entries indicate channels whose branching fractions have not been measured.

decay mode	branching fraction
$\Lambda_c^+\ D_s^-$	(1.1 ± 0.1) % [19]
$\Lambda_c^+\ D_s^{*-}$	–
$\Lambda_c^{*+} D_s^{(*)-}$	–
$(\Lambda_c^+ + \Lambda_c^{(*)+})(D^{(*)0} + D^{(*)-})$ K	–
$D_s^{(*)-} D^{(*)+}$	–
$\Lambda_c^+\ D_{(s)}^{-/0}\ \pi$	–
$\Lambda_c^+\ D_{(s)}^{(*)-}$	–
$\Lambda_c^+\ D_s^{*-}$	–
$\Lambda_c^{*+} D_s^{(*)-}$	–
$(\Lambda_c^+ + \Lambda_c^{(*)+})(D^{(*)0} + D^{(*)-})$ K	–
$D_s^{(*)-} D^{(*)+}$	–
$\Lambda_c^+\ D_{(s)}^{-/0}\ \pi$	–
$\Lambda_c^+\ D_{(s)}^{(*)-}$	–

A.2 Overall efficiency tables

Table A.21: Overall reconstruction and selection efficiencies as a function of p_{T} ($D^0 + \mu$) and $\eta(H_b)$ including particle identification and trigger efficiencies for the D^0 mode determined from 7 TeV simulated decays weighted with efficiencies obtained from data-driven methods.

	efficiency [%]					
p_{T} [GeV/c]	$2 < \eta < 2.5$	$2.5 < \eta < 3$	$3 < \eta < 3.5$	$3.5 < \eta < 4$	$4 < \eta < 4.5$	$4.5 < \eta < 5$
$0 < 2$	0.00 ± 0.00	0.00 ± 0.00	0.08 ± 0.01	0.30 ± 0.02	0.55 ± 0.02	0.65 ± 0.03
$2 < 4$	0.01 ± 0.00	0.21 ± 0.01	0.88 ± 0.03	1.45 ± 0.04	1.25 ± 0.04	0.74 ± 0.04
$4 < 5$	0.07 ± 0.01	0.96 ± 0.04	2.39 ± 0.08	2.47 ± 0.09	1.67 ± 0.09	0.44 ± 0.06
$5 < 6$	0.21 ± 0.02	1.70 ± 0.07	3.26 ± 0.11	2.97 ± 0.12	1.65 ± 0.11	0.49 ± 0.09
$6 < 7$	0.44 ± 0.04	2.34 ± 0.10	3.86 ± 0.15	3.33 ± 0.16	1.78 ± 0.15	0.31 ± 0.09
$7 < 8$	0.75 ± 0.07	3.28 ± 0.15	4.28 ± 0.19	3.69 ± 0.22	1.55 ± 0.19	0.37 ± 0.14
$8 < 9$	1.03 ± 0.09	3.77 ± 0.19	4.67 ± 0.25	3.55 ± 0.27	1.68 ± 0.26	0.52 ± 0.22
$9 < 10$	1.34 ± 0.13	4.19 ± 0.25	4.68 ± 0.31	3.52 ± 0.35	1.76 ± 0.36	0.36 ± 0.26
$10 < 11$	1.56 ± 0.17	4.87 ± 0.33	4.52 ± 0.38	3.22 ± 0.42	1.59 ± 0.44	0.05 ± 0.13
$11 < 12$	1.92 ± 0.22	4.51 ± 0.39	4.79 ± 0.48	2.50 ± 0.46	1.58 ± 0.55	0.20 ± 0.37
$12 < 13$	2.19 ± 0.29	4.65 ± 0.46	4.55 ± 0.57	3.24 ± 0.64	1.22 ± 0.61	0.00 ± 0.00
$13 < 14$	2.67 ± 0.38	4.65 ± 0.56	4.15 ± 0.64	2.39 ± 0.68	1.46 ± 0.77	0.06 ± 0.28
$14 < 25$	2.27 ± 0.20	3.77 ± 0.31	3.11 ± 0.36	2.35 ± 0.44	0.59 ± 0.38	0.00 ± 0.00

Table A.22: Overall reconstruction and selection efficiencies as a function of p_{T} ($D^+ + \mu$) and $\eta(H_b)$ including particle identification and trigger efficiencies for the D^+ mode determined from 7 TeV simulated decays weighted with efficiencies obtained from data-driven methods.

	efficiency [%]					
p_{T} [GeV/c]	$2 < \eta < 2.5$	$2.5 < \eta < 3$	$3 < \eta < 3.5$	$3.5 < \eta < 4$	$4 < \eta < 4.5$	$4.5 < \eta < 5$
$0 < 2$	0.00 ± 0.00	0.00 ± 0.00	0.01 ± 0.00	0.04 ± 0.01	0.08 ± 0.01	0.10 ± 0.01
$2 < 4$	0.00 ± 0.00	0.04 ± 0.01	0.22 ± 0.01	0.36 ± 0.02	0.29 ± 0.02	0.15 ± 0.02
$4 < 5$	0.01 ± 0.01	0.29 ± 0.03	0.88 ± 0.05	1.11 ± 0.07	0.62 ± 0.06	0.18 ± 0.04
$5 < 6$	0.06 ± 0.01	0.73 ± 0.05	1.58 ± 0.08	1.46 ± 0.09	0.85 ± 0.09	0.15 ± 0.05
$6 < 7$	0.13 ± 0.02	1.23 ± 0.08	2.15 ± 0.12	2.03 ± 0.14	0.84 ± 0.12	0.25 ± 0.09
$7 < 8$	0.28 ± 0.04	1.58 ± 0.11	2.58 ± 0.17	2.42 ± 0.19	1.07 ± 0.17	0.16 ± 0.10
$8 < 9$	0.52 ± 0.07	2.05 ± 0.16	3.14 ± 0.23	2.63 ± 0.27	1.47 ± 0.27	0.08 ± 0.10
$9 < 10$	0.61 ± 0.10	2.49 ± 0.22	3.13 ± 0.29	2.13 ± 0.30	1.36 ± 0.33	0.04 ± 0.09
$10 < 11$	0.72 ± 0.13	2.75 ± 0.28	3.70 ± 0.39	2.43 ± 0.41	0.96 ± 0.35	0.62 ± 0.51
$11 < 12$	0.86 ± 0.17	2.83 ± 0.34	3.27 ± 0.44	2.15 ± 0.46	1.30 ± 0.55	0.04 ± 0.18
$12 < 13$	0.97 ± 0.21	3.46 ± 0.45	3.51 ± 0.56	2.66 ± 0.65	0.77 ± 0.54	0.00 ± 0.00
$13 < 14$	1.45 ± 0.31	3.25 ± 0.53	3.83 ± 0.70	2.82 ± 0.88	1.20 ± 0.90	0.00 ± 0.00
$14 < 25$	1.08 ± 0.16	2.43 ± 0.28	2.90 ± 0.39	1.63 ± 0.43	0.89 ± 0.52	0.00 ± 0.00

Table A.23: Overall reconstruction and selection efficiencies as a function of p_{T} ($D_s^+ + \mu$) and $\eta(H_b)$ including particle identification and trigger efficiencies for the D_s^+ mode determined from 7 TeV simulated decays weighted with efficiencies obtained from data-driven methods.

	efficiency [%]					
p_{T} [GeV/c]	$2 < \eta < 2.5$	$2.5 < \eta < 3$	$3 < \eta < 3.5$	$3.5 < \eta < 4$	$4 < \eta < 4.5$	$4.5 < \eta < 5$
$0 < 2$	0.00 ± 0.00	0.00 ± 0.00	0.01 ± 0.00	0.06 ± 0.01	0.09 ± 0.01	0.10 ± 0.01
$2 < 4$	0.00 ± 0.00	0.04 ± 0.01	0.24 ± 0.01	0.36 ± 0.02	0.29 ± 0.02	0.14 ± 0.02
$4 < 5$	0.02 ± 0.01	0.37 ± 0.03	1.07 ± 0.05	0.99 ± 0.06	0.53 ± 0.05	0.13 ± 0.03
$5 < 6$	0.06 ± 0.01	0.73 ± 0.05	1.65 ± 0.08	1.51 ± 0.09	0.74 ± 0.08	0.19 ± 0.06
$6 < 7$	0.15 ± 0.02	1.23 ± 0.08	2.15 ± 0.11	1.85 ± 0.13	0.97 ± 0.12	0.21 ± 0.08
$7 < 8$	0.31 ± 0.04	1.83 ± 0.11	2.74 ± 0.16	2.08 ± 0.17	0.71 ± 0.13	0.13 ± 0.08
$8 < 9$	0.58 ± 0.07	2.31 ± 0.16	2.99 ± 0.21	2.09 ± 0.21	0.96 ± 0.19	0.07 ± 0.08
$9 < 10$	0.79 ± 0.10	2.54 ± 0.20	3.22 ± 0.26	2.20 ± 0.27	0.91 ± 0.25	0.00 ± 0.02
$10 < 11$	0.80 ± 0.12	2.95 ± 0.26	3.69 ± 0.34	3.17 ± 0.41	0.63 ± 0.26	0.02 ± 0.08
$11 < 12$	1.13 ± 0.18	3.12 ± 0.32	4.41 ± 0.46	2.36 ± 0.45	0.27 ± 0.22	0.00 ± 0.04
$12 < 13$	1.03 ± 0.20	2.86 ± 0.37	4.21 ± 0.54	1.31 ± 0.41	1.10 ± 0.54	0.00 ± 0.05
$13 < 14$	1.09 ± 0.24	3.47 ± 0.50	3.44 ± 0.59	1.34 ± 0.48	0.73 ± 0.55	0.00 ± 0.00
$14 < 25$	1.61 ± 0.17	2.93 ± 0.28	2.88 ± 0.35	1.04 ± 0.30	0.73 ± 0.44	0.00 ± 0.00

Table A.24: Overall reconstruction and selection efficiencies as a function of p_{T} ($\Lambda_c^+ + \mu$) and $\eta(H_b)$ including particle identification and trigger efficiencies for the Λ_c^+ mode determined from 7 TeV simulated decays weighted with efficiencies obtained from data-driven methods.

	efficiency [%]					
p_{T} [GeV/c]	$2 < \eta < 2.5$	$2.5 < \eta < 3$	$3 < \eta < 3.5$	$3.5 < \eta < 4$	$4 < \eta < 4.5$	$4.5 < \eta < 5$
$0 < 2$	0.00 ± 0.00	0.00 ± 0.00	0.00 ± 0.00	0.03 ± 0.00	0.06 ± 0.01	0.07 ± 0.01
$2 < 4$	0.00 ± 0.00	0.02 ± 0.00	0.11 ± 0.01	0.19 ± 0.01	0.18 ± 0.01	0.08 ± 0.01
$4 < 5$	0.01 ± 0.00	0.14 ± 0.01	0.54 ± 0.03	0.59 ± 0.03	0.40 ± 0.03	0.11 ± 0.02
$5 < 6$	0.02 ± 0.00	0.36 ± 0.03	0.96 ± 0.04	1.11 ± 0.06	0.57 ± 0.05	0.08 ± 0.02
$6 < 7$	0.06 ± 0.01	0.71 ± 0.04	1.44 ± 0.07	1.42 ± 0.08	0.60 ± 0.06	0.09 ± 0.03
$7 < 8$	0.14 ± 0.02	1.01 ± 0.06	1.79 ± 0.09	1.63 ± 0.10	0.73 ± 0.09	0.09 ± 0.04
$8 < 9$	0.24 ± 0.03	1.52 ± 0.09	2.24 ± 0.12	1.96 ± 0.14	0.72 ± 0.11	0.12 ± 0.07
$9 < 10$	0.44 ± 0.05	1.76 ± 0.12	2.46 ± 0.16	2.23 ± 0.19	0.80 ± 0.16	0.04 ± 0.06
$10 < 11$	0.51 ± 0.07	2.22 ± 0.16	2.53 ± 0.20	2.21 ± 0.23	0.61 ± 0.17	0.16 ± 0.15
$11 < 12$	0.73 ± 0.10	2.43 ± 0.20	3.16 ± 0.27	2.02 ± 0.28	0.82 ± 0.25	0.01 ± 0.05
$12 < 13$	0.92 ± 0.13	2.61 ± 0.25	3.50 ± 0.34	1.95 ± 0.33	0.80 ± 0.31	0.00 ± 0.03
$13 < 14$	0.68 ± 0.13	2.22 ± 0.27	3.17 ± 0.39	1.69 ± 0.37	0.77 ± 0.40	0.00 ± 0.00
$14 < 25$	1.03 ± 0.09	2.67 ± 0.18	2.37 ± 0.21	1.25 ± 0.22	0.55 ± 0.23	0.00 ± 0.02

Table A.25: Overall reconstruction and selection efficiencies as a function of p_{T} (D^0 $+\mu$) and $\eta(H_b)$ including particle identification and trigger efficiencies for the D^0 mode determined from 13 TeV simulated decays weighted with efficiencies obtained from data-driven methods.

	efficiency [%]					
p_{T} [GeV/c]	$2 < \eta < 2.5$	$2.5 < \eta < 3$	$3 < \eta < 3.5$	$3.5 < \eta < 4$	$4 < \eta < 4.5$	$4.5 < \eta < 5$
$0 < 2$	0.00 ± 0.00	0.02 ± 0.01	0.41 ± 0.03	1.29 ± 0.05	2.01 ± 0.07	2.01 ± 0.08
$2 < 4$	0.04 ± 0.01	1.00 ± 0.04	3.40 ± 0.07	4.74 ± 0.09	3.99 ± 0.10	2.25 ± 0.08
$4 < 5$	0.28 ± 0.03	3.94 ± 0.13	7.83 ± 0.19	7.53 ± 0.21	5.00 ± 0.20	1.43 ± 0.13
$5 < 6$	0.96 ± 0.07	6.56 ± 0.19	10.59 ± 0.26	9.68 ± 0.28	5.36 ± 0.25	1.31 ± 0.16
$6 < 7$	1.87 ± 0.12	9.16 ± 0.26	12.79 ± 0.34	10.90 ± 0.36	5.28 ± 0.31	1.09 ± 0.19
$7 < 8$	3.25 ± 0.18	11.74 ± 0.35	14.28 ± 0.43	11.31 ± 0.45	5.10 ± 0.38	1.16 ± 0.25
$8 < 9$	4.13 ± 0.25	14.27 ± 0.46	15.81 ± 0.54	12.10 ± 0.56	5.67 ± 0.50	0.85 ± 0.26
$9 < 10$	6.06 ± 0.35	14.61 ± 0.55	16.80 ± 0.67	12.37 ± 0.70	4.86 ± 0.58	0.91 ± 0.35
$10 < 11$	7.48 ± 0.45	15.84 ± 0.70	17.67 ± 0.83	11.55 ± 0.80	4.99 ± 0.73	0.85 ± 0.44
$11 < 12$	7.71 ± 0.54	16.43 ± 0.85	18.20 ± 1.00	10.74 ± 0.94	4.04 ± 0.78	0.50 ± 0.43
$12 < 13$	8.69 ± 0.67	17.47 ± 0.99	15.61 ± 1.11	10.09 ± 1.17	5.36 ± 1.10	0.90 ± 0.72
$13 < 14$	9.70 ± 0.82	17.35 ± 1.19	15.89 ± 1.36	10.64 ± 1.40	4.84 ± 1.30	0.66 ± 0.85
$14 < 25$	11.06 ± 0.50	17.24 ± 0.69	15.18 ± 0.79	9.39 ± 0.80	3.05 ± 0.68	0.55 ± 0.51

Table A.26: Overall reconstruction and selection efficiencies as a function of p_{T} (D^+ $+\mu$) and $\eta(H_b)$ including particle identification and trigger efficiencies for the D^+ mode determined from 13 TeV simulated decays weighted with efficiencies obtained from data-driven methods.

	efficiency [%]					
p_{T} [GeV/c]	$2 < \eta < 2.5$	$2.5 < \eta < 3$	$3 < \eta < 3.5$	$3.5 < \eta < 4$	$4 < \eta < 4.5$	$4.5 < \eta < 5$
$0 < 2$	0.00 ± 0.00	0.00 ± 0.00	0.05 ± 0.01	0.24 ± 0.02	0.38 ± 0.03	0.41 ± 0.04
$2 < 4$	0.00 ± 0.00	0.21 ± 0.02	0.92 ± 0.04	1.39 ± 0.05	1.11 ± 0.05	0.49 ± 0.04
$4 < 5$	0.05 ± 0.01	1.23 ± 0.07	3.44 ± 0.13	3.65 ± 0.15	2.30 ± 0.14	0.50 ± 0.08
$5 < 6$	0.25 ± 0.04	2.62 ± 0.13	5.18 ± 0.19	5.33 ± 0.21	2.72 ± 0.18	0.64 ± 0.12
$6 < 7$	0.56 ± 0.07	4.74 ± 0.20	7.27 ± 0.27	6.66 ± 0.30	3.26 ± 0.26	0.59 ± 0.15
$7 < 8$	1.18 ± 0.12	6.44 ± 0.28	8.99 ± 0.36	7.87 ± 0.40	3.43 ± 0.33	0.39 ± 0.15
$8 < 9$	1.91 ± 0.17	8.30 ± 0.38	10.40 ± 0.47	8.47 ± 0.51	4.00 ± 0.45	0.92 ± 0.32
$9 < 10$	2.33 ± 0.23	9.31 ± 0.48	10.66 ± 0.58	9.79 ± 0.66	4.04 ± 0.58	0.68 ± 0.33
$10 < 11$	3.21 ± 0.32	11.11 ± 0.63	12.25 ± 0.74	9.81 ± 0.82	3.40 ± 0.64	0.26 ± 0.29
$11 < 12$	4.13 ± 0.42	11.23 ± 0.74	14.24 ± 0.97	8.61 ± 0.95	4.16 ± 0.89	0.17 ± 0.29
$12 < 13$	4.97 ± 0.55	10.77 ± 0.88	11.30 ± 1.03	9.38 ± 1.12	3.98 ± 1.04	0.52 ± 0.65
$13 < 14$	5.34 ± 0.66	14.74 ± 1.19	13.36 ± 1.34	8.94 ± 1.39	2.05 ± 0.97	0.69 ± 1.01
$14 < 25$	6.70 ± 0.43	12.60 ± 0.63	13.77 ± 0.79	9.28 ± 0.86	2.61 ± 0.71	0.18 ± 0.34

Table A.27: Overall reconstruction and selection efficiencies as a function of p_{T} ($D_s^+ +\mu$) and $\eta(H_b)$ including particle identification and trigger efficiencies for the D_s^+ mode determined from 13 TeV simulated decays weighted with efficiencies obtained from data-driven methods.

	efficiency [%]					
p_{T} [GeV/c]	$2 < \eta < 2.5$	$2.5 < \eta < 3$	$3 < \eta < 3.5$	$3.5 < \eta < 4$	$4 < \eta < 4.5$	$4.5 < \eta < 5$
$0 < 2$	0.00 ± 0.00	0.00 ± 0.00	0.04 ± 0.01	0.18 ± 0.02	0.40 ± 0.03	0.33 ± 0.03
$2 < 4$	0.00 ± 0.00	0.13 ± 0.01	0.66 ± 0.03	0.99 ± 0.05	0.84 ± 0.05	0.40 ± 0.04
$4 < 5$	0.05 ± 0.01	1.01 ± 0.07	2.65 ± 0.12	3.15 ± 0.14	1.71 ± 0.12	0.34 ± 0.07
$5 < 6$	0.12 ± 0.03	2.36 ± 0.12	4.69 ± 0.18	4.54 ± 0.20	2.03 ± 0.16	0.36 ± 0.09
$6 < 7$	0.52 ± 0.06	4.13 ± 0.19	6.55 ± 0.26	5.58 ± 0.27	2.35 ± 0.21	0.28 ± 0.10
$7 < 8$	1.23 ± 0.12	5.56 ± 0.25	8.60 ± 0.35	7.43 ± 0.37	2.95 ± 0.29	0.51 ± 0.16
$8 < 9$	1.42 ± 0.15	7.24 ± 0.34	9.36 ± 0.44	7.86 ± 0.47	2.31 ± 0.32	0.42 ± 0.19
$9 < 10$	3.01 ± 0.25	9.23 ± 0.46	11.40 ± 0.56	7.25 ± 0.55	3.07 ± 0.46	0.10 ± 0.12
$10 < 11$	2.85 ± 0.29	11.08 ± 0.60	11.94 ± 0.69	8.27 ± 0.70	3.63 ± 0.64	0.18 ± 0.20
$11 < 12$	3.50 ± 0.37	11.94 ± 0.73	14.02 ± 0.90	7.48 ± 0.81	2.59 ± 0.63	0.63 ± 0.46
$12 < 13$	4.90 ± 0.53	10.14 ± 0.78	13.16 ± 1.00	8.50 ± 1.03	2.93 ± 0.81	0.01 ± 0.05
$13 < 14$	6.44 ± 0.69	14.13 ± 1.08	12.58 ± 1.25	8.06 ± 1.23	2.55 ± 0.91	0.03 ± 0.15
$14 < 25$	6.91 ± 0.40	12.39 ± 0.58	11.67 ± 0.68	6.78 ± 0.72	1.79 ± 0.54	0.05 ± 0.14

Table A.28: Overall reconstruction and selection efficiencies as a function of p_{T} ($\Lambda_c^+ +\mu$) and $\eta(H_b)$ including particle identification and trigger efficiencies for the Λ_c^+ mode determined from 13 TeV simulated decays weighted with efficiencies obtained from data-driven methods.

	efficiency [%]					
p_{T} [GeV/c]	$2 < \eta < 2.5$	$2.5 < \eta < 3$	$3 < \eta < 3.5$	$3.5 < \eta < 4$	$4 < \eta < 4.5$	$4.5 < \eta < 5$
$0 < 2$	0.00 ± 0.00	0.00 ± 0.00	0.01 ± 0.01	0.09 ± 0.02	0.15 ± 0.02	0.17 ± 0.03
$2 < 4$	0.00 ± 0.00	0.03 ± 0.01	0.30 ± 0.02	0.58 ± 0.03	0.47 ± 0.03	0.20 ± 0.03
$4 < 5$	0.00 ± 0.00	0.31 ± 0.04	1.46 ± 0.09	1.98 ± 0.11	0.94 ± 0.09	0.23 ± 0.05
$5 < 6$	0.06 ± 0.02	0.97 ± 0.07	3.31 ± 0.15	2.67 ± 0.15	1.28 ± 0.12	0.27 ± 0.07
$6 < 7$	0.18 ± 0.04	2.03 ± 0.12	4.88 ± 0.21	4.07 ± 0.22	1.69 ± 0.17	0.18 ± 0.07
$7 < 8$	0.44 ± 0.06	4.16 ± 0.21	6.50 ± 0.28	4.95 ± 0.29	1.65 ± 0.20	0.31 ± 0.12
$8 < 9$	0.85 ± 0.11	5.54 ± 0.28	7.99 ± 0.38	6.13 ± 0.38	2.04 ± 0.27	0.11 ± 0.09
$9 < 10$	1.28 ± 0.15	6.84 ± 0.37	9.60 ± 0.49	6.35 ± 0.47	2.31 ± 0.35	0.14 ± 0.13
$10 < 11$	2.28 ± 0.24	8.02 ± 0.47	9.48 ± 0.58	7.33 ± 0.63	2.07 ± 0.41	0.39 ± 0.27
$11 < 12$	2.62 ± 0.30	8.94 ± 0.60	10.78 ± 0.72	6.54 ± 0.70	1.21 ± 0.40	0.17 ± 0.23
$12 < 13$	4.22 ± 0.44	10.08 ± 0.72	9.81 ± 0.81	6.22 ± 0.85	1.41 ± 0.49	0.04 ± 0.14
$13 < 14$	4.92 ± 0.54	10.62 ± 0.87	11.59 ± 1.06	6.44 ± 0.95	1.92 ± 0.74	0.00 ± 0.00
$14 < 25$	5.19 ± 0.32	11.77 ± 0.52	10.74 ± 0.60	5.57 ± 0.54	1.42 ± 0.39	0.03 ± 0.09

B Part II: Measurement of CP violation in $B_s^0 \to \phi\phi$ decays

B.1 Distributions of the BDT training variables

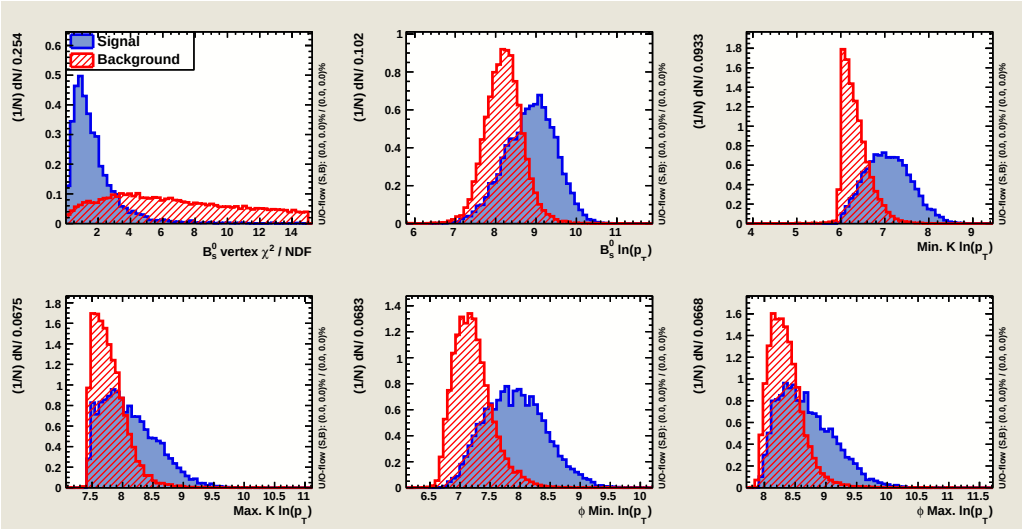

Figure B.1: Normalised distributions of B_s^0 vertex χ^2/n_{dof}, logarithmic B_s^0 transverse momentum, minimum and maximum logarithmic kaon transverse momenta and minimum and maximum logarithmic ϕ-meson transverse momenta used as inputs for the 7 TeV BDT. Fully simulated $B_s^0 \to \phi\phi$ decays are used as training sample (solid blue area) and data outside a mass window of $\pm 120\,\mathrm{MeV}/c^2$ around the known B_s^0 mass is used as background sample (shaded red area).

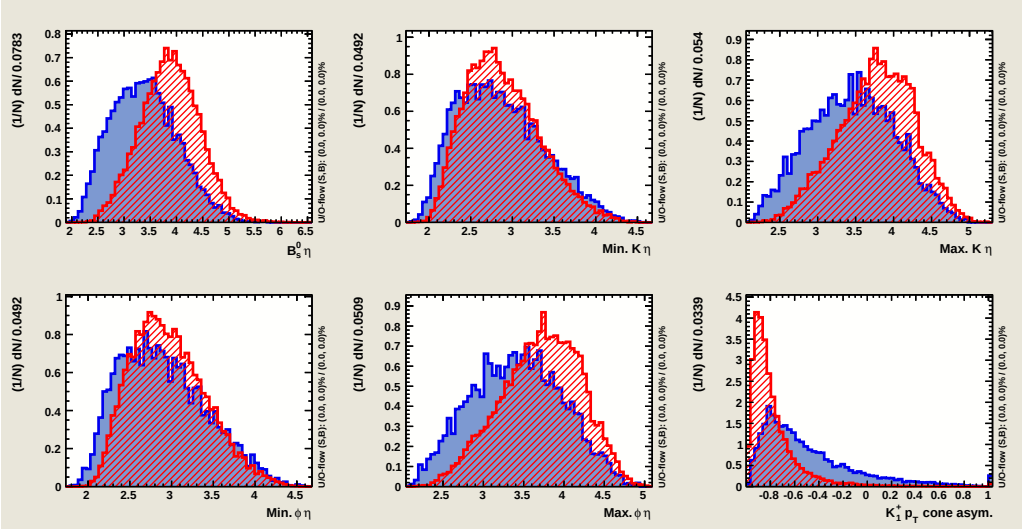

Figure B.2: Normalised distributions of the pseudorapidity of the B_s^0, the minimum and maximum pseudorapidities of the kaon tracks and the ϕ mesons and the p_T cone asymmetry of one of the K^+ tracks used as inputs for the BDT 7 TeV. Fully simulated $B_s^0 \to \phi\phi$ decays are used as training sample (solid blue area) and data outside a mass window of $\pm 120\,\text{MeV}/c^2$ around the known B_s^0 mass is used as background sample (shaded red area).

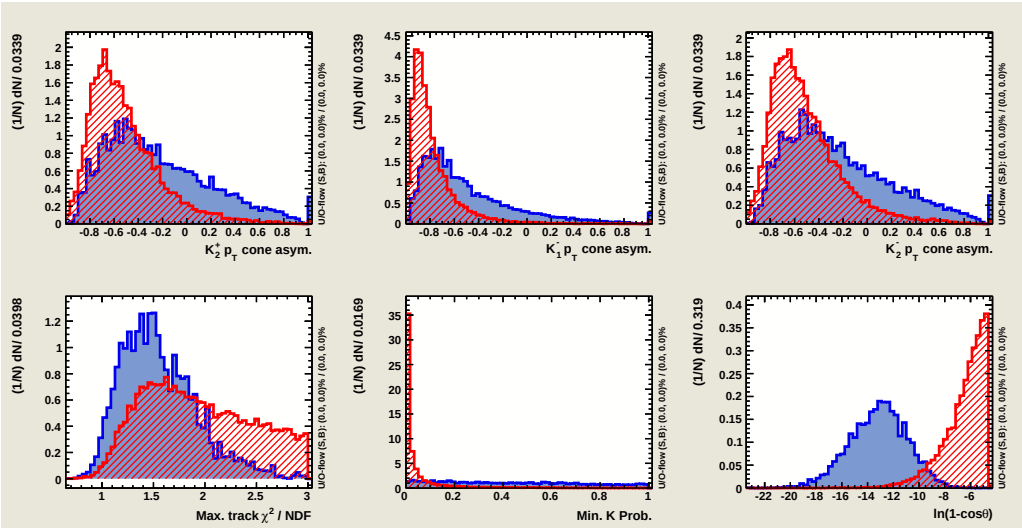

Figure B.3: Normalised distributions of the p_T cone asymmetries of the second K^+ track and of the two K^- tracks, the maximum track χ^2/n_{dof} value of the tracks, the minimum ProbbNN$_K$ value of the tracks and the logarithm of $(1 - \cos\theta)$ of the pointing angle θ used as inputs for the BDT 7 TeV. Fully simulated $B_s^0 \to \phi\phi$ decays are used as training sample (solid blue area) and data outside a mass window of $\pm 120\,\text{MeV}/c^2$ around the known B_s^0 mass is used as background sample (shaded red area).

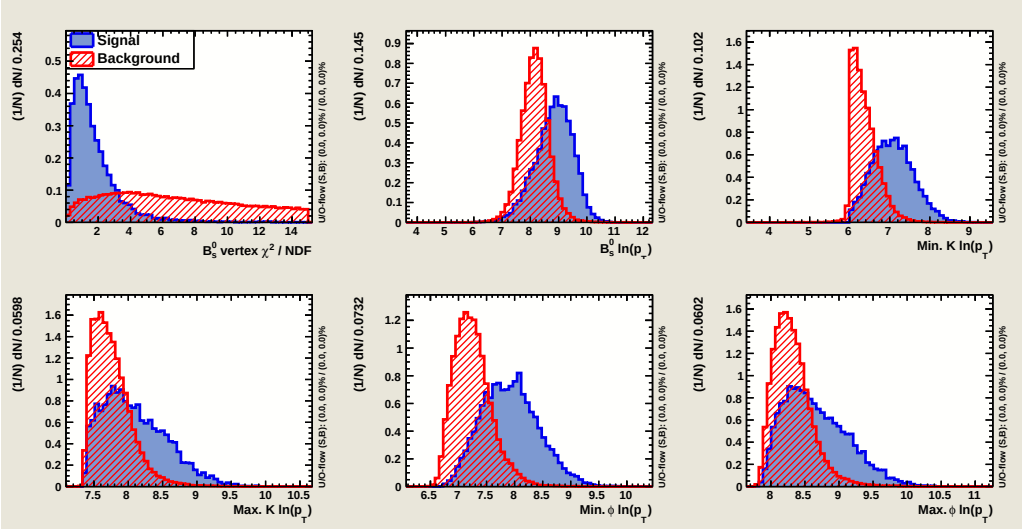

Figure B.4: Normalised distributions of B_s^0 vertex χ^2/n_{dof}, logarithmic B_s^0 transverse momentum, minimum and maximum logarithmic kaon transverse momenta and minimum and maximum logarithmic ϕ-meson transverse momenta used as inputs for the 8 TeV BDT. Fully simulated $B_s^0 \to \phi\phi$ decays are used as training sample (solid blue area) and data outside a mass window of $\pm 120\,\mathrm{MeV}/c^2$ around the known B_s^0 mass is used as background sample (shaded red area).

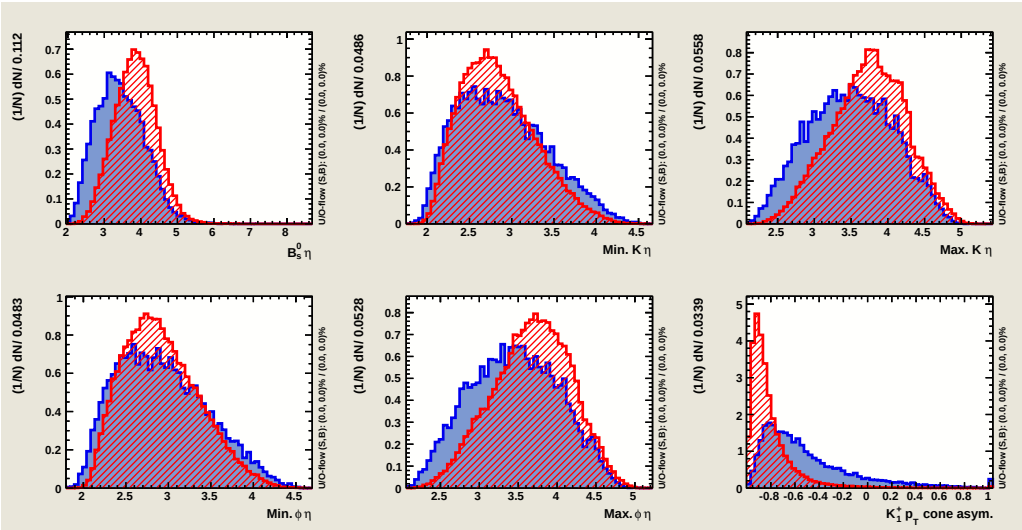

Figure B.5: Normalised distributions of the pseudorapidity of the B_s^0, the minimum and maximum pseudorapidities of the kaon tracks and the ϕ mesons and the p_{T} cone asymmetry of one of the K^+ tracks used as inputs for the BDT 8 TeV. Fully simulated $B_s^0 \to \phi\phi$ decays are used as training sample (solid blue area) and data outside a mass window of $\pm 120\,\mathrm{MeV}/c^2$ around the known B_s^0 mass is used as background sample (shaded red area).

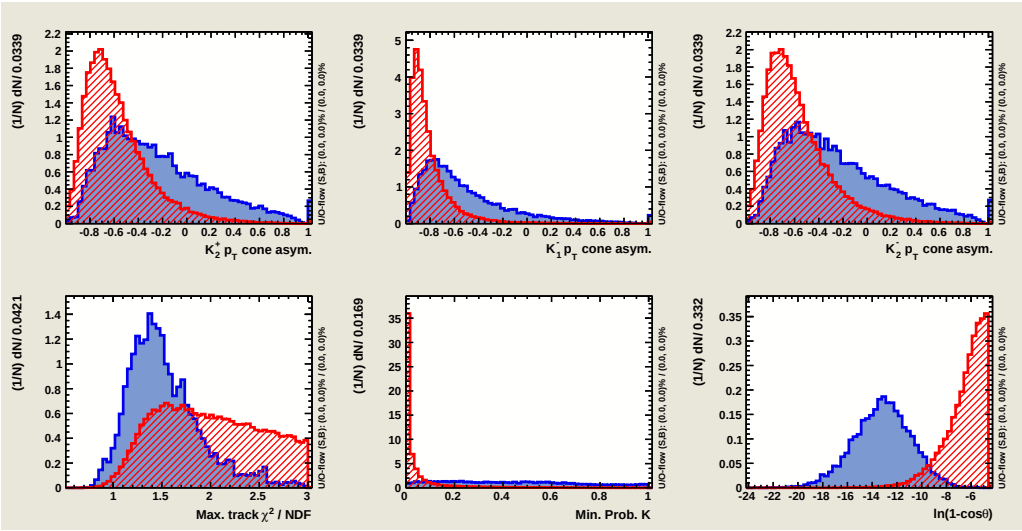

Figure B.6: Normalised distributions of the p_{T} cone asymmetries of the second K^+ track and the two K^- tracks, the maximum track χ^2/n_{dof} value of the tracks, the minimum ProbbNN$_K$ value of the tracks and the logarithm of $(1-\cos\theta)$ of the pointing angle θ used as inputs for the BDT 8 TeV. Fully simulated $B_s^0 \to \phi\phi$ decays are used as training sample (solid blue area) and data outside a mass window of $\pm 120\,\mathrm{MeV}/c^2$ around the known B_s^0 mass is used as background sample (shaded red area).

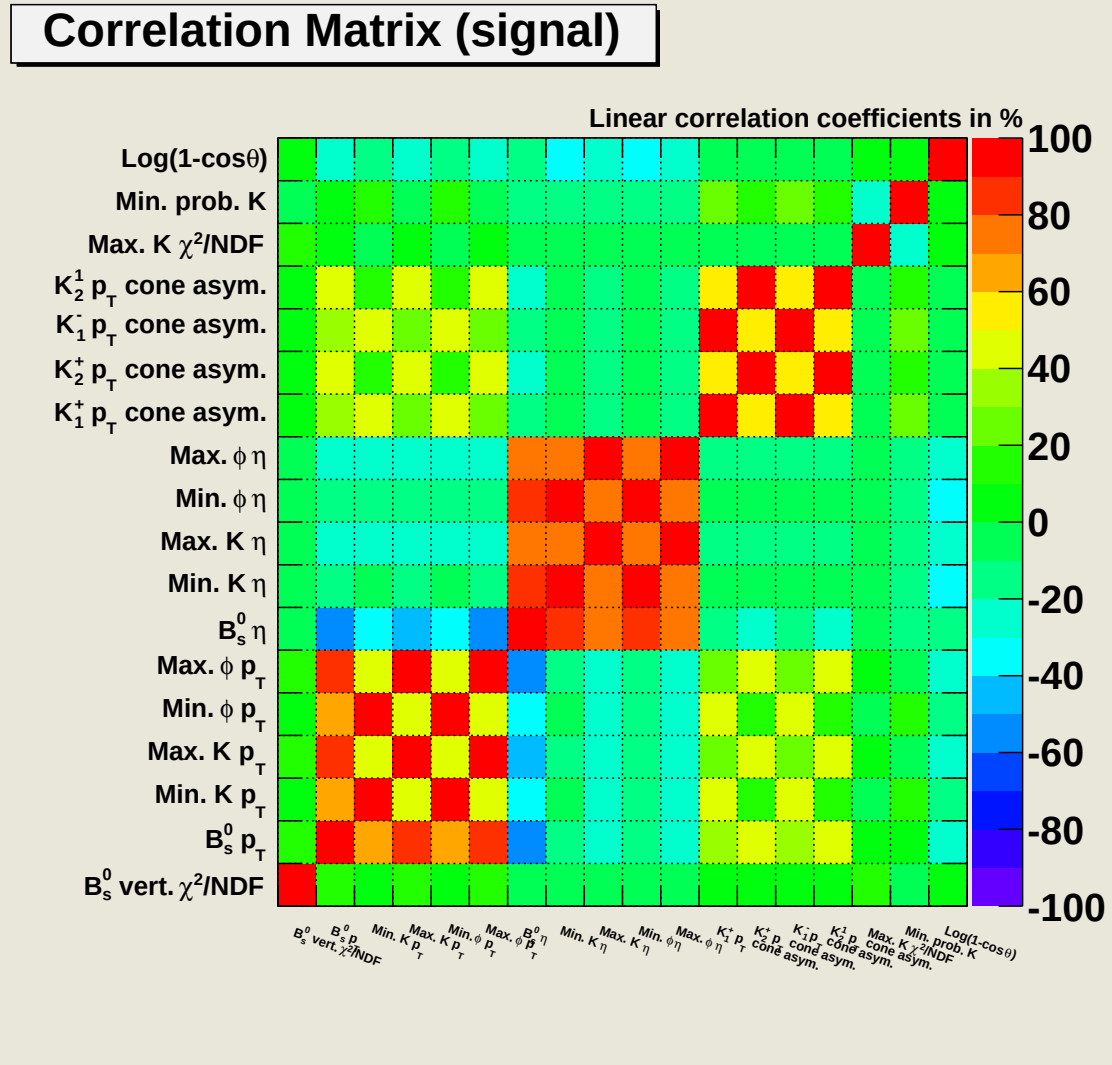

Figure B.7: Correlation Matrix between input variables for the simulated $B_s^0 \to \phi\phi$ 8 TeV events.

C Part III: Performance of the LHCb scintillating fibe tracker

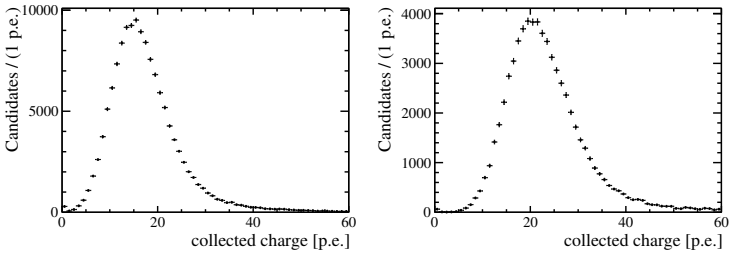

(a) (b)

Figure C.1: Light yield distributions of clusters found in the DUT of all accepted events for tracks at a distance of (a) 240 cm and (b) 50 cm from the SiPM arrays. The angle of the module with respect to the beam is 10°. The light yields are not corrected for crosstalk.

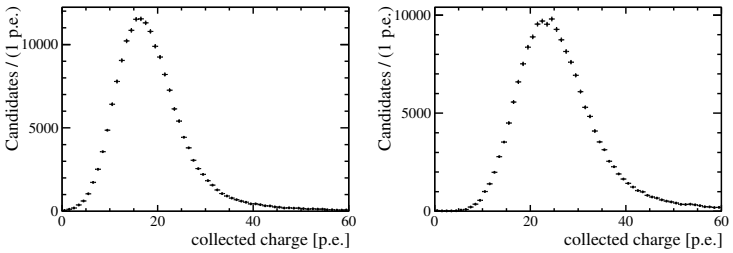

(a) (b)

Figure C.2: Light yield distributions of clusters found in the DUT of all accepted events for tracks at a distance of (a) 240 cm and (b) 50 cm from the SiPM arrays. The angle of the module with respect to the beam is 20°. The light yields are not corrected for crosstalk.

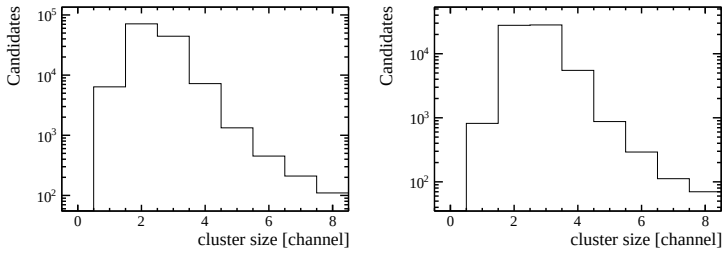

(a) (b)

Figure C.3: Cluster size distributions of clusters found in the DUT of all accepted events when applying the foreseen LHCb thresholds of (1.5, 2.5, 4.0) for tracks at a distance of (a) 240 cm and (b) 50 cm from the SiPM arrays. The angle of the module with respect to the beam is 10°. The light yields are not corrected for crosstalk.

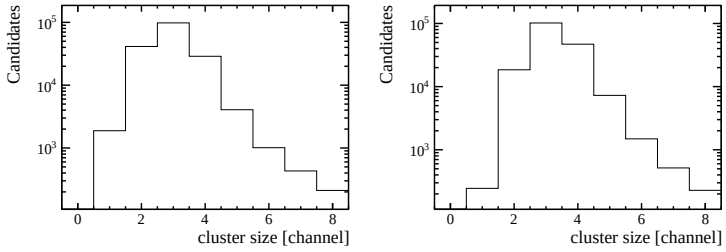

(a) (b)

Figure C.4: Cluster size distributions of clusters found in the DUT of all accepted events when applying the foreseen LHCb thresholds of (1.5, 2.5, 4.0) for tracks at a distance of (a) 240 cm and (b) 50 cm from the SiPM arrays. The angle of the module with respect to the beam is 20°. The light yields are not corrected for crosstalk.

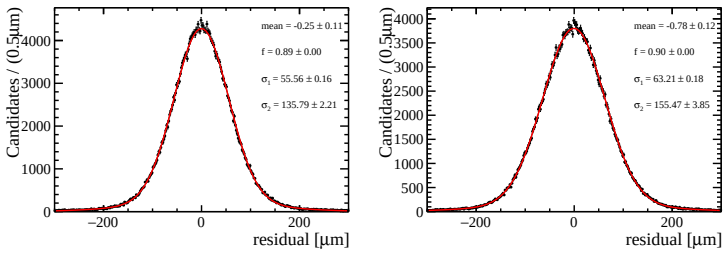

(a) (b)

Figure C.5: Residual distributions of the SciFi cluster positions with respect to the reconstructed TimePix tracks using the (a) charge-weighted mean and (b) PACIFIC-like hit-weighted mean for tracks at a distance of 120 cm from the SiPM arrays. The angle of the module with respect to the beam is 0°.

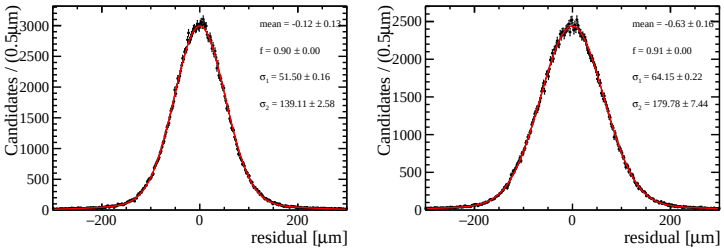

(a) (b)

Figure C.6: Residual distributions of the SciFi cluster positions with respect to the reconstructed TimePix tracks using the (a) charge-weighted mean and (b) PACIFIC-like hit-weighted mean for tracks at a distance of 50 cm from the SiPM arrays. The angle of the module with respect to the beam is 0°.

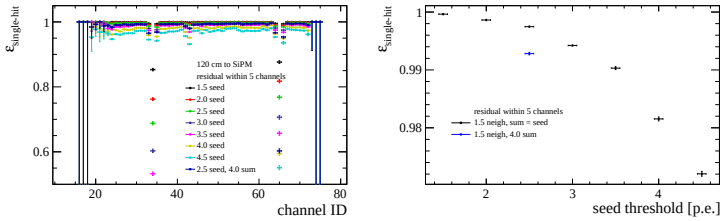

(a) (b)

Figure C.7: (a) Single-hit efficiency vs. SiPM channels ID for tracks at a distance of 120 cm from the SiPM arrays. For illustration purposes, channel 65 corresponds to the gap between the two dies. Channel 33 is a dead channel. (b) Fitted single-hit efficiency obtained from a fit to the plateau for channels with ID larger than 45 and less than 60, significantly away from the gap, as a function of the seed threshold. The blue point refers to the foreseen LHCb thresholds of (1.5, 2.5, 4.0).

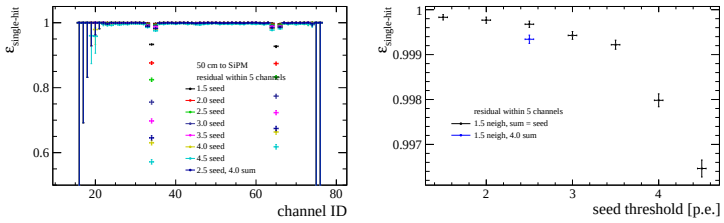

(a) (b)

Figure C.8: (a) Single-hit efficiency vs. SiPM channels ID for tracks at a distance of 50 cm from the SiPM arrays. For illustration purposes, channel 65 corresponds to the gap between the two dies. (b) Fitted single-hit efficiency obtained from a fit to the plateau for channels with ID larger than 45 and less than 60, significantly away from the gap, as a function of the seed threshold. The blue point refers to the foreseen LHCb thresholds of (1.5, 2.5, 4.0).